VOL. 107 NO. HY12. DEC. 1981

JOURNAL OF THE HYDRAULICS DIVISION

PROCEEDINGS OF
THE AMERICAN SOCIETY
OF CIVIL ENGINEERS

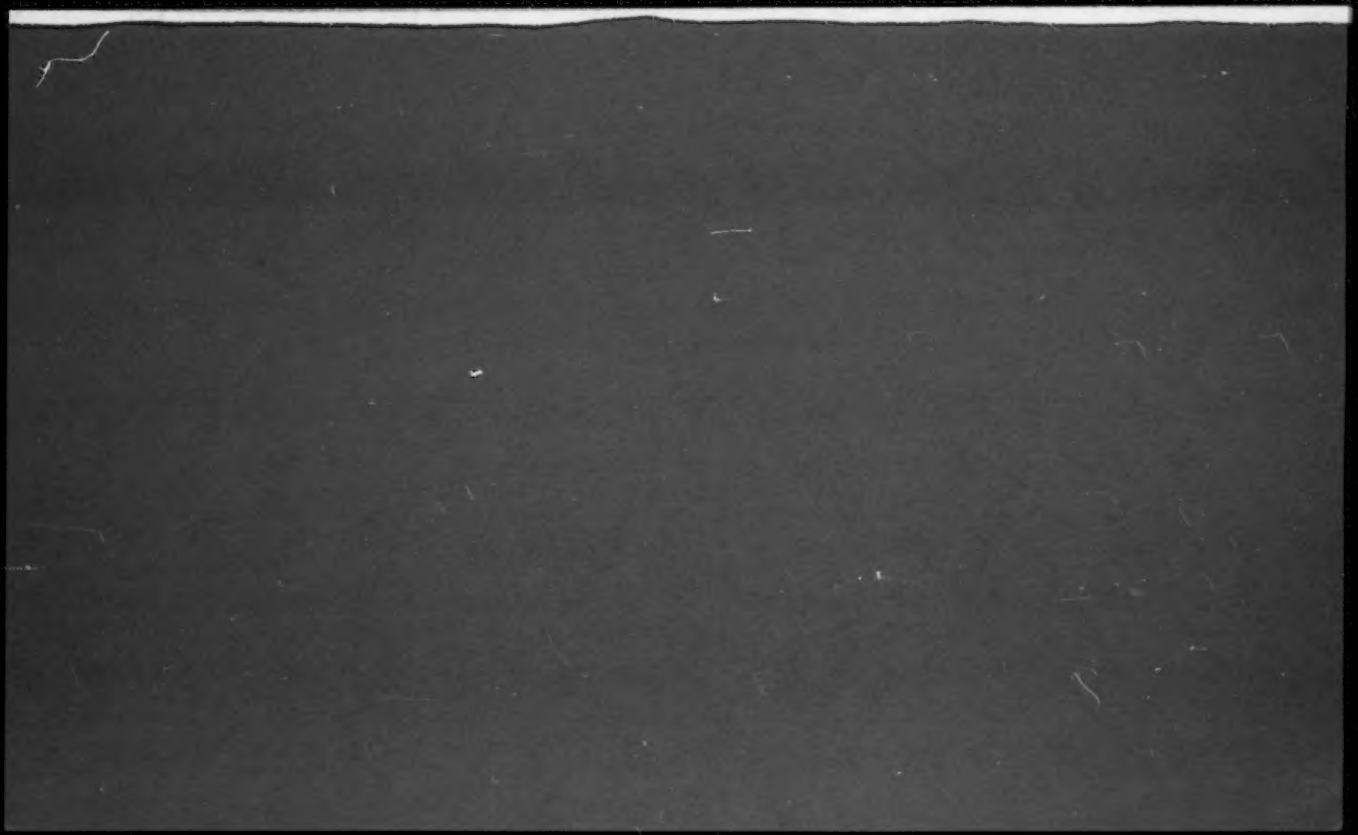

VOL. 107 NO. HY12. DEC. 1981

JOURNAL OF THE HYDRAULICS DIVISION

PROCEEDINGS OF
THE AMERICAN SOCIETY
OF CIVIL ENGINEERS

Copyright© 1981 by
American Society
of Civil Engineers
All Rights Reserved
ISSN 0044-796X

Melvin W. Anderson, Editor
University of South Florida

AMERICAN SOCIETY OF CIVIL ENGINEERS

BOARD OF DIRECTION

President
James R. Sims

Past President
Irvan F. Mendenhall

President Elect
John H. Wiedeman

Vice Presidents
Lyman R. Gillis
Albert A. Grant
Paul A. Kuhn
William H. Taylor

Directors
Martin G. Abegg
L. G. Byrd
Frederick W. DeWitt
Larry J. Feeser
John A. Focht, Jr.
Sergio Gonzalez-Karg
Kenneth D. Hansen
Ronald C. Hirschfield
Louis M. Laushey
Leon D. Luck
Arthur R. McDaniel
Robert L. Morris
Paul R. Munger
William R. Neuman
Leonard S. Oberman
John D. Parkhurst
Celestino R. Pennoni
Robert B. Rhode
Gerald E. Speitel
Lawrence E. Wilson, Jr.
Richard S. Woodruff

EXECUTIVE OFFICERS

Eugene Zwoyer, *Executive Director*
Julie E. Gibouleau, *Assistant to the Executive Director*
Louis L. Meier, *Washington Counsel/Assistant Secretary*
William H. Wisely, *Executive Director Emeritus*
Michael N. Salgo, *Treasurer*
Elmer B. Isaak, *Assistant Treasurer*

STAFF DIRECTORS

Donald A. Buzzell, *Managing Director for Education and Professional Affairs*
Robert A. Crist, Jr., *Managing Director for Publications and Technical Affairs*
Alexandra Bellow, *Director, Human Resources*
Joseph A. DeFiglia, *Director, Management Information Services*
David Dresia, *Director, Publications Production and Marketing*
Barker D. Herr, *Director, Membership*
Richard A. Jeffers, *Controller*
Carl E. Nelson, *Director, Field Services*
Don P. Reynolds, *Director, Policy, Planning and Public Affairs*
Bruce Rickerson, *Director, Legislative Services*
Albert W. Turchick, *Director, Technical Services*
George K. Wadlin, *Director, Education Services*
R. Lawrence Whipple, *Director, Engineering Management Services*

COMMITTEE ON PUBLICATIONS

William R. Neuman, *Chairman*
Martin G. Abegg
John A. Focht, Jr.
Ronald C. Hirschfield
Paul R. Munger
Lawrence E. Wilson, Jr.

HYDRAULICS DIVISION

Executive Committee
Rudolph P. Savage, *Chairman*
George E. Hecker, *Vice Chairman*
Ronald E. Nece
Patrick J. Ryan
Charles S. Mifkovic, *Secretary*
John J. Cassidy, *Management Group D Contact Member*

Publications Committee
Melvin W. Anderson, ***Chairman and Editor***
John A. Hoopes, ***Vice Chairman***
Philip H. Burgi, *Hydraulic Structures*
Richard H. (Pete) Hawkins, *Surface Water Hydrology*
John A. Hoopes, *Hydromechanics, General*
Gerhard H. Jirka, *Hydraulic Transport and Dispersion*
Chintu Lai, *Hydromechanics, Open Channels*
Frederick A. Locher, *Hydromechanics, Open Channels*
Donn G. DeCoursey, *Sedimentation*
Bryan R. Pearce, *Tidal Hydraulics*
John A. Roberson, *Hydromechanics, Closed Conduits*
John L. Wilson, *Groundwater Hydrology*
George E. Hecker, *Exec. Comm. Contact Member*

PUBLICATION SERVICES DEPARTMENT

David Dresia, *Director, Publications Production and Marketing*

Technical and Professional Publications

Richard R. Torrens, *Manager*
Chuck Wahrhaftig, *Chief Copy Editor*
Corinne Bernstein, *Copy Editor*
Linda Ellington, *Copy Editor*
Walter Friedman, *Copy Editor*
Richard C. Scheblein, *Draftsman*

Information Services

Melanie G. Edwards, *Editor*

PERMISSION TO PHOTOCOPY JOURNAL PAPERS

Permission to photocopy for personal or internal reference beyond the limits in Sections 107 and 108 of the U.S. Copyright Law is granted by the American Society of Civil Engineers for libraries and other users registered with the Copyright Clearance Center, 21 Congress Street, Salem, Mass. 01970, provided the appropriate fee is paid to the CCC for all articles bearing the CCC code. Requests for special permission or bulk copying should be addressed to the Manager of Technical and Professional Publications, American Society of Civil Engineers.

CONTENTS

The General Hydrologic System Model
by Roger C. McCann and Vijay P. Singh 1581

Resistance Equation for Large-Scale Roughness
by James C. Bathurst, Ruh-Ming Li, and Daryl B. Simons 1593

Measurement of Air in Flowing Water
by Alan F. Babb and Henry C. Aus 1615

Radial Source-Sink Flow in Stratified Ocean
by Gerhard H. Jirka, R. Peter Johnson, and Frank E. Sargent 1631

Vertical Round Buoyant Jet in Shallow Water
by Joseph H. W. Lee and Gerhard H. Jirka 1651

Transverse Bed Slope in Alluvial Channel Bends
by A. Jacob Odgaard 1677

Shear Stress Distribution at Channel Constrictions
by Bishnu P. Das and Ronald D. Townsend 1695

The Journal of the Hydraulics Division (ISSN 0044-796X) is published monthly by the American Society of Civil Engineers. Publications office is at 345 East 47th Street, New York, N.Y. 10017. Address all ASCE correspondence to the Editorial and General Offices at 345 East 47th Street, New York, N.Y. 10017. Allow six weeks for change of address to become effective. Subscription price to members is $16.50. Nonmember subscriptions available; prices obtainable on request. Second-class postage paid at New York, N.Y. and at additional mailing offices. HY.

POSTMASTER: Send address changes to American Society of Civil Engineers, 345 East 47th Street, New York, NY 10017.

The Society is not responsible for any statement made or opinion expressed in its publications.

Conformal Mapping for Channel Junction Flow
by Pashupati N. Modi, Pitamber D. Ariel, and Mohan M. Dandekar 1713

DISCUSSION

Proc. Paper 16684

Heat Loss from Sidearms of Cooling Lakes, by Terry W. Sturm and John F. Kennedy (May, 1980. Prior Discussions: Apr., 1981).
closure 1737
errata 1738

Transverse Mixing Tests in Natural Streams, by Spyridon Beltaos (Oct., 1980. Prior Discussions: June, 1981).
closure 1738
errata 1746

Sedimentation in Iron Gates Reservoir on the Danube,[a] by Vlad Focsa (Oct., 1980).
by S. Bruk, Vera Miloradov, and V. Milišić 1746

Total Load Transport in Alluvial Channels,[a] by Kittur G. Ranga Raju, Ramachandra J. Garde, and Ramesh C. Bhardwaj (Feb., 1981).
by William R. Brownlie 1750

INFORMATION RETRIEVAL

The key words, abstract, and reference "cards" for each article in this Journal represent part of the ASCE participation in the EJC information retrieval plan. The retrieval data are placed herein so that each can be cut out, placed on a 3 × 5 card and given an accession number for the user's file. The accession number is then entered on key word cards so that the user can subsequently match key words to choose the articles he wishes. Details of this program were given in an August, 1962 article in CIVIL ENGINEERING, reprints of which are available on request to ASCE headquarters.

[a] Discussion period closed for this paper. Any other discussion received during this discussion period will be published in subsequent Journals.

16755 THE GENERAL HYDROLOGIC SYSTEM MODEL

KEY WORDS: **Data uniformity; Hydrologic models; Instantaneous unit hydrograph;** Rainfall-runoff relationships; Runoff; Watersheds

ABSTRACT: The general Hydrologic System (GHS) model is considered. It is found that there are inconsistencies in equations for the instantaneous unit hydrograph (IUH) which were derived using the GHS Model. The existence of these inconsistencies is supported by an analysis of the data reported in the literature dealing with watershed runoff modeling and flood routing in open channels. It is shown that if simple, yet realistic, initial conditions are assumed then the GHS model becomes considerably simpler, and the above inconsistencies no longer remain. The reported data supports this assumption.

REFERENCE: McCann, Roger C. (Assoc. Prof., Dept. of Mathematics, Mississippi State Univ., Mississippi State, Miss. 39762), and Singh, Vijay P., "The General Hydrologic System Model," *Journal of the Hydraulics Division,* ASCE, Vol. 107, No. HY12, **Proc. Paper 16755**, December, 1981, pp. 1581-1592

16743 RESISTANCE EQUATION FOR LARGE-SCALE ROUGHNESS

KEY WORDS: Boulders; Channels (waterways); **Drag;** Equations; **Flow resistance;** Fluid flow; **Flumes; Fluvial hydraulics; River flow; Roughness (hydraulic);** Slopes

ABSTRACT: A theory of flow resistance for large-scale roughness is developed, the main points of which are supported by a flume study from which the outline of a process-based resistance equation is determined. Rivers with large-scale roughness have steep slopes and depths of the same order of magnitude as the bed material size. Flow resistance depends on the form drag of the roughness elements and their disposition in the channel. Theoretical considerations show resistance to be a function of Reynolds number, Froude number, roughness geometry, and channel geometry. These processes are examined using the results of flume experiments based on five different roughness beds and a wide range of flows. Semi-empirical analysis supports the theory and allows the development of a theoretical power law resistance equation which accounts for most of the processes. A summary of the data is presented for use in other research studies.

REFERENCE: Bathurst, James C. (Sr. Scientific Officer, Inst. of Hydrology, Wallingford, Oxon, United Kingdom), Li, Ruh-Ming, and Simons, Daryl B., "Resistance Equation for Large-Scale Roughness," *Journal of the Hydraulics Division,* ASCE, Vol. 107, No. HY12, **Proc. Paper 16743**, December, 1981, pp. 1593-1613

16742 MEASUREMENT OF AIR IN FLOWING WATER

KEY WORDS: **Aeration; Air entrainment;** Gamma rays; Hot film anemometers; **Hydraulic jump; Hydraulics; Two phase flow;** Void ratio; Water flow

ABSTRACT: Procedures are developed using gamma ray and hot-film anemometer methods for determining void fraction and sizes of air bubbles entrained in flowing water. The hot-film data are analyzed by computer. The gamma ray data are used to determine the duration factor, a term accounting for the additional time that must be added to the time sensed by the hot-film anemometer to arrive at the true bubble duration. The duration factor is found to be a function of velocity. The procedures are developed using a hydraulic jump with Froude number 6. The continuity equation is used in conjunction with void fraction and mean velocity data to compute the location of air entering and leaving the jump.

REFERENCE: Babb, Alan F. (Head of Albrook Hydr, Lab., and Prof. of Civ. and Environmental Engrg., Washington State Univ., Pullman, Wash. 99164), and Aus, Henry C., "Measurement of Air in Flowing Water," *Journal of the Hydraulics Division,* ASCE, Vol. 107, No. HY12, **Proc. Paper 16742**, December, 1981, pp. 1615-1630

16766 RADIAL SOURCE-SINK FLOW IN STRATIFIED OCEAN

KEY WORDS: Buoyancy; **Energy conversion; Energy conversion heat sources;** Fluid mechanics; Mixing; Ocean environments; **Oceanic Processes; Solar energy;** Stratified flow

ABSTRACT: Proposed ocean thermal energy conversion (OTEC) plants represent large sources of momentum discharging into the stratifies tropical ocean. The mixing characteristics induced by such sources in combination with simultaneous sink flows into the plant intake are considered under the assumption of a discretely stratified ocean with radial symmetry about the OTEC plant. The problem is formulated with radial jet integral equations which account for the loss of jet momentum and for the pressure gradient, both arising from the sink flow action, and for buoyant damping of vertical entrainment. For extreme shallow upper layer conditions or for large momentum sources, the source-sink flow is predicted to break down into a recirculating eddy giving rise to undesirable temperature reductions of the OTEC plant intake. The model predictions are verified in laboratory experiments which have a somewhat different geometry but a similar dynamic interaction. Design considerations and estimates of maximum OTEC plant sizes are given.

REFERENCE: Jirka, Gerhard H. (Asst. Prof., School of Civ. and Environmental Engrg., Cornell Univ., Ithaca, N.Y. 14853), Johnson, R. Peter, and Sargent, Frank E., "Radial Source-Sink Flow in Stratified Ocean," *Journal of the Hydraulics Division*, ASCE, Vol. 107, No. HY12, **Proc. Paper 16766**, December, 1981, pp. 1631-1650

16744 VERTICAL ROUND BUOYANT JET IN SHALLOW WATER

KEY WORDS: Buoyancy; **Entrainment; Environmental engineering;** Hydraulic jump; Hydraulics; Stratified flow; **Temperature distribution; Thermal pollution; Waste heat**

ABSTRACT: The stability and bulk mixing characteristics of an axisymmetric turbulent buoyant jet discharging vertically into a stagnant waterbody of large horizontal extent is studied theoretically and experimentally. A stable discharge configuration is defined as one in which a buoyant surface layer is formed which spreads radially from the source and does not communicate with the initial buoyant jet region. On the other hand, the discharge configuration is unstable when recirculation cells exist around the jet efflux. A semi-empirical theory shows the discharge stability is only dependent on the dynamic interaction of three near-field regions—the buoyant jet region, surface impingement region, and radial internal hydraulic jump region. A series of laboratory experiments were performed with a half-jet, using heat as source of buoyancy, and inserting a plane of symmetry in a large model basin. The experimental results are in good agreement with the theoretical predictions, both as regards the stability criterion and the near field mixing characteristics.

REFERENCE: Lee, Joseph H. W. (Asst. Prof., Dept. of Civ. Engrg., Univ. of Delaware, Newark, Del.), and Jirka, Gerhard H., "Vertical Round Buoyant Jet in Shallow Water," *Journal of the Hydraulics Division*, ASCE, Vol. 107, No. HY12, **Proc. Paper 16744**, December, 1981, pp. 1651-1675

16750 TRANSVERSE BED SLOPE IN ALLUVIAL CHANNEL BENDS

KEY WORDS: **Alluvial streams; Channel bends;** Channels; Erosion; **Fluid flow; Hydraulics;** Rivers; **Sediments;** Shear stress; Water flow; **Waterways**

ABSTRACT: The study has reviewed existing analytical models for the prediction of the steady-state transverse bed profile in channel bends, formulated an alternative model, and compared their predictive capability by laboratory and field data. The alternative model, which is based on a theory for the critical conditions for sediment entrainment, gives good agreement between measured and predicted bed slopes. The study shows that the key parameter in all available models is grain size. The prediction of the complete bed topography of a given bend for a given flow data requires knowledge of the spatial variation of the grain size.

REFERENCE: Odgaard, A. Jacob (Asst. Prof., Inst. of Hydr. Research, Univ. of Iowa, Iowa City, Iowa 52242), "Transverse Bed Slope in Alluvial Channel Bends," *Journal of the Hydraulics Division*, ASCE, Vol. 107, No. HY12, **Proc. Paper 16750**, December, 1981, pp. 1677-1694

16760 SHEAR DISTRIBUTION AT CHANNEL CONSTRICTIONS

KEY WORDS: **Boundary shear; Channels; Constrictions;** Contraction; Shear distribution; Velocity; **Velocity distribution**

ABSTRACT: A Comprehensive laboratory study, employing an appropriate range of flow Froude Number and contraction ratio, was undertaken for curvilinear and accelerating flow occuring against the advancing face and through the gap at end-dumped channel constrictions. Pertinent results on flow pattern, velocity distribution and boundary shear distribution, are reported and discussed. The locus of the shear maxima, which attains its highest point value on the advancing face of the constriction is observed to essentially overlap the path of the high velocity filament; a pattern that is similar to that found in a channel bend. Results show that which an increase in the contraction ratio, the corresponding increase in boundary shear over that in the uncontracted channel is exponential, although the increase in velocity is only nominal. A followup laboratory study on shear distribution at over-bank channel constrictions shows an identical trend.

REFERENCE: Das, Bishnu P. (Superintending Engr., (Civ.) Dept. of Irrigation, Orissa, India.), and Townsend, Ronald D., "Shear Stress Distribution at Channel Constrictions," *Journal of the Hydraulics Division,* ASCE, Vol. 107, No. HY12, **Proc. Paper 16760**, December, 1981, pp. 1695-1711

16763 CONFORMAL MAPPING FOR CHANNEL JUNCTION FLOW

KEY WORDS: Channel bends; **Channel flow; Channels (waterways); Conformal mapping;** Free streamlines; **Hydraulics; Hydrodynamics;** Stagnation point

ABSTRACT: An analysis of the flow behavior at rectangular channel junctions with combining flow using the conformal mapping technique has been presented. Equations for the location of the stagnation point and the free-streamline for different flow conditions at rectangular channel junctions have been developed. These equations have been solved numerically by using Simpsons rule. It is observed that for each channel junction there is a unique value of discharge ratio corresponding to which the stagnation point coincides with the upstream corner of the junction. The value of the discharge ratio depends on the junction angle as well as on the bed-widths of the channels. It is also indicated that the zone of stagnant fluid between the free-streamline and the channel boundary depends on the junction angle and the location of the stagnation point.

REFERENCE: Modi, Pashupati N. (Reader, Dept. of Civ. Engrg., Malaviya Regional Engrg. Coll.,Jaipur, India.), Ariel, Pitamber D., and Dandekar, Mohan M., "Conformal Mapping for Channel Junction Flow," *Journal of the Hydraulics Division,* ASCE, Vol. 107, No. HY12, **Proc. Paper 16763**, December, 1981, pp. 1713-1733

U.S. Customary-SI Conversion Factors

In accordance with the October, 1970 action of the ASCE Board of Direction, which stated that all publications of the Society should list all measurements in both U.S. Customary and SI (International System) units, the following list contains conversion factors to enable readers to compute the SI unit values of measurements. A complete guide to the SI system and its use has been published by the American Society for Testing and Materials. Copies of this publication (ASTM E-380) can be purchased from ASCE at a price of $3.00 each; orders must be prepaid.

All authors of *Journal* papers are being asked to prepare their papers in this dual-unit format. To provide preliminary assistance to authors, the following list of conversion factors and guides are recommended by the ASCE Committee on Metrication.

To convert	To	Multiply by
inches (in.)	millimeters (mm)	25.4
feet (ft)	meters (m)	0.305
yards (yd)	meters (m)	0.914
miles (miles)	kilometers (km)	1.61
square inches (sq in.)	square millimeters (mm^2)	645
square feet (sq ft)	square meters (m^2)	0.093
square yards (sq yd)	square meters (m^2)	0.836
square miles (sq miles)	square kilometers (km^2)	2.59
acres (acre)	hectares (ha)	0.405
cubic inches (cu in.)	cubic millimeters (mm^3)	16,400
cubic feet (cu ft)	cubic meters (m^3)	0.028
cubic yards (cu yd)	cubic meters (m^3)	0.765
pounds (lb) mass	kilograms (kg)	0.453
tons (ton) mass	kilograms (kg)	907
pound force (lbf)	newtons (N)	4.45
kilogram force (kgf)	newtons (N)	9.81
pounds per square foot (psf)	pascals (Pa)	47.9
pounds per square inch (psi)	kilopascals (kPa)	6.89
U.S. gallons (gal)	liters (L)	3.79
acre-feet (acre-ft)	cubic meters (m^3)	1,233

THE GENERAL HYDROLOGIC SYSTEM MODEL

By Roger C. McCann[1] and Vijay P. Singh,[2] A. M. ASCE

INTRODUCTION

The General Hydrologic System (GHS) model developed by Chow and Kulandaiswamy (4,5,7) has been reported and utilized in several studies (2,3,6,8, 9,10,11,12) dealing with watershed runoff modeling, and flood routing in open channels. In its general form, the GHS model, as expressed by Kulandaiswamy (7), Chow (4), and Chow and Kulandaiswamy (5), can be written as

$$Q + \sum_{i=0}^{M} a_i \frac{d^{i+1}Q}{dt^{i+1}} = I - \sum_{j=0}^{N} b_j \frac{d^{j+1}I}{dt^{j+1}} \quad \ldots\ldots\ldots\ldots\ldots\ldots\ldots\ldots (1)$$

in which Q = surface runoff; I = rainfall excess; t = time; d^iQ/dt^i = ith derivative of Q with respect to t; d^jI/dt^j = jth derivative of I with respect to t; a_i = ith coefficient associated with $(i + 1)$st time derivative of Q; b_j = jth coefficient associated with $(j + 1)$st derivative of I; M = nonnegative integer; and N = nonnegative integer with $M > N$. The coefficients a_i and b_j are functions of I and Q. By fitting various forms of Eq. 1 to observed watershed runoff data, Chow and Kulandaiswamy (5) concluded that M and N could be taken as 2 and 1, respectively. They reported that higher derivatives of I and Q were insignificant for the cases which they studied and could, therefore, be ignored without sacrificing accuracy of the model. Further, the coefficients, a_i and b_j, were assumed to be either constant, or only functions of some characteristics of Q and I, such as mean or maximum. In this paper we will consider them to be constant.

Thus, the GHS model was reduced to

$$Q + a_0\frac{dQ}{dt} + a_1\frac{d^2Q}{dt^2} + a_2\frac{d^3Q}{dt^3} = I - b_0\frac{dI}{dt} - b_1\frac{d^2I}{dt^2} \quad \ldots\ldots\ldots\ldots (2)$$

which was further written, using linear operator notation, as

[1]Assoc. Prof., Dept. of Mathematics, Mississippi State Univ., Mississippi State, Miss. 39762.

[2]Assoc. Prof., Dept. of Civ. Engrg., Louisiana State Univ., Baton Rouge, La. 70803.

Note.—Discussion open until May 1, 1982. To extend the closing date one month, a written request must be filed with the Manager of Technical and Professional Publications, ASCE. Manuscript was submitted for review for possible publication on July 28, 1980. This paper is part of the Journal of the Hydraulics Division, Proceedings of the American Society of Civil Engineers, ©ASCE, Vol. 107, No. HY12, December, 1981. ISSN 0044-796X/81/0006-1581/$01.00.

$$Q = \left[\frac{(1 - b_0 D - b_1 D^2)}{1 + a_0 D + a_1 D^2 + a_2 D^3}\right] I \quad \ldots\ldots (3)$$

in which $D = d/dt$. Eq. 3 is valid on the assumption that there is no common factor between the numerator and denominator. The instantaneous unit hydrograph (IUH), hereafter denoted by $u(t)$, is a solution of Eq. 3 when I is the delta function $\delta(t)$.

Chow and Kulandaiswamy (4,5,7) derived instantaneous unit hydrographs using Eq. 3 for four different cases depending upon the nature of the three roots of the denominator in Eq. 3. These cases are: (1) The three roots are real and unequal; (2) all are real with two being equal; (3) all are real and equal; and (4) one is real and two are complex conjugates. We reproduce their solutions for each of the four cases with m, n, and p being the three roots.

Case 1: $m \neq n \neq p$. The IUH, $u(t)$, is

$$u(t) = -mnp\,(Ae^{mt} + Be^{nt} + Ce^{pt}) \quad \ldots\ldots (4a)$$

in which $$A = \frac{1 - b_0 m - b_1 m^2}{m^2 - m(n + p) + np} \quad \ldots\ldots (4b)$$

$$B = \frac{1 - b_0 n - b_1 n^2}{n^2 - n(m + p) + mp} \quad \ldots\ldots (4c)$$

$$C = \frac{1 - b_0 p - b_1 p^2}{p^2 - p(m + n) + mn} \quad \ldots\ldots (4d)$$

Case 2: m, n, p Real and $n = p$. The IUH, $u(t)$, is

$$u(t) = -mn^2\,(Ae^{mt} + Be^{nt} + Ce^{pt}) \quad \ldots\ldots (5a)$$

in which $$C = \frac{1 - b_0 n - b_1 n^2}{(n - m)} \quad \ldots\ldots (5b)$$

$$B = \frac{b_0 n + C(n - 2m) - 2}{n^2 - mn} \quad \ldots\ldots (5c)$$

$$A = -b_1 - B \quad \ldots\ldots (5d)$$

$$\frac{A}{m} + \frac{B}{n} - \frac{C}{n^2} = \frac{1}{mn^2} \quad \ldots\ldots (5e)$$

Case 3: m, n, p, Real and $m = n = p$. The IUH, $u(t)$, is

$$u(t) = (A + Bt + Ct^2)\,e^{mt} \quad \ldots\ldots (6a)$$

in which $$A = -b_1 m^3 \quad \ldots\ldots (6b)$$

$$B = -b_0 m^2 - 2b_1 m^4 \quad \ldots\ldots (6c)$$

$$C = -\frac{1}{2}(m^3 - b_0 m^4 - b_1 m^5) \quad \ldots\ldots (6d)$$

$$\frac{A}{m} - \frac{B}{m^2} + \frac{2C}{m^3} = 1 \quad \ldots \ldots \ldots

Kulandaiswamy (5,7) and reproduced in Eqs. 4–7. A straight forward calculation using Eqs. 4–7 shows the following:

1. In the first case, when $m \neq n \neq p$, $u(0) = +mnpb_1 = -b_1/a_2$.
2. In the second case, when m, n, p are real and $n = p$, $u(0) = -b_1/a_2$.
3. In the third case, when m, n, p are real and $m = n = p$, $u(0) = b_1/a_2$.
4. In the fourth case, when m is real, and n and p are complex conjugates, $u(0) = -b_1/a_2$.

Thus, it is clear that $u(0) \neq 0$ in any of the four cases, since $b_1 \neq 0$ in any of the 47 rainfall excess-runoff patterns on seven different watersheds analyzed in (5,7) for the GHS model. Therefore, this result is not consistent with what the preceding quote implies. Moreover, if $b_1 \neq 0$, the solutions in the four cases do not satisfy the same initial conditions.

Since the roots of m, n, and p are functions of a_0, a_1, and a_2, the initial value of the IUH is not a constant function of the coefficients in Eq. 3. There is no apparent reason why this should be the case.

For the sake of argument, suppose that $u(0) \neq 0$, i.e., suppose $b_1 \neq 0$. If m, n, and p are distinct real numbers which are close to some number q, then $1 + a_0D + a_1D^2 + a_2D^3 = a_2(D + m)(D + n)(D + p)$ and $u(0) = -b_1/a_2$. However, if $m = n = p = q$, then $1 + a_0D + a_1D^2 + a_2D^3 = a_2(D + q)^3$, and $u(0) = b_1/b_2$. Thus, if $u(0) \neq 0$, the IUH does not depend continuously on the coefficients a_1 and a_0. We believe that it is unreasonable to assume that the problem of computing the IUH is ill posed in this manner. Therefore, we consider $u(0) = 0$ to be a reasonable initial condition for the IUH.

For brevity and purposes of conserving space, we will hereafter restrict our analysis to the first case, $m \neq n \neq p$. Not only is this case the most important of all, but the ensuing analysis, and the conclusions reached for this case, will also hold for the remainder of the cases.

The question now is: If the preceding initial conditions were not used to determine the IUH or USR, what conditions were used to obtain a unique solution of the differential equation in Eq. 3? No method of solution is indicated (5). However, it is indicated that the method of partial fraction was used. Using the method of partial fraction we find that

$$Q(t) = -mnp\left(\frac{A}{D-m} + \frac{B}{D-n} + \frac{C}{D-p}\right) i(t) \quad \ldots\ldots\ldots\ldots\ldots\ldots (8)$$

in which A, B, C are given in Eqs. 4*a–d*. We now consider the case $i(t) = \delta(t)$ so that $u(t)$ is a solution of

$$u(t) = -mnp\left(\frac{A}{D-m} + \frac{B}{D-n} + \frac{C}{D-p}\right)\delta(t) \quad \ldots\ldots\ldots\ldots\ldots\ldots (9)$$

Inverting the preceding differential operators, we have

$$u(t) = -mnp\,[Ae^{-mt} \int e^{mt}\delta(t)\,dt + Be^{-nt} \int e^{nt}\delta(t)\,dt$$

$$+ ce^{pt} \int e^{-pt}\delta(t)\,dt] \quad \ldots\ldots\ldots\ldots\ldots\ldots\ldots\ldots\ldots\ldots (10)$$

It is known that the derivative of the Heaviside function

$$H(t) = \begin{cases} 1 & \text{if } t > 0 \\ 0 & \text{if } t \le 0 \end{cases} \quad \ldots\ldots\ldots\ldots\ldots\ldots\ldots\ldots\ldots\ldots\ldots\ldots\ldots\ldots (11)$$

is the delta function, i.e., $H'(t) = \delta(t)$. It is also known that if f is a continuous function on $(-\infty, \infty)$ with $f(0) = 1$, then $f(t)\delta(t) = \delta(t)$. Thus

$$\int e^{mt}\delta(t)\,dt = H(t) + C_1'; \quad \int e^{nt}\delta(t)dt = H(t) + C_2';$$

$$\int e^{pt}\delta(t)dt = H(t) + C_3' \quad \ldots\ldots\ldots\ldots\ldots\ldots\ldots\ldots\ldots\ldots\ldots\ldots\ldots\ldots (12)$$

in which C_1', C_2', C_3' = arbitrary constants. It follows from Eq. 10 that for $t > 0$ the IUH has the form (in which $c_i = C_i' + 1$ for $i = 1, 2, 3$):

$$u(t) = -mnp\,(Ac_1e^{mt} + Bc_2e^{nt} + Cc_3e^{pt}) \quad \ldots\ldots\ldots\ldots\ldots\ldots\ldots\ldots\ldots\ldots (13)$$

for some choice of the constants c_1, c_2, c_3. Comparing Eq. 13 with the IUH given in Refs. 5 and 7, and reproduced in Eq. 4*a*, we conclude that $c_1 = c_2 = c_3 = 1$ or, equivalently, $C_1', C_2', C_3' = 0$. Without initial conditions, or

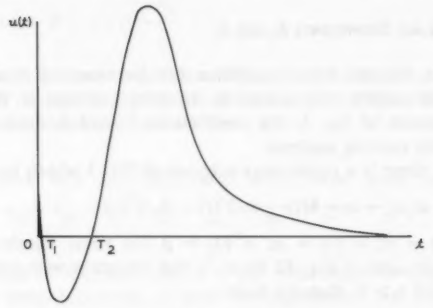

FIG. 1.—Typical IUH Obtained from GHS Model of Chow and Kulandaiswamy (4,5,7)

some other conditions, there is no way to justify this choice of these constants.

Furthermore, Kulandaiswamy (7) graphs his IUH for a number of rainfall excess-runoff events on seven different watersheds. For purposes of illustration, we will consider only the graphs in Ref. 7. In each case the graph resembles Fig. 1. Let T_1, and T_2, $T_1 < T_2$, be the times at which the IUH is zero. From the graph in Fig. 1 (and those cited), it is clear that

$$\int_0^{T_2} u(t)\,dt < 0 \quad \ldots\ldots\ldots\ldots\ldots\ldots\ldots\ldots\ldots\ldots\ldots\ldots\ldots\ldots\ldots\ldots (14)$$

This is physically unrealistic. Moreover, an examination of the IUH graphs given by Kulandaiswamy (7) indicates that $T_2 - T_1$ can be as high as approx 40% of T_p, IUH peak time. Thus, the period of negative IUH ordinates is significant in several cases which they studied.

It may be appropriate to remark that, using strictly black-box methods of system identification (6), it is sometimes found that the IUH, determined from a given rainfall excess-runoff event, has some of its ordinates as negative (1). If this same IUH is used in conjunction with the same rainfall excess, the

runoff thus reproduced is identical to the given runoff hydrograph. The negative ordinates may arise from one or more of the reasons: (1) Errors in data; (2) errors in model approximating the prototype system; and (3) errors in model parameters. However, the IUH with negative ordinates is physically unrealizable (1), and cannot be used for other rainfall excess events. In this respect, it may be worthwhile to quote Boneh and Golan (1):

> The answer to the question posed in the title of this paper is yes, provided that some restrictions are imposed on the rainfall excess which is the input to the surface runoff system. Obviously impulsive inputs are not admissible when the instantaneous unit hydrograph (IUH) has negative ordinates. Since the IUH is the direct surface runoff response (known as the 'output') to an instantaneous rainfall burst of unit volume and such runoff, by definition, cannot be negative. Is an instaneous unit hydrograph with negative ordinates (IUH WHO) desirable? Here the answer is no, because of the restrictions that have been imposed on the input.

Initial Conditions and Coefficients b_0 and b_1

A simple, yet realistic initial condition can be assumed as $u(0) = 0$. Most IUH models (6) satisfy this condition. It turns out that if this condition is used in the solution of Eq. 3, the coefficients b_0 and b_1 must vanish, as will be clear from the ensuing analysis.

Suppose that there is a continuous solution of Eq. 3 which we rewrite as

$$a_2 u''' + a_1 u'' + a_0 u' + u = \delta(t) - b_0 \delta'(t) - b_1 \delta''(t) \quad \ldots\ldots\ldots\ldots \quad (15)$$

subject to $u(0) = 0$; $u'(0) = \alpha$; $u''(0) = \beta$ for some numbers α and β. If we multiply each side of Eq. 12 by e^{-st}, and integrate with respect to t from $-\epsilon$ to ∞, in which $\epsilon > 0$, then we have

$$\int_{-\epsilon}^{-\infty} [a_2 u'''(t) + a_1 u''(t) + a_0 u'(t) + u(t)]\, e^{-st}\, dt = \int_{-\epsilon}^{\infty} \delta(t)\, e^{-st}\, dt$$

$$- b_0 \int_{-\epsilon}^{\infty} \delta'(t) e^{-st}\, dt - b_1 \int_{-\epsilon}^{\infty} \delta''(t)\, e^{-st}\, dt = 1 + b_0 s - b_1 s^2 \quad \ldots\ldots \quad (16)$$

since $\int_{-\infty}^{\infty} \delta^{i}(t) f(t)\, dt = (-1)^{i} f^{i}(0)$. Since Eq. 16 holds for all $\epsilon > 0$ we must have (where $L[u]$ is the Laplace transform of u):

$$(a_2 s^3 + a_1 s^2 + a_0 s + 1)\, L[u] - (s\alpha + \beta + \alpha) = 1 + b_0 s - b_1 s^2 \quad \ldots\ldots \quad (17)$$

$$\text{so that} \quad L[u] = \frac{1}{a_2} \left[\frac{1 + \alpha + \beta + (\alpha + b_0) s - b_1 s^2}{(s - m)(s - n)(s - p)} \right] \quad \ldots\ldots\ldots \quad (18)$$

in which m, n, and p are the roots of

$$f(x) = a_2 x^3 + a_1 x^2 + a_0 x + 1 \quad \ldots\ldots\ldots\ldots\ldots\ldots\ldots \quad (19)$$

Using the method of partial fractions, we can write $L(u)$ as

$$L[u] = \frac{1}{a_2} \left(\frac{A}{s - m} + \frac{B}{s - n} + \frac{C}{s - p} \right) \quad \ldots\ldots\ldots\ldots\ldots\ldots \quad (20)$$

for some choice of the number A, B, and C, whenever the numerator and denominator of the quotient in Eq. 18 have no common root. In determining A, B, and C by the usual method, a system of three equations is obtained:

$$A + B + C = -b_1 \quad \ldots\ldots\ldots\ldots\ldots\ldots\ldots\ldots\ldots\ldots \quad (21a)$$

$$-(n+p)A - (m+p)B - (m+n)C = \alpha + b_o \quad \ldots\ldots\ldots\ldots\ldots \quad (21b)$$

$$np\,A + mp\,B + mn\,C = 1 + \alpha + \beta \quad \ldots\ldots\ldots\ldots\ldots\ldots \quad (21c)$$

Once A, B, and C have been determined, the solution $u(t)$ of Eq. 15, with given initial conditions, can be obtained by inverting $L[u]$ as given in Eq. 20:

$$u(t) = \frac{1}{a_2}(Ae^{mt} + Be^{nt} + Ce^{pt}) \quad \ldots\ldots\ldots\ldots\ldots\ldots\ldots\ldots \quad (22)$$

Then, by Eq. 21:

$$0 = u(0) = \frac{1}{a_2}(A + B + C) = -\frac{b_1}{a_2} \quad \ldots\ldots\ldots\ldots\ldots\ldots\ldots\ldots \quad (23)$$

Thus, Eq. 15 has a continuous solution with $u(0) = 0$ only if $b_1 = 0$.

An analysis of the results reported in (5,7), for 47 rainfall excess-runoff storm on seven different watersheds, shows that

$\left\lvert\frac{b_1}{a_2}\right\rvert$	≤ 1	≤ 0.8	≤ 0.6	≤ 0.4	≤ 0.2	≤ 0.1	≤ 0.08	≤ 0.06	≤ 0.04	≤ 0.02	≤ 0.01
Number of Storms	45	44	39	35	27	22	20	19	17	6	0

(24)

Thus, in over half of the cases $|u(0)| \leq 0.2$. This supports our argument that $u(0)$ should be zero. Moreover, it must be emphasized that the coefficient b_1 was obtained by using a difference approximation to the second derivative of rainfall excess (5,7). Since rainfall excess is given as a piecewise constant function (histogram), this difference approximation may introduce significant error into the calculation of b_1. This accounts, at least partially, for the relatively large values of $|b_1/a_2|$.

To show that $u'(0) = 0$ and $u''(0) = 0$, the following argument is developed. The primary purpose of obtaining the IUH is to write the solution of Eq. 2 as

$$Q(t) = \int_0^t u(t-\tau)\,I(\tau)\,d\tau \quad \ldots\ldots\ldots\ldots\ldots\ldots\ldots\ldots\ldots\ldots \quad (25)$$

Since I is given in histograph form, $I(t)$ = some constant $c > 0$ on some interval $0 < t < t_1$. Using Leibnitz's rule, we have on the interval $0 < t < t_1$

$$Q'(t) = u(0)I(t) + \int_0^t u'(t-\tau)I(\tau)\,d\tau = c\int_0^t u'(t-\tau)\,d\tau;$$

$$Q''(t) = cu'(0) + c\int_0^t u''(t-\tau)\,d\tau = c\alpha + c\int_0^t u''(t-\tau)\,d\tau;$$

$$Q'''(t) = cu''(0) + c\int_0^t u'''(t-\tau)\,d\tau = c\beta + c\int_0^t u'''(t-\tau)\,d\tau \quad \ldots\ldots \quad (26)$$

On the interval $0 < t < t_1$

$$c = I - b_0 I' - b_1 I'' = a_2 Q''' + a_1 Q'' + a_0 Q' + Q = a_2 c\beta + a_1 c\alpha$$

$$+ c\int_0^\infty [a_2 u'''(t-\tau) + a_1 u''(t-\tau)$$

$$+ a_0 u'(t-\tau) + u(t-\tau)]\,d\tau$$

$$= a_2 c\beta + a_1 c\alpha + c\int_0^\infty [\delta(t-\tau) - b_0\delta'(t-\tau) - b_1\delta''(t-\tau)]\,d\tau \quad \ldots \quad (27)$$

If we now use the identities $\int_0^\infty \delta^m(t-\tau)f(\tau)\,d\tau = (-1)^m f^m(t)$ for $t > 0$, we have

$$c = a_2 c\beta + a_1 c\alpha + c \quad \ldots\ldots\ldots\ldots\ldots\ldots\ldots\ldots \quad (28)$$

$$\text{Thus} \quad a_2\beta + a_1\alpha = 0 \quad \ldots\ldots\ldots\ldots\ldots\ldots\ldots\ldots \quad (29)$$

In order that volume be preserved under convolution with the IUH, we must have $\int_0^\infty u(t)\,dt = 1$. Since $-a_2 mnp = 1$, we have from Eqs. 22 and 21*c*:

$$1 = \int_0^\infty u(t)\,dt = -mnp\int_0^\infty (Ae^{mt} + Be^{nt} + Ce^{pt})\,dt$$

$$= (-n\,Ae^{mt} - mpBe^{nt} - mnCe^{pt})\Big|_0^\infty$$

$$= npA + mpB + mnC = 1 + \alpha + \beta \quad \ldots\ldots\ldots\ldots\ldots\ldots \quad (30)$$

$$\text{Thus,} \quad \alpha + \beta = 0 \quad \ldots\ldots\ldots\ldots\ldots\ldots\ldots\ldots \quad (31)$$

in which $\alpha = -\beta$. With this choice for α, Eq. 29 becomes $(a_2 - a_1)\,\beta = 0$. Therefore, $a_2 = a_1$, or $\beta = 0$. If $\beta = 0$, then by Eq. 31, $\alpha = 0$. Thus, $a_2 = a_1$, or $\alpha = -\beta = 0$.

In none of the 47 reported cases (in none of the six possible models for each case) are a_1 and a_2 even close to being equal. Thus, we must have $\alpha = -\beta = 0$, i.e.,

$$u'(0) = 0, \quad \text{and} \quad u''(0) = 0 \quad \ldots\ldots\ldots\ldots\ldots\ldots \quad (32)$$

These initial conditions are reflected in the direct surface runoff hydrographs (DSRO) reported in Ref. 7. In all 36 of the DSRO's reported, the graph of the DSRO's resemble Fig. 2(*a*) near $t = 0$. In at least 22 of the 36 cases, the graph of the DSRO has the form as shown in Fig. 2(*b*) near $t = 0$. Let $R(t)$ denote the DSRO at time t. Then in at least 60% of the cases, $\lim_{t\to 0^+} R''(t) = 0$, and in the remaining cases it appears that we also have $\lim_{t\to 0^+} R''(t) = 0$. Thus, to model the runoff near $t = 0$, it appears that we should choose IUH so that $\lim_{t\to 0^+} Q''(t) = 0$ whenever Q is given by Eq. 25. From Eq. 26 we have

$$0 = \lim_{t \to 0^+} Q''(t) = c\alpha \quad \ldots \ldots \ldots \ldots \ldots \ldots \ldots \ldots \ldots \ldots \ldots \ldots \ldots \quad (33)$$

in which $\alpha = 0$, and, from Eq. 31, $\beta = 0$.

Thus, choosing $u(0) = 0$, $u'(0) = 0$, and $u''(0) = 0$ appear to be the logical initial conditions for determing the IUH. Therefore, $\alpha = 0$ and $\beta = 0$.

Furthermore, if $\alpha = 0$ in Eq. 18, we may solve the system of Eqs. 21*a–c* to obtain:

$$A = \frac{1 + \beta + b_0 m}{(m-n)(m-p)}; \quad B = \frac{1 + \beta + b_0 n}{(n-m)(n-p)}; \quad C = \frac{1 + \beta + b_0 p}{(p-m)(p-n)} \quad (34)$$

$$\text{Then} \quad u'(0) = \frac{1}{a_2}\left[\frac{m(1 + \beta + b_0 m)}{(m-n)(m-p)}\right. \quad \ldots \ldots \ldots \ldots \ldots \ldots \quad (35)$$

$$\left. + \frac{n(1 + \beta + b_0 n)}{(n-m)(n-p)} + \frac{p(1 + \beta + b_0 p)}{(p-n)(p-m)}\right]$$

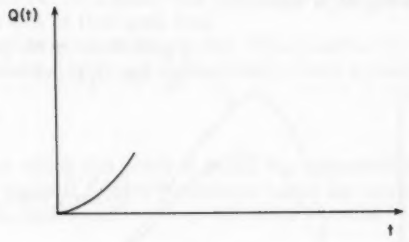

(a)

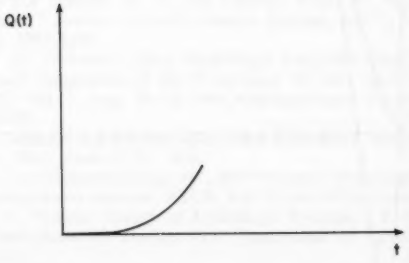

(b)

FIG. 2.—Beginning of DSRO Obtained from GHS Model of Chow and Kulandaiswamy (4,5,7)

Upon simplification we obtain:

$$u'(0) = \frac{b_0}{a_2} \quad \ldots \ldots \ldots \ldots \ldots \ldots \ldots \ldots \ldots \ldots \ldots \ldots \ldots \ldots \quad (36)$$

Thus, Eq. 15 has a continuous solution with $u(0) = u'(0) = 0$ only if $b_0 = b_1 = 0$.

If $b_1 = 0$, the data reported (5,7) also indicate that b_0 should also be zero. Of the 47 rainstorms analyzed (5,7), we find:

$\left\lvert \frac{b_0}{a_2} \right\rvert$	≤ 0.1	≤ 0.07	≤ 0.5	≤ 0.03	≤ 0.02	≤ 0.01	≤ 0.005	≤ 0.001	≤ 0.0005
Number of Storms	30	30	30	28	23	16	10	8	4

(37)

Thus, b_0 is usually very small when compared with a_2 and, therefore, highly susceptible to error when computed empirically. In fact, b_0/a_2 is so small that choosing it to be zero does not seem to be unwarranted in most cases. If $b_0 = 0$, then from Eq. 36, $u'(0) = 0$.

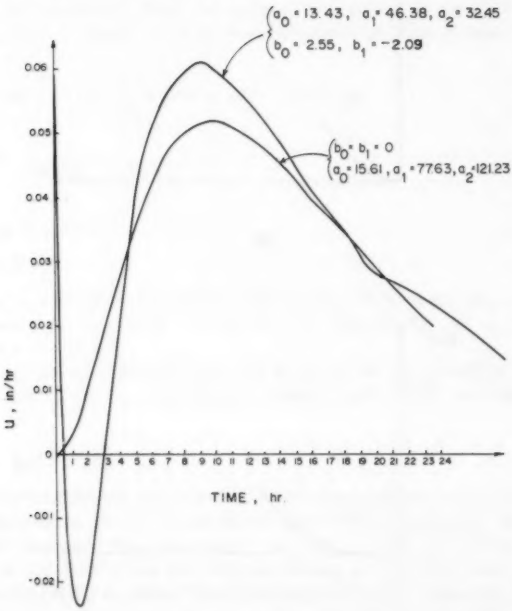

FIG. 3.—Comparison of IUH's for Data of Kulandaiswamy (7, p. 149; Storm No. 1, N. Br. Potomac River Basin) for Two Cases: (1) When the Coefficients b_0 and b_1 Are Not Zero, and (2) $b_0 = b_1 = 0$

To illustrate the difference between the two cases: Including (1) $b_0 = b_1 = 0$; and (2) b_1, b_0 not zero, the IUH's were computed for one storm in North Branch Potomac River Basin near Cumberland, Maryland, for which data has been given by Kulandaiswamy (7). Fig. 3 shows this comparison. It is seen that the case with $b_0 = b_1 = 0$ may produce reasonable IUH without greatly reducing the accuracy of the GHS model.

Conclusions

The following conclusions can be drawn from this study:

1. The derivations of the IUH reported by Chow and Kulandaiswamy (4,5,7) are inconsistent with regard to the initial conditions. That is perhaps why their IUH has negative ordinates.
2. If $u(0) = 0$ can be assumed, then the terms containing derivatives of rainfall excess vanish.
3. An analysis of the results reported in Ref. 7 reveals that the second conclusion holds.
4. Their results (4,5,7) indicate that the period of negative IUH ordinates can be as high as 40% of IUH peak time.
5. Removal of the inconsistency in Ref. 4 (i.e., $u(0) = b_0 = b_1 = 0$) makes the GHS model much simpler and more attractive from a practical standpoint.

Acknowledgments

The work upon which this study is based was supported in part by funds provided by the National Science Foundation under the project, "A Hydrodynamic Study of Surface Runoff," Grant No. ENG 79-05560.

Appendix I.—References

1. Boneh, A., and Golan, A., "Instantaneous Unit Hydrograph with Negative Ordinates—Possible?," *Water Resources Research*, Vol. 15, No. 1, 1979, pp. 121–130.
2. Chaudhary, F. H., Simoes, M. A., and Ferreira Filho, W. M., "Chow's General Hydrologic Model," *Journal of the Hydraulics Division*, ASCE, Vol. 102, No. HY9, Sept., 1976, pp. 1387–1390.
3. Chaudhary, F. H., "General Linear Hydrologic Response Models," *Proceedings of the Third Annual Symposium of the Waterways, Harbors and Coastal Engineering Division*, ASCE, Vol. 1, Aug. 10–12, 1976, Colorado State University, Fort Collins, Colo., pp. 367–376.
4. Chow, V. T., "Runoff," *Handbook of Applied Hydrology*, Section 14, McGraw-Hill Book Co., Inc., New York, N.Y., 1964.
5. Chow, V. T., and Kulandaiswamy, V. C., "General Hydrologic System Model," *Journal of the Hydraulics Division*, ASCE, Vol. 97, No. HY6, June, 1971, pp. 791–804.
6. Dooge, J. C. I., "Linear Theory of Hydrologic Systems," *Technical Bulletin No. 1468*, Agricultural Research Service, U.S. Department of Agriculture, Washington, D.C., Oct., 1973.
7. Kulandaiswamy, V. C., "A Basic Study of the Rainfall Excess-Surface Runoff Relationship in a Basin System," thesis presented to the University of Illinois, at Urbana, Ill., in 1964, in partial fulfillment of the requirements for the degree of Doctor of Philosophy.
8. Kulandaiswamy, V. C., Krishnaswamy, M., and Ramalingam, T. N., "Flood Routing Through Channels," *Journal of Hydrology*, Vol. 5, 1967, pp. 279–285.

9. Kulandaiswamy, V. C., and Subramanian, C. V., "A Nonlinear Approach to Runoff Studies," Proceedings of the Sept. 6–8, 1967, International Hydrology Symposium, held at Colorado State University, Fort Collins, Colo., pp. 72–85.
10. Kulandaiswamy, V. C., and Rao, T. B., "Digital Simulation of a Drainage Basin," *Proceedings of the Warsaw Symposium on Mathematical Models in Hydrology*, July, 1971, in Warsaw, Poland, Vol. 2, pp. 443–454.
11. Kulandaiswamy, V. C., and Rao, T. B., "An Investigation of Nonlinearity in Storage-Discharge Relationship for Watersheds," *Report No. 4*, Council of Scientific and Industrial Research Project, 1970, Hydraulics and Water Resources Department, College of Engineering, Madras-25, India.
12. Kulandaiswamy, V. C., and Rao, T. B., "An Investigation of Nonlinearity in Runoff Process," *Proceedings of International Symposium on Water Resources*, held May 11–16, Banglore, India, 1971.
13. Mays, L. W., and Coles, L., "Optimization of Unit Hydrograph Determination," *Journal of the Hydraulics Division*, ASCE, Vol. 106, No. HY1, Jan., 1980, pp. 85–97.
14. Singh, V. P., and McCann, R. C., "A Mathematical Study of the General Hydrologic System Model," *Technical Report*, Engineering and Industrial Research Station, Mississippi State University, Mississippi State, Miss., 1980.

Appendix II.—Notation

The following symbols are used in this paper:

a = coefficient associated with derivative of runoff;
b = coefficient associated with derivative of rainfall excess;
$d^i[\ ]/dt^i$ = ith derivative of the quantity [ ] with respect to t;
I = rainfall excess;
j = imaginary number equal to -1;
$L[\ ]$ = Laplace transform of the quantity [ ];
M = number of derivatives of runoff;
m = root of the denominator in Eq. 3;
N = number of derivatives of rainfall excess;
n = root of denominator in Eq. 3;
p = root of denominator in Eq. 3;
Q = runoff;
S = Laplace transform variable;
$u(t)$ = instantaneous unit hydrograph;
$u^i(t)$ = ith derivative of u with respect to t;
$\delta(t)$ = delta function;
γ = real part of complex root; and
ω = imaginary part of complex root.

Resistance Equation for Large-Scale Roughness

By James C. Bathurst,[1] Ruh-Ming Li,[2] M. ASCE, and Daryl B. Simons,[3] F. ASCE

Introduction

Boulder-bed channels with large-scale roughness, for which the size of the bed material is of the same order of magnitude as the depth of flow, have received relatively little attention compared with channels with finer bed materials. However, with the increasing development of mountain regions, especially in less industrialized countries, such channels are beginning to be featured in engineering projects and, consequently, there have recently been a few studies of their general characteristics (1,13,16,20). This paper is a further contribution to the subject and reports the results of a flume study of large-scale roughness carried out at Colorado State University (2). The aim of the study, which was intended to be of general scientific interest as well as of engineering use, was to identify the processes affecting the flow hydraulics, construct a theory of flow resistance, and test the theory by using the flume data to develop a theoretical flow resistance equation. Some of the work, particularly the description of flow processes, has been published elsewhere (3). This paper, therefore, concentrates on the flume work and the subsequent development of the resistance equation and provides only a brief survey of the theory. A summary of the data is provided which, it is hoped, may be of use to other research efforts.

Flow Characteristics

The roughness is large-scale if the roughness elements affect the free surface, a condition requiring that the relative submergence, or ratio of depth, d, to mean element height, be less than about four (7). The roughness is intermediate-scale if the relative submergence lies between about four and 15, the latter limit marking the boundary with small-scale roughness and the more familiar

[1]Sr. Scientific Officer, Inst. of Hydro., Wallingford, Oxon, United Kingdom.
[2]Assoc. Prof. of Civ. Engrg., Colorado State Univ., Fort Collins, Colo.
[3]Assoc. Dean, Coll. of Engrg., and Prof. of Civ. Engrg., Colorado State Univ., Fort Collins, Colo.

Note.—Discussion open until May 1, 1982. To extend the closing date one month, a written request must be filed with the Manager of Technical and Professional Publications, ASCE. Manuscript was submitted for review for possible publication on November 17, 1980. This paper is part of the Journal of the Hydraulics Division, Proceedings of the American Society of Civil Engineers, ©ASCE, Vol. 107, No. HY12, December, 1981. ISSN 0044-796X/81/0012-1593/$01.00.

type of flow which may be described by boundary-layer theory. For river sediments it is assumed that element height is given by the short axis (4,12,13). However, for typical bed materials the equivalent ranges, in terms of the more easily measured median axis, are approximately:

$$\text{Large-scale roughness } \left(\frac{d}{S_{50}} < 4\right): \quad \frac{d}{D_{50}} < 2; \quad \frac{d}{D_{84}} < 1.2 \quad \ldots\ldots\ldots (1)$$

$$\text{Intermediate-scale roughness } \left(4 < \frac{d}{S_{50}} < 15\right): \quad 2 < \frac{d}{D_{50}} < 7.5;$$

$$1.2 < \frac{d}{D_{84}} < 4 \quad \ldots\ldots\ldots\ldots\ldots\ldots\ldots\ldots\ldots\ldots\ldots\ldots\ldots\ldots (2)$$

in which S_n = the size of the short axis, which is bigger than or equal to n% of short axes; and D_n is similarly defined for the median axis.

Under natural conditions, boulder-bed channels are likely to have slopes greater than 0.1–0.4% (8), but less than about 5–10%, and Froude numbers can attain supercritical values (17). Entrainment of air can be significant (9,18) but more probably at very steep slopes, so it is not considered here.

Flow Resistance Theory

Previous studies have indicated that the flow resistance of large-scale roughness is related mainly to the form drag of the elements and their disposition in the channel (1,7,10,13,20). Since the associated resistance processes are different from those for small-scale roughness, it is not possible to use the semilogarithmic resistance equations developed for small-scale roughness. Instead, it appears that for large-scale roughness a power law is more suitable (1,6,13), while for intermediate-scale roughness a semilogarithmic law (different from that for small-scale roughness) is more appropriate (2,4,20).

In developing a theoretical process-based equation for large-scale roughness, it is necessary to account separately for the processes of fluid mechanics related to Reynolds number and Froude number which determine the drag of individual elements, and the processes of roughness geometry and channel geometry which determine the combined effect of the elements on the flow. Previous equations have considered the combined effect only.

Processes of Resistance

Reynolds Number.—The form drag of an object varies according to whether the boundary layer on the object is laminar, turbulent, or transitional between these states, and this is determined by the Reynolds number, $\bar{U} D_{50}/\nu$, in which $\bar{U}$ = mean velocity of flow, and ν = kinematic viscosity. If the boundary layer is laminar or turbulent, the drag coefficient does not vary much with Reynolds number except at extreme values. In the intermediate transitional region, though, the drag coefficient falls as Reynolds number increases.

In many cases the transitional region extends over a relatively narrow range of Reynolds numbers (19) so the effect of Reynolds number is limited. With large-scale roughness, though, a combination of factors causes the transitional

region to be relatively wide, lying between Reynolds numbers of about 3×10^4 and 2×10^5 (2,7). As this range is typical of that found in channel flows, the flow resistance could be significantly affected, generally decreasing as Reynolds number increases.

Froude Number.—An element which protrudes through or nearly through the free surface causes distortions in the surface which represent an energy loss. The component of form drag generated in this way is referred to here as free surface drag and varies with Froude number and relative submergence.

Flammer, Tullis, and Mason (7) found that for a constant Froude number and for relative submergences greater than about 0.8, the drag coefficient decreases as relative submergence increases, until at a relative submergence of about 4 it is negligible. On the other hand, with relative submergence constant, an increase in Froude number causes the drag coefficient first to rise to a peak and then to decrease until, at a Froude number of about 1.5, it is again negligible. The Froude number at which the peak occurs is about 1 for relative submergences less than about 0.5, and about 0.5 for relative submergences greater than about 0.8, a variation which is probably related to differential formation of hydraulic jumps around the element (2,3). The result of this dependency is that for a constant Froude number of a relatively low value, and for relative submergences less than about 0.8, it is possible for the drag coefficient to increase as relative submergence increases.

Roughness Geometry.—The combined effect of the elements on flow resistance depends on the proportion of the bed material which has a significant form drag, and this is determined by the geometry and disposition of the elements. Most resistance equations have accounted for roughness geometry with relative submergence only and have left unquantified the effects of size distribution, shape, and areal distribution. A more suitable parameter which would account for all these factors, including relative submergence, is the effective roughness concentration, λ_e, defined as the ratio of the sum of the wetted frontal cross-sectional areas, A_F, of the elements, to the area of bed on which they lie:

$$\lambda_e = \frac{\sum_1^n A_F}{A_{\text{bed}}} \quad \ldots \ldots \ldots

Theoretical analysis (2,3) indicates that the effective roughness concentration should vary inversely with relative submergence, the rate of change depending on σ. In addition, the absolute magnitude should be a function of roughness shape and the number of elements. Therefore, assuming a power law representation, a functional relationship for λ_e is

$$\lambda_e = \left[\frac{S_{50}}{d} \times fn\left(\frac{w}{Y_{50}}, \chi\right)\right]^{fn(\sigma)} \quad \ldots\ldots\ldots\ldots\ldots\ldots\ldots\ldots\ldots\ldots (5)$$

in which χ = a parameter of roughness shape; and $fn(\ )$ = a function (2,3). The flow resistance of the bed is directly proportional to this quantity.

Channel Geometry.—In flows where the roughness elements occupy a significant proportion of the channel cross-section, the flow is funnelled between the elements (10). The greater the proportion, the greater is the degree of funnelling and the higher is the mean velocity of flow. This effect can be monitored using the ratio of the total wetted cross-sectional area of the elements at a

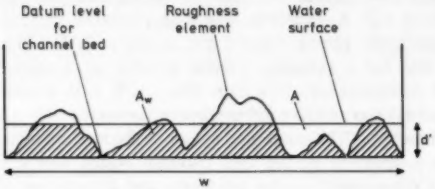

A = flow cross-sectional area
A_w = wetted roughness cross-sectional area

$A + A_w = wd'$

A_w / wd' = relative roughness area

FIG. 1.—Definition Diagram for Relative Roughness Area

section, A_w, to the total channel cross-sectional area wd' (in which d' = depth from the free surface to the bed datum level), a term which is here called the relative roughness area (Fig. 1). Research elsewhere has independently reached the same conclusion (20).

Since it may not be convenient to measure the relative roughness area directly, it would be useful if it could be calculated from the relevant parameters of channel shape and roughness geometry. Theoretical analysis (2,3) suggests that it should vary directly with the channel width/depth ratio, and that the rate of change should depend on the degree to which the roughness elements project into the flow at any given depth (quantified by the effective roughness concentration). Still using a power law, a functional relationship is therefore

$$\frac{A_w}{wd'} = \left(\frac{w}{d}\right)^{fn(\lambda_e)} \quad \ldots\ldots\ldots\ldots\ldots\ldots\ldots\ldots\ldots\ldots\ldots\ldots (6)$$

in which d = mean flow depth (2,3). This term is very similar to parameters of channel shape derived empirically in other studies (1,13).

Basic Resistance Equation

A variety of mathematical relationships between flow resistance and its determining factors could be specified. However, previous research has found that a power law is the most suitable for large-scale roughness (1,6,13). Consequently, combining the foregoing analyses, and denoting resistance as in small-scale roughness with the function $(8/f)^{1/2}$ from the Darch-Weisbach equation (3,11), the basic resistance equation for large-scale roughness with steady, uniform flow is

$$\left(\frac{8}{f}\right)^{1/2} = \frac{\bar{U}}{(gRS)^{1/2}} = fn(\mathsf{R}) \times fn(\mathsf{F}) \times fn(\lambda_e) \times fn\left(\frac{A_w}{wd'}\right) \quad \ldots\ldots\ldots (7)$$

in which f = the Darcy-Weisbach resistance coefficient; g = acceleration due to gravity; R = hydraulic radius; S = channel slope; R = Reynolds number $\bar{U}\, D_{50}/\nu$; and F = Froude number $\bar{U}/(gR)^{1/2}$.

Mathematical descriptions of the resistance processes are not sufficiently advanced to permit theoretical quantification of Eq. 7. Consequently, it is necessary to resort to more empirical procedures based on experimental data.

Experimental Work

Data were obtained for five different fixed roughness beds using the steep stream flume at Colorado State University.

Bed Material.—The five bed materials are classified as 0.5, 0.75, 1.5, 2.0 and 2.5 in. (respectively, 12.7, 19.05, 38.1, 50.8 and 63.5 mm); these figures

TABLE 1.—Size Distributions of Bed Materials

Bed material size, in inches (1)	Bed material axis (2)	SIZE OF AXIS, in millimeters: Percentile 84 (3)	Percentile 50 (4)	Percentile 16 (5)	Standard deviation of distribution (6)
0.5	Long	17.0	13.6	9.6	0.097
	Median	11.5	8.8	6.4	0.116
	Short	7.8	5.8	2.3	0.129
0.75	Long	28.0	19.75	12.4	0.152
	Median	19.3	13.0	8.5	0.172
	Short	12.3	8.0	5.2	0.187
1.5	Long	59.0	47.0	34.0	0.099
	Median	43.0	34.0	23.5	0.102
	Short	27.0	19.0	13.8	0.153
2.0	Long	73.0	59.0	49.0	0.0925
	Median	47.0	43.0	38.5	0.0386
	Short	34.0	29.75	22.5	0.0580
2.5	Long	90.0	73.0	62.5	0.0909
	Median	58.0	54.25	50.0	0.0290
	Short	44.0	39.5	28.5	0.0469

Note: 1 mm = 0.00328 ft; 1 in. = 25.4 mm.

referring rather approximately to the maximum size of each material. The first three were commercially available gravels, consisting of chips derived by crushing larger cobbles. The 2.0 and 2.5 in. materials were cobbles which had been collected by hand. Size distributions for the long, median, and short axes of the materials were determined by the Wolman method (21), and standard deviations of the distributions were calculated using Eq. 4 for each axis in turn. (Details are given in Table 1.)

Flume.—The flume is of the open, recirculating type and is 9.54 m (31.33 ft) long, and 1.168 m (3.833 ft) wide. Discharge is measured by a *V*-notch weir in the sediment settling tank at the end of the flume. Further details are given elsewhere (2,15).

TABLE 2.—Flume Data for 0.5 in. Roughness Bed

Channel slope (1)	Discharge, in cubic meters per second (2)	Mean velocity, in meters per second (3)	Mean depth d, in meters (4)	Depth d' of bed datum, in meters (5)	Relative roughness area A_w/wd' (6)	Kinematic viscosity of water, in square meters per second ($\times 10^6$) (7)	Froude number $U/(gd)^{0.5}$ (8)	Darcy-Weisbach resistance coefficient (9)	Relative submergence d/S_{50} (10)	Function of effective roughness concentration b (11)
0.02	0.00241	0.146	0.0141	0.0192	0.2659	1.173	0.392	1.044	2.436	0.300
0.02	0.01274	0.391	0.0279	0.0324	0.1398	1.173	0.748	0.286	4.806	0.527
0.02	0.03046	0.584	0.0446	0.0489	0.0874	1.173	0.883	0.205	7.695	0.747
0.02	0.05746	0.785	0.0627	0.0669	0.0635	1.173	1.001	0.160	10.804	0.942
0.02	0.07197	0.877	0.0702	0.0743	0.0540	1.173	1.056	0.143	12.111	1.038
0.05	0.00143	0.161	0.0076	0.0129	0.4104	1.110	0.590	1.151	1.312	0.177
0.05	0.00522	0.296	0.0151	0.0197	0.2318	1.110	0.768	0.679	2.606	0.336
0.05	0.01737	0.619	0.0240	0.0291	0.1739	1.095	1.275	0.246	4.141	0.450
0.05	0.03249	0.823	0.0338	0.0385	0.1227	1.110	1.429	0.196	5.827	0.592
0.05	0.04896	1.017	0.0412	0.0461	0.1068	1.125	1.600	0.156	7.103	0.669
0.08	0.00196	0.201	0.0084	0.0124	0.3262	1.345	0.701	1.303	1.441	0.227
0.08	0.00610	0.392	0.0133	0.0179	0.2532	1.205	1.083	0.545	2.299	0.307
0.08	0.01355	0.563	0.0206	0.0248	0.1701	1.205	1.252	0.408	3.552	0.439
0.08	0.03576	0.965	0.0317	0.0358	0.1149	1.222	1.731	0.214	5.466	0.600
0.08	0.06061	1.225	0.0424	0.0466	0.0903	1.222	1.900	0.177	7.303	0.725
0.08	0.07065	1.301	0.0465	0.0507	0.0829	1.222	1.927	0.172	8.013	0.772

Note: 1 m = 3.281 ft; 1 m^2 = 10.77 sq ft; 1 m^3 = 35.3 cu ft.

Each roughness bed was constructed by smearing masonite boards with fiberglass resin and covering them with the respective material. The boards were then screwed to the bed of the flume. Each bed was one element thick and, as there were no obvious patches of smooth board visible between the elements, had the approximate appearance of a natural river bed.

The flume sidewalls (one perspex, the other painted wood) were not covered. It was expected that, because of the extreme bed roughness and high ratios of width to depth, resistance would be little affected by the sidewalls and the flow would be approximately two-dimensional.

It is assumed (as for river sediments (4,12,13)) that the height of each element

on the bed was equal to its short axis. The cross-stream axis Y_{50} is assumed to have been the average of the long L_{50} and median axes and is calculated as

$$Y_{50} = \frac{L_{50} + D_{50}}{2} \quad \ldots \ldots \ldots

intervals of 12.7 m (0.5 in.), that interval being equal to the smallest size of bed material. Total flow cross-sectional area, A (Fig. 1), was then calculated from the bed and free surface elevations by computer integration using the trapezoidal rule. Cross-sectional area of the roughness, A_w, was calculated from the bed elevations by the same method, the datum level for the channel bed being the top of the boards to which the elements were fixed (Fig. 1). Adding A and A_w gave the total channel cross-sectional area, wd', and thus the relative roughness area, A_w/wd'.

Wetted perimeter is based on the datum level of the bed rather than the outline of the elements as they project into the flow. Consequently, assuming

TABLE 4.—Flume Data for 1.5 in. Roughness Bed

Channel slope (1)	Discharge, in cubic meters per second (2)	Mean velocity, in meters per second (3)	Mean depth d, in meters (4)	Depth d' of bed datum, in meters (5)	Relative roughness area A_w/wd' (6)	Kinematic viscosity of water, in square meters per second ($\times 10^{-6}$) (7)	Froude number $U/(gd)^{0.5}$ (8)	Darcy-Weisbach resistance coefficient (9)	Relative submergence d/S_{50} (10)	Function of effective roughness concentration b (11)
0.02	0.00250	0.116	0.0184	0.0297	0.3803	1.110	0.274	2.135	0.967	0.233
0.02	0.00868	0.239	0.0311	0.0425	0.2677	1.081	0.432	0.858	1.638	0.364
0.02	0.01893	0.375	0.0432	0.0548	0.2115	1.053	0.575	0.483	2.276	0.471
0.02	0.04352	0.587	0.0634	0.0751	0.1559	1.067	0.745	0.288	3.337	0.638
0.02	0.06763	0.721	0.0803	0.0921	0.1285	1.067	0.812	0.242	4.225	0.766
0.02	0.08020	0.764	0.0899	0.1009	0.1090	1.140	0.813	0.242	4.731	0.864
0.05	0.00181	0.132	0.0117	0.0230	0.4909	1.110	0.389	2.650	0.617	0.155
0.05	0.00636	0.264	0.0206	0.0328	0.3696	1.081	0.586	1.164	1.087	0.247
0.05	0.01456	0.419	0.0298	0.0416	0.2839	1.053	0.775	0.666	1.566	0.343
0.05	0.03073	0.625	0.0420	0.0542	0.2237	1.038	0.974	0.422	2.213	0.450
0.05	0.06061	0.869	0.0597	0.0716	0.1663	1.081	1.136	0.310	3.141	0.603
0.05	0.07421	0.932	0.0681	0.0792	0.1400	1.081	1.140	0.308	3.585	0.692
0.08	0.00389	0.267	0.0124	0.0249	0.5002	1.205	0.765	1.093	0.655	0.153
0.08	0.01092	0.457	0.0204	0.0361	0.4340	1.205	1.021	0.614	1.076	0.206
0.08	0.02100	0.616	0.0292	0.0436	0.3307	1.205	1.151	0.483	1.536	0.300
0.08	0.03126	0.721	0.0371	0.0505	0.2661	1.173	1.196	0.448	1.952	0.384
0.08	0.05498	0.971	0.0484	0.0603	0.1964	1.173	1.409	0.322	2.550	0.511
0.08	0.05574	0.883	0.0540	0.0657	0.1779	1.140	1.213	0.435	2.843	0.562

Note: 1 m = 3.281 ft; 1 m^2 = 10.77 sq ft; 1 m^3 = 35.3 cu ft.

that the flow was two-dimensional, wetted perimeter is equal to width. Hydraulic radius is therefore equal to mean depth, d, given by the ratio of flow cross-sectional area, A, to width, w.

Finally, at the end of each gaging the water temperature was noted so that the kinematic viscosity could be obtained. The measured data and their derivatives are given in Tables 2–6.

Development of Resistance Equation

Quantification of Eq. 7 was carried out, term by term, using the precepts of the theoretical analysis.

Reynolds Number.—Reynolds number, $\bar{U} D_{50}/\nu$, varied from about 10^3 to 4.4×10^4. In this range, the boundary layer on an object is typically laminar and the drag coefficient is independent of Reynolds number. Consequently, for the flume flows the function of Reynolds number in Eq. 7 is a constant.

Effective Roughness Concentration.—Eq. 6 can be rewritten to define the function of effective roughness concentration, in terms of measured quantities, as $-b$ so that

$$\frac{A_w}{wd'} = \left(\frac{w}{d}\right)^{-b} \quad \ldots \ldots \ldots

variation with σ was studied (Fig. 3). The results support the theory, giving

$$c = 0.648\,\sigma^{-0.134} \quad \ldots\ldots\ldots\

sign must appear with b in Eq. 9, otherwise the variations of Eqs. 6 and 9 are inconsistent.

Relative Roughness Area.—For a given depth of flow, the bigger the relative roughness area, the greater is the funnelling of the flow between elements, and the bigger is the mean velocity of flow, $\bar{U}$. It is therefore assumed that the resistance function, $(8/f)^{1/2}$ (Eq. 7), varies directly with A_w/wd'. This

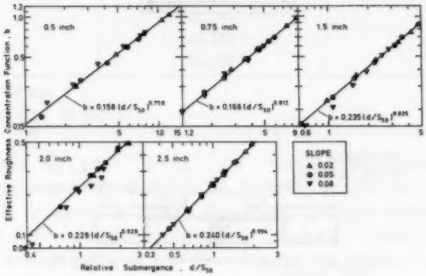

FIG. 2.—Variation of Function of Effective Roughness Concentration with Relative Submergence for Each Roughness Bed (1 in. = 25.4 mm)

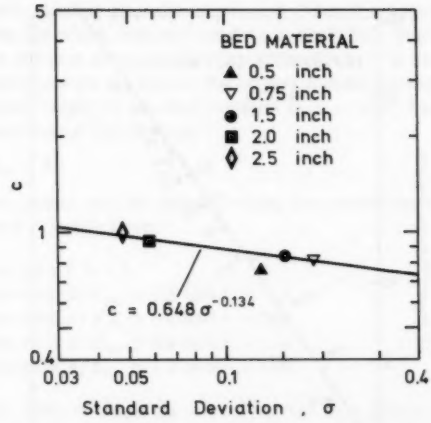

FIG. 3.—Variation of Parameter c with Bed Material Standard Deviation of Size Distribution (1 in. = 25.4 mm)

mathematical dependency is supported by earlier studies (1,13), but it is probably applicable only to large-scale roughness. As relative submergence becomes larger, the value of A_w/wd' becomes so small that a power law such as Eq. 7 breaks down.

Roughness Geometry.—In order to quantify the function of roughness geometry

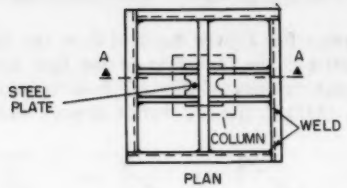

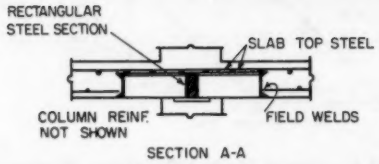

FIG. 4.—Variation of Parameter $a^{1/c}$ with Parameter Y_{50}/w (1 in. = 25.4 mm)

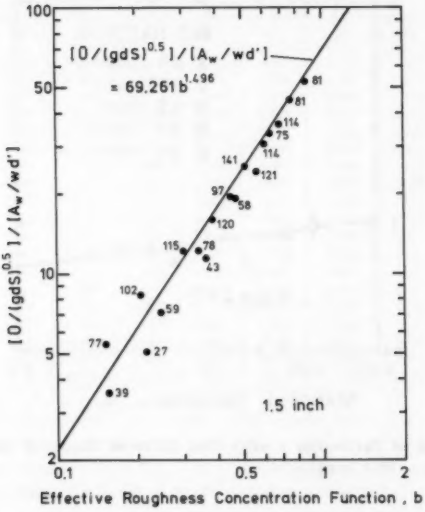

FIG. 5.—Variation of $(\bar{U}/(gdS)^{1/2})/(A_w/wd')$ with Function of Effective Roughness Concentration for 1.5 in. Bed; Corresponding Froude Numbers, Multiplied by 100, Are Given by Each Data Point (1 in. = 25.4 mm)

TABLE 7.—Parameters of Eq. 15

Bed material size, in inches (1)	Constant e (2)	Constant m (3)
0.5	127.794	1.698
0.75	116.565	1.817
1.5	69.261	1.496
2.0	62.702*	1.483*
2.5	56.236*	1.445*

Note: 1 in. = 25.4 mm.
*Calculated with Eqs. 16 and 17

in Eq. 7, the ratio $\bar{U}/(gdS)^{1/2}]/(A_w/wd')$ was plotted against the function of effective roughness concentration on separate graphs for each roughness bed. An example is shown in Fig. 5. Generally, the data points lie about one line for each bed, but scatter is obvious at the lower values of b. For these points, relative submergence is low (less than about 4) and free surface drag is presumably significant (7). This is supported by the variation of their associated Froude numbers which shows that for a given value of b, the lower the Froude number, the higher is the resistance.

In order to define the variation related to roughness geometry only, the variation related to Froude number must be eliminated. This is achieved by choosing only those points for which free surface drag is negligible. Since this condition requires that no element must be affecting the surface, it is necessary to base the selection procedure on the size of the biggest element on the bed. Assuming that the maximum height of the bed material is S_{100}, and that approximately (for a logarithmic-normal distribution)

$$\log S_{100} = \log S_{50} + 3\sigma \quad \ldots\ldots\ldots\ldots\ldots\ldots\ldots\ldots\ldots\ldots\ldots\ldots \quad (14)$$

then appropriate points may be selected using the measurements of Flammer, Tullis, and Mason (7) as follows:

1. Data points with $\mathrm{F} > 1.5$.
2. Data points with $d/S_{100} \geq 1.5$ and $\mathrm{F} > 1.3$.
3. Data points with $d/S_{100} \geq 2.5$ and $\mathrm{F} > 1.1$.
4. Data points with $d/S_{100} \geq 3.0$ and $\mathrm{F} > 1.0$.
5. Data points with $d/S_{100} \geq 3.5$ and $\mathrm{F} > 0.9$.

This segregation reduces the number of available data points to eight for the 0.5 in. material, six for the 0.75 in. material, one for the 1.5 in. material, and none for the 2.0 and 2.5 in. materials. For these rather limited data it was found that

$$\frac{\left[\dfrac{\bar{U}}{(gdS)^{1/2}}\right]}{\left[\dfrac{A_w}{wd'}\right]} = e\,b^m \quad \ldots\ldots\ldots\ldots\ldots\ldots\ldots\ldots\ldots\ldots\ldots\ldots \quad (15)$$

in which e and m = constants varying with bed material properties (Fig. 5). Their values are given in Table 7.

With values available for only three bed materials, the functions defining e and m cannot be derived with great certainty. The physical meaning of the

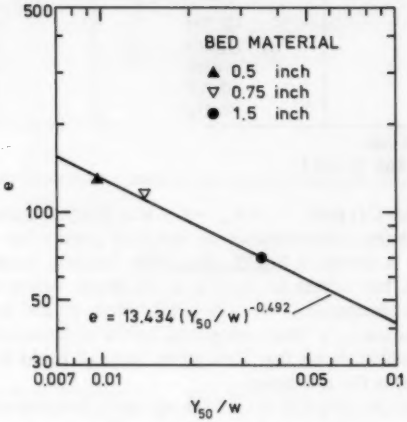

FIG. 6.—Variation of Parameter e with Parameter Y_{50}/w (1 in. = 25.4 mm)

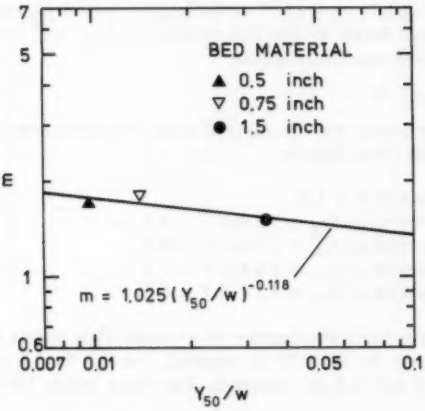

FIG. 7.—Variation of Parameter m with Parameter Y_{50}/w (1 in. = 25.4 mm)

constants is not clear and it may be that they are a reflection of the shortcomings in the analysis concerning roughness shape. However, it is also possible that, since e affects the magnitude of the function, it depends on the number of

elements at a section, given as a function of w/Y_{50}. This theory is tested in Fig. 6 which shows that

$$e = 13.434\left(\frac{w}{Y_{50}}\right)^{0.492} \quad \ldots\ldots\ldots\

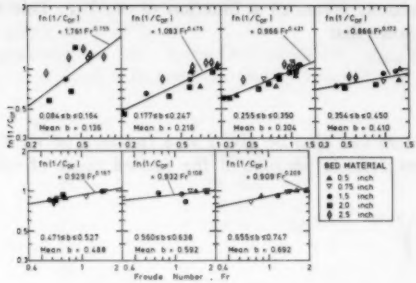

FIG. 8.—Variation of Function of Free Surface Drag Coefficient with Froude Number and Function of Effective Roughness Concentration (1 in. = 25.4 mm)

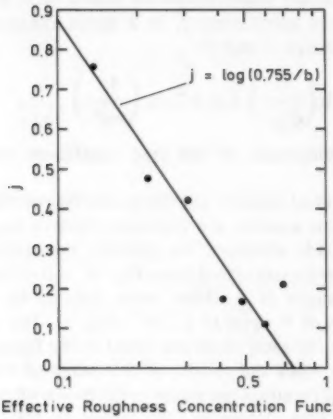

FIG. 9.—Variation of Parameter *j* with Function of Effective Roughness Concentration

b at a constant Froude number. Theoretically, at low relative submergences (or values of *b*) drag should increase and the value of *i* should decrease as relative submergence increases, but the effect should disappear at higher relative submergences. This is supported by the observed variation in the value of *i* (Fig. 8) and, for the range of the data (Fig. 10):

$$i^{1/j} = \frac{0.28}{b} \quad \ldots\ldots\ldots\

Once b rises to a value of 0.755, the constant j becomes zero and the function of the drag coefficient equals unity, corresponding to the disappearance of free surface drag. For bigger values of b this mathematical condition should be

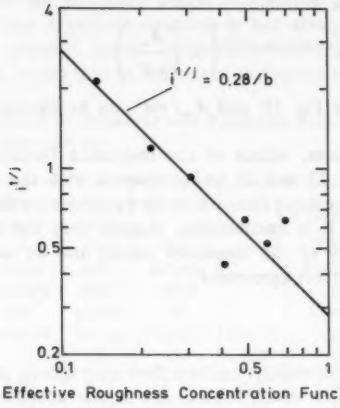

FIG. 10.—Variation of Parameter $i^{1/j}$ with Function of Effective Roughness Concentration

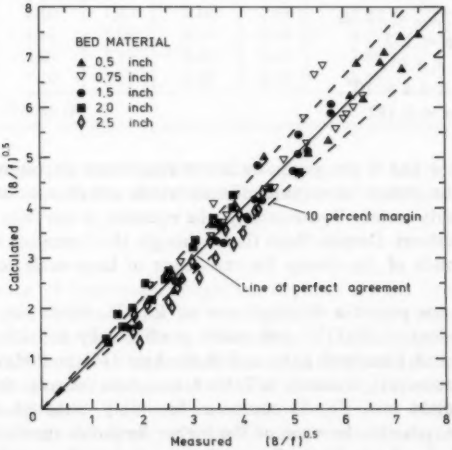

FIG. 11.—Comparison of Measured Values of Resistance Function $(8/f)^{1/2}$ with Values Calculated Using Eqs. 9, 13, and 23 (1 in. = 25.4 mm)

maintained since, physically, free surface drag continues to be absent. A value for b of 0.755 therefore defines the boundary between large-scale and intermediate-scale roughnesses.

Resistance Equation.—Combination of Eqs. 7, 16, 17, 18 and 22 gives:

$$\left(\frac{8}{f}\right)^{1/2} = \frac{\bar{U}}{(gdS)^{1/2}} = \left(\frac{0.28}{b}\mathsf{F}\right)^{\log(0.755/b)} \times \left[13.434\left(\frac{w}{Y_{50}}\right)^{0.492} b^{1.025(w/Y_{50})^{0.118}}\right] \times \left(\frac{A_w}{wd'}\right) \quad \ldots\ldots\ldots\ldots (23)$$

in which b is defined by Eq. 13; and A_w/wd' can be calculated for channels from Eq. 9.

Using all the flume data, values of the resistance function $(8/f)^{1/2}$ were calculated from Eqs. 9, 13 and 23 and compared with the measured values (Fig. 11). Since the data are those from which the equations are derived, agreement is naturally reasonable. It is encouraging, though, that the calculated values are generally within 10% of the measured values and do not exhibit trends away from the line of perfect agreement.

Application

Eq. 23 was developed for steady, uniform flow over closely packed roughness beds with nonuniform size distributions, and in the absence of vegetal and sediment transport effects, under the following conditions:

1. $0.1 < b < 1.0$.
2. $0.41 < d/S_{50} < 12.10$.
3. $13 < w/d < 153$.
4. $0.19 < \mathsf{F} < 1.93$.
5. $10^3 < \mathsf{R} < 4.4 \times 10^4$.
6. $0.047 < \sigma < 0.187$.

The values of σ and R are generally lower than those encountered in natural rivers, while the effects of varying channel width and element shape have also not been properly tested. Consequently, the equation is not fully representative of natural conditions. Despite these flaws, though, the formation of the equation has allowed much of the theory for resistance of large-scale roughness to be checked.

Space does not permit a thorough test of Eq. 23. However, a comparison of observed values of $(8/f)^{1/2}$ and values predicted by Eq. 23, the equations of Thompson and Campbell (20), and Kellerhals (14) and Hey's small-scale roughness equation (11), is shown in Table 8, based on the river data of Bathurst (1). In this limited test, Eq. 23 compares favorably, although its predictions are a little low, possibly because of the higher Reynolds numbers in the river compared with the steep stream flume. A more thorough survey of large-scale roughness equations, including Eq. 23, is given in Ref. 3.

A general theoretical resistance equation such as Eq. 23 must inevitably appear complex because the processes which it describes are complex. Simpler equations can be devised (1,5,14,20), but, while these may be very suitable under certain circumstances, they are less general and may need to be calibrated for individual sites. They do not fully elucidate the processes of flow, nor do they show

which processes are the most important in a given flow, and which may safely be neglected when making simplifications. In addition, the limits of applicability of a process-based equation can be more easily defined in advance of its use, since the range of the processes which it describes is known. Nevertheless, it is recognized that a general equation is not always the most appropriate and that Eq. 23 requires further refinement before it can be considered to be of practical use, rather than as a means of testing the theory of flow resistance.

TABLE 8.—Comparison of Observed and Predicted Values of $(8/f)^{1/2}$ Using Data from Upper River Tees, UK (1)

Site (1)	Discharge, in cubic meters per second (2)	Relative submergence R/D_{50} (3)	Observed value of $(8/f)^{1/2}$ (4)	Predicted Value of $(8/f)^{1/2}$ Using Equation of			
				Eq. 23 (5)	Thompson and Campbell (20) (6)	Kellerhals (14) (7)	Hey (11) (8)
Whiddybank	0.90	0.73	2.18	1.83	0.61	1.54	0.77
	3.90	1.34	3.07	2.81	2.07	2.28	2.23
	7.20	1.77	3.50	3.34	2.83	2.68	2.92
Cronkley A	1.37	1.02	1.60	1.52	1.36	1.59	1.74
	4.00	1.36	2.50	2.16	2.10	2.13	2.47
	7.10	1.65	3.18	2.65	2.62	2.44	2.95
Cronkley B	1.10	1.09	2.35	1.89	1.53	2.08	2.19
	4.00	1.79	3.33	2.86	2.86	2.79	3.41
	7.10	2.17	4.22	3.38	3.39	3.23	3.88

Note: 1 m^3 = 35.3 cu ft.

Eq. 23 does not apply to intermediate-scale roughness ($b > 0.755$) where standing waves, sediment movement, and other effects alter the variation of resistance.

Conclusions

Flow resistance of large-scale roughness depends on the form drag of the elements and their disposition in the channel. The relevant processes of flow can be described as functions of Reynolds number (affecting the element boundary layer), Froude number (affecting free surface drag), roughness geometry (affecting the effective roughness concentration), and channel geometry (affecting the relative roughness area). Full mathematical quantification of the functions is not yet possible, but semi-empirical analysis using extensive flume data supports the theory and has allowed the development of a basic theoretical resistance equation. Development of a more general equation depends on detailed studies of individual processes.

Acknowledgments

The writers thank those students and staff of Colorado State University

(unfortunately too numerous to mention) who helped with the flume work. James Bathurst thanks the Commonwealth Fund of New York for the Fellowship which supported his stay at Colorado State University.

Appendix.—References

1. Bathurst, J. C., "Flow Resistance of Large-Scale Roughness," *Journal of the Hydraulics Division*, ASCE, Vol. 104, No. HY12, Proc. Paper 14239, Dec., 1978, pp. 1587–1603.
2. Bathurst, J. C., Li, R-M., and Simons, D. B., "Hydraulics of Mountain Rivers," *Report No. CER78-79JCB-RML-DBS55*, Civil Engineering Department, Colorado State University, Fort Collins, Colo., 1979.
3. Bathurst, J. C., "Flow Resistance in Boulder-Bed Streams," presented at the June 22–28, 1980, University East Anglia/Institute Hydrology/Colorado State University International Workshop on Engineering Problems in the Management of Gravel-Bed Rivers, held at Gregynog, Newtown, Wales, U.K. (Proceedings to be published by John Wiley and Sons, Inc., New York, N.Y.)
4. Charlton, F. G., Brown, P. M., and Benson, R. W., "The Hydraulic Geometry of Some Gravel Rivers in Britain," *Report No. IT180*, Hydraulics Research Station, Wallingford, U.K., July, 1978.
5. Day, T., "The Channel Geometry of Mountain Streams," *Mountain Geomorphology*, Olav Slaymaker and H. J. McPherson, eds., Tantalus Research Ltd., Vancouver, B.C., 1972, pp. 141–149.
6. Day, T. J., discussion of "Resistance Equation for Alluvial-Channel Flow," by D. E. Burkham and D. R. Dawdy, *Journal of the Hydraulics Division*, ASCE, Vol. 103, No. HY5, Proc. Paper 12896, May, 1977, pp. 582–584.
7. Flammer, G. H., Tullis, J. P., and Mason, E. S., "Free Surface, Velocity Gradient Flow Past Hemisphere," *Journal of the Hydraulics Division*, ASCE, Vol. 96, No. HY7, Proc. Paper 7418, July, 1970, pp. 1485–1502.
8. Golubtsov, V. V., "Hydraulic Resistance and Formula for Computing the Average Flow Velocity of Mountain Rivers," *Soviet Hydrology: Selected Papers*, American Geophysical Union, No. 5, 1969, pp. 500–511.
9. Hartung, F., and Scheuerlein, H., "Macroturbulent Flow in Steep Open Channels with High Natural Roughness," *Proceedings of the Twelfth Congress of the International Association for Hydraulic Research*, Fort Collins, Colo., Vol. 1, Sept., 1967, pp. 1–8.
10. Herbich, J. B., and Shulits, S., "Large-Scale Roughness in Open Channel Flow," *Journal of the Hydraulics Division*, ASCE, Vol. 90, No. HY6, Proc. Paper 4145, Nov., 1964, pp. 203–230.
11. Hey, R. D., "Flow Resistance in Gravel-Bed Rivers," *Journal of the Hydraulics Division*, ASCE, Vol. 105, No. HY4, Proc. Paper 14500, Apr., 1979, pp. 365–379.
12. Johansson, C. E., "Orientation of Pebbles in Running Water," *Geografiska Annaler*, Vol. 45, Stockholm, Sweden, 1963, pp. 85–112.
13. Judd, H. E., and Peterson, D. F., "Hydraulics of Large Bed Element Channels," *Report No. PRWG 17-6*, Utah Water Research Laboratory, Utah State University, Logan, Utah, 1969.
14. Kellerhals, R., "Runoff Routing Through Steep Natural Streams," *Journal of the Hydraulics Division*, ASCE, Vol. 96, No. HY11, Proc. Paper 7666, Nov., 1970, pp. 2201–2217.
15. Li, R-M., Simons, D. B., Ward, T. J., and Steele, K. S., "Phase 1 Report: Hydraulic Model Study of Flow Control Structures," *Report No. CER77-78RML-DBS-TJW-KSS15*, Department of Civil Engineering, Colorado State University, Fort Collins, Colo., Nov., 1977.
16. Miller, J. P., "High Mountain Streams: Effects of Geology on Channel Characteristics and Bed Material," *Memoir No. 4*, State Bureau of Mines and Mineral Resources, New Mexico Institute of Mining and Technology, Socorro, N.M., 1958.
17. Peterson, D. F., and Mohanty, P. K., "Flume Studies of Flow in Steep, Rough Channels," *Journal of the Hydraulics Division*, ASCE, Vol. 86, No. HY9, Proc. Paper 2653, Nov., 1960, pp. 55–76.

18. Scheuerlein, H., "The Mechanics of Flow in Steep, Rough, Open Channels," *Proceedings of the Fifteenth Congress of the International Association for Hydraulic Research*, Vol. 1, Istanbul, Turkey, 1973, pp. 457–465.
19. Schlichting, H., *Boundary-Layer Theory*, 6th ed., McGraw-Hill Book Co., Inc., New York, N.Y., 1968, p. 622.
20. Thompson, S. M., and Campbell, P. L., "Hydraulics of a Large Channel Paved with Boulders," *Journal of Hydraulic Research*, International Association for Hydraulic Research, Vol. 17, No. 4, Netherlands, 1979, pp. 341–354.
21. Wolman, M. G., "A Method of Sampling Coarse River-Bed Material," *Transactions*, American Geophysical Union, Vol. 35, No. 6, Part 1, Dec., 1954, pp. 951–956.

MEASUREMENT OF AIR IN FLOWING WATER

By Alan F. Babb,[1] M. ASCE and Henry C. Aus[2]

INTRODUCTION

The need for measuring concentrations of entrained air often arises in hydraulic engineering studies, in both the field and the laboratory. In some instances, knowledge of the bubble sizes constituting the entrained air is also important. The writers have been interested in developing instrumentation to measure both air concentration (void fraction), and bubble size to assist in assessing the effect of structural geometry on dissolved air downstream from spillways.

Martin (3) and Schrock (5) used gamma-ray attenuation methods to measure void fraction with considerable accuracy, but those methods are not suitable for measuring bubble size. Much of the development of the gamma-ray method has taken place in those disciplines involved with the measurement of soil moisture content. The work of Gardner and Calissendorff (2), for example, provides useful information for designing a gamma-ray system. In this method, a portion of the gamma-ray beam is absorbed in passing through the medium. The density affects the amount of absorption and is determined by measuring the residual portion of the beam.

A hot-film anemometer method has been used to measure both void fraction and bubble size. Delhaye (1) studied the interaction of ascending bubbles with a conical-shaped film probe, and Resch et al. (4) studied the two-phase flow of a hydraulic jump, also using a conical hot-film probe and a digital computer. In these studies, a threshold signal is used to detect the presence of a bubble. A disadvantage with the hot-film method, however has been its dependence on empirical constants determined for conditions that frequently differ from those to which the method is to be applied.

One major objective of this paper is to introduce and describe a substantial refinement of the previously used hot-film method. The important feature of this refinement is use of the gamma-ray method for determining constants in the more versatile hot-film procedure. A second major objective is to describe the movement and distribution of entrained air in a hydraulic jump which was

[1]Head of Albrook Hydraulics Lab., and Prof. of Civ. and Environmental Engrg., Washington State Univ., Pullman, Wash. 99164.

[2]Project Mgr., Pazooki and McMenamin Consulting Engrs., Silverdale, Wash. 98383.

Note.—Discussion open until May 1, 1982. To extend the closing date one month, a written request must be filed with the Manager of Technical and Professional Publications, ASCE. Manuscript was submitted for review for possible publication on November 13, 1980. This paper is part of the Journal of the Hydraulics Division, Proceedings of the American Society of Civil Engineers, ©ASCE, Vol. 107, No. HY12, December, 1981. ISSN 0044-796X/81/0012-1615/$01.00.

used to assist in the development of the hot-film procedure.

Many aspects of the study have been treated previously but this paper treats portions of the subject in a more comprehensive manner, particularly with respect to improving procedures for predicting bubble sizes with the hot-film anemometer. In addition, the continuity equation is used in conjunction with the void fraction and mean velocity data to compute the spatial distribution of air flow entering and leaving the hydraulic jump. The mechanics of air entrainment in a hydraulic jump have been studied by Thandaveswara and Rao (6) using photographic procedures.

Apparatus for Hydraulic Jump

A flume 46 cm wide was used to generate the hydraulic jump. The test section was located at the upstream end of the flume and consisted of three 73 cm long glass panels on each side. Water was supplied from a constant head tank and measured with a magnetic flow meter before entering the flume. The flow was maintained with 1% of the predetermined 0.0566 m^3/s which produced a stable hydraulic jump at a Froude number of 6.

Gamma-Ray Attenuation Method

Fig. 1 shows the experimental system used for measuring the attenuation of a gamma-ray beam transmitted through an air-water mixture. A carriage straddling the flume was designed to move the source and detector together in vertical and longitudinal motion.

The source was Cs^{137} which emitted gamma rays with an energy level of 0.662 Mev with a half-life of 30 yr. The size of the source was 100 mc which produced a count rate of 3,600 cpm through the 46 cm wide flume filled with water, and a count rate of 192,000 cpm through the flume when it was empty. Cs^{137} was used because its gamma rays are easily absorbed by water and easily counted.

The source was housed in a lead shield 7.9 cm thick with a collimator hole 0.437 cm in diameter and 9 cm long. As the size of the collimator hole is decreased, the resolution is increased, but this also reduces the count and increases error.

Radiation was detected with a thallium-activated, sodium iodide crystal and photomultiplier tube. The crystal detector was mounted in a shield of lead 5.1 cm thick and received the beam through a collimator 0.635 cm in diameter. The two collimators were leveled and adjusted optically for alignment. The source was positioned behind the collimator to achieve maximum count.

The crystal detector emitted a voltage pulse that was proportional to the energy of the radiation pulse. The discriminator was used to select only the higher energy levels to be counted by the scaler. This procedure eliminated the scattered lower energy radiation. The discriminator had two adjustments: One selected the energy level, and the other selected the energy band width at that energy level. A pulse must have an energy within this band width to be counted.

Gamma-ray emissions are known to follow a Poisson distribution which produces an error in the measured void fraction that depends greatly on the

void fraction itself and the counting time. For example, a high void fraction (10%) and five minute counts produce a percentage standard deviation in void fraction of 2%. At low void fractions (0.1%), four hour counts are needed to reduce the percentage standard deviation in the void fraction below 40%.

Other errors can be reduced or eliminated. Due to variations in the flume width and the thickness of the glass walls, counts were made with the flume full of water at every location. Corrections were also made for the dead time of the counting equipment and the natural radiation count.

Another important error involves measurement near the free water surface

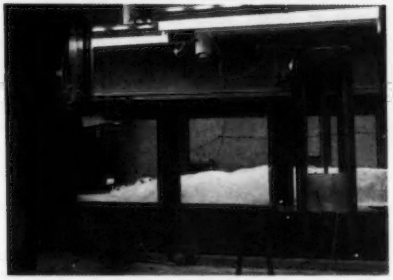

FIG. 1(*a*).—Glass-Walled Flume Showing Hydraulic Jump (Carriage for Gamma-Ray Device at Right)

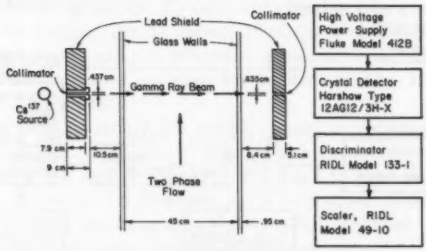

FIG. 1(*b*).—Gamma-Ray System Schematic

where the count rate increases. This error is believed to be caused by photons scattering above the surface which are not being attenuated by the water.

As a check on the system, the attentuation coefficient for pure water was measured and found to be within 0.6% of the published value.

Hot-Film Anemometer Method

The rate of heat lost by a hot-film anemometer is proportional to the temperature difference between the sensor and the fluid and the square root of the mass flow rate. Therefore, the hot-film anemometer measures a combination of temperature, density, and velocity. If temperature and velocity are held constant,

or their variation is known, the change of phase in a liquid can be detected, such as air bubbles in water.

Of the two types of heated sensors, the hot-film probe is preferable for measuring air concentration and bubble size in an air-water mixture for two basic reasons: (1) It is stronger and more durable than the wire probe; and (2) it can be electrically insulated from the ambient conducting liquid (water), whereas the wire probe cannot. This prevents decomposition by electrolysis and also the formation of carbonate, which can cause a shift in the signal (1). A conical film probe (DISA 55R42) was used in this study. It has a nickle film sputtered around a cone 0.4 mm from the apex of the cone and a quartz

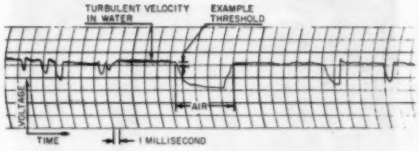

FIG. 2.—Sample Record of Hot-Film Anemometer in Two-Phase Flow

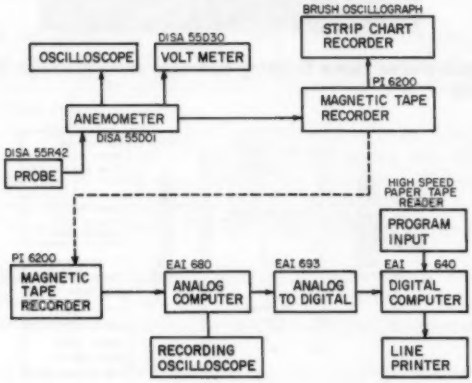

FIG. 3.—Block Diagram of Components Used

insulation coating 2μ thick. The maximum-rated velocity is 25 msec for this probe, and the upper frequency response is approx 30 kHz. The conical probe was selected because its shape provides the least distortion of available probes to bubbles moving past it, and it is able to be operated at higher velocities. In this study a DISA 55D01 anemometer was used in the constant temperature mode.

When a bubble comes in contact with the probe, there is a significant drop in the bridge voltage, as shown in Fig. 2. Delhaye (1) has found that when the bubble first comes in contact with the probe, time is taken for the water to leave the sensor. As the bubble leaves the probe, a meniscus quickly forms

and the probe is almost instantaneously back in the water, even before the bubble has completed its passage by the probe. Both of these phenomena tend to shorten the length of time the probe senses it is in a bubble, t_b, compared with the time the bubble would have taken to pass the same point without the probe. A duration factor, f_d, is used to express the additional time that must be added to t_b to arrive at the true duration of the bubble, t_a. These variables are related by:

$$t_a = t_b + f_d \quad \ldots \ldots \ldots

a standard deviation less than 10% of the mean void fraction, a minimum record length of 10 sec was used. A computer program was developed to analyze the data directly from the magnetic tape. The program required 17 min and printed out the void fraction, average velocity, total number of bubbles, average bubble size, and bubble size distribution.

Computational Procedures for Hot-Film Anemometer Method

Basic Method.—Because of limited computer storage, each piece of data was processed as it came from the digitizer. The digitizer was set to take a sample

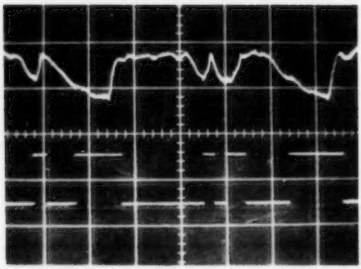

FIG. 4.—Photograph of Scope Showing Signal from Computer Indicating Bubbles Were Detected Properly

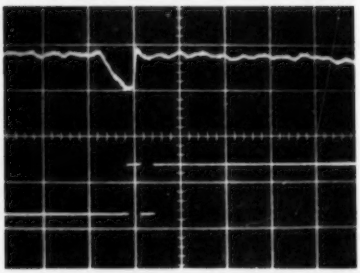

FIG. 5.—Example of Start of False Bubble at End of True Bubble

from the magnetic tape every 10 msec, the time for the computer to complete the longest loop. The magnetic tape recorder was played at a 100:1 reduction in speed which, in effect, gave a data sample each 0.1 msec from the anemometer signal.

The method for detecting bubbles was based on the fact that there is a larger drop in signal voltage during the presence of a bubble than for turbulent velocity fluctuations. If the voltage drop exceeds a predetermined value, hereafter referred to as the signal threshold (Fig. 2), a bubble is assumed to have been detected. The end of the bubble was detected by noting an increase in voltage exceeding

the signal threshold. The true bubble duration, t_a, was determined in accordance with Eq. 1 by adding the time from the beginning of the bubble to the end of the bubble, t_b, to the bubble duration factor, f_d. All the bubble durations were summed for the void fraction calculation in accordance with Eq. 2.

The development of the program required careful tuning so that bubble initiation and termination were detected properly. To assist in this development, an oscilloscope was used to view concurrently the hot-film signal and a signal from the computer that indicated when the computer detected a bubble. Fig. 4 shows the program working properly. When the broken, horizontal line at the bottom of the photograph in Fig. 4 is in a high position, the computer

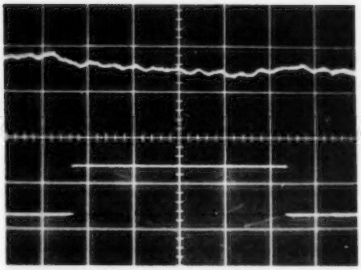

FIG. 6.—Example of False Bubble Detected on General Decrease in Flow Velocity

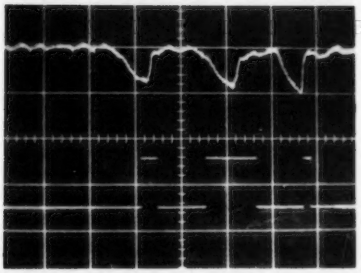

FIG. 7.—Example of End of True Bubble Detection Too Late

is detecting a bubble. Fig. 5 shows a bubble having a pronounced end point which started a false bubble at the end of the true bubble. The program would end this false bubble at the end of the next true bubble, suggesting a bubble of a very large size. The computer was programmed to disregard these large bubble sizes when they exceeded a predetermined value. Fig. 6 shows a false bubble that was detected because of a general decrease in velocity. The false bubbles in Figs. 5 and 6 could have been eliminated by increasing the signal threshold. But when this was done, the computer would miss many of the smaller bubbles not shown in these figures. The center bubble in Fig. 7 is an example of where the program did not sense the end of the bubble soon

enough. In this case the high point in the signal did not occur at the end of the bubble. The bubble in Fig. 8 is an example of where the program stopped sensing the bubble too soon. A small peak was found on the slowly rising signal before the end of the bubble was reached.

The program was designed to eliminate the error types previously analyzed by using the average of a number of the most recent data points, instead of one point, to find the beginning of the bubble. The maximum number of data points used, called an array, was specified at the beginning of the program.

A bubble is detected when the difference between the array average and the latest data point is greater than the specified threshold. This is the bubble detection point. The end of the bubble is detected either when the difference between the average of the array and the signal is again less than the specified threshold, or when the difference between data points is greater than one volt. The last condition was designed to end the bubble on the characteristic sharp rise in signal, even if the signal never rose far enough to satisfy the first condition. The beginning and end of the bubble were calculated at the intersections of the falling and rising slopes of the signal and the average of the array (Fig. 2).

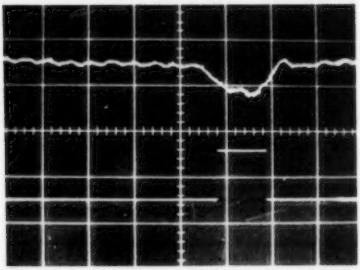

FIG. 8.—Example of End of True Bubble Detection Too Early

This program was tested using square, triangular, and sine waves from a signal generator. Using the oscilloscope as a visual check on the detection of bubbles by the computer, the number of errors was tabulated for a specific length of run using different factors for both the threshold and the length of array. The minimum number of errors was found using an array length of 15 and a threshold of 0.72 v. For these values, from a total of 677 bubbles detected on the oscilloscope, 21 of the smaller bubbles, or 3.1%, were missed by the computer program. In addition, 15 bubbles, or 2.2%, were not started or ended correctly. This latter condition occurred when the bubbles were spaced very close together. The insertion of a program statement signaling the end of a bubble at a sharp rise in signal eliminated this problem.

Duration Factor, Function of Velocity.—The value of the duration factor does not affect the detection of the bubble and thus was adjusted after the optimum values of threshold and array length were found. The duration factor is a function of how the bubble passes the probe and was used to correct the length of time the computer sensed the probe was in a bubble. Both the bubble size

and void fraction are dependent on the duration factor, which was adjusted to achieve a void fraction equal to that found by the gamma-ray method. The duration factor was found to be a function of the velocity of flow.

Data were taken at seven different locations in the hydraulic jump, with the average velocity varying from 0.48 m/s to 3.21 m/s. The duration factor is plotted against average velocity in Fig. 9. The following exponential equations fits the plotted data from this study:

$$f_d = 1.91\, e^{-0.39\,V} \quad \ldots\ldots\ldots\

void fraction as the gamma-ray method. The effect of bubble size, however, was not considered in establishing the duration factor. This may affect to some extent the distribution of measured bubble sizes, even though they produce the same void fraction measured with the gamma-ray method.

The assumptions made are that a bubble is a sphere and the probe always intercepts a bubble along its diameter. Photographs indicate that the bubbles in the highly turbulent hydraulic jump are not always spherical, and the probe, of course, does not always intercept the bubble through its center. The gamma-ray method, however, furnishes the calibration that permits these difficulties to be partially overcome. The calibrated hot-film method is able to produce average bubble sizes within the accuracy of the gamma-ray method and a bubble size distribution that will be at least qualitatively correct.

If a bubble is sufficiently small it will not be detected by the hot-film method. Minimum bubble sizes were computed using Fig. 9 and the assumption that it would take a minimum of twice the sampling time to detect a bubble, and the sampling time itself to end the bubble. This is expressed as

$$d_{b_{min}} = V(f_d + 3t_s) \quad \ldots\ldots\ldots\

method. Due to the surface effect reviewed earlier, it was not possible to measure void fraction near the surface. The locations where air enters and leaves the hydraulic jump can be identified by using the void fraction values from Fig. 11 and mean velocities from Fig. 12 in the continuity equation for the air component. Considering the finite control volume shown in Fig. 13, and assuming that the velocity of the air bubbles is equal to the adjacent water velocity, the steady-state continuity equation for the air component, which expresses

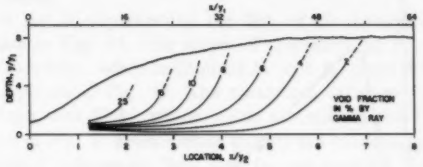

FIG. 11.—Void Fraction in Hydraulic Jump

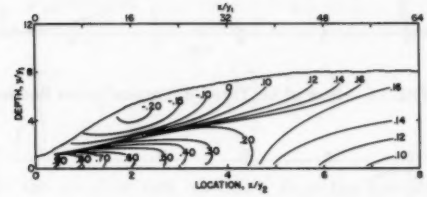

FIG. 12.—Distribution of Dimensionless Mean Velocity, V/V_1

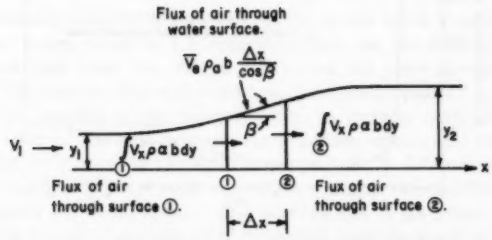

FIG. 13.—Control Volume for Development of Continuity Equation for Air Component

that the net flux of air through the control surfaces (outflow-inflow) is zero, is

$$\int_{②} V_x \rho \alpha b dy - \int_{①} V_x \rho \alpha b dy - \bar{V}_e \rho_a b \frac{\Delta x}{\cos \beta} = 0 \quad \ldots \ldots \ldots \ldots \ldots \quad (6)$$

in which $\bar{V}_e$ = the average velocity of air entering the jump over Δx; V_x = the temporal average velocity in the x-direction at a point; α = the corresponding

temporal average void fraction; ρ = the density of air in the bubbles and varies with depth; ρ_a = the density of air at atmospheric pressure; y = the vertical distance from the channel invert; x = the horizontal distance referenced to the upstream end of the jump; β = the slope of the water surface; and b = the width of the jump.

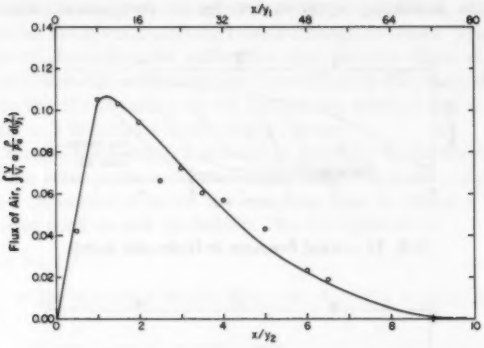

FIG. 14.—Flux of Air Through Vertical Cross Section

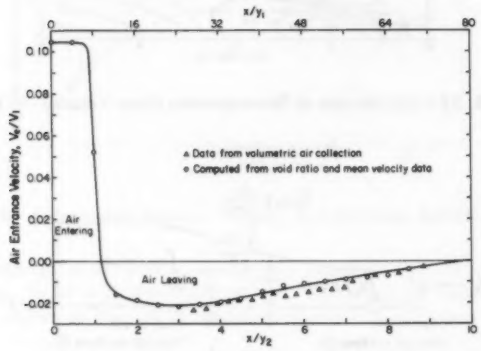

FIG. 15.—Dimensionless Air Entrance Velocity

From Eq. 6, V_e, the temporal average velocity of air entering the jump at a particular location x, is given by

$$V_e = \frac{\cos\beta}{\rho_a} \lim_{\Delta x \to 0} \frac{\Delta \int_o^{y_o} V_x \rho \alpha \, dy}{\Delta x} = \frac{\cos\beta}{\rho_a} \frac{d}{dx} \int_o^{y_o} V_x \rho \alpha \, dy \quad \ldots\ldots\ldots\ldots (7)$$

in which $\Delta \int_o^{y_o} V_x \rho \alpha \, dy$ = the net flux of air through the control surfaces

① and ②; and y_o = the water depth. In dimensionless form, Eq. 7 becomes

$$\frac{1}{\cos\beta}\frac{V_e}{V_1} = \frac{d}{d\left(\frac{x}{y_1}\right)}\int_o^{y_o/y_1}\frac{V_x}{V_1}\frac{\rho}{\rho_a}\alpha\, d\left(\frac{y}{y_1}\right) \quad \ldots\ldots\ldots\ldots\ldots\ldots (8)$$

in which V_1 = the depth averaged velocity upstream from the jump; and y_1 = the upstream depth.

The integral in Eq. 8, representing the flux of air through a vertical cross section, is plotted in Fig. 14. The slope of the curve in Fig. 14 is equal to $(1/\cos\beta)(V_e/V_1)$ which, when multiplied by cos β, gives the dimensionless velocity V_e/V_1, ploted in Fig. 15. The maximum value measured for β, the water surface slope, was 17.3°, which yields a minimum cosine of 0.95. Thus, the values plotted in Fig. 15 approximate closely the curve slope in Fig. 14.

The dimensionless volumetric flow rate for air entering through the water surface of the jump upstream from a location x is given by

$$\frac{Q_{a_x}}{Q_1} = \frac{1}{V_1 b y_1}\int_o^x V_e b\frac{dx}{\cos\beta} = \int_o^{x/y_1}\frac{1}{\cos\beta}\frac{V_e}{V_1}d\left(\frac{x}{y_1}\right)$$

$$= \int_o^{x/y_1}\left[\frac{d}{d\left(\frac{x}{y_1}\right)}\int_o^{y_o/y_1}\frac{V_x}{V_1}\frac{\rho}{\rho_a}\alpha\, d\left(\frac{y}{y_1}\right)\right] d\left(\frac{x}{y_1}\right) \quad \ldots\ldots\ldots\ldots (9)$$

in which Q_{a_x} = the air flow rate upstream from the location x; and Q_1 = the water flow rate upstream from the jump.

The accumulated area under the curve in Fig. 15 represents closely the ratio Q_{a_x}/Q_1.

The air entrance velocity is zero at x/y_2 (y_2 is the depth downstream from the hydraulic jump) equal to 1.2, indicating that, on the average, air enters the jump upstream from this station and leaves the jump downstream from this station. The equality of positive and negative areas shown in Fig. 15 provides a check on the validity of the measurements, as there is negligible air in the flow at the end of the test section. As a further check, air was collected volumetrically as it escaped through the water surface. These measurements, also plotted in Fig. 15, show good agreement with the values determined from the void fraction and mean velocity data near the end of the jump.

Bubble sizes for nine locations were calculated from the hot-film anemometer data. To assist in the analysis of the bubble size distribution, a density function, $f(d_b)$, was defined as the limit of the volume fraction of the detected air in a range of bubble size, Δd_b, divided by the range, Δd_b, and multiplied by the void fraction α. This is expressed mathematically as

$$f(d_b) = \lim_{\Delta d_b \to 0}\frac{\text{volume of air of } \Delta d_b}{\text{volume of air in all bubbles in sample}}\cdot\frac{\alpha}{\Delta d_b} \quad \ldots\ldots\ldots (10)$$

A cumulative distribution function, $F(d_b)$, giving the volume fraction of air in bubbles less than diameter d_b, was defined as

$$F(d_b) = \int_o^{d_b} f(d_b)\, d(d_b) \quad \ldots\ldots\ldots\

with noise, and would eliminate the necessity for the computation time to be restricted by a data sample interval. This would allow the computer to work much faster and would allow for the use of more time-consuming calculations, such as a velocity calibration curve and a function that would correlate the duration factor with velocity.

Summary

Procedures to determine the void fraction and bubble sizes in an air-water mixture were developed using a hot-film probe and digital computer. A gamma-ray method for measuring void fraction was used to calibrate the duration factor for the hot-film method. The duration factor was found to be a function of velocity and varied from about 1.5 msec for a velocity of 0.5 m/s, to about 0.5 msec for 3.5 m/s.

The hot-film method is described in detail by identifying possible sources of error and then outlining procedures for their elimination. These errors primarily involved the identification by the computer of a bubble that did not exist, and the failure to properly detect the end of all bubbles. Concurrent display on a recording oscilloscope of both the anemometer signal, and an indication of whether or not the computer was detecting air or water, was used to optimize the method.

The minimum size of bubble detectable by this method was shown to be a function of the size of the duration factor and, therefore, a function of velocity.

Measurements of void ratio and bubble size in a hydraulic jump of Froude number 6 were used to both assist in the development of the experimental methods, and also to develop an understanding of the movement of air in and out of the hydraulic jump. Use of the void fraction and mean velocity measurements with the continuity equation showed that air was entrained upstream from x/y_2 equal to 1.2. Air escaped from the jump downstream from this location. The maximum air velocity entering the jump upstream from x/y_2 equal to 1.2 was estimated to be constant at 10.4% of the water velocity upstream from the jump. The maximum measured air velocity leaving the jump was equal to 2.1% of the water velocity upstream of the jump, and occurred at x/y_2 equal to 3. The total air entering the jump was equal to the total air leaving, providing a check on accuracy. Independent measurements of escape velocities also checked well with computed values.

Bubble size measurements indicated that larger bubble sizes (maximum of 10 mm) are located near the upstream end of the jump. The longevity of larger bubble sizes is very short because of turbulence, shear, and buoyancy.

Appendix I.—References

1. Delhaye, J. M., "Hot-Film Anemometry in Two-Phase Flow," presented at the August 3–6, 1969, National American Society of Mechanical Engineers/American Institute of Chemical Engineers Heat Transfer Conference, Minneapolis, Minn.
2. Gardner, W. H., and Calissendorff, C., "Gamma Ray and Neutron Attenuation in Measurement of Soil Bulk Density and Water Content," *Proceedings, Symposium on Isotope and Radiation Techniques in Soil Physics and Irrigation Studies*, IAEA, 1967.
3. Martin, C. Samuel, "Characteristics of an Air-Water Mixture in a Vertical Shaft," *Proceedings, 21st Annual Hydraulics Division Specialty Conference*, ASCE, Aug., 1973.

4. Resch, Francois J., Leutheusser, Hans J., and Alema, Solomon, "Bubbly Two-Phase Flow in Hydraulic Jump," *Journal of the Hydraulics Division*, ASCE, Vol. 100, Proc. Paper 10297, Jan., 1974, pp. 137–149.
5. Schrock, V. E., "Radiation Attenuation Techniques in Two-Phase Flow Measurements," *Proceedings*, 11th National American Society of Mechanical Engineers/American Institute of Chemical Engineers Heat Transfer Conference, August, 1969.
6. Thandaveswara, B. S., and Rao, N. S. Lakshmana, "Bubble Characteristics in Hydraulic Jumps," *Indian Journal of Technology*, Vol. 16, New Delhi, India, Dec., 1978, pp. 559–566.

Appendix II.—Notation

The following symbols are used in this paper:

b = width of jump;
d_b = bubble diameter;
$d_{b_{min}}$ = minimum bubble diameter;
$d_{b_{50}}$ = bubble size for which 50% of air is contained in smaller bubble sizes;
$F(d_b)$ = cumulative distribution function for bubble sizes;
f_d = bubble duration factor in msec;
$f(d_b)$ = density function for bubble sizes;
n = total number of bubbles in test;
Q_{a_x} = air flow rate upstream from location x;
Q_1 = water flow rate upstream from jump;
T_a = total time probe is in air;
T_w = total time probe is in water;
t_a = true duration of bubble;
t_b = time probe senses it is in bubble;
t_s = data sampling time;
V = average flow velocity at point;
V_e = average velocity of air entering jump;
$\bar{V}_e$ = average velocity of air entering jump over Δx;
V_x = temporal average velocity in x-direction;
V_1 = velocity immediately upstream from jump;
x = horizontal distance referenced to upstream end of jump;
y = vertical distance from channel invert;
y_o = water depth;
y_1 = depth upstream from hydraulic jump;
y_2 = depth downstream from hydraulic jump;
α = void fraction;
β = slope of water surface;
ρ = mass density of air in bubble; and
ρ_a = mass density of air at atmospheric pressure.

RADIAL SOURCE-SINK FLOW IN STRATIFIED OCEAN

By Gerhard H. Jirka,[1] M. ASCE, R. Peter Johnson,[2] and Frank E. Sargent[3]

INTRODUCTION

The fluid motions and mixing characteristics resulting from a turbulent buoyant discharge flow, and a simultaneous sink flow within a discretely stratified medium, are considered under conditions of radial symmetry about a vertical axis.

The motivation for the study of this problem derives from an analysis of the operating characteristics and environmental perturbations induced by ocean thermal energy conversion (OTEC) plants. OTEC is a method of generating useful power using the vertical temperature gradient of the tropical ocean as a source for energy availability. The upper layer of the ocean collects heat by absorbing solar radiation. The underlying water is colder due to the return flow from polar regions which occurs within the global ocean circulation. Thus, a temperature stratified system is formed, as shown in Fig. 1(*a*), for different tropical ocean localities. The vertical salinity distribution is usually locality dependent. However, its effect on density is generally much weaker than that of temperature. In total, a stable density stratified system (Fig. 1(*b*)) is formed, consisting of a relatively thin upper layer (of the order of 50–100 m) and a deep lower layer, separated by a thermocline-pycnocline with strong gradients of temperature and density.

An OTEC plant is basically a conventional thermodynamic engine operating on the Rankine principle. Water from the warm upper layer and the cold lower layer is taken in and passes through an evaporator and a condenser, respectively. These heat exchangers evaporate and condense into an internal working fluid (e.g., ammonia) which, in turn, drives a turbine generator. The major distinction from conventional power plants is its very low thermal efficiency, of the order of 2%, because of the small ocean temperature difference, of the order of 20° C. Thus, in order to produce electric power at a significant level, an OTEC plant must use very large water flow rates to exploit its low-grade energy resource.

[1]Assoc. Prof., School of Civ. and Environmental Engrg., Cornell Univ., Ithaca, N.Y. 14853.

[2]Engr., Arctec Inc., Columbia, Md., 21045.

[3]Research Asst., School of Civ. and Environmental Engrg., Cornell Univ., Ithaca, N.Y. 14853.

Note.—Discussion open until May 1, 1982. To extend the closing date one month, a written request must be filed with the Manager of Technical and Professional Publications, ASCE. Manuscript was submitted for review for possible publication on July 16, 1980. This paper is part of the Journal of the Hydraulics Division, Proceedings of the American Society of Civil Enginers, ©ASCE, Vol. 107, No. HY12, December, 1981. ISSN 0044-796X/81/0012-1631/$01.00.

For example, to produce 100 MW, a total flow rate of 1,000 m^3/s is required (8), which is large by any standard of engineering design. For a potential 1,000 MW plant, the flow rate is correspondingly higher and represents about half of the Mississippi River's mean discharge!

Various OTEC design options are being pursued within the research and development programs which are in progress in the U.S. and abroad (5,11). One of the critical problems, in view of the large flow rates involved, is the potential for recirculation. Recirculation is defined as the repeated intake of diluted water which has passed through the evaporator or condenser. Recirculation will have a detrimental effect on plant efficiency due to a further reduction of the available temperature difference. Recirculation could also lead to adverse

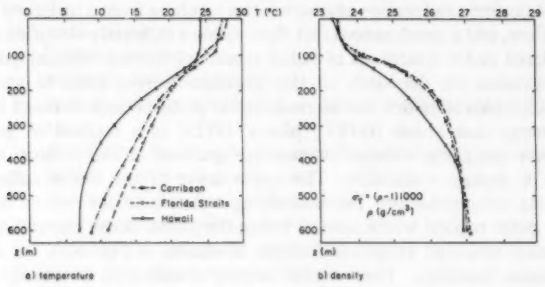

FIG. 1.—Examples of Observed Vertical Temperature and Density Profiles for Different Tropical Ocean Localities (8)

environmental impact due to the local accumulation of control chemicals (for biofouling and corrosion) used in plant operation.

Problem Schematization

The actual ocean density stratification (Fig. 1) is idealized as a two-layered system with densities ρ_1 and ρ_2, and upper layer thickness H (Fig. 2(*a*)). This idealization preserves the major characteristics of the actual ambient potential (buoyant) energy distribution, while introducing a considerable simplification into the analysis. The ambient ocean is assumed to be stagnant. This is considered to represent the most restrictive condition for plant recirculation. In fact, observations on current conditions at several candidate sites for OTEC installation (e.g., Hawaii, Puerto Rico) show periods of very low velocity or of complete stagnation (reversal episodes).

The OTEC plant is schematized as a simple cylindrical structure with intakes at the top (evaporator flow) and the bottom (condenser flow). Two types of discharge schemes are considered.

Separate Discharge Scheme.—The evaporator and condenser flow are discharged through separate radial slots above and below the thermocline, respectively. As recirculation is much more critical in the shallow upper layer, the evaporator discharge is located as deep as possible, just above the thermocline. (In principle,

the evaporator discharge would also be below the thermocline; however, this appears to be very complicated and costly from the standpoint of internal plant design.) The evaporator discharge density is $\rho_0 = \rho_1 + \Delta\rho$ in which $\Delta\rho$ = the density change corresponding to the evaporator flow temperature change, which is small (order of 2° C). Thus, as $\Delta\rho << (\rho_2 - \rho_1)$, the turbulent discharge

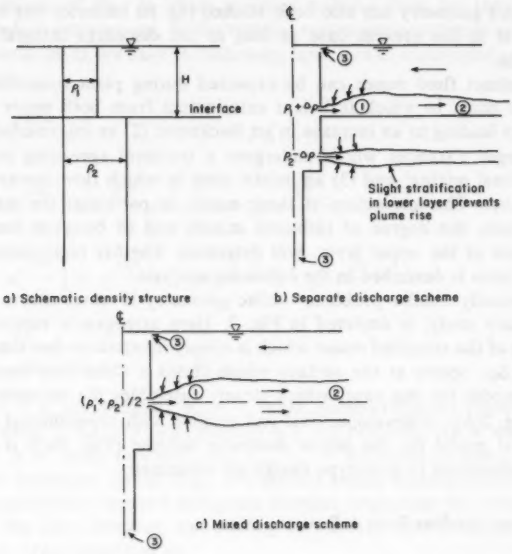

FIG. 2.—Schematizations of Density Structure and OTEC Discharge Schemes

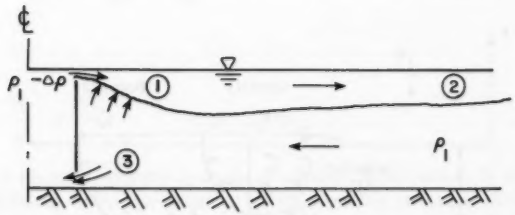

FIG. 3.—Single Layer Simulation in Laboratory Experiment

flow will experience strong buoyant damping with respect to the lower layer, but only weak damping with respect to the upper layer.

Mixed Discharge Scheme.—The evaporator and condenser flow are combined and discharged through a radial slot at the interface level. In practice, the flows may be combined within the plant or they may mix externally—if the discharge

openings are close to each other—by virtue of the Coanda effect. The discharge density is $\rho_0 = (\rho_1 + \rho_2)/2$. In fact, both discharge schemes are under consideration in the current OTEC development program.

In addition to its recirculation potential, each scheme has certain advantages and drawbacks, as far as plant design, operation, and environmental impacts are concerned. The alternate possibility of a separate port design instead of the radial slot geometry has also been studied (8). Its behavior has been shown to be similar to the present case as long as the discharge integral properties are the same.

Three distinct fluid zones can be expected during plant operation: (1) The buoyant jet zone, in which turbulent entrainment from both upper and lower layer occurs leading to an increase in jet thickness; (2) an intermediate buoyant layer at larger distances which undergoes a transient spreading motion with little additional mixing; and (3) an intake zone in which flow toward the plant intakes occurs. The interaction of these zones, in particular the magnitude of the flow rates, the degree of turbulent mixing and of buoyant damping, and the thickness of the upper layer, will determine whether recirculation occurs. This interaction is described in the following analysis.

A dynamically similar problem, whose geometry is much more convenient for laboratory study, is depicted in Fig. 3. Here attention is restricted to the upper layer of the stratified ocean which is simply inverted so that the discharge, $\rho_0 = \rho_1 - \Delta\rho$, occurs at the surface which forms a shear-feee boundary. An analytical model for this case, which closely resembles the separate discharge scheme (Fig. 2(*b*)), is developed first and verified with experimental data. Then an analytical model for the mixed discharge scheme (Fig. 2(*c*)) is presented. Finally, applications to prototype design are examined.

Radial Surface Jet-Sink Flow in Shallow Layer

Governing Equations.—In the following, the source-sink flow interaction is modeled by considering simply zones 1 and 3 (Figs. 2, 3) and neglecting the

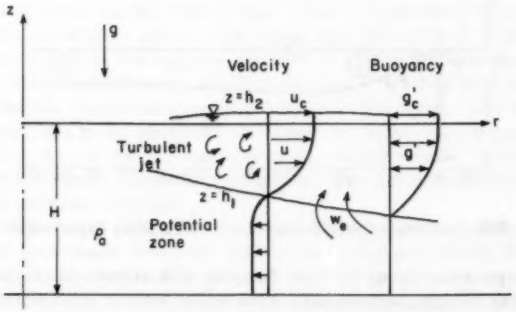

FIG. 4.—Structure of Turbulent Surface Jet Flow with Potential Return Flow in Single Layer Model

dynamics of the intermediate buoyant layer. This is justified in hindsight by the theoretical and experimental results which indicate a considerable horizontal extent of the jet zone, which then controls any potential recirculation.

The flow in the shallow layer surrounding the source-sink is made up (Fig. 4) of a turbulent zone with active momentum and heat diffusion, and a potential return flow zone (neglecting any thin boundary layers which would develop under conditions of Fig. 3) which supplies ambient fluid for the intake and for the turbulent entrainment. In the radially symmetric coordinate system fixed to the still-water level, we have the following equations of motion and of buoyancy conservation:

$$\frac{1}{r}\frac{\partial}{\partial r}(ru) + \frac{\partial w}{\partial z} = 0 \quad \ldots\ldots (1)$$

$$\rho\left(u\frac{\partial u}{\partial r} + w\frac{\partial u}{\partial z}\right) = -\frac{\partial p}{\partial r} + \frac{1}{r}\frac{\partial}{\partial r}(r\tau_{rr}) + \frac{\partial \tau_{rz}}{\partial z} \quad \ldots\ldots (2)$$

$$\rho\left(u\frac{\partial w}{\partial r} + w\frac{\partial w}{\partial z}\right) = -\frac{\partial p}{\partial z} + \rho g + \frac{1}{r}\frac{\partial}{\partial r}(r\tau_{rz}) + \frac{\partial \tau_{zz}}{\partial z} \quad \ldots\ldots (3)$$

$$u\frac{\partial g'}{\partial r} + w\frac{\partial g'}{\partial z} = \frac{1}{r}\frac{\partial}{\partial r}(rj_r) + \frac{\partial j_z}{\partial z} \quad \ldots\ldots (4)$$

in which r, z = coordinates; u, w = mean (time-averaged) velocities; g' = mean buoyancy = $\Delta\rho/\rho\, g$; g = gravity; ρ = total density; $\Delta\rho$ = mean density difference; p = mean pressure; τ_{rr}, τ_{zz}, τ_{rz} = Reynolds stresses; and j_r, j_z = turbulent buoyancy fluxes. Eqs. 1–4 assume steady incompressible flow and neglect all molecular transport processes. Further, neglecting the normal stresses relative to the shear stresses, and making a boundary layer assumption, $w << u$, $\partial/\partial z >> \partial/\partial r$, simplifies to

$$\rho\left(u\frac{\partial u}{\partial r} + w\frac{\partial u}{\partial z}\right) = -\frac{\partial p}{\partial r} + \frac{\partial \tau_{rz}}{\partial z} \quad \ldots\ldots (5)$$

$$0 = -\frac{\partial p}{\partial z} - \rho g \quad \ldots\ldots (6)$$

$$u\frac{\partial g'}{\partial r} + w\frac{\partial g'}{\partial z} = \frac{\partial j_z}{\partial z} \quad \ldots\ldots (7)$$

Thus, Eq. 6 assumes a purely hydrostatic pressure distribution. In the extreme of a recirculating flow, this omission of the dynamic pressure should remain valid as long as the horizontal extent of the recirculating motion is larger than the layer depth. Eq. 6 can be integrated, $\rho = \rho_a - \Delta\rho$:

$$p = -\int_{-H}^{z} (\rho_a - \Delta\rho)\, g\, dz + p_H \quad \ldots\ldots (8)$$

in which p_H = the reference pressure at $z = -H$. This is found by applying a Bernoulli equation for the streamline between r and ∞:

$$p_H = \rho_a g H - \rho_a \frac{u_B^2}{2} \quad \ldots\ldots\ldots\ldots\ldots\ldots\ldots\ldots\ldots\ldots\ldots\ldots (9)$$

in which u_B = the local, vertically uniform potential flow velocity. Thus, the pressure gradient in Eq. 5, which applies over the turbulent layer $h_1 < z < h_2$, becomes

$$\frac{\partial p}{\partial r} = \frac{\partial}{\partial r} \int_{h_1}^{z} \Delta\rho\, g\, dz - \frac{\partial}{\partial r}\left(\rho_a \frac{u_B^2}{2}\right) \quad \ldots\ldots\ldots\ldots\ldots\ldots\ldots\ldots (10)$$

Integral equations are formed by vertically integrating over the turbulent layer and observing the kinematic and dynamic conditions at the boundaries. This gives, after multiplying by $2\pi r$, use of the Boussinesq assumption, and by further manipulation, the following conservation equations:

$$\text{Volume flux:} \quad \frac{dQ}{dr} = 2\pi r\, w_e \quad \ldots\ldots\ldots\ldots\ldots\ldots\ldots\ldots\ldots\ldots (11)$$

$$\text{Momentum flux:} \quad \frac{dM}{dr} = -2\pi r\, w_e\, u_B - 2\pi r \frac{d}{dr} \int_{h_1}^{h_2} \int_{h_1}^{z} g'\, dz\, dz$$

$$+ \pi r\, h \frac{du_B^2}{dr} \quad \ldots\ldots\ldots\ldots\ldots\ldots\ldots\ldots\ldots\ldots\ldots\ldots\ldots (12)$$

$$\text{Buoyancy flux:} \quad \frac{dJ}{dr} = 0 \quad \ldots\ldots\ldots\ldots\ldots\ldots\ldots\ldots\ldots\ldots\ldots\ldots (13)$$

for which these definitions have been made:

$$\text{Volume flux} \quad Q = 2\pi r\, I_1\, u_c\, h \quad \ldots\ldots\ldots\ldots\ldots\ldots\ldots\ldots\ldots\ldots (14)$$

$$\text{Momentum flux:} \quad M = 2\pi r\, I_2\, u_c^2\, h \quad \ldots\ldots\ldots\ldots\ldots\ldots\ldots\ldots\ldots\ldots (15)$$

$$\text{Buoyancy flux:} \quad J = 2\pi r\, I_3\, u_c\, g_c'\, h \quad \ldots\ldots\ldots\ldots\ldots\ldots\ldots\ldots\ldots\ldots (16)$$

in which h = the layer thickness, $h_2 - h_1$; u_c and g_c' = maximum values of velocity and buoyancy, respectively; and w_e = the local vertical entrainment velocity which incorporates nonturbulent fluid into the turbulent zone. Inherent in the above integration process is the assumption of self-similarity, i.e., an internal force balance which is independent of position. This is clearly not valid in the present problem which involves several length and dynamic scales, but should not be of serious consequence due to the bulk nature of the integral approach. Assumed self-similarity implies constant values of the integral coefficients which are defined as

$$I_1 = \int_0^1 f(\eta)\, d\eta, \quad I_2 = \int_0^1 f^2(\eta)\, d\eta, \quad I_3 = \int_0^1 f(\eta)\, g(\eta)\, d\eta \quad \ldots\ldots\ldots (17)$$

in which $\eta = z/h$; and f and g = the velocity and buoyancy profiles normalized by h and their maximum values. Denoting the total pressure force

$$P = 2\pi r\, I_4\, g_c'\, h^2 \quad \ldots\ldots\ldots\ldots\ldots\ldots\ldots\ldots\ldots\ldots\ldots\ldots\ldots (18)$$

in which $I_4 = \int_0^1 \int_0^\eta f \, d\eta d\eta$, and defining the momentum function or flow force, with Benjamin (3)

$$M_F = M + P \quad \ldots\ldots\ldots\ldots\ldots\ldots\ldots\ldots\ldots\ldots\ldots\ldots\ldots\ldots\ldots\ldots\ldots\ldots \quad (19)$$

an alternative conservation equation is obtained

$$\frac{d M_F}{dr} = -2\pi r \, w_e \, u_B + \frac{P}{r} + \pi r h \frac{d u_B^2}{dr} \quad \ldots\ldots\ldots\ldots\ldots\ldots\ldots\ldots\ldots\ldots\ldots\ldots\ldots\ldots \quad (20)$$

The use of Eq. 15 has advantages in the numerical solution scheme as the flow force is an approximately conserved quantity, while other parameters (e.g., M, u_c, h) can undergo jump-like transitions. This conservative aspect of M_F is readily seen by considering in Eq. 20 the limiting two-dimensional case, $r \to \infty$, with a deep layer, $u_B \to 0$.

Thus, Eqs. 11, 13, and 20 are the governing differential equations of the problem, Eq. 13 being trivial. Several algebraic equations relate the auxiliary variables to the three main quantities. These are Eqs. 15, 18, and 19 from which follows

$$u_c = \frac{M}{Q} \frac{I_1}{I_2}, \quad g_c' = \frac{J}{Q} \frac{I_1}{I_3} \quad \ldots\ldots\ldots\ldots\ldots\ldots\ldots\ldots\ldots\ldots\ldots\ldots\ldots\ldots\ldots\ldots\ldots\ldots \quad (21)$$

and h is the solution of the third order equation

$$2\pi r \frac{I_1 I_4}{I_3} \frac{J}{Q} h^3 - M_F h + \frac{1}{2\pi r} \frac{I_2}{I_1^2} Q^2 = 0 \quad \ldots\ldots\ldots\ldots\ldots\ldots\ldots\ldots\ldots\ldots\ldots\ldots\ldots\ldots \quad (22)$$

Furthermore, continuity over the entire layer implies equal return flow and thus

$$u_B = \frac{Q}{2\pi r (H - h)} \quad \ldots\ldots\ldots\ldots\ldots\ldots\ldots\ldots\ldots\ldots\ldots\ldots\ldots\ldots\ldots\ldots\ldots\ldots\ldots\ldots \quad (23)$$

Entrainment Rate.—The only remaining unknown in the equation system is the entrainment velocity, w_e. Following the usual convention in free turbulent shear flows, it is taken as proportional to the jet velocity scale u_c:

$$w_e = \alpha_r^* \, u_c \quad \ldots\ldots\ldots\ldots\ldots\ldots\ldots\ldots\ldots\ldots\ldots\ldots\ldots\ldots\ldots\ldots\ldots\ldots\ldots\ldots \quad (24)$$

in which α_r^* = the entrainment coefficient which describes the effects of radial geometry and of buoyant damping of turbulence.

For the nonbuoyant case and a deep stagnant ambient fluid the momentum, Eq. 12, indicates conservation, $dM/dr = 0$. The mixing length arguments for free turbulent motions given by Schlichting (13) can be readily extended to the radial jet, indicating a constant (linear) spreading rate

$$\frac{dh}{dr} = k \quad \ldots\ldots\ldots\ldots\ldots\ldots\ldots\ldots\ldots\ldots\ldots\ldots\ldots\ldots\ldots\ldots\ldots\ldots\ldots\ldots \quad (25)$$

Using the volume flux conservation $dQ/dr = 2\pi r \, \alpha_r \, u_c$, together with $dM/dr = 0$ and the appropriate definitions, gives the following relation for the nonbuoyant radial entrainment coefficient:

$$\alpha_r = \frac{I_1}{2}\left(k + \frac{h}{r}\right) \quad \ldots \quad (26)$$

Thus, the entrainment coefficient will depend on the initial conditions r_o and h_o and attains an asymptotic condition $\hat{\alpha}_r = I_1\, k$ for $r \to \infty$, $(h/r \to dh/dr)$. Available experimental data (15, 7, and, most extensively, 17) indeed support a constant spreading rate at sufficiently large distances when similarity has been attained. Witze and Dwyer's data give a gradient $k_{0.5} = 0.106$ for the half-velocity width for $r_o/h_o \geq 20$ in which r_o = the initial radius, and h_o = the slot half-height. Somewhat larger gradients are found for $r_o/h_o < 20$, but are discounted here as they appear to be caused by efflux nonuniformities at these small r_o/h_o ratios. In the sequel, a polynomial velocity profile (1) is adopted:

$$f(\eta) = (1 - \eta^{3/2})^2;$$

$$I_1 = 0.45;$$

$$I_2 = 0.316 \quad \ldots \quad (27)$$

together with a buoyancy profile:

$$g(\eta) = 1 - \eta^{3/2};$$

$$I_3 = 0.368;$$

$$I_4 = 0.2143 \quad \ldots \quad (28)$$

Thus, the total width is 2.27 times larger than the velocity half-width, so that the experimental radial jet spreading gradient is $k = 0.241$. Consequently, $\alpha_r = 0.054 + 0.225\ h/r$ and is limited to the aforementioned profile.

Turbulent entrainment is strongly suppressed if buoyancy acts on the shear layer, as has been shown by the seminal experiments of Ellison and Turner (6). Different empirical damping factors, all dependent on local Froude or bulk Richardson numbers, have been proposed (10,12,14). An exponential relationship (14):

$$\alpha_r^* = \alpha_r\, e^{-5/\mathrm{F}_r^2} \quad \ldots \quad (29)$$

in which $\mathrm{F}_r^2 = u_c^2/(g_c' h)$ is used in this study. Other relationships, including those which give a complete cutoff, $\alpha_r^* = 0$, at some critical Froude number (10), yielded practically identical results.

Nondimensionalization.—For the present case of high Reynolds number, Boussinesq-type flow, we expect any jet property Φ (e.g., velocity, jet depth, volume flux, etc.) to be a function of position r, initial integral quantities M_o, J_o, Q_o, and geometry r_o, H, or

$$\Phi = f(r, M_o, J_o, Q_o, r_o, H) \quad \ldots \quad (30)$$

in which $M_o = U_o^2\, \ell_o^2$, $J_o = U_o\, g_o' \ell_o^2$, $Q_o = U_o\, \ell_o^2$ (assuming top-hat efflux profiles); and $\ell_o^2 = 2\pi r_o h_o$. Then, taking M_o and J_o as the two normalizing variables because of their fundamental destabilizing and stabilizing roles, respectively, in buoyant jet behavior, we obtain the following scales and their relationship to the non-integral initial conditions (U_o, g_o', ℓ_o): (1) Length scale $M_o^{3/4}/J_o^{1/2} = \ell_o\, \mathrm{F}_s$; (2) volume flux scale $M_o^{5/4}/J_o^{1/2} = Q_o\, \mathrm{F}_s$; (3) velocity scale $J_o^{1/2}/M_o^{1/4}$

$= U_o/F_s$; and (4) buoyancy scale $J_o^{3/2}/M_o^{5/4} = g'_o/F_s$.

In the aforementioned, F_s denotes the discharge densimetric Froude number

$$F_s = U_o(g'_o\ell_o)^{-1/2} \quad \ldots\ldots\ldots\ldots\ldots\ldots\ldots\ldots\ldots\ldots\ldots\ldots \quad (31)$$

Thus, the nondimensional form of Eq. 30 is written as

$$\hat{\Phi} = f\left(\hat{r} = \frac{r J_o^{1/2}}{M_o^{3/4}}, \frac{1}{F_s}, \hat{r}_o = \frac{r_o J_o^{1/2}}{M_o^{3/4}}, \hat{H} = \frac{H J_o^{1/2}}{M_o^{3/4}}\right) \quad \ldots\ldots\ldots\ldots \quad (32)$$

Three parameters define the radial surface jet problem: (1) The Froude number F_s, whose inverse is proportional to the initial source flow or slot height,

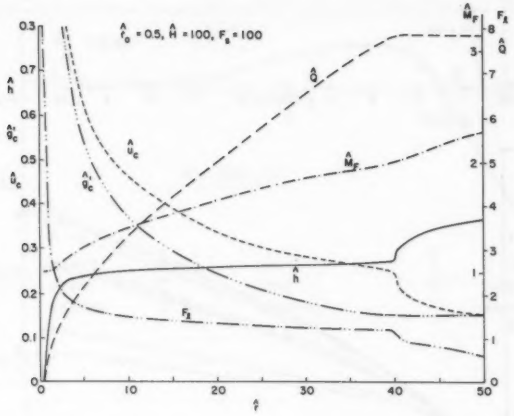

FIG. 5.—Radial Surface Jet as Line Source in Deep Water

respectively; note that, $\hat{h}_o = h_o J_o^{1/2}/M_o^{3/4} = (2\pi F_s^2 \hat{r}_o)^{-1}$; (2) the radius $\hat{r}_o$; and (3) the layer depth $\hat{H}$. Special cases are: Radial line source, $F_s \to \infty$; radial point source, $F_s \to \infty$, $\hat{r}_o \to 0$; and the two-dimensional line source, $F_s \to \infty$, $\hat{r}_o \to \infty$; furthermore, deep layer conditions, $\hat{H} \to \infty$, in which the jet dynamics are unaffected by the layer depth; the incipient condition for recirculation denoted by a critical depth value $\hat{H}_c$; and shallow layer condition, with significant recirculation, given by the range $\hat{H}_c > \hat{H} > 0$.

The governing equations are put into nondimensional form and solved with a fourth-order Runge-Kutta algorithm, Eqs. 11 and 20, and a Newton-Raphson technique for Eq. 22.

Model Results.—The results for a radial line source in deep water ($\hat{r}_o = 0.5$, $F_s = 100, \hat{H} = 100$) are summarized in Fig. 5. This includes all integral ($\hat{Q} = QJ_o^{1/2}/M_o^{5/4}$, $\hat{M}_F = M_F/M_o$) and non-integral variables ($\hat{h} = h J_o^{1/2}/M_o^{3/4}$, $\hat{g}'_c = g'_c M_o^{5/4}/J_o^{3/2}$, $\hat{u}_c = u_c M_o^{1/4}/J_o^{1/2}$, F_r). Three major regions can be distinguished:

1. An initial high entrainment region in which the jet behaves as largely nonbuoyant ($F_f \geq 2, M_F \approx 1$), and a significant depth increase occurs.

2. A gradually expanding, super-critical region with strongly damped entrainment whose cumulative effect, however, is significant, due to the growth of

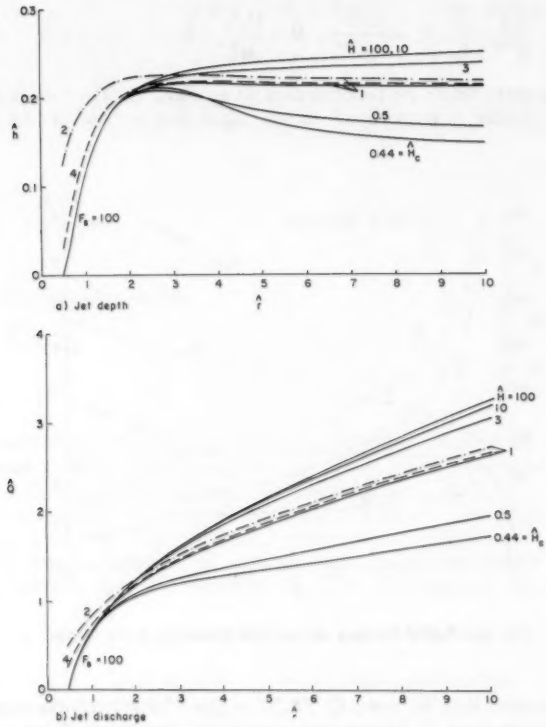

FIG. 6.—Radial Surface Jet: Effect of Shallowness $\hat{H}$ and Finite Source Flow F_s

the entraining surface. The jet momentum function M_F increases due to the contribution of the pressure term, P/r, in Eq. 20.

3. A subcritical expanding region in which entrainment becomes rapidly damped so that $\hat{Q}$ and $\hat{g}'_c$ approach a constant.

The transition from super to subcritical jet flow is characterized by rapid changes in $\hat{u}_c$, $\hat{h}$, and F_f. The critical Froude number if $F_{fc} = \sqrt{2I_4/I_2} = 1.08$ which is found readily by forming the equation for dh/dr and setting

the denominator to zero. The solution plotted in Fig. 5 can be considered as entirely upstream controlled. Yet, the super-subcritical flow transition in stratified flow, just as in free surface flow, should be downstream controlled as well.

In the laboratory, such a control can be created through a radial weir or an unsteady layer build-up in a finite basin. In that case, and depending on the strength of the control, a jump transition would occur at a distance $\hat{r}$ less than that in Fig. 5 (~40). Mathematically, this is given by choosing the alternate, larger root for $\hat{h}$ in Eq. 22. If the subcritical region is reached earlier in that manner, then the overall flow rate $\hat{Q}$ is limited. Thus, Fig. 5 can be considered as the "maximum entraining" solution to the radial buoyant jet equations. Solutions of this type are assumed in the sequel since the downstream build-up effect was avoided in the experiment, since the OTEC field conditions probably lack a control due to some residual ocean currents which are always active,

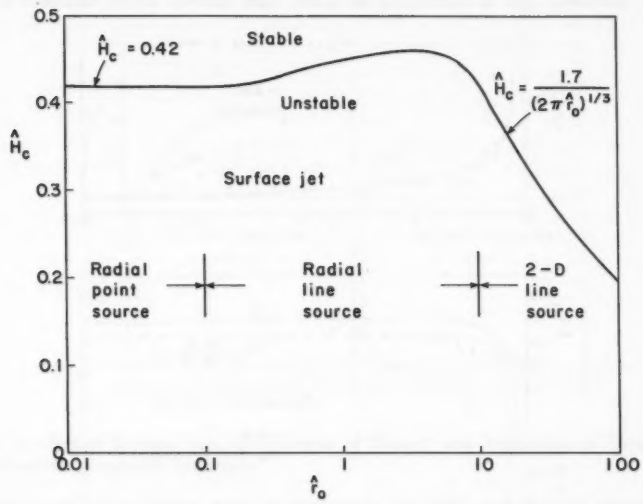

FIG. 7.—Radial Surface Jet Stability Diagram: Condition of Incipient Recirculation as Function of Radius $\hat{r}_o$

and since the dynamic instabilities which lead to recirculation in shallow $\hat{H}$ conditions occur usually at much smaller distances within region *a*. For comparison, it may be noted that solutions for the "maximum entraining type" are not possible beyond the critical section in the two-dimensional case, $\hat{r}_o \to \infty$, due to absence of the radial expansion term. This is evident from the work of Wilkinson and Wood (16) and Chu and Vanvari (4).

The effect of shallowness and finite discharge flows is indicated in Fig. 6, now restricting attention to $\hat{r} \leq 10$. Thus, $F_r \geq 4$ can be approximated as line source flow, and $\hat{H} \geq 3$ represents practically deep conditions. Further decrease in depth causes a distinct region of maximum thickness, h_{max} at $\hat{r}$ between 2–3, and subsequent thinning of the jet until the subcritical region is reached

(not shown in Fig. 6*a*). Finally, if $\hat{H}$ falls below a critical value $\hat{H}_c$($\hat{H}_c$ = 0.44 for $\hat{r}_o$ = 0.5), then a real solution of Eq. 22 for $\hat{h}$ cannot be found at a certain position $\hat{r}$, which is of the order of 2–3 for $\hat{H} \lesssim \hat{H}_c$ and becomes small as $\hat{H} << \hat{H}_c$. Thus, a buoyant jet flow with a given momentum function cannot be sustained within a shallow ambient fluid layer. Physically, this condition can be interpreted as leading to instabilities and recirculation. It may be noted that $\hat{H}_{max} \approx 1/2\ \hat{H}$ under incipient recirculation.

Finally, Fig. 7 gives a comprete radial buoyant jet stability diagram as a

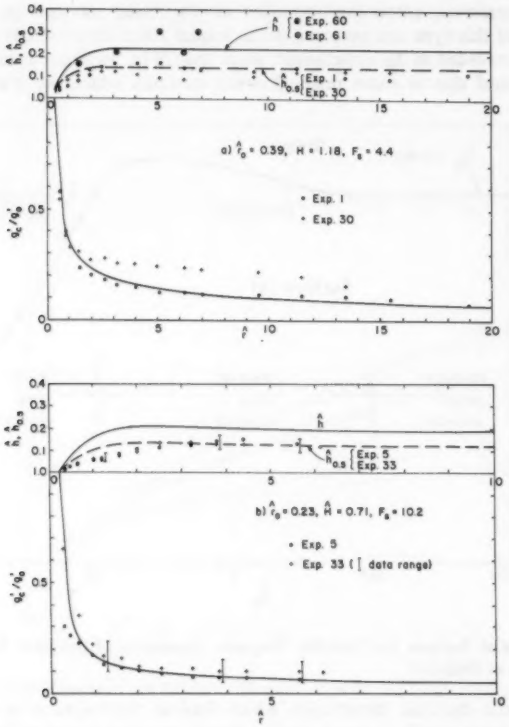

FIG. 8.—Radial Surface Jet: Comparison of Theory and Experimental Data for Non-Recirculating Stable Conditions

function of radius $\hat{r}_o$ as obtained by repeated model application. For $\hat{r}_o \lesssim 0.1$, the behavior seems independent of $\hat{r}_o$ giving the radial point source regime $\hat{H}_c = 0.42$; while the range $0.1 < \hat{r}_o < 10$ is characteristic of radial line sources with some dependence on $\hat{r}_o$. A different behavior ($\hat{H}_c \sim \hat{r}_o^{-1/3}$ due to differences in the line source quantities) is expected to result for large $\hat{r}_o > 10$ approaching the two-dimensional conditions.

Experimental Study.—Experiments were conducted in a 12.2 m × 18.3 m × 0.35 m shallow basin at the R. M. Parsons Laboratory for Water Resources and Hydrodynamics at M.I.T. A cylindrical Plexiglas model of the radial intake-discharge device could be installed either in the basin center or as a half-model at the basin boundary which then can form a symmetry line for the flow field. A window along the basin boundary allowed direct lateral observation. The jet was formed by discharging heated water through a radial slot at the water surface. An equal amount of water was withdrawn from near the bottom. A series of 28 experiments was performed with stagnant layer conditions, covering the following parameter range: $\hat{H} = 0.24$–2.5; $\hat{r}_o = 0.08$–0.83; $F_s = 2.0$–30.5. The discharge Reynolds number, based on slot height and velocity, varied from 3,000–12,000. Temperature measurements were taken with 100 thermistor probes (1.0 sec time constant), mounted along five radial sections on a movable frame so that they could be positioned at any elevation. The

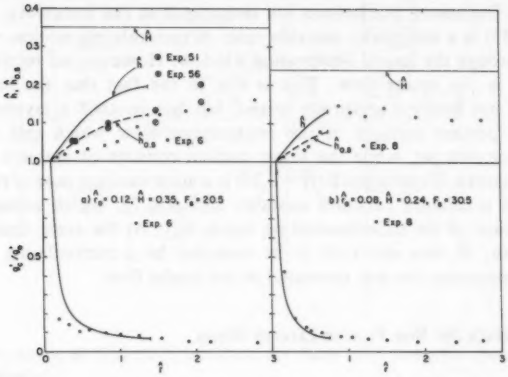

FIG. 9.—Radial Surface Jet: Comparison of Theory and Experimental Data for Recirculating Unstable Conditions

readings of these probes were automatically recorded and radially averaged, thereby producing the mean temperature field and, thus, buoyancy field $g'(r, z)$. Other measurements included: vertical temperature profiles via a traversing fast thermistor probe, velocity profile determinations from dye streaks released from dye coated vertical threads, flow visualization through dye release into the discharge water, and direct recirculation measurements by monitoring the temperature or fluorescent dye concentration in the intake flow. Details of the experimental set-up and procedure are given in a separate report (8).

Two experimental error sources are of concern here, namely radial nonuniformity and unsteady temperature build-up. The radially expanding flow within the model tended to instabilities and thus unevenness in the exit flow distribution. This effect was minimized through use of internal baffles and flow dissipators. Repeated checks of the surface temperature distribution showed satisfactory radial symmetry, although minor deficiencies (of the order of ±20%) persisted. The finite basin size limited the steady-state experimental period to about 20–30

minutes. After that, the mixed water buildup in the basin "far-field" started to move in toward the near-field with hydraulic jump-like conditions and ultimate near-field flooding. The data taking was limited to the steady-state period.

All of the experiments were within the shallowness affected range, $\hat{H} \lesssim 3$. Fig. 8 summarizes experimental data and model predictions for several stable (i.e., non-recirculating) experiments. Temperature half-depth, $\hat{h}_{0.5}$ (= 0.63 $\hat{h}$ for the chosen profile), normalized centerline buoyancy, g'_c/g'_o, and, in some instances, total layer depth $\hat{h}$, as obtained from local velocity profiles, is given. The data range obtained in the detailed investigation of Experiment 33 is typical for all runs and a probable measure of residual radial nonuniformity. Except for a slight over prediction of the initial non-buoyant jet growth, $\hat{h}$, which is due to the direct adoption of Witze and Dwyer's growth rate, the agreement of theory and data is good.

Fig. 9 shows two experiments in which recirculation was observed to occur. This is coincident with an instability occuring in the mathematical model, as $\hat{H} < \hat{H}_c$. The model predictions are terminated at the instability. Experiment 6 ($\hat{H} = 0.35$) is a marginally unstable case. A recirculating motion could readily be seen through the lateral observation window. However, no recirculation was measured in the intake flow. This is due to the fact that the inward return flow does not become uniformly mixed, but has in itself a layered structure: the upper portion consists of the recirculating flow which gets re-entrained into the buoyant jet, while the lower portion consists of ambient flow which enters the intake. Experiment 8 ($\hat{H} = 0.24$) is a more extreme case of recirculation. The model prediction becomes unstable at $\hat{r} = 0.75$, which coincides with a rapid increase of the experimental jet depth, $\hat{h}_{0.5}$. At the same time, the entire water depth, $\hat{H}$, was observed to be occupied by a recirculating eddy and a direct temperature rise was measured in the intake flow.

Radial Interface Jet-Sink Flow in Layered Ocean

Governing Equations.—Fig. 10 summarizes the flow and buoyancy structure consisting of a finite upper layer and an infinite lower layer. Thus, return velocities and pressure deviations in the lower layer are negligible. The radial momentum source is located at the interface. The governing equations are Eqs. 1–4, as before, and the same global dynamical interaction for the surface jet is expected to govern mixing and stability of the interface jet. Assuming vertical symmetry for the turbulent zone, i.e., $h_1 = -h$, $h_2 = +h$, the integral equations, in conservation form for the upper jet portion, are the volume flux equation, Eq. 11, the momentum force equation, Eq. 20, and the total buoyancy conservation equation

$$\frac{d\,g'_o}{dr} = 0 \quad \ldots\ldots\ldots\

$$2\pi r\, g'_o I_4 h^3 - M_F h + \frac{1}{2\pi r}\frac{I_2}{I_1^2} Q^2 = 0 \quad \ldots\ldots\ldots\ldots\ldots\ldots\ldots\ldots \quad (34)$$

Nondimensionalization.—For the interface jet, any jet property Φ will be a function

$$\Phi = f(r, M_o, g'_o, Q_o, r_o, H) \quad \ldots\ldots\ldots\ldots\ldots\ldots\ldots\ldots\ldots\ldots \quad (35)$$

Using M_o and g'_o as the normalizing variables, the following scales are obtained: length scale $M_o^{1/3} g_o'^{1/3} = \ell_o \mathrm{F}_l^{2/3}$; volume flux scale $M_o^{5/6}/g_o'^{1/3} = Q_o \mathrm{F}_l^{2/3}$; and velocity scale $M_o^{1/6} g_o'^{1/3} = U_o/\mathrm{F}_l^{2/3}$ in which the interface jet Froude number

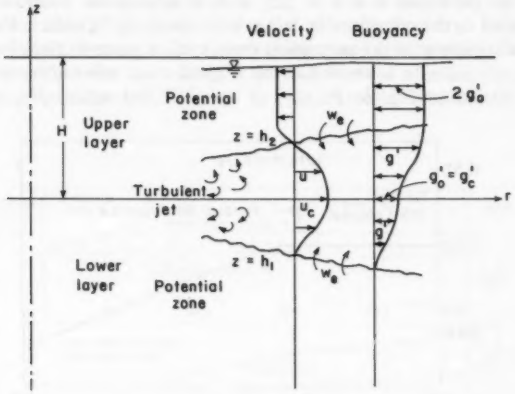

FIG. 10.—Structure of Turbulent Interface Jet Flow with Potential Return Flow in Two Layer Model

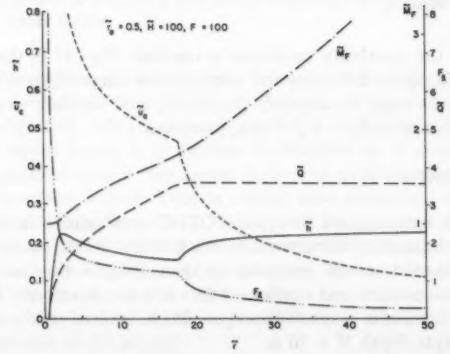

FIG. 11.—Radial Interface Jet as Line Source with Deep Upper Layer

$$F_l = U_o(g'_o l_o)^{-1/2} \quad \ldots\ldots\ldots\

relative to the upper layer. Its discharge buoyancy relative to the lower layer is considerably higher (factor of 5–10) so that mixing with lower layer water is neglected. The "inverted surface jet" variables are, therefore, $\hat{H} = 0.63$, $\hat{r}_o = 0.22$, and $F_s = 7.12$ indicating line source behavior with significant shallowness effects.

Mixed Discharge Scheme.—The combined flow is emitted at approximately the thermocline, which is characterized by a total buoyancy difference $2g'_o = 0.02\ m/s^2$ (corresponding to the density change over the upper 150 m of the ocean (Fig. 1(*b*)). Thus, the interface jet parameters are $\bar{H} = 1.5$, $\bar{r}_o = 0.54$, and $F_i = 5.0$, giving a relatively deep line source regime. The model predictions for jet depth at an undistorted scale, and total induced radial flow in the upper layer, are summarized in Fig. 13 for a near-field region of 500 m surrounding the OTEC plant. Thus, the separate discharge scheme tends to induce considerably more vertical perturbations and mixing within the stratified ocean structure than the more damped mixed scheme.

Secondly, the maximum OTEC plant size can be calculated under the condition

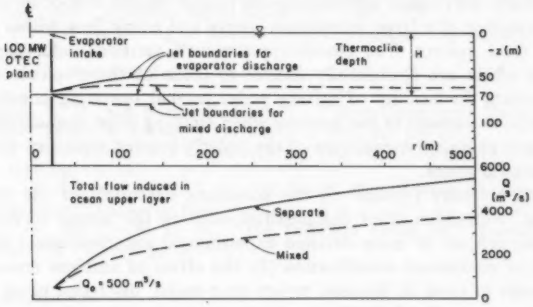

FIG. 13.—Comparison of Separate and Mixed Discharge Schemes for 100 MW OTEC in 70 m Mixed Layer Depth

of complete prevention of recirculation. In view of the extreme sensitivity of OTEC power delivery to the available temperature difference, this is, indeed, a reasonable objective. Also, since recirculation is tantamount to a full agitation of the entire upper layer, it is further undesirable as it destroys any small temperature gradient within the upper layer and precludes utilization of the warmest near-surface waters. Despite strong data campaigns in recent years, the environmental data base for OTEC is still very limited, particularly for extreme conditions. Yet it appears that, for many OTEC localities under current consideration, the minimum mixed layer depth is of the order of 50 m. It seems prudent to reduce this by another 20% to allow for short-term weather related fluctuations and for internal wave activity. Thus, a minimum layer depth, $H = 40$ m, is assumed in the sequel:

Separate Discharge Scheme.—The point source recirculation condition, $\hat{H}_c = 0.42$, can be expressed using the earlier definitions ($M_o = Q_o U_o$):

$$Q_{o_{max}} = \left(\frac{H}{0.42}\right)^4 \frac{g_o'^2}{U_o^3} \quad \ldots \ldots \ldots \ldots \ldots \ldots \ldots \ldots \ldots \ldots \ldots \ldots \quad (38)$$

With the design values from above, the evaporator flow = $Q_{o_{max}}$ = 250 m^3/s which corresponds to a 50 MW plant size.

Mixed Discharge Scheme.—The recirculation condition, $\tilde{H}_c = 0.50$, translates to

$$Q_{o_{max}} = \left(\frac{H}{0.50}\right)^3 \frac{g_o'}{U_o} \quad \ldots \ldots \ldots \ldots \ldots \ldots \ldots \ldots \ldots \ldots \ldots \ldots \quad (39)$$

This is evaluated as $Q_{o_{max}}$ = 2,560 m^3/s which stands for one half of the mixed discharge flow so that the corresponding plant size is about 500 MW. Thus, the separate discharge of the evaporator flow in the upper layer is extremely prone to recirculation. Mixed discharge schemes seem preferable. In any case, the results suggest that the external fluid mechanics of OTEC plants are a definite limiting factor on plant size and seem to preclude very large plants (in the 1,000 MW range) which have been suggested in the literature.

In summary, the present analysis appears to give reliable first-order predictions on the interaction of a large momentum source and a sink flow within a layered, stratified fluid system. The model appears well verified under experimental conditions which are dynamically similar to those of the tropical ocean. The model predicts the amount of mixing under normal operating conditions and, if the system is stressed to the extreme when emitting large momentum sources, it indicates a complete breakdown of the orderly layered structure of discharge and withdrawal zones.

The present study focused on the schematic essentials of the source-sink interaction. Numerous other complexities exist in the actual OTEC problem and are the subject of more detailed experimental and theoretical work, e.g., the effect of continuous stratification (2), the effect of ambient cross flow (8), design details in form of discrete, rather than radial, discharge ports (2,8), and the transition to the far-field (9).

Acknowledgments

This work was supported by contracts from the U.S. Department of Energy, Division of Central Solar Technology, with the Massachusetts Institute of Technology and Cornell University, respectively. The assistance in the experimental program of David Fry, research assistant at M.I.T., is gratefully acknowledged.

Appendix I.—References

1. Abramovich, G. N., *The Theory of Turbulent Jets*, Massachusetts Institute of Technology Press, Cambridge, Mass., 1963.
2. Adams, E. E., Fry, D. J., Coxe, D. H., and Harleman, D. R. F., "Research on the External Fluid Mechanics of Ocean Thermal Energy Conversion Plants. Report Covering Experiments in Stagnant Water," *Technical Report No. 250*, R. M. Parsons Lab. for Water Resources and Hydrodynamics, Massachusetts Institute of Technology, Cambridge, Mass., June, 1979.

3. Benjamin, T. B., "Gravity Currents and Related Phenomena," *Journal of Fluid Mechanics*, Vol. 31, 1968, pp. 209–248.
4. Chu, V. H., and Vanvari, M. R., "Experimental Study of Turbulent Stratified Shearing Flow," *Journal of the Hydraulics Division*, ASCE, Vol. 102, No. HY6, 1976, pp. 691–706.
5. Dugger, G. L., ed., *Proceedings of the Sixth Ocean Thermal Energy Conversion Conference*, Washington, D.C., June, 1979.
6. Ellison, T. H., and Turner, J. S., "Turbulent Entrainment in Stratified Flows," *Journal of Fluid Mechanics*, Vol. 6, 1959, pp. 423–448.
7. Heskestad, G., "Hot-wire Measurements in a Radial Turbulent Jet," *Journal of Applied Mechanics*, Vol. 88, 1966, pp. 417–424.
8. Jirka, G. H., Johnson, R. P., Fry, D. J., and Harleman, D. R. F., "Ocean Thermal Energy Conversion Plant: Experimental and Analytical Study of Mixing and Recirculation," *Technical Report No. 231*, R. M. Parsons Lab. for Water Resources and Hydrodynamics, Massachusetts Institute of Technology, Cambridge, Mass., 1977.
9. Jirka, G. H., Jones, J. M., and Sargent, F. M., "Theoretical and Experimental Study of the Intermediate Field Motions of Ocean Thermal Energy Conversion Plants," *Technical Report*, School of Civil and Environmental Engineering, Cornell University, 1980.
10. Koh, R. C. Y., "Two-Dimensional Surface Warm Jet," *Journal of the Hydraulics Division*, ASCE, Vol. 97, No. HY6, 1971, pp. 819–836.
11. Lavi, A., and Veziroglu, T. N., editors, *Proceedings of the Fifth Ocean Thermal Energy Conversion Conference*, Miami Beach, Fla., Feb., 1978.
12. Price, J. F., "On the Scaling of Stress-Driven Entrainment Experiments," *Journal of Fluid Mechanics*, Vol. 90, 1979, pp. 509–529.
13. Schlichting, H., *Boundary Layer Theory*, McGraw Hill Book Co., New York, N.Y., 1968.
14. Stolzenbach, K. D., and Harleman, D. R. F., "Three-Dimensional Heated Surface Jets," *Water Resources Research*, Vol. 9, No. 1, 1973, pp. 129–137.
15. Tuve, G. L., "Air Velocities in Ventilating Jets," *Heating, Piping and Air Conditioning*, Vol. 25, 1953, pp. 181–192.
16. Wilkinson, D. L., and Wood, I. R., "A Rapidly Varied Flow Phenomenon in a Two-Layer Flow," *Journal of Fluid Mechanics*, Vol. 47, 1971, pp. 241–256.
17. Witze, P. O., and Dwyer, H. A., "The Turbulent Radial Jet," *Journal of Fluid Mechanics*, Vol. 75, 1976, pp. 401–417.

Appendix II.—Notation

The following symbols are used in this paper:

F_i = interface jet Froude number;
F_ℓ = local Froude number;
F_s = surface jet Froude number;
g = gravity;
g' = buoyancy;
g'_o = initial (surface jet) or total (interface jet) buoyancy;
H = layer depth;
H_c = critical layer depth for incipient recirculation;
h = local jet height;
$h_{0.5}$ = local jet half height;
I = integral constants;
J = total radial buoyancy flux;
j = turbulent buoyancy flux;
k = jet spreading rate (non-buoyant);
l_o = jet initial length = $(2\pi r_o h_o)^{1/2}$;

M = total radial momentum flux;
M_F = total radial momentum force;
P = total radial pressure force;
p = pressure;
Q = total radial volume flux;
r, z = radial and vertical distance, respectively;
u, w = radial and vertical velocity, respectively;
U_o = discharge velocity;
u_B = sink flow return velocity;
w_e = entrainment velocity;
α_r = non-buoyant radial entrainment coefficient;
α_r^* = buoyant radial entrainment coefficient;
Φ = any jet property;
$\Delta\rho$ = density difference;
ρ = density; and
τ = turbulent shear stress.

Subscripts

1, 2 = upper, lower layer;
o = initial conditions;
a = ambient; and
c = centerline (maximum) values.

Superscripts

$\hat{}$ = normalized surface jet property; and
$\tilde{}$ = normalized interface jet property.

VERTICAL ROUND BUOYANT JET IN SHALLOW WATER

By Joseph H. W. Lee,[1] A. M. ASCE and Gerhard H. Jirka,[2] M. ASCE

INTRODUCTION

A simple way to dispose of the large quantities of waste heat, resulting from steam electric power generation, is to discharge the heated condenser water through a submerged round outfall located at the bottom of the receiving water. An understanding of the induced excess temperature distribution, in relationship to the hydrodynamic characteristics of the buoyant discharge, is essential for a sound design which utilizes to its fullest the cooling capacity of the ambient waterbody. The information also provides a basis for an assessment of the aquatic impact of the thermal effluent.

In recent years, high velocity injection schemes such as multiport diffusers have increasingly been used as effective mixing devices to dissipate the heat rapidly within a small area. Many once-through condenser cooling systems currently in operation, however, involve only single or dual-submerged ports discharging either vertically or horizontally. The San Onofre Nuclear Plant and Redondo Beach Fossil fueled plant on the Pacific Coast, and the Littlebrook and Sizewell power stations on the Thames estuary, United Kingdom, are two cases in point. Frequently, these discharges are located in waters only a few port diameters deep. Significant surface and bottom interaction may then dominate the mixing characteristics of such depth-restricted thermal discharges.

This paper reports an analytical and experimental investigation of the stability and mixing characteristics of a round turbulent buoyant jet discharging vertically into an otherwise stagnant uniform waterbody of large horizontal extent. The discharge configuration is termed stable if the discharged fluid is not re-entrained into the buoyant jet (Fig. 1(*a*)). In such a case, four flow regimes of distinct hydrodynamic properties can be discerned: (1) Initial Buoyant Jet Region, in which the discharge mixes with the ambient fluid by turbulent entrainment as it rises to the surface; (2) a Surface Impingement Region, within which the buoyant mixed flow is turned into a radially outward moving supercritical flow; (3) Radial Internal Hydraulic Jump Region, transforming the flow into a subcritical

[1]Asst. Prof., Dept. of Civ. Engrg., Univ. of Delaware, Newark, Del. 19711.
[2]Associate Prof., School of Civ. and Environmental Engrg., Cornell Univ., Ithaca, N.Y. 14853.

Note.—Discussion open until May 1, 1982. To extend the closing date one month, a written request must be filed with the Manager of Technical and Professional Publications, ASCE. Manuscript was submitted for review for possible publication on October 17, 1980. This paper is part of the Journal of the Hydraulics Division, Proceedings of the American Society of Civil Engineers, ©ASCE, Vol. 107, No. HY12, December, 1981. ISSN 0044-796X/81/0012-1651/$01.00.

region downstream with an abrupt change of upper layer thickness and loss of energy; (4) Stratified Counterflow Region, with negligible entrainment across the interface. In general, stability can be maintained for deep water high buoyancy discharges that are characteristic of sewage applications. For these cases, the minimum dilution at the surface in the vicinity of the discharge can be estimated using various buoyant jet models that have tacitly assumed the existence of a stably stratified system (9).

On the other hand, under high momentum, low buoyancy, and shallow water conditions, the energy input by the buoyant jet into the receiving water may be so strong that the buoyancy contained in the discharge is not sufficient to establish a stable stratified flow. Recirculation cells are set up near the jet efflux, leading to heat re-entrainment into the discharge and thus an impairment in mixing capacity. Such a discharge configuration is termed unstable (Fig. 1(*b*)).

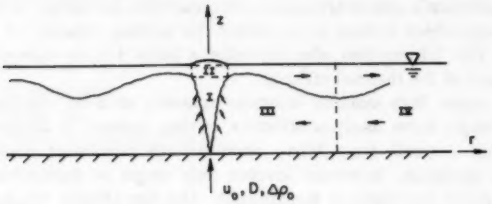

Fig. 1a.

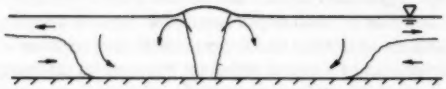

Fig. 1b.

FIG. 1.—Vertical Round Buoyant Discharge in Shallow Water: (*a*) Stable Discharge Configuration; (*b*) Unstable Discharge Configuration

The near-field stability and mixing characteristics of a plane slot buoyant jet in stagnant water has been studied in considerable detail by Jirka and Harleman (7). The same line of approach has been adopted in the present work: The salient features of the four regions are separately analyzed and the solutions coupled together to give a prediction of the stability criterion. Results of a series of laboratory experiments carried out with a half jet are compared with the theoretical predictions. Practical implications of the results are discussed.

Theory

Consider a vertical axisymmetric buoyant jet of fluid (discharge velocity u_o),

issuing from a source of finite diameter D into a quiescent homogeneous fluid of depth H (temperature T_a, density ρ_a). Of interest are the velocity field $q(z,r)$, and the temperature field $T(z,r)$ generated by the buoyant discharge (temperature T_o, density ρ_o) in a cylindrical coordinate system.

In the following sections, a steady-state formulation of the problem, which incorporates the dynamic interaction of three near-field regions—the buoyant jet region, surface impingement region, and the radial internal hydraulic jump region—will be presented. The buoyant jet region is analyzed with the assumption of a constant jet spreading angle. Properties of the surface impingement and

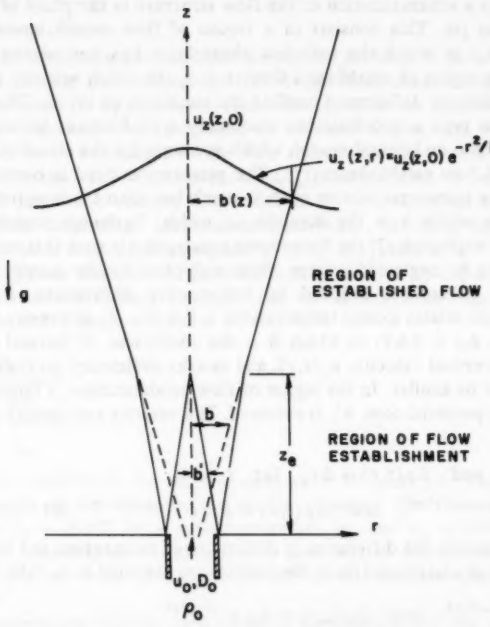

FIG. 2.—Schematized Structure of Initial Buoyant Jet Region

internal jump regions are determined on the basis of control volume analysis. A coupling of the solutions of the three regions yields a prediction of the near-field stability, as well as the bulk mixing characteristics of the buoyant discharge.

Buoyant Jet Region.—The mechanics of a pure axisymmetric turbulent free jet or plume, in an infinite field, has been extensively studied (2,17,19). Thus, the detailed physical description of jet or plume behavior will not be belabored upon here. Suffice it to say, in the general case of a buoyant jet—a source with finite initial volume, momentum, and buoyancy fluxes—the governing dimensionless parameter is the densimetric Froude number

$$F_o = \frac{u_o}{\sqrt{g\frac{\Delta\rho_o}{\rho_a}D}} \quad \ldots\ldots\ldots\ldots\ldots\ldots\ldots\ldots\ldots\ldots\ldots\ldots\ldots\ldots (1)$$

in which $\Delta\rho_o/\rho_a = \rho_o - \rho_a/\rho_a$ = the discharge relative density difference; and g = the acceleration due to gravity. The extreme values of F_o (the ratio of inertial to buoyancy force per unit mass) define the two limiting cases of a pure source of momentum, $F_o \rightarrow \infty$, and a pure source of buoyancy, $F_o \rightarrow 0$.

Fig. 2 shows a schematization of the flow structure in the plane of symmetry of the buoyant jet. This consists of a region of flow establishment near the source, $z \leq z_e$, in which the turbulent shear layer has not penetrated to the jet axis, and a region of established flow, $z > z_e$, in which velocity and excess temperature (density deficiency) profiles are similar at all levels. The following boundary layer type approximations customary with buoyant jet analysis can be introduced into an integral model, which accounts for the effect of buoyancy in the zone of flow establishment: (1) The piezometric head is constant across the jet, and the transverse mixing scale is much less than the longitudinal scale, $b/z << 1$, in which b is the nominal jet width. Turbulent transfers in the z direction are neglected; (2) the Boussinesq assumption is such that small density differences can be neglected except when multiplied by the gravity term. For small density differences induced by temperature differences, a linearized equation of state relates excess temperatures $\Delta T = T - T_a$ to density deficiency $\Delta\rho = \rho_a - \rho$, $\Delta\rho = \beta\Delta T$, in which β = the coefficient of thermal expansion at T_a; (3) the vertical velocity, $u_z(z,r)$, and density deficiency profiles, $\Delta\rho(z,r)$, are assumed to be similar. In the region of flow establishment, a linear decrease of width of the potential core, b', is assumed. The velocity and density deficiency profiles are

$$u_z(z,r) = u_B \quad \text{and} \quad \Delta\rho(z,r) = \Delta\rho_o \quad \text{for} \quad r \leq b';$$

$$u_z(z,r) = u_B e^{-(r-b')^2/b^2}; \quad \text{and} \quad \Delta\rho(z,r) = \Delta\rho_o e^{-(r-b')^2/\lambda^2 b^2} \quad \text{for} \quad r > b' \qquad (2)$$

in which λ measures the difference in diffusivity of momentum and heat.

In the region of established flow, the profiles are assumed to be fully Gaussian:

$$u_z(z,r) = u_c e^{-r^2/b^2}; \quad \text{and} \quad \Delta\rho(z,r) = \Delta\rho_c e^{-r^2/\lambda^2 b^2} \quad \ldots\ldots\ldots\ldots\ldots (3)$$

in which the subscript c = center line quantities. By invoking these assumptions, the equations of continuity, momentum, and energy (heat conservation) can be integrated across the buoyant jet from $r = 0$ to $r = \infty$ to yield a set of governing equations in terms of the volume flux Q, momentum flux M, and density deficiency flux J:

$$\text{Continuity:} \quad \frac{dQ}{dz} = \frac{d}{dz}\int_0^\infty u_z 2\pi r dr = Q_e \quad \ldots\ldots\ldots\ldots\ldots\ldots (4)$$

$$\text{Momentum:} \quad \frac{dM}{dz} = \frac{d}{dz}\int_0^\infty u_z^2 2\pi r dr = \int_0^\infty \frac{\Delta\rho}{\rho_a} g 2\pi r dr = f \quad \ldots\ldots\ldots (5)$$

$$\text{Energy:}\quad \frac{dJ}{dz} = \frac{d}{dx}\int_0^\infty \Delta\rho\, u_z 2\pi r dr = 0 \qquad (6)$$

in which Q_e = the rate of entrainment of ambient fluid into the buoyant jet. The integral quantities, Q, M, J, f, can be related to the centerline quantities, u_c, b, $\Delta\rho_c$, in the zone of established flow as

$$Q = \pi u_c b^2;\quad M = \frac{\pi u_c^2 b^2}{2};\quad J = \frac{\lambda^2}{1+\lambda^2}\pi u_c b^2 \Delta\rho_c$$

$$\text{and}\quad f = \pi\lambda^2 b^2 \frac{\Delta\rho_c}{\rho_a} g \qquad (7)$$

In this type of integral formulation, the closure problem in turbulent diffusion amounts to relating the entrainment flux to the local characteristic quantities. In many buoyant jet applications, (9,6), this problem is circumvented by an entrainment hypothesis first proposed by Morton, Taylor, and Turner (17) to describe the broad mechanics of the flow rather than the details of the actual mixing mechanism. The entrainment flux, Q_e, is assumed to be proportional to the local centerline velocity and width as $Q_e = 2\pi\alpha b u_c$ in which α = an experimentally determined entrainment coefficient. Invoking this assumption in Eqs. 4–6 yields a set of three equations in u_c, $\Delta\rho_c$, and b.

Based on purely dimensional grounds, and confirmed by experiments (6,12), the entrainment coefficient, however, can be shown to be dependent on the local densimetric Froude number:

$$F_L = \frac{u_c}{\sqrt{g\dfrac{\Delta\rho_c}{\rho_a} b}} \qquad (8)$$

and thus is variable in the general case of a buoyant jet. The exact value for α depends on the shape of the profile assumed. For Gaussian profiles it is equal to $\alpha_j = 0.057$ for a pure momentum jet, and $\alpha_p = 0.085$ for a pure plume. The considerable variability of α necessitates a numerical solution of Eqs. 4–6, if some form of dependence of the entrainment coefficient on F_L is assumed.

As an alternative that is deemed more appropriate for the present work, the entrainment hypothesis can be replaced by an assumption of a constant jet spreading angle, first proposed by Abraham (1). The diffusion layer, b, is assumed to spread linearly:

$$\frac{db}{dz} = \epsilon = \text{constant} \qquad (9)$$

The continuity equation then can be bypassed and an analytical solution can be obtained by solving Eqs. 5 and 6. The coefficient ϵ, of course, has to be experimentally determined. Jirka et al. (6) have shown that, in order for the two approaches to be consistent, certain relations have to hold between α and ϵ. For the pure momentum jet and plume, it can be shown that $\epsilon_j = 2\alpha_j =$

0.114 and $\epsilon_p = 6/5\ \alpha_p = 0.106$ independent of the profile assumptions. Thus, whereas α varies considerably as a function of F_o, there is a difference of less than 10% between the jet spreading angle in the two limiting cases. Throughout the subsequent analysis, ϵ and λ are taken to be 0.109 and 1.14, respectively. These represent intermediate values in the jet-plume range.

Following Abraham (1), the solution of the characteristic quantities in the region of established flow can be found:

$$\frac{u_c}{u_o} = \left(\frac{z}{D}\right)^{-1} \left\{ \left(\frac{M_e}{2\epsilon^2 M_o}\right)^{3/2} + \frac{3(1+\lambda^2)}{8\epsilon^2 F_o^2} \left[\left(\frac{z}{D}\right)^2 - \left(\frac{z_e}{D}\right)^2 \right] \right\}^{1/3} \quad (10)$$

$$\frac{\Delta\rho_c}{\Delta\rho_o} = \frac{(1+\lambda^2)}{4\lambda^2\epsilon^2} \left(\frac{z}{D}\right)^{-1} \left\{ \left(\frac{M_e}{2\epsilon^2 M_o}\right)^{3/2} + \frac{3(1+\lambda^2)}{8\epsilon^2 F_o^2} \left[\left(\frac{z}{D}\right)^2 - \left(\frac{z_e}{D}\right)^2 \right] \right\}^{-1/3} \quad (11)$$

in which subscript e = the condition at the end of the region of flow establishment.

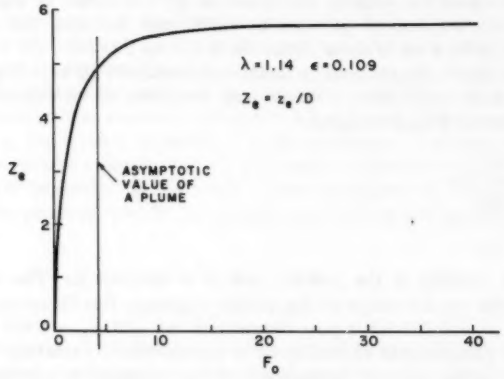

FIG. 3.—Length of Region of Flow Establishment as a Function of Source Densimetric Froude Number

The momentum flux within the region of flow establishment is given by integrating Eq. 5:

$$M = M_o + \int_0^z \int_0^\infty \frac{\rho_a - \rho}{\rho_a} g\, 2\pi\, r dr dz \quad (12)$$

Defining $Z = z/D$, Eq. 12 can be evaluated as

$$\frac{M}{M_o} = 1 + \frac{4}{F_o^2} \left(\frac{Z}{12} + \frac{\sqrt{\pi}\,\lambda\epsilon}{12} Z^2 + \frac{\lambda^2\epsilon^2}{3} Z^3 \right) \quad (13)$$

The length of flow establishment, Z_e, then can be evaluated by invoking $\Delta\rho/\Delta\rho_o = 1$ at $z = z_e$ in Eq. 11 and combining with Eq. 13:

$$1 + \frac{4}{F_o^2}\left(\frac{Z_e}{12} + \frac{\sqrt{\pi}\,\lambda\epsilon}{12} Z_e^2 + \frac{\lambda^2\epsilon^2}{3} Z_e^3\right) = \frac{(1+\lambda^2)^2}{8\lambda^4\epsilon^2}\frac{1}{Z_e^2} \quad \ldots\ldots\ldots (14)$$

The solution of Z_e as a function of F_o is shown in Fig. 3. Z_e increases rapidly from zero for $F_o = 0.0$, to an asymptotic value of 5.74 for F_o beyond 25.0; this is somewhat smaller than the value of $Z_e = 6.2$ determined by Albertson et al. (2) for the three dimensional momentum jet, indicating that heat diffuses faster than momentum. (Eq. 14 is a slight modification of Abraham's solution (1) for Z_e, the effect of buoyancy being properly accounted for in the evaluation of M_e). In shallow water, the length of flow establishment can constitute a significant portion of the water depth, and its inclusion in the analysis is important. Given Z_e, the characteristic quantities $\Delta\rho_c$, u_c can be obtained from Eqs. 10

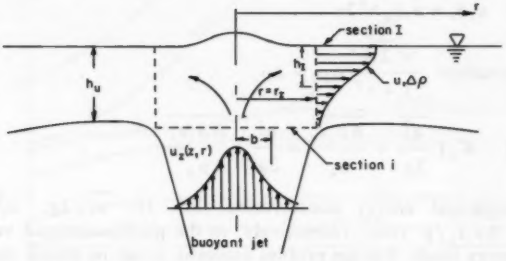

FIG. 4.—Surface Impingement Region

and 11 for $z > z_e$. For $z < z_e$, the velocity in the potential core, u_B, can be derived from Eq. 13 as

$$\left(\frac{u_B}{u_o}\right)^2 = \frac{1 + \frac{4}{F_o^2}\left(\frac{Z}{12} + \frac{\sqrt{\pi}\,\epsilon\lambda Z^2}{12} + \frac{\lambda^2\epsilon^2 Z^3}{3}\right)}{1 + \left(\sqrt{2\pi}\,\epsilon - \frac{2}{Z_e}\right)Z + \left(2\epsilon^2 + \frac{1}{Z_e^2} - \frac{\sqrt{2\pi}\,\epsilon}{Z_e}\right)Z^2} \quad \ldots\ldots (15)$$

in which $Z = z/D$.

Surface Impingement Region

When the buoyant jet impinges on the free surface, the dynamic pressure causes a surface hump, which gives rise to a radial pressure gradient and horizontal spreading of the mixed discharge (Fig. 4). Intense turbulent mixing occurs in this region. Instead of attempting to describe the complicated flow details, a simplified control volume analysis is given in this section to relate the properties of the vertical buoyant jet at the entrance of the surface impingement region, to the characteristic parameters of the horizontal axisymmetric buoyant surface

jet at the exit of this region. For brevity, the flow is assumed to be fully established at the entrance section i, with center line velocity u_i, density deficiency $\Delta\rho_i$, and jet width b_i. The case when the entrance flow is not fully established can be treated in an entirely analogous manner. The following assumptions are made: (1) The outer radius of the region, $r = r_I$, corresponds to the location in the entering buoyant jet where the vertical velocity is 5% of the center line value, i.e., $r_I = \sqrt{3}\, b_i$; (2) at the exit section, the vertical profiles of the radial velocity and density deficiency are assumed to be half-Gaussian:

$$u(r_I, z) = u_I e^{-(z/h_I)^2}; \quad \Delta\rho(r_I, z) = \Delta\rho_I e^{-(z/h_I)^2} \quad \ldots\ldots\ldots\ldots\ldots (16)$$

in which h_I = characteristic length scale of the upper layer. An appropriate measure of the upper layer thickness h_u can then be defined as the point in which $\Delta\rho = 0.05\,\Delta\rho_I$, or $h_u = \sqrt{3}\, h_I$.

Neglecting turbulent entrainment into the control volume, the governing equations for the control volume are then

$$\text{Continuity:} \quad u_i b_i = u_I h_I \sqrt{3\pi} \quad \ldots\ldots\ldots\ldots\ldots\ldots\ldots (17)$$

$$\text{Heat Conservation:} \quad \frac{\sqrt{2}\,\lambda^2}{1+\lambda^2}\Delta\rho_i = \Delta\rho_I \quad \ldots\ldots\ldots\ldots\ldots (18)$$

$$\text{Energy:} \quad (1 - K_L)\frac{\overline{u_i^2}}{2g} + \frac{\overline{\Delta\rho_i z_i}}{\rho_a} = \frac{u_I^2}{2g} + \frac{\overline{\Delta\rho_I z_I}}{\rho_a} \quad \ldots\ldots\ldots\ldots (19)$$

In the mechanical energy conservation, Eq. 19, $\overline{u_i^2}/2g$, $\overline{u_I^2}/2g$, and $\Delta\rho_I z_I/\rho_a$, $\Delta\rho_i z_i/\rho$ refer, respectively, to the profile-averaged velocity and potential energy heads. For the profiles assumed, it can be shown that

$$\overline{u_i^2} = \frac{u_i^2}{3}; \quad \overline{u_I^2} = \frac{u_I^2}{\sqrt{3}}; \quad \overline{\Delta\rho_i z_i} - \overline{\Delta\rho_I z_I} = \frac{\Delta\rho_I h_I}{2\sqrt{\pi}} \quad \ldots\ldots\ldots\ldots (20)$$

K_L is a head loss coefficient, accounting for the turbulent energy dissipation in the transition. $K_L = 0.2$ is adopted as appropriate for a 90° bend and a wide range of curvatures (5). The results are not sensitive to K_L.

The preceding analysis is applicable only if $z_i > z_e$. When $z_i < z_e$, the entrance flow into the surface impingement region is not fully developed, and thus the velocity and density deficiency profiles are not Gaussian. This has to be accounted for in the analysis because: (1) Very often practical submerged discharge designs fall within the small H/D range; and (2) z_e is also a function of F_o (Eq. 14). An analogous set of governing equations, based on the same principles just outlined, can be developed.

Coupling Buoyant Jet and Surface Impingement Region.—Noting that the geometric condition relating entrance section i and the exit section I is $z_i = H - \sqrt{3}\, h_I$, and $b_i = \epsilon z_i$, Eqs. 17–19 can be rearranged to yield

$$\mathsf{F}_i^2\left(\frac{b_i}{h_I}\right)\left[\frac{\left(\frac{b_i}{h_I}\right)^2}{6\sqrt{3}\,\pi} - \frac{(1-K_L)}{6}\right] = \frac{\lambda^2}{1+\lambda^2}\left(\sqrt{3} - \frac{1}{\sqrt{2}\,\pi}\right) \quad \ldots\ldots (21)$$

in which $$F_i = \frac{u_i}{\sqrt{g \frac{\Delta\rho_i}{\rho_a} b_i}} \quad \ldots \ldots \ldots \ldots \ldots \ldots \ldots \ldots \ldots \ldots \quad (22)$$

is the local densimetric Froude number of the entering buoyant jet; this can be related to the source conditions by

$$F_i = \left(\frac{u_i}{u_o}\right)\left[\left(\frac{\Delta\rho_i}{\Delta\rho_o}\right)\left(\frac{b_i}{H}\right)\left(\frac{H}{D}\right)\right]^{-1/2} F_o \quad \ldots \ldots \ldots \ldots \ldots \ldots \quad (23)$$

Eq. 22 can be solved numerically as a function of h_I (via the analytical solution

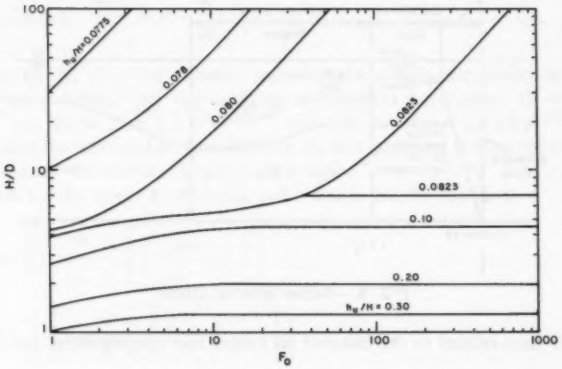

FIG. 5(*a*).—Solution for Surface Impingement Region Upper Layer Thickness

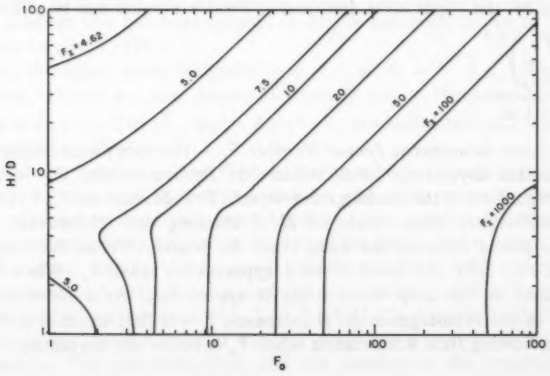

FIG. 5(*b*).—Solution for Surface Impingement Region, Densimetric Froude Number

(Eqs. 10 and 11)) for any source conditions F_o, H/D. The solutions for the dimensionless upper layer thickness h_u/H, and the densimetric Froude number defined by $F_I = u_r/\sqrt{g\Delta\rho_I/\rho_a h_I}$ are shown in Figs. 5(*a*) and 5(*b*), respectively.

Upper Layer Thickness.—In the deep water range, i.e., when $z_I \geq z_e$, h_u/H is quite insensitive to F_o or H/D, and is equal to about 0.08 or 1/12. However, as the shallow water range is approached, h_u/H increases to about 0.2–0.4 in the low H/D range. It is interesting to note that for $H/D \leq 4$, $h_u/D \sim 0.4$, indicating that D replaces H as a characteristic length scale in the shallow water range. Given the solution of h_u/H, all the characteristic properties at the entrance section, u_I, $\Delta\rho_I$, F_I, can be evaluated at z_I. The near field bulk

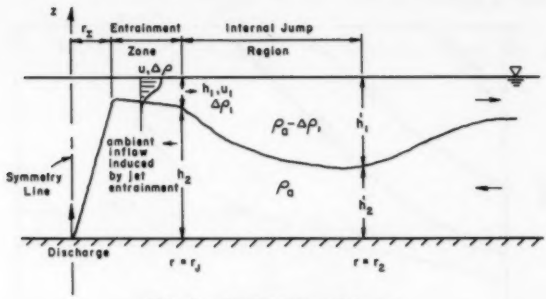

FIG. 6.—Radial Internal Jump

dilution is then related to the buoyant jet center line concentration as

$$S = \frac{\Delta\rho_o}{\Delta\rho_I} = \frac{1+\lambda^2}{\sqrt{2}\,\lambda^2}\frac{\Delta\rho_o}{\Delta\rho_I} \quad \ldots\ldots\ldots\ldots\ldots\ldots\ldots\ldots\ldots\ldots\ldots\ldots \quad (24)$$

Furthermore, the upper layer densimetric Froude number can be obtained as

$$F_I = \frac{F_i\left(\frac{b_I}{h_I}\right)^{3/2}}{\sqrt{3\pi}} \quad \ldots\ldots\ldots\ldots\ldots\ldots\ldots\ldots\ldots\ldots\ldots\ldots \quad (25)$$

Upper Layer Densimetric Froude Number, F_I.—The pure plume is characterized by a constant asymptotic local densimetric Froude number $F_L = \sqrt{3\lambda^2/2\epsilon} = 4.45$. Regardless of the discharge densimetric Froude number, F_o, F_I approaches F_L for sufficiently large values of H/D showing that all buoyant jets tend to exhibit plume behavior far away from the source. Within the range of F_o, shown in Fig. 5(*b*), this trend is more apparent for small F_o. When $F_o > F_L$, F_I decreases as the deep water range is approached. As a contrast, if $F_o < F_L$, then as the submergence H/D increases, F_I will first increase and then decrease, indicating fluid acceleration when F_o is below the asymptotic value F_L.

Radial Internal Jump Region

As the supercritical upper layer flow moves radially outwards from the surface

impingement region, it entrains fluid from the lower layer and spreads like an axisymmetric surface jet. At some radial distance, $r = r_J$, the high momentum, 'shooting' flow is observed to transform abruptly into a low momentum, 'tranquil' flow, with a thickening of the upper layer depth and accompanied by a loss of specific energy (Fig. 6). The characteristic properties of the upper layer at the toe of the jump, $r = r_J$, can be coupled to those at the exit of the surface impingement region. A bulk momentum analysis yields the conjugate jump heights of the respective layers.

Coupling Surface Impingement and Internal Jump Region.—The governing equations for the upper layer flow prior to the jump are (assuming half-Gaussian velocity and density deficiency profiles as before (3,8)):

$$\frac{dQ}{dr} = \alpha(2\pi ru); \quad \frac{dM}{dr} = 0; \quad \frac{dJ}{dr} = 0 \qquad (26)$$

in which Q, M, J = the volume, momentum, and density deficiency fluxes of the radial surface jet; and α = an entrainment coefficient; $Q = 2\pi r \int_0^\infty u e^{-(z/h)^2}\, dz$; $M = 2\pi r \int_0^\infty u^2 e^{-2(z/h)^2}\, dz$; and $J = 2\pi r \int_0^\infty u\Delta\rho e^{-2(z/h)^2}\, dz$. Substituting the assumed profiles into Eq. 26, and imposing the known conditions at the end of the surface impingement region, $r = r_J = \sqrt{3}\, b_J$ ($\sim 0.2\, H$), a solution for the upper layer depth and velocity can be obtained:

$$u(r) = u_J \left\{ 1 + \frac{\alpha}{c_1} \frac{r_J}{h_J} \left[\left(\frac{r}{r_J} \right)^2 - 1 \right] \right\}^{-1/2};$$

$$h(r) = h_J \frac{r_J}{r} \left\{ 1 + \frac{\alpha}{c_1} \frac{r_J}{h_J} \left[\left(\frac{r}{r_J} \right)^2 - 1 \right] \right\} \qquad (27)$$

in which $c_1 = \int_0^\infty e^{-\eta^2}\, d\eta$. The entrainment coefficient for the radial wall jet (4) has been set as approximately the same as that for the circular free turbulent jet: $\alpha = 0.057$ for Gaussian profiles. The buoyancy induced radial pressure gradient that has been ignored in Eq. 26 has been shown to introduce a negligible error for $r/H \lesssim 1$.

Defining the upper layer thickness at $r = r_J$ as $h_1 = \sqrt{3}\, h_J$, the average upper layer velocity u_1, and density deficiency $\Delta\rho_1$ at the jump toe, can be evaluated as $u_1 = Q_J/2\pi r_J h_1$; $\Delta\rho_1 = \Delta\rho_J/\sqrt{2}$, in which subscript J = properties at the jump toe.

Internal Jump Analysis.—The flow in the internal jump region is treated as a two-layer system with a distinct interface, and with constant densities ρ_a, $\rho_a - \Delta\rho$. The upper and lower layer depth at $r = r_J$ are h_1, h_2, respectively, and their conjugate jump heights at the end of the jump, $r = r_2$, are h_1', h_2'.

Whereas radial internal jumps have hitherto received little attention, both the two-dimensional internal jump, and the free surface radial hydraulic jump, have been studied quite extensively (7,15,16,20,22,23). An approximate momentum analysis of two-dimensional internal jumps in a two-layer system was formulated by Yih and Guha (23), and the solution to the resulting system of equations sought by various investigators. Using a Boussinesq approximation, the two-dimensional internal jump was also studied by Jirka and Harleman (7)

in the context of the stability of plane vertical buoyant jets in confined depth. On the other hand, the radial free surface hydraulic jump has been studied experimentally and theoretically by Sadler and Higgins (20) in connection with the design of channel transitions for free surface flow. In this case, since the discharge per unit depth varies with radial position, both the location of the jump toe and the length of the jump, $r_2 - r_j$, may be important determinants of the resulting conjugate jump heights. By imposing a downstream control, and assuming an abrupt vertical jump of zero length, Mehrota also presented a solution of the inviscid circular free surface hydraulic jump (16).

The present problem, i.e., the internal jump created by a vertical round buoyant jet in shallow water of large horizontal extent, differs from the previous works in two major respects. Firstly, there is no downstream control in the near field of the vertical buoyant discharge. The present experimental investigation reveals that the jump occurs at approximately $r_j = 0.6\ H$. This is an average value representing conditions over a wide range of water depths. Secondly, since the conjugate jump height, $h_1' \sim H$, is of the same order of radial position of the jump toe, $r_j \sim H$, it can be shown (21) that the length of the jump cannot be neglected in the momentum analysis. Whereas there is no basic experimental data on the jump length of radial internal jumps, the little data available for radial free surface jumps allow a crude approximation in relating jump length to jump height

$$r_2 = r_j + T(h_1' - h_1) \quad \ldots\ldots\ldots\ldots\ldots\ldots\ldots\ldots\ldots\ldots \quad (28)$$

in which $T = 4$ has been obtained experimentally by Sadler and Higgins (20).

By neglecting interfacial and bottom shear stresses, assuming hydrostatic pressure and uniform velocity distributions, and an average head of $1/2\ (h_1 + h_1')$ over the jump length, a force balance of the two layers gives the governing equations for the conjugate jump heights h_1', h_2' of the respective layers

$$F_1^{*2} r_j^2 \left(\frac{1}{r_j h_1} - \frac{1}{r_2 h_1'}\right) = \left(\frac{r_j + r_2}{2}\right)\left(\frac{h_1 + h_1'}{2}\right)(h_1' + h_2' - h_1 - h_2)\frac{1}{h_1^3} \quad \ldots\ldots\ldots\ldots \quad (29)$$

$$F_2^{*2} r_j^2 \left(\frac{1}{r_j h_2} - \frac{1}{r_2 h_2'}\right) = \left(\frac{r_j + r_2}{2}\right)\left(\frac{h_2 + h_2'}{2}\right)\left[\frac{\rho_1}{\rho_a}(h_1' - h_1) + (h_2' - h_2)\right]\frac{1}{h_2^3} \quad \ldots\ldots\ldots \quad (30)$$

in which F_1^*, F_2^* = the free surface Froude numbers defined by

$$F_1^{*2} = \frac{\left(\dfrac{Q_1}{2\pi r_j h_1}\right)^2}{g h_1}; \quad F_2^{*2} = \frac{\left(\dfrac{Q_2}{2\pi r_j h_2}\right)}{g h_2} \quad \ldots\ldots\ldots\ldots\ldots\ldots \quad (31)$$

in which Q_1, Q_2 = discharges in the upper and lower layers, respectively; and $\rho_1 = \rho_a - \Delta\rho$. The layer depths before and after the jump represent two possible dynamic states for the same given flow force. By equating alternate

expressions of $h_2' - h_2/h_1' - h_1$ derived from Eqs. 29 and 30, and introducing the Boussinesq approximation, $\Delta\rho/\rho << 1$ (a condition satisfied by most submerged buoyant discharge applications), to the resulting expressions, the governing equations for the internal jump become

$$\frac{4F_1^2\left(1-\frac{r_2h_1'}{r_Jh_1}\right)}{\frac{r_2h_1'}{r_Jh_1}\left(1+\frac{r_2}{r_J}\right)\left(1+\frac{h_1'}{h_1}\right)\left(1-\frac{h_1'}{h_1}\right)}-1$$

$$=\frac{4F_2^2\left(1-\frac{r_2h_2'}{r_Jh_2}\right)\frac{h_2}{h_1}}{\frac{r_2h_2'}{r_Jh_2}\left(1+\frac{r_2}{r_J}\right)\left(1+\frac{h_2'}{h_2}\right)\left(1-\frac{h_1'}{h_1}\right)} \quad \ldots\ldots\ldots\ldots\ldots\ldots \quad (32)$$

$$\left[\frac{r_2h_1'}{r_Jh_1}\left(1+\frac{r_2}{r_J}\right)\left(1-\frac{h_1'^2}{h_1^2}\right)\right.$$

$$\left.-4F_1^2\left(1-\frac{r_2h_1'}{r_Jh_1}\right)\right]\left[\frac{r_2h_2'}{r_Jh_2}\left(1+\frac{r_2}{r_J}\right)\left(1+\frac{h_2'}{h_2}\right)\left(1-\frac{h_1'}{h_1}\right)\right.$$

$$\left.-4F_2^2\left(1-\frac{r_2h_2'}{r_Jh_2}\right)\right]=16F_1^2F_2^2\left(1-\frac{r_2h_1'}{r_Jh_1}\right)\left(1-\frac{r_2h_2'}{r_Jh_2}\right) \quad \ldots\ldots\ldots \quad (33)$$

in which $F_1^2 = F_1^{*2}/\Delta\rho/\rho$; $F_2^2 = F_2^{*2}/\Delta\rho/\rho$. For typical values of F_1, F_2, and $\Delta\rho/\rho$, the solution to the approximate Eqs. 32 and 33 differ from that of the exact governing Eqs. 29 and 30 by, at most, 1%. It can be shown that Eqs. 32 and 33 imply a constant total water depth $h_1 + h_2 = h_1' + h_2'$ which results in the equation governing the upper layer change:

$$f\left(\frac{h_1'}{H}\right)=\frac{4F_1^2\left(1-\frac{r_2h_1'}{r_Jh_1}\right)}{\frac{r_2h_1'}{r_Jh_1}\left(1+\frac{r_2}{r_J}\right)\left(1+\frac{h_1'}{h_1}\right)\left(1-\frac{h_1'}{h_1}\right)}$$

$$-\frac{4F_2^2\left[1-\frac{r_2}{r_J}\left(\frac{H-h_1'}{h_2}\right)\right]\frac{h_2}{h_1}}{\frac{r_2}{r_J}\frac{(H-h_1')}{h_2}\left(1+\frac{r_2}{r_J}\right)\left(1+\frac{H-h_1'}{h_2}\right)\left(1-\frac{h_1'}{h_1}\right)}-1=0,$$

$$\text{with} \quad r_2 = r_J + 4(h_1' - h_1) \quad \ldots\ldots\ldots\ldots\ldots\ldots\ldots \quad (34)$$

Defining the critical state as that which is conjugate to itself, $h_1' \rightarrow h_1$, $h_2' \rightarrow h_2$, $r_2 \rightarrow r_J$, we have the criterion for criticality:

$$F_1^2 + F_2^2 = 1 \quad \ldots\ldots\ldots\ldots\ldots\ldots\ldots\ldots\ldots\ldots\ldots \quad (35)$$

The flow is supercritical upstream of the jump (compare Fig. 5), $F_1^2 + F_2^2 >$

1, and usually, but not necessarily, subcritical downstream of it, $F_1^2 + F_2^2 < 1$.

In general, the governing equation for the conjugate jump height, h_1', possesses two solutions that lie within the physically feasible range $0 < h_1' < H$. One of these can be discarded by energy considerations. However, for high densimetric Froude numbers of the upper layer F_1 (or large values of h_1/h_2), Eq. 34 does not yield a solution. The nonexistence of a solution can be interpreted physically as a hydrodynamically unstable situation. Under these high momentum conditions, the buoyancy contained in the upper layer flow is not sufficient to establish stable conjugate downstream conditions, leading to a breakdown of the stratified flow and heat re-entrainment into the buoyant jet region.

Near Field Stability

For given discharge conditions F_o and H/D, the solution to the buoyant jet and surface impingement region (Eq. 21) can be coupled to the internal

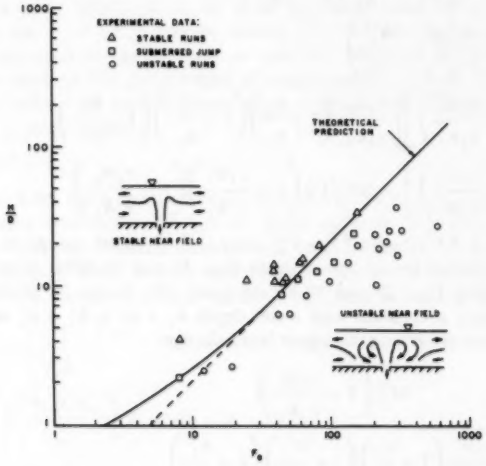

FIG. 7.—Stability Criterion of Vertical Round Buoyant Discharge in Shallow Water

jump region via the surface jet solution (Eq. 27) to determine the flow conditions prior to the jump at $r = r_j$. A predictive criterion of the near field stability is then provided by the equation for upper layer change, Eq. 34. In terms of the discharge parameters, this stability criterion—the line delimiting the stable and unstable jump conditions—is predicted to be

$$F_o = 4.6\left(\frac{H}{D}\right) \quad \text{for} \quad \frac{H}{D} > 6 \qquad (38)$$

Fig. 7 shows that for a given submergence H/D, the unstable domain is approached by increasing the source densimetric Foude number F_o. The departure of the stability criterion from Eq. 38 for low H/D indicates initial size effects. It

is interesting to note that the pure plume (low F_o, high H/D) falls within the stable discharge domain.

In summary, the discharge stability, as a function of source conditions, is determined solely by the dynamics of the buoyant jet, surface impingement, and internal jump regions.

Laboratory Experiment

A total of 33 experiments were carried out with a vertical semicircular buoyant wall jet (i.e., a half jet in lieu of a full round jet) in a 37 × 18 × 1 ft (11.3

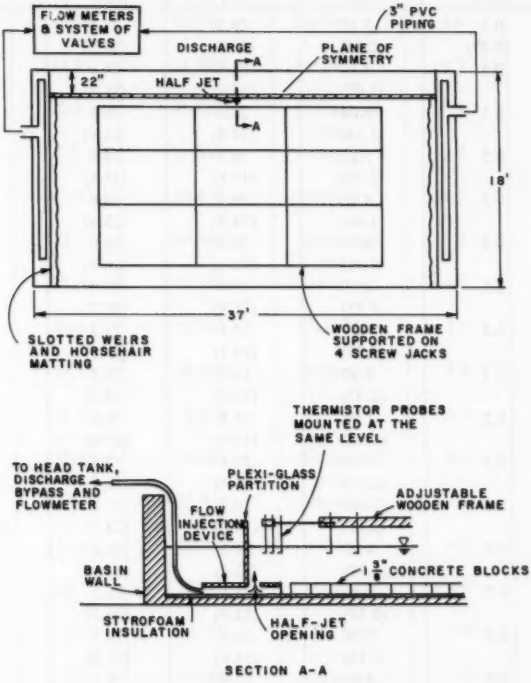

FIG. 8.—Experimental Set-Up

× 5.5 × 0.3 m) hydraulic scale model basin which had a false floor made of styrofoam insulation material and concrete blocks (Fig. 8). A 16 × 34 ft (4.9 × 10.4 m) area was formed by constructing a partition which formed a plane of symmetry for the axisymmetric jet along the whole length of the basin. The center portion of the partition was made of 0.5 in. (13 mm) thick Plexiglas, rendering partial flow visualization possible at an oblique angle.

TABLE 1.—Summary of

Run number (1)	Jet diameter, D, in inches (centimeters) (2)	Discharge velocity, U_o, in feet per second (meters per second) (3)	Discharge excess temperature, ΔT_o, in degrees Fahrenheit (degrees centigrade) (4)	Initial ambient temperature, T_a, in degrees Fahrenheit (degrees centigrade) (5)	Discharge flow, Q_o, in gallons per minute (in cubic meters per second) (6)
1	0.5	3.10	28.2	72.5	0.95
	(1.27)	(0.95)	(15.7)	(22.5)	(3.6)
2	0.5	3.50	26.5	74.9	1.07
		(1.07)	(14.7)	(23.8)	(4.05)
3	0.5	5.06	26.0	76.2	1.55
		(1.54)	(14.4)	(24.6)	(5.87)
4	0.5	5.22	28.1	74.8	1.60
		(1.59)	(15.6)	(23.8)	(6.06)
5	0.5	4.90	26.8	74.9	1.50
		(1.49)	(14.9)	(23.8)	(5.68)
6	0.5	6.70	29.0	76.0	2.05
		(2.04)	(16.1)	(24.4)	(7.76)
7	0.5	2.72	21.4	78.3	0.83
		(0.83)	(11.9)	(25.7)	(3.14)
8	0.5	7.52	27.1	73.2	2.30
		(2.29)	(15.1)	(22.9)	(8.71)
9	0.5	8.10	24.2	75.7	2.48
		(2.47)	(13.4)	(24.3)	(9.39)
10	0.5	1.96	25.8	78.0	0.60
		(0.60)	(14.3)	(25.6)	(2.27)
11	0.5	8.24	27.8	72.8	2.52
		(2.51)	(15.4)	(22.7)	(9.54)
12	0.5	10.46	26.9	73.9	3.20
		(3.19)	(14.9)	(23.3)	(12.11)
13	0.5	4.50	24.8	75.0	1.38
		(1.37)	(13.8)	(23.9)	(5.22)
14	0.5	2.88	23.2	75.7	0.88
		(0.88)	(12.9)	(24.3)	(3.33)
15	0.5	3.76	26.2	71.3	1.15
		(1.15)	(14.6)	(21.8)	(4.35)
16	0.5	2.94	23.9	73.3	0.90
		(0.90)	(13.3)	(22.9)	(3.41)
17	0.25	8.5	28.7	70.2	0.65
	(0.64)	(2.59)	(15.9)	(21.2)	(2.46)
18	0.25	4.06	23.1	72.1	0.31
		(1.24)	(12.8)	(22.3)	(1.17)
19	0.25	7.72	23.5	73.4	0.59
		(2.35)	(13.1)	(23.0)	(2.23)
20	0.25	10.46	22.4	74.7	0.80
		(3.19)	(12.4)	(23.7)	(3.03)

Experimental Run Parameters

Densimetric Froude number, F_o (7)	Submergence H/D (8)	Reynold's number $R_j = U_o D/\nu$ (9)	Observed flow field (10)	Observed near field dilution S (11)	Predicted near field dilution S^* (12)
38.9	10.6	12,900	Stable	4.4	3.1
44.6	10.8	14,700	Stable	4.3	3.1
64.8	10.8	21,100	Submerged jump	3.8	NA
64.5	8.7	21,800	Unstable	2.0	
62.2	12.4	20,400	Stable	5.2	3.6
80.4	12.7	27,900	Submerged jump	4.2	NA
38.3	13.0	11,300	Stable	4.3	3.8
95.9	10.6	31,300	Unstable	2.1	
46.0	11.1	14,300	Stable	4.5	3.2
24.9	11.2	8,200	Stable	5.5	3.3
103.9	13.9	34,300	Submerged jump	4.3	NA
131.9	14.1	43,500	Unstable	3.5	
59.9	14.4	18,800	Stable	4.5	4.2
39.5	14.5	12,000	Stable	4.0	4.2
49.7	6.2	15,700	Unstable	1.9	
40.4	6.3	12,200	Unstable	2.2	
151.8	19.3	17,700	Unstable	4.6	
81.2	19.3	8,400	Stable	7.7	5.6
146.6	23.5	16,000	Submerged jump	9.1	NA
208.8	23.4	21,700	Unstable	7.1	

TABLE 1.—

(1)	(2)	(3)	(4)	(5)	(6)
21	0.25	14.38	26.8	73.2	1.10
		(4.38)	(14.9)	(22.9)	(4.16)
22	0.25	17.0	24.7	75.4	1.30
		(5.18)	(13.7)	(24.1)	(4.92)
23	0.25	10.2	34.8	76.0	0.78
		(3.11)	(19.3)	(24.4)	(2.95)
24	0.25	30.0	22.6	77.9	2.30
		(9.15)	(12.6)	(25.5)	(8.71)
25	0.25	16.86	26.5	79.1	1.29
		(5.14)	(14.7)	(26.2)	(4.88)
26	0.25	11.24	27.1	71.9	0.86
		(3.43)	(15.1)	(22.2)	(3.26)
27	0.25	17.00	28.4	73.9	1.30
		(5.18)	(15.8)	(23.3)	(4.92)
28	0.25	12.16	26.3	75.5	0.93
		(3.71)	(14.6)	(24.2)	(3.52)
29	0.25	19.60	26.3	76.3	1.50
		(5.98)	(14.6)	(24.6)	(5.68)
30	1.0	1.32	25.1	78.9	1.52
	(2.54)	(0.40)	(13.9)	(26.1)	(6.13)
31	1.0	1.94	23.2	74.5	2.37
		(0.59)	(12.9)	(23.6)	(8.97)
32	1.0	0.94	28.2	76.1	1.15
		(0.29)	(15.7)	(24.5)	(4.35)
33	1.0	0.82	21.9	76.1	1.00
		(0.25)	(12.2)	(24.5)	(3.79)

The flow injection device for the half jet was a rectangular Plexiglas box with a semicircular fitting sealed onto its top (Fig. 8); different jet diameters could be obtained by using different fittings. Flow entered the box at one end and exited upwards through a semicircular opening. To avoid flow separation, the exit section of the half jet was rounded off smoothly.

Temperatures were measured with 44 thermistor probes (YSI 701, time constant = 9 sec, accuracy 0.3° F) which were individually calibrated and mounted at the same level on a wooden platform supported on four screw jacks. Soon after the start of the experiment, dye was injected to observe the flow. The first scan of the surface temperatures was started when the dye front had gone past a substantial area. After two or three surface scans were taken, the wooden platform was then lowered to record vertical temperature profiles. To ensure that some kind of quasi-steady situation was reached in the experiment, a surface scan was always taken at the end of the experiment. In all the runs, the temperature recordings of the last surface scan in the near field were very close to those of the first few scans. The majority of the runs took about 20 min. The character of the near-field flow in the plane of symmetry was visually observed by due injection. Pertinent flow features such as the upper layer thickness, the location of the jump toe (for the stable discharge configuration) were also noted. A summary of run parameters and results are presented in Table 1.

—*Continued*

(7)	(8)	(9)	(10)	(11)	(12)
261.6	24.1	29,900	Unstable	4.2	
318.6	24.2	35,300	Unstable	3.6	
154.8	32.3	21,200	Stable	8.6	9.4
583.4	32.3	62,500	Unstable	3.3	
295.3	32.7	35,000	Unstable	7.1	
205.2	10.1	23,400	Unstable	2.2	
296.7	15.8	35,300	Unstable	2.6	
219.5	17.7	25,300	Unstable	3.1	
246.4	19.7	28,500	Unstable	2.6	
11.9	2.4	11,000	Unstable	2.1	
19.0	2.6	16,100	Unstable	1.2	
8.0	2.2	7,800	Submerged jump	2.04	NA
8.2	4.0	6,800	Stable	2.5	1.5

In general, visual observations of stability and other features of the flow are in every way consistent with the temperature data. Fig. 9 shows typical radial temperature transects corresponding to the possible near-field conditions. Vertical excess temperature profiles, $\Delta T(z,r)$, averaged in the azimuth, (Θ), direction, are shown at various radial positions r/H from the source. The vertical homogeneity of the near-field temperatures, in the case of an instability, contrasts sharply with the vertical temperature profile of a stably stratified system in the stable configuration. In addition to the stable and unstable near-field conditions, a weak instability was also sometimes observed as a transition phenomenon. This was characterized by a thickening of the upper layer, followed by an internal jump with a conjugate depth that exceeded the water depth (submerged jump), causing slight re-entrainment of the upper layer mixed water. Further details of the experimental program can be found in Lee et al. (10).

Comparison of Theory and Experimental Data

Near Field Stability

From visual observations of the upper layer flow (and confirmed by the temperature data) over a wide range of experimental conditions ($F_o \sim$ 10–80; $H/D \sim$ 10–30), the location of the jump toe is determined to be $r_j \sim 0.6$

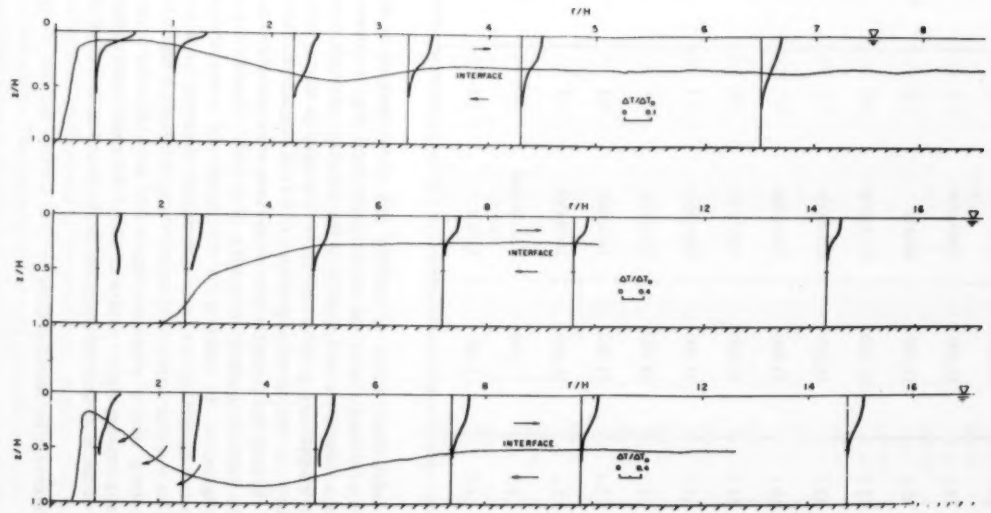

FIG. 9.—Radial Temperature Transect for Three Discharge Configurations. From Top to Bottom: (*a*) $F_o = 46$, $H/D = 11$; Stable Jump. (*b*) $F_o = 205$, $H/D = 10$; Unstable Jump. (*c*) $F_o = 8$, $H/D = 2$; Submerged Jump

H. The observed discharge stability (Fig. 7) is well predicted by the stability criterion. Under deep water, stable discharge conditions, the upper layer thickness in the surface impingement region is about 0.1 H. This compares favorably with the theoretical prediction (Fig. 5), and also Rawn's data (18) for sewage plumes.

Near Field Mixing

Under stable discharge conditions, the theoretical near field dilution is defined volumetrically as the ratio of the upper layer flow at the exit of the surface impingement region, $r = r_I$, to the discharge flow, $S = Q_I/Q_o$. Experimentally, the near field dilution is taken to be the ratio of the discharge excess temperature to the maximum observed excess temperature in the upper layer, $S_{EXP} = \Delta T_o/\Delta T_{max}$. Predicted dilution contours are shown in Fig. 10 and compared to the observed experimental results. In general, good agreement is obtained, the observed dilution being somewhat higher than predicted. This could be attributed to the additional entrainment in the surface impingement region, and

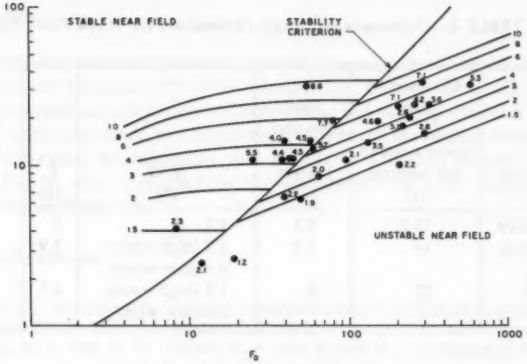

FIG. 10.—Comparison of Observed and Predicted Near Field Dilution

also the fact that in most experiments even the temperature probe closest to the discharge may lie outside the surface impingement region. In the case of an unstable discharge configuration, an eddying zone is observed close to the jet, leading to considerable heat re-entrainment. The extent of this mixing zone can vary substantially depending on experimental conditions. For the range of experimental conditions reported herein, the outer edge of this mixing zone, $r = r_c$, is located at 2–3.5 H. At the edge, the interfacial height changes sharply, and a stably stratified counter-flow system is observed beyond this point.

The dilution capacity of the discharge is severely impaired if the discharge parameters fall within the unstable domain. For this case it is reasonable to postulate that the buoyancy driven exchange flow Q_c of the counterflow system depends only on source flow Q_o, the source buoyancy flux $B_o = Q_o g\, \Delta\rho_o/\rho_a$, and the water depth, H:

$$f(Q_c, Q_o, B_o, H) = 0 \quad \ldots\ldots\ldots\ldots\ldots\ldots\ldots\ldots\ldots\ldots\ldots\ldots \quad (39)$$

Noting that $Q_o = u_o \pi D^2/4$, and the dimensions $Q_o = L^3/T$; $B_o = L^4/T^3$, a dimensional analysis of Eq. 39 yields

$$S = \frac{Q_c}{Q_o} \approx \frac{B_o^{1/3} H^{5/3}}{Q_o} \approx F_o^{-2/3} \left(\frac{H}{D}\right)^{5/3} \quad \ldots\ldots\ldots\ldots\ldots\ldots \quad (40)$$

Thus, lines of constant dilution in the unstable domain follow slopes of 2/5 ($H/D \sim F_o^{2/5}$). A best fit of the dilution data gives

$$S = 0.9\, F_o^{-2/3} \left(\frac{H}{D}\right)^{5/3} \quad \ldots\ldots\ldots\ldots\ldots\ldots\ldots\ldots \quad (41)$$

Design Implication

The preceding presentation demonstrates that the mixing and stability characteristics of large diameter outfalls discharging buoyant water vertically into the ambient is dependent on two dimensional parameters: F_o, a measure of discharge momentum and buoyancy, and H/D, a measure of the shallowness of the receiving water. An evaluation of typical conditions at existing cooling water discharge sites (the 450 MW unit of the San Onofre Plant in California, and the Littlebrook and Sizewell Power Stations (500 MW each) on the Thames River estuary) is given in Table 2. Using the stability criterion of Fig. 7, it would appear that all these existing discharge designs operate in the unstable discharge domain. Some field information (14) seems to support this fact. On the other hand, design details, such as the height of the port (which is one-half of the total depth at San Onofre), may alter the near field behavior.

TABLE 2.—Summary of Design Parameters for Three Plant Sites

Plant site (1)	Condenser flow, Q_o, in meters cubed per second (2)	Port diameter, D, in meters (3)	H/D (4)	F_o (5)	Predicted discharge stability (6)
San Onofre	25.2	4.3	1.1	7	Unstable
Littlebrook	19	3.5	1.7 (high water) 0.9 (low water)	7.9	Unstable
Sizewell	25	4	1.5 (high water) 1.0 (low water)	4.5	Unstable

The major conclusion of this paper lies in the observation that the shallowness of a site has a pronounced effect on the dynamics of a discharge. Accordingly, entirely different predictive techniques have to be employed in the design of an unstable discharge, compared to the simple buoyant jet theories which can be used for stable jet analysis.

A secondary question that arises, namely, which discharge configuration is more desirable in actual design practice, is considerably more difficult to answer. Given a plant heat rejection rate $Q_o \Delta T_o$, a condenser flow Q_o, and a chosen

water depth H, it can be seen from the dilution diagram, Fig. 10, that regardless of the choice of diameter, D (covering both the stable and unstable conditions with reasonable limits on the exit velocity $u_o = Q/(\pi D^2/4)$), approximately similar dilutions, S, are attained. Thus, no obvious design strategy exists if maximization of near-field dilution is the only objective. However, other considerations may favor the choice of a stable discharge design: For example, the prevention of a recirculating eddy and the associated large benthic temperature rises from an ecological viewpoint, or the fact that a stable discharge experiences additional dilution, beyond the near-field value, S, in the internal hydraulic jump stage.

In summary, it is clear from the preceding arguments that shallow site conditions limit the dilution that can be obtained with single part discharges. Moving the outfall to sites with larger depths, or using a multiport diffuser design, are the obvious alternatives to avoid that constraint. Possible extensions of the present work to tidal situations and non-vertical discharges in shallow water have been reported elsewhere (11,14).

Acknowledgment

The bulk of the research presented herein was supported under the Waste Heat Management Program, 1974–1977, administered through the Energy Laboratory of the Massachusetts Institute of Technology, and was reported in a technical report (10). Additional work, notably in the treatment of the surface impingement region and the radial internal jump, and leading to a slightly revised criterion, Eq. 38 or Fig. 7, was supported by the Department of Civil Engineering at the University of Delaware.

Appendix I.—References

1. Abraham, G., "Jet Diffusion in Stagnant Ambient Fluid," *Delft Hydrology Laboratory Publication No. 29,* Delft, the Netherlands, 1963.
2. Albertson, M. I., Dai, Y. N., Jensen, R. A., and Rouse, H., "Diffusion of Submerged Jets," *Transactions,* ASCE, Vol. 115, 1950, pp. 639–664.
3. Alpert, R. L., "Turbulent Ceiling-Jet Induced by Large Scale Fires," *Technical Report No. 22357-2,* Factory Mutual Research Corp., Boston, Massachusetts, 1974.
4. Bakke, P., "An Experimental Investigation of a Wall Jet," *Journal of Fluid Mechanics,* Vol. 2, 1957, pp. 467–472.
5. Ito, H., "Pressure Losses in Smooth Pipe Bends," *Journal of Basic Engineering Transactions,* American Society of Mechanical Engineers, Vol. 82, 1960, pp. 131–143.
6. Jirka, G. H., Abraham, G., and Harleman, D. R. F., "An Assessment of Techniques for Hydrothermal Prediction," *Report 203,* Parsons Laboratory for Water Resources & Hydrodynamics, Massachusetts Institute of Technology, Cambridge, Mass., 1975.
7. Jirka, G. H., and Harleman, D. R. F., "Stability and Mixing of a Vertical Plane Buoyant Jet in Confined Depth," *Journal of Fluid Mechanics,* Vol. 94, 1979, pp. 275–304.
8. Koh, R. C. Y., and Fan, L. N., "Mathematical Models for the Prediction of Temperature Distributions Resulting from the Discharge of Heated Water into Large Bodies of Water," *Environmental Protection Agency Water Pollution Control Research Series 16130 DWO.*
9. Koh, R. C. Y., and Brooks, N. H., "Fluid Mechanics of Waste Water Disposal in the Ocean" *Annual Review of Fluid Mechanics,* Vol. 7, 1975, pp. 187–211.
10. Lee, J. H. W., Jirka, G. H., and Harleman, D. R. F., "Stability and Mixing of a Vertical Round Buoyant Jet in Shallow Water," *Report 195,* Parsons Laboratory

for Water Resources & Hydrodynamics, Massachusetts Institute of Technology, Cambridge, Mass., 1974.
11. Lee, J. H. W., and Jirka, G., discussion of "Horizontal Buoyant Jets in Quiescent Shallow Water," by V. Balasurbramanian and S. C. Jain, *Journal of the Environmental Engineering Division*, ASCE, Vol. 105, No. EE4, 1979, pp. 790–792.
12. List, E. J., and Imberger, J., "Turbulent Entrainment in Buoyant Jets and Plumes," *Journal of the Hydraulics Division*, ASCE, Vol. 99, No. HY8, 1973.
13. Long, R. R., "Blocking Effects in Flows Over Obstacles," *Tellus*, Vol. 22, 1970, pp. 471–480.
14. Macqueen, J. F., "On the Near Field Flow Associated with Submerged, Vertical Cooling Water Discharges," *Central Electricity Research Laboratories*, United Kingdom, 1977.
15. Mehrotra, S. C., and Kelly, R. E., "On the Question of Non-Uniqueness of Internal Hydraulic Jumps and Drops in a Two-Fluid System," *Tellus*, Vol. 25, 1973, pp. 560–567.
16. Mehrotra, S. C., "Circular Jumps," *Journal of the Hydraulics Division, Proceedings*, ASCE, Vol. 100, No. HY8, 1974, pp. 1133–1140.
17. Morton, B. R., Taylor, G. I., and Turner, J. S., "Turbulent Gravitational Convection from Maintained and Instantaneous Sources," *Proceedings of the Royal Society of London*, Series A, Vol. 234, 1965, pp. 1–23.
18. Rawn, A. M., and Palmer, H. K., "Predetermining the Extent of a Sewage Field in Seawater," *Transactions*, ASCE, Vol. 94, 1930, pp. 1036–1060.
19. Rouse, H., Yih, C. S., and Humphreys, H. W., "Gravitational Convection from a Boundary Source," *Tellus*, Vol. 4, 1952, pp. 201–210.
20. Sadler, C., and Higgins, M., "Radial Free Surface Flow," Thesis presented to the Massachusetts Institute of Technology, at Cambridge, Mass., in 1963, in partial fulfillment of the requirements for the degree of Master of Science.
21. Watson, E. J., "The Radial Spread of a Liquid Jet over a Horizontal Plane," *Journal of Fluid Mechanics*, Vol. 20, 1964, pp. 481–499.
22. Wilkinson, D. L. and Wood, I. R., "A Rapidly Varied Flow Phenomenon in a Two-Layer Flow," *Journal of Fluid Mechanics*, Vol. 47, 1971, pp. 241–256.
23. Yih, C. S., and Guha, C. R., "Hydraulic Jump in a Fluid System of Two Layers," *Tellus*, Vol. 7, 1955, pp. 358–366.

Appendix II.—Notation

The following symbols are used in this paper:

B_o = source buoyancy flux;
b = jet width or diffusion thickness;
b' = width of jet potential core in region of flow establishment;
D = jet diameter;
F = densimetric Froude number;
F^* = free surface Froude number;
H = water depth;
h = characteristic upper layer thickness;
J = density deficiency flux;
L_D = diffuser length;
M = momentum flux;
N = number of ports;
Q = volume flux;
r_j = location of jump toe;
r_2 = radial position of end of jump;
S = near field dilution;
T = temperature, ratio of jump length to jump height;
$\Delta T = T - T_a$ = excess temperature;

u = velocity;
r, z = cylindrical coordinates;
α = entrainment coefficient;
β = coefficient of thermal expansion;
ϵ = jet spreading angle;
λ = ratio of temperature diffusion thickness to momentum diffusion thickness;
ρ = density; and
$\Delta\rho = \rho_a - \rho$ = density deficiency.

Subscripts

a = ambient values;
c = center line values, value at critical section;
e = entrainment, end of region of flow establishment;
i = entrance to surface impingement region;
I = exit of surface impingement region;
j = jet;
p = plume;
o = discharge values; and
1,2 = upper and lower layer.

TRANSVERSE BED SLOPE IN ALLUVIAL CHANNEL BENDS

By A. Jacob Odgaard,[1] M. ASCE

INTRODUCTION

Flows in alluvial channel bends are among the more difficult encountered by hydraulic engineers. The main difficulty encountered is the description of the helical flow pattern in the bend, and its interaction with the topography of the channel bed. The balance between the centrifugal forces due to the vertical nonuniformity of the velocity profile, combined with the flow curvature, the shear stresses, and the radial pressure gradients, tends to produce strong secondary currents and a transverse slope of the channel bed, with an increase in the depth toward the outer (concave) bank. As a result, the outer bank is often undermined and eroded.

This paper examines and compares existing models for the prediction of the steady-state transverse bed slope in channel bends, using laboratory and field data, and proposes an alternative model. While traditional models are based on equations of motion for the sediment particles in the bed load, this model is based on a theory for the critical conditions for sediment entrainment. The model gives good agreement between measured and predicted bed slopes. The analysis herein may lead to: (1) An improved understanding of the problems involved in the description of bend bed topography; and (2) improved analytical tools for development of channel-protection measures that are effective, environmentally acceptable, and economically justifiable.

SUMMARY OF EXISTING THEORIES

Several analytical models have been developed for the prediction of the steady-state transverse bed slope in a curved, erodible bed channel. Among them are the models by van Bendegom (19), NEDECO (13), Yen (21), El-Khudairy (7), Ikeda (11), Allen (1), Engelund (8), Kikkawa, Ikeda, and Kitagawa (12), Zimmermann and Kennedy (22), and Falcon (9). Each of the models is based on the radial balance of forces acting on a sediment particle moving along a radially inclined bed. The equilibrium transverse bed slope calculated is that

[1]Asst. Prof., Inst. of Hydr. Research, The Univ. of Iowa, Iowa City, Iowa 52242.

Note.—Discussion open until May 1, 1982. To extend the closing date one month, a written request must be filed with the Manager of Technical and Professional Publications, ASCE. Manuscript was submitted for review for possible publication on January 27, 1981. This paper is part of the Journal of the Hydraulics Division, Proceedings of the American Society of Civil Engineers, ©ASCE, Vol. 107, No. HY12, December, 1981. ISSN 0044-796X/81/0012-1677/$01.00.

for which the radial-plane components, parallel to the bed, of the fluid drag, F_r, and the particle submerged weight, W_s are equal:

$$F_r = W_s \sin\beta \quad \ldots\ldots\ldots\

in which ρ_s = density of sediment particle; g = acceleration of gravity; and D = mean particle diameter. In deriving Eq. 2, van Bendegom assumed that: (1) The longitudinal drag, F_d, on a sediment particle is determined by $F_d = A\ \rho\ g\ \bar{V}^2/C^2$, in which C = Chezy's coefficient; (2) $C = 50\ m^{1/2}/s$; and (3) the direction of F_d deviates from the mean flow direction by an angle, δ, determined by $\tan \delta = 10\ d/r$.

Van Bendegom's results were later used by NEDECO (13) with $\sin \beta$ replaced by the derivative $d(d)/dr$ to yield a differential equation which was solved to obtain an expression for the radial profile of the bed. Yen (21), in his analysis, related F_r in Eq. 1 to the radial component of the flow velocity and obtained a relationship between $\sin \beta$ and the maximum radial velocity. El-Khudairy's (7), and Ikeda's (11) analyses are very similar to the analysis by Yen (21), except that the radial velocities used in the calculation of F_r were computed from Rozovskii's (16) velocity-distribution formulas. Allen (1), who was unaware of van Bendegom's results, used a force balance similar to that of van Bendegom (19). He obtained a relation between: (1) Transverse slope, $\sin \beta$; (2) deviation angle, δ; (3) bed shear stress, τ_o; and (4) mean particle diameter, D. If the bed shear stress were related to mean velocity by Chezy's coefficient, Allen's result becomes identical to that of van Bendegom (19).

Engelund (8), and Kikkawa, Ikeda, and Kitagawa (12) assumed that the longitudinal drag on a sediment particle is balanced by the friction force on the particle from the channel bed:

$$F_d = \mu\ (W_s \cos \beta - F_\ell) \quad \ldots\ldots\ldots\

He assumed that F_r is determined from a relationship equating the centrifugal force on a unit volume to the radial pressure gradient and the vertical gradient of the radial shear stress. The pressure gradient in his relationship is determined by equating: (1) The integral over depth of the moment of the pressure gradient with respect to a longitudinal axis; and (2) the integral over depth of the moment of the centrifugal force about the same axis. Using the power law

$$\frac{V}{\bar{V}} = \frac{n+1}{n}\left(\frac{y}{d}\right)^{1/n} \quad \ldots\ldots\ldots\ldots\ldots\ldots\ldots\ldots\ldots\ldots\ldots\ldots\ldots\ldots\ldots\ldots (6)$$

in which V = point velocity at distance y from the bed; and n = dimensionless factor (which will be termed velocity-profile exponent). The radial shear stress, τ_r, is determined as a function of y by integration. Falcon then obtained the

TABLE 1.—Summary of Key Relations in Reviewed Models

Author, or authors (1)	Bed-friction parameter (2)	Ratio of local bed slope to depth/radius ratio, K (3)
van Bendegom (19)	$C = 50\ \mathrm{m}^{1/2}/\mathrm{s}$	$0.0585 F_D^2$
Engelund (8)	$\mu = \tan \Phi$	7μ
Kikkawa, Ikeda, Kitagawa (12)	$M = (2.75 - 4.35\ V_*/\bar{V}) f_v^2$	MF_D
Zimmermann, Kennedy (22)	$N = (n+1)/[n(n+2)]$	$(\alpha/2)\ NF_D^2$
Falcon (9)	$N = (n+1)/[n(n+2)]$	$(3\alpha/2)\ NF_D^2$

Note: 1 ft = 0.305 m; α = ratio of projected surface area to volume for a sediment particle divided by that for a sphere.

radial drag, F_r, by multiplying τ_r at bed level by the projected surface area of a sediment particle, A:

$$F_r = \rho A \bar{V}^2 N \frac{d}{r} \quad \ldots\ldots\ldots\ldots\ldots\ldots\ldots\ldots\ldots\ldots\ldots\ldots\ldots\ldots\ldots\ldots (7)$$

$$\text{in which} \quad N = \frac{n+1}{n(n+2)} \quad \ldots\ldots\ldots\ldots\ldots\ldots\ldots\ldots\ldots\ldots\ldots\ldots\ldots\ldots\ldots\ldots (8)$$

According to Zimmermann and Kennedy (22), n^2 = the inverse of the overall friction factor f. In Falcon's (9) analysis, n is determined from the longitudinal slope, S, of the water surface, using the Darcy-Weisbach formula modified by Falcon (9). Both Zimmermann and Kennedy (22), and Falcon (9) obtained Eq. 2, with

$$K = c N F_D^2 \quad \ldots\ldots\ldots\ldots\ldots\ldots\ldots\ldots\ldots\ldots\ldots\ldots\ldots\ldots\ldots\ldots\ldots\ldots (9)$$

in which c = constant. In Zimmermann and Kennedy's analysis, the value of c is one-third that in Falcon's analysis, because Falcon neglected the moment contribution of vertical shear stresses. (Table 1 is a summary of key relations in the reviewed models.)

Alternative Approach

The preceding models are based on the assumption that the sediment particles shaping the bed are moving or being dragged over the bed in the longitudinal direction, with no velocity component in the radial or transverse direction. The relations for the transverse bed slope are obtained from the expression of no net radial force on these particles. The grain size, D, used in these relations is that of the moving particles. Considering that natural channel beds usually consist of nonuniform sediments, and often have an armoring of coarser sediments at the bed surface, there may be a significant difference between the grain size distribution of the bed load and that of the bed surface. To be consistent with theory, estimates of the bed slope by the above models must be based on bed-load characteristics rather than the characteristics of the bed surface.

The writer's approach is an attempt to relate the transverse bed slope to bed-surface characteristics. It is assumed that, in the state of equilibrium, the sediment particles shaping the bed surface are statically stable in both radial and longitudinal direction, but at impending motion in the longitudinal direction.

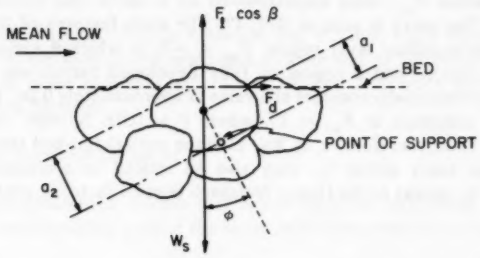

FIG. 2.—Vertical Longitudinal-Plane Components of Forces on Sediment Particle

That is, the size of the bed-forming particles is such that the particles are just about to move in the longitudinal direction by rolling about their points of support. Fig. 2 shows the vertical longitudinal-plane force diagram for one such particle. Equating moments of gravity (W_s), lift (F_ℓ), and drag (F_d) forces about the support point yields

$$F_d = \frac{a_1}{a_2}(W_s - F_\ell \cos\beta)\tan\phi \quad \ldots\ldots\ldots\ldots\ldots\ldots\ldots\ldots\ldots\ldots (10)$$

in which a_1 and a_2 = the distances shown in Fig. 2; and ϕ = angle of repose of the submerged sediment. This analysis is similar to the one proposed by White (20). White, however, did not include the effect of lift force. According to Raudkivi (14), Chepil (6) was one of the first researchers to consider lift force. Based on experimental results, Chepil concluded that for nearly spherical grains $F_\ell \simeq c_1 F_d$, in which c_1 = a constant of the order of 0.85. Introducing Chepil's result into Eq. 10, and assuming that $\cos\beta = 1$, yields

$$F_d = c_2 W_s \quad \ldots\ldots\ldots\ldots\ldots\ldots\ldots\ldots\ldots\ldots\ldots\ldots\ldots\ldots\ldots\ldots (11)$$

in which $$c_2 = \frac{\frac{a_1}{a_2}\tan\phi}{1 + c_1\frac{a_1}{a_2}\tan\phi} \quad \ldots\ldots\ldots\ldots\ldots\ldots\ldots\ldots\ldots\ldots \quad (12)$$

Eq. 11 may also be written

$$\tau_c = \theta\,(\rho_s - \rho)\,g\,D_c \quad \ldots\ldots\ldots\ldots\ldots\ldots\ldots\ldots\ldots\ldots \quad (13)$$

in which τ_c = critical bed shear stress; D_c = diameter of the particle whose motion is impending; and θ = dimensionless factor. Experiments by White (20), and a comprehensive data analysis by Shields (18), have shown that θ is a function of a critical boundary Reynolds number, R_{*c}, defined as

$$\mathsf{R}_{*c} = \frac{V_{*c}\,D_c}{\nu} \quad \ldots\ldots\ldots\ldots\ldots\ldots\ldots\ldots\ldots\ldots \quad (14)$$

in which V_{*c} = critical shear velocity defined by $V_{*c} = \sqrt{\tau_c/\rho}$; and ν = kinematic viscosity of the fluid. Shields' results, which appeared as a plot of $\tau_c/[(\rho_s - \rho)g\,D_c]$ versus R_{*c}, were approximated by a curve (the Shields curve) by Rouse (15). The curve is seen in Ref. 17. The main features of Shields' curve are a laminar-boundary layer region, $\mathsf{R}_{*c} < \sim 2$, in which θ varies as $(\mathsf{R}_{*c})^{-1}$, a transition region, and a region of fully developed turbulence, $\mathsf{R}_{*c} > 400$, in which θ is substantially constant at a value of approximately 0.06. The transition curve has a minimum at $\mathsf{R}_{*c} \simeq 10$, where $\theta \simeq 0.03$. Shields' curve is valid only for flat beds; therefore, τ_c in Eq. 13 is the critical flat-bed shear stress.

The critical shear stress, τ_c, may also be related to a critical mean flow velocity, $\bar{V}_c$, by means of the Darcy-Weisbach friction factor, f_f (flat-bed friction factor):

$$\tau_c = \frac{f_f}{8}\rho\,\bar{V}_c^2 \quad \ldots\ldots\ldots\ldots\ldots\ldots\ldots\ldots\ldots\ldots \quad (15)$$

Introduction of $f_f = 8\kappa^2 n_f^{-2}$, and equating Eqs. 13 and 15, yields

$$\bar{V}_c^2 = \theta\kappa^{-2} n_f^2\,g\,D_c\frac{\rho_s - \rho}{\rho} \quad \ldots\ldots\ldots\ldots\ldots\ldots\ldots\ldots \quad (16)$$

in which κ = Karman's constant. Eq. 16 may be reduced to

$$n_f = \kappa\,\mathsf{F}_{Dc}\,\theta^{-1/2} \quad \ldots\ldots\ldots\ldots\ldots\ldots\ldots\ldots\ldots\ldots \quad (17)$$

in which F_{Dc} = the particle Froude number based on $\bar{V}_c$ and D_c; that is

$$\mathsf{F}_{Dc} = \frac{\bar{V}_c}{\sqrt{\frac{\rho_s - \rho}{\rho}\,g\,D_c}} \quad \ldots\ldots\ldots\ldots\ldots\ldots\ldots\ldots\ldots\ldots \quad (18)$$

By assuming that Falcon's relationship, Eq. 7, holds, Eq. 1 is written

$$\rho A\,\bar{V}_c^2 N_f\frac{d}{r} = (\rho_s - \rho)\,g\,\forall\sin\beta \quad \ldots\ldots\ldots\ldots\ldots\ldots\ldots \quad (19)$$

in which $\forall$, A = volume and projected surface area, respectively, of a sediment particle; and

$$N_f = \frac{n_f + 1}{n_f(n_f + 2)} \quad \ldots \ldots \ldots \ldots \ldots \ldots \ldots \ldots \ldots \ldots \ldots \ldots \quad (20)$$

Substituting Eq. 16 into Eq. 19, yields

$$\sin \beta = K \frac{d}{r} \quad \ldots \ldots \ldots \ldots \ldots \ldots \ldots \ldots \ldots \ldots \ldots \ldots \quad (21)$$

$$\text{in which} \quad K = \frac{3\alpha}{2} \theta \kappa^{-2} n_f^2 N_f \quad \ldots \ldots \ldots \ldots \ldots \ldots \ldots \ldots \quad (22)$$

in which α = ratio of projected surface area to volume for a sediment particle divided by that for a sphere.

By introducing Eq. 17 into Eq. 22, K can be expressed

$$K = \frac{3\alpha}{2} N_f \mathsf{F}_{Dc}^2 \quad \ldots \ldots \ldots \ldots \ldots \ldots \ldots \ldots \ldots \ldots \ldots \ldots \quad (23)$$

which is similar in form to Falcon's relation, Eq. 9. Thus, while Falcon's K-value is a function of the overall bed resistance and the size of the bed-load particles, the writer's K-value is a function of the flat-bed resistance and the size of the bed-surface particles.

Comparison of Predictive Capability

All the aforementioned models that relate the local transverse bed slope to mean flow characteristics predict the slope to be proportional to the ratio d/r:

$$\frac{d(d)}{dr} = K \frac{d}{r} \quad \ldots \ldots \ldots \ldots \ldots \ldots \ldots \ldots \ldots \ldots \ldots \ldots \quad (24)$$

The difference between the models is the factor of proportionality, K. Therefore, a comparison of their performance may be limited to a comparison of their capability of predicting the local slope, which may be taken at the center line of the cross section, in which $r = r_c$ and $d = d_c$. Eq. 24 is then expressed

$$\frac{S_T}{\left(\frac{d_c}{r_c}\right)} = K \quad \ldots \ldots \ldots \ldots \ldots \ldots \ldots \ldots \ldots \ldots \ldots \ldots \quad (25)$$

in which $S_T = d(d)/dr$ at the center line.

Comparison by Laboratory Data.—Initially, the performance of the models was tested by means of Zimmermann and Kennedy's (22) experimental results. Fig. 3 (*a*, *b*, *c*, *d*, and *e*) shows a comparison of measured and predicted slopes, the ordinate being the measured values of $S_T/(d_c/r_c)$, and the abscissa the values determined by the formula for K, using measured values of d, D, and $\bar{V}$.

Fig. 3(*a*) shows the performance of the van Bendegom model (19). The

agreement between measured slopes and slopes predicted by this model (calibrated by a factor of 3.55) is quite good at smaller values of S_T. Systematic deviation of the measured values of S_T from the predicted is seen to occur at the larger slopes.

As seen in Fig. 3(*b*), the correlation between observed slopes, and slopes predicted by Engelund's (8) model, is fairly small. Since the dynamic friction

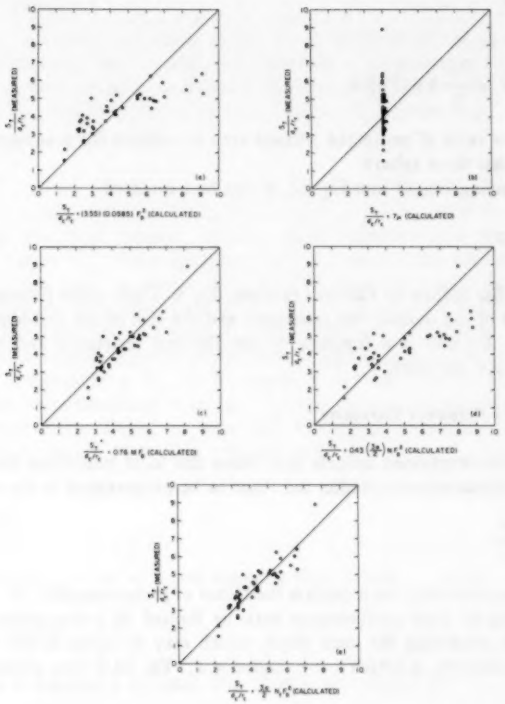

FIG. 3.—Comparison of Transverse Bed Slopes Measured by Zimmermann and Kennedy (22), with Slopes Computed by (*a*) van Bendegom's; (*b*) Engelund's; (*c*) Kikkawa, Ikeda, and Kitagawa's; (*d*) Zimmermann and Kennedy's or Falcon's; and (*e*) the Writer's Model

coefficient, μ, is more or less constant, Engelund's model almost always predicts the same value of $S_T/(d_c/r_c)$. The reason for the poor agreement may be that Engelund's model cannot be applied to Zimmermann and Kennedy's data. The flow in the test section was a fully developed bend flow, and Engelund's model was never validated (or intended) for such a flow. Engelund's model seems to perform very well for weakly meandering flows, in which the secondary

current is in its developing stage and probably influenced by residual currents from previous bends.

To apply Kikkawa, et al. (12) model, the function M (Table 1) must be evaluated at the center line of the channel. Using: (1) A value of one for the forced vortex distribution (which is the value to be expected at the center line); (2) $V_* / \bar{V} = \sqrt{f/8} = 1/(n\sqrt{8})$; and (3) a sheltering factor of 0.592, Kikkawa, et al., K-value is reduced to $F_D(1.628–0.912/n)$. The value of n for each experiment was determined experimentally by Zimmermann and Kennedy, using the side-wall correction procedure of Vanoni and Brooks (17). As seen in Fig. 3(*c*), the agreement between observed slopes and slopes predicted by Kikkawa, et al., (calibrated by a factor of 0.76) is very good. Fig. 3(*d*) compares the observed slopes and the slopes predicted by Zimmermann and Kennedy's/Falcon's model. The agreement is seen to be somewhat smaller than when Kikkawa, et al., model is applied.

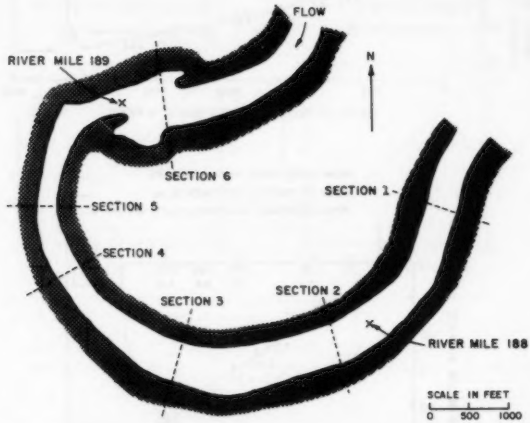

FIG. 4.—Schematic Plan View of Sacramento River Study Bend

To apply the author's model, n_f must be evaluated using Eq. 17. Since θ is a function of R_*, which, in turn, is a function of n_f (at least, at lower values of R_*), the value of n_f has to be determined by iteration. The value of R_* is found to be approximately four in Zimmermann and Kennedy's (22) Runs 1–1 through 3–12, and approximately nine in the remaining runs. According to Shields' curve, these values of R_* correspond to values of θ of 0.04 and 0.03, respectively. As shown in Fig. 3(*e*), the agreement between observed slopes and slopes predicted by the writer's model is good. The writer's model was applied without introduction of a calibration factor.

Comparison by Field Data.—The ultimate test of a model's predictive capability is against field data. A measurement program was carried out by the U.S. Geological Survey, Sacramento, on a bend of the Sacramento River between river miles 187.5 and 189.5. Fig. 4 shows a schematic plan view of the site.

Six cross sections of the bend were surveyed in April and May 1979, and March 1980 to define the channel geometry at two different times for two different flow rates. Also, detailed velocity measurements and bed-material samples were taken at each cross section to determine the variations in the velocity profiles and the size of the bed sediment. The direction and magnitude of the flow velocity were measured over 4–10 verticals across each section, using a Marsh-McBirney flow meter. In each vertical, the velocity, V, was measured at 1–2 ft depth intervals; the recording time was from 3–5 min at

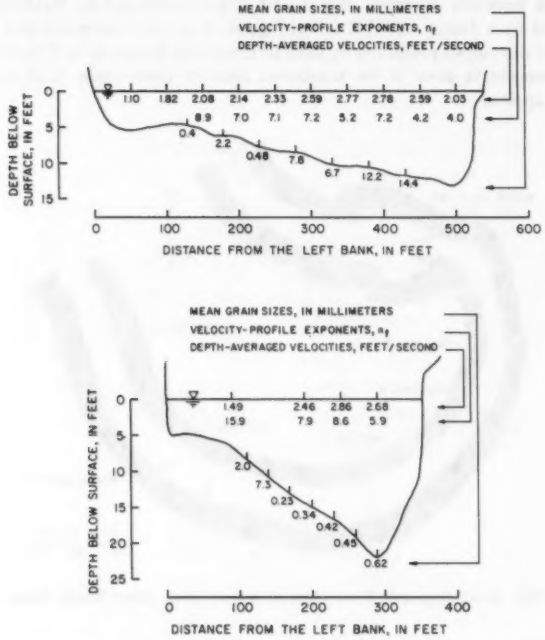
MEAN GRAIN SIZES, IN MILLIMETERS
VELOCITY-PROFILE EXPONENTS, n_f
DEPTH-AVERAGED VELOCITIES, FEET/SECOND
DEPTH BELOW SURFACE, IN FEET
1.10 1.82 2.08 2.14 2.33 2.59 2.77 2.78 2.59 2.03
8.9 7.0 7.1 7.2 5.2 7.2 4.2 4.0
0.4 2.2 0.48 7.8 6.7 12.2 14.4
0 5 10 15
0 100 200 300 400 500 600
DISTANCE FROM THE LEFT BANK, IN FEET
MEAN GRAIN SIZES, IN MILLIMETERS
VELOCITY-PROFILE EXPONENTS, n_f
DEPTH-AVERAGED VELOCITIES, FEET/SECOND
DEPTH BELOW SURFACE, IN FEET
1.49 2.46 2.86 2.68
15.9 7.9 8.6 5.9
2.0 7.3 0.23 0.34 0.42 0.45 0.62
0 5 10 15 20 25
0 100 200 300 400
DISTANCE FROM THE LEFT BANK, IN FEET

FIG. 5.—Cross Sections No. 3 and 4 of the Sacramento River Study Bend at Low Flow, 9,100 Cubic Feet per Second (260 Cubic Meters per Second)

each point of the vertical. Based on these measurements, a depth-averaged velocity, $\bar{V}$, was determined for each vertical. The cross-sectional average velocity, V_a, was determined by dividing the known (gaged) flow rate by the measured cross-sectional area. The bed samples were taken by a "Digging sampler" (USBM-54), which samples to a depth of 2–3 in. below the bed surface.

The n-values were determined on the basis of the longitudinal slope, S, of the water surface, using the Darcy-Weisbach formula modified by Falcon (9). The procedure for the determination of n may be seen in Falcon (9). The slope of the water surface was measured and found to be of the order of magnitude

of 0.0003. According to Brice (4), the average slope of the bed between river miles 190 and 185 is also approximately 0.0003. The n_f-values were determined by plotting, in log-log diagram, $V/\bar{V}$ versus y/d for each vertical, and measuring the slope of the best fitting line. The cross-sectional average value, n_{fa}, was determined as the arithmetic mean of the n_f-values in the cross section. The transverse bed slope was measured at the channel center line; however, the

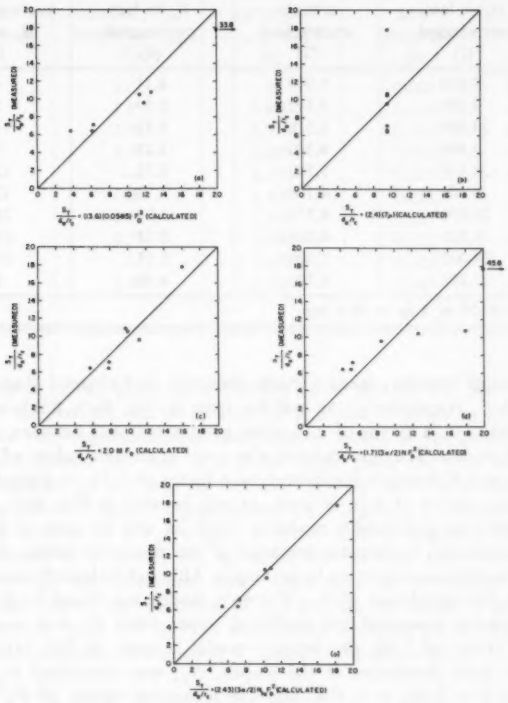

FIG. 6.—Comparison of Transverse Bed Slopes Measured in Sacramento River Bend with Slopes Computed by (*a*) van Bendegom's; (*b*) Engelund's; (*c*) Kikkawa, Ikeda, and Kitagawa's; (*d*) Zimmermann and Kennedy's or Falcon's; and (*e*) the Writer's Model

slope appeared to be practically constant across most sections. (A summary of the data and computational results is presented in Table 2. Fig. 5 shows Cross Sections No. 3 and 4 at low flow.)

Fig. 6 (*a*, *b*, *c*, *d*, and *e*) shows a comparison of measured and predicted slopes. The ordinate is the measured value of $S_T/(d_a/r_c)$, and the abscissa is the value calculated by the formula for K, using measured cross-sectional

TABLE 2.—Sacramento River

Section number (1)	Flow rate, in cubic feet per second (2)	Cross-sectional area, in square feet (3)	Cross-sectional average velocity, V_a, in feet per second (4)	Cross-sectional average depth, d_a, in feet (5)
1-L	7,800	1,900	4.11	4.4
2-L	8,300	3,190	2.60	5.6
2-H	24,900	6,510	3.82	11.1
3-L	9,900	4,340	2.28	8.1
3-H	28,400	7,580	3.75	12.5
4-L	9,100	4,290	2.12	12.2
4-H	24,900	6,370	3.91	23.1
5-L	9,100	4,000	2.28	15.2
5-H	24,000	7,600	3.15	19.7
6-H	26,800	6,700	4.00	8.6

Note: 1 ft = 0.305 m; 1 in. = 25.4 mm.

average-values of velocity, mean particle diameter, and channel slope; that is, V_a, D_{50}, and S, respectively. As will be seen in Fig. 6(*c*), Kikkawa, et al. model (calibrated by a factor of 2.0) gives good agreement between measured and predicted slopes. The agreement is also good at smaller values of S_T when Zimmermann and Kennedy's (calibrated by a factor of 5.1), or Falcon's model (calibrated by a factor of 1.7), is used, as will be seen in Fig. 6(*d*), or when van Bendegom's or Engelund's model is used, as will be seen in Figs. 6(*a*) and 6(*b*), respectively. Systematic deviation of the measured values of S_T from the predicted is seen to occur at the larger slopes. Although Falcon (9) recommends using D_{95} for the calculation of F_D, Falcon's model was found to give better agreement between measured and predicted slopes when D_{50} was used. Using a calibration factor of 2.43, the writer's model is seen, in Fig. 6(*e*), to give a surprisingly good prediction of the slopes. N_{fa} was calculated by Eqs. 20 and 17, using $\theta = 0.06$, $\kappa = 0.4$, and the measured values of F_D for F_{Dc}. The calibration factor (2.43) may reflect the difference between F_D and F_{Dc}, or the fact that κ and θ are not constant in movable bed channels, or both.

So far the comparison of the models has been made on the basis of their capability of predicting the transverse bed slope at the center line of the cross sections. Strictly, an evaluation of the models should also include a comparison of the complete solutions in the form recommended by the respective authors. Engelund (8), Kikkawa, Ikeda, and Kitagawa (12), and Falcon (9) recommend using their integrated solutions, while Zimmermann and Kennedy (22) and the writer recommend using constant slopes across the sections. However, it is easily verified that the trend seen in Fig. 6 remains unchanged whether integrated solutions or constant slopes are used with the present data. At small and moderate slopes, there is little difference between the predictions. In all models, the

Bend Flow Data

Mean particle diameter, D_{50}, in millimeters (6)	Particle Froude number, F_D, based on D_{50} (7)	Radius of curvature r_c, in feet (8)	Transverse bed slope, S_T (9)	Cross-Sectional Average Velocity Profile Exponents	
				n (10)	n_{fa} (11)
21.5	2.12	∞	0.000	7.0	5.8
4.9	2.81	3,920	0.010	4.0	6.3
10.8	2.78	3,920	0.018	4.1	6.2
6.3	2.17	2,640	0.020	2.9	6.4
—	—	2,640	0.018	3.8	5.8
1.6	4.00	1,800	0.073	2.2	9.6
6.1	3.78	1,800	0.135	2.9	9.4
0.7	6.51	1,800	0.150	2.3	10.5
—	—	1,800	0.145	2.6	12.5
6.1	3.87	2,000	0.041	4.9	8.9

key parameter is the grain size, whether it be that of the bed load or that of the bed surface. As will be seen in Table 2, the variation of D_{50} throughout the bend is very significant. No technique or model is yet available that can simulate a variation like that in a given bend, given the flow data. Instead, a rough estimate of D_{50} may be obtained on the basis of a combination of a Manning-Strickler type of equation and Eq. 17, giving a relationship between the Froude number, $F = V_a/\sqrt{gd_a}$, and the relative roughness, D_{50}/d_a. Fig. 7 shows a plot of F versus D_{50}/d_a based on the data from the Sacramento River. Although the theoretical curve approximating the points cannot be a straight line, due to the variation of n_{fa} through the bend, it is seen that a straight line of slope 3.5 may be sufficiently accurate for a rough, tentative estimate of D_{50}, given the values of V_a and d_a. The line is given by the equation

$$D_{50} = 0.76\, d_a\, F^{3.5} \quad \ldots\ldots\ldots\

F_{Dc} are functions of mean velocity and grain size, both of which vary in a yet unknown manner across the channel sections. However, the field data indicate that a reasonable first approximation may be obtained by considering sin β to be constant across a section. In that case, the transverse depth variation may be described by the equation

$$\frac{d}{d_c} = 1 + K\left(\frac{r}{r_c} - 1\right) \quad \ldots\ldots\ldots\ldots\ldots\ldots\ldots\ldots\ldots\ldots\ldots\ldots \quad (27)$$

Assuming that: (1) The local mean flow velocity is determined by the Darcy-Weisbach equation, $\bar{V} = n_f\sqrt{8gSd}$; (2) n_f is constant, which appears to be a reason-

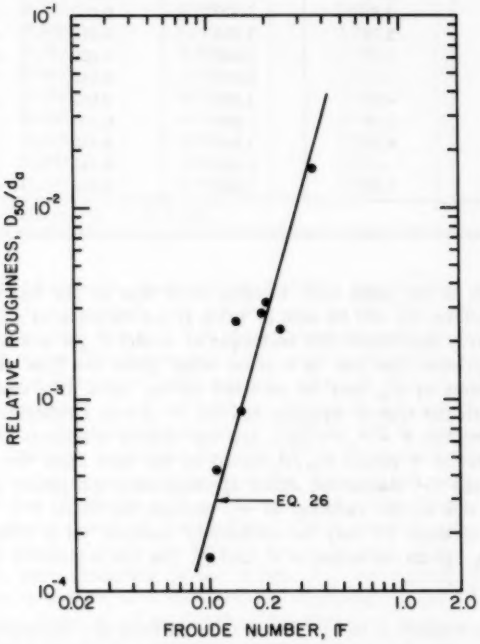

FIG. 7.—Relative Roughness as Function of Froude Number for Sacramento River Study Bend

able approximation over the central section of the channel where bank effects are small; and (3) the local longitudianl slope varies as $S = S_c r_c/r$, in which S_c = local longitudinal slope at the center line of the channel, the variation of mean velocity over the central channel section may be estimated by

$$\frac{\bar{V}}{\bar{V}_c} = \sqrt{\left(\frac{d}{d_c}\right)\left(\frac{r_c}{r}\right)} \quad \ldots\ldots\ldots\ldots\ldots\ldots\ldots\ldots\ldots\ldots\ldots\ldots \quad (28)$$

in which (d/d_c) may be estimated by Eq. 27; and $\bar{V}_c$ = the mean flow velocity at the channel center line.

Summary and Conclusions

The study has: (1) Reviewed existing models for the prediction of the steady-state transverse bed profile in channel bends; (2) formulated an alternative model, and (3) compared the models, analytically and by laboratory and field data.

Existing models are all based on the equations of motion for the sediment particles in the bed load. The writer's model is based on the assumption that the bed topography is determined by the critical conditions for sediment entrainment. All models that relate the local transverse bed slope to mean flow characteristics, which includes the writer's model, are alike in the sense that they all predict the local transverse slope to be proportional to the ratio between depth, d, and radius of curvature, r. The difference between the models is the factor of proportionality, K.

Engelund's model predicts K to be essentially constant throughout the channel bend. In van Bendegom's model, K is a function of the bed-load particle Froude number, F_D. The models by Kikkawa, et al., Zimmermann and Kennedy, and Falcon, predict K to be a function of both the velocity-profile exponent n (corresponding to the Darcy-Weisbach friction factor f), and F_D. While, Kikkawa, et al. model predicts K to be linearly dependent on F_D, Zimmermann and Kennedy and Falcon's models predict K to vary with F_D to the second power. In the writer's model, K depends on only the flat-bed velocity-profile exponent, n_f (corresponding to the flat-bed friction factor f_f). Since, according to the writer's theory, n_f is proportional to the bed-surface particle Froude number, F_{Dc}, at fully developed turbulent flow, the writer's K-value may be expressed exclusively in terms of F_{Dc}, thereby reducing the problem of predicting the transverse bed slope to, essentially, one of predicting the overall grain size distribution of the bed surface, given the flow rate. The writer's K-value is largely proportional to F_{Dc}.

Using proper calibration factors, all the models give reasonable agreement between measured and predicted slopes at smaller transverse slopes. Systematic deviation of measured slopes from the predicted occurs at larger slopes, except when the models by Kikkawa, et al. (12), and the writer, are used.

The study has shown that the key parameter in all available models is grain size. The prediction of the complete bed topography of a given bend for given flow data requires knowledge of the spatial variation of the grain size. Unfortunately, no technique or model is yet available that can simulate this variation in a given bend, given the flow data.

Acknowledgment

Support for this study was provided by the U.S. Army Corps of Engineers' Sacramento District, California, under Contract No. DACW05-80-C-0083.

Appendix I.—References

1. Allen, J. R. L., "A Quantitative Model of Grain Size and Sedimentary Structures

in Lateral Deposits," *Journal of Geology*, Vol. 7, 1970, pp. 129–146.
2. Allen, J. R. L., "L. Van Bendegom: A Neglected Innovator in Meander Studies," *Fluvial Sedimentology*, A. D. Miall, ed., Memoir No. 5, Canadian Society of Petroleum Geologists, Calgary, Aug., 1978.
3. Bagnold, R. A., "Experiments on a Gravity-Free Dispersion of Large Solid Spheres in a Newtonian Liquid under Shear," *Proceedings of the Royal Society of London*, London, England, Vol. A225, 1954, pp. 46–63.
4. Brice, J., "Lateral Migration of the Middle Sacramento River, California," *Water-Resources Investigations 77-43*, U.S. Geological Survey, United States Department of the Interior, July, 1977.
5. Bridge, J. S., "Bed Topography and Grain Size in Open Channel Bends," *Sedimentology*, Vol. 23, 1976, pp. 407–414.
6. Chepil, W. S., "Equilibrium of Soil Grains at the Threshold of Movement by Wind," *Proceedings, Soil Science Society of America*, Vol. 23, Madison, Wisc., 1959, pp. 422–428.
7. El-Khudairy, M., "Stable Bed Profiles in Continuous Bends," thesis presented to the University of California, at Berkeley, Calif., in 1970, in partial fulfillment of the requirements for the degree of Doctor of Philosophy.
8. Engelund, F., "Flow and Bed Topography in Channel Bends," *Journal of the Hydraulics Division*, ASCE, Vol. 100, No. HY11, Proc. Paper 10963, Nov., 1974, pp. 1631–1648.
9. Falcon, M. A., "Analysis of Flow in Alluvial Channel Bends," thesis presented to The University of Iowa, Iowa City, Iowa, in 1979, in partial fulfillment of the requirements for the degree of Doctor of Philosophy.
10. Gottlieb, L., "Three-Dimensional Flow Pattern and Bed Topography in Meandering Channels," *Series Paper 11*, Institute of Hydrodynamics and Hydraulic Engineering, Technical University of Denmark, Feb., 1976.
11. Ikeda, S., "On Secondary Flow and Dynamic Equilibrium of Transverse Bed Profile in Alluvial Curved Open Channel," *Proceedings of the Japanese Society of Civil Engineers*, No. 229, 1974, pp. 55–65.
12. Kikkawa, H., Ikeda, S., and Kitagawa, A., "Flow and Bed Topography in Curved Open Channels," *Journal of the Hydraulics Division*, ASCE, Vol. 102, No. HY9, Proc. Paper 12416, Sept., 1976, pp. 1327–1342.
13. NEDECO (Netherlands Engineering Consultants), *River Studies and Recommendations on Improvement of Niger and Benue*, North-Holland Publ. Co., Amsterdam, 1959.
14. Raudkivi, A. J., *Loose Boundary Hydraulics*, Pergamon Press, Inc., New York, N.Y., 1976.
15. Rouse, H., "An Analysis of Sediment Transportation in the Light of Fluid Turbulence," *Report No. SCS-TP-25*, Soil Conservation Service, United States Department of Agriculture, Washington, D.C., 1939.
16. Rozovskii, L. L., "Flow of Water in Bends of Open Channels," Israel Program for Scientific Translations, Jerusalem, Israel, 1961 (available from Office of Technical Services, U.S. Department of Commerce, Washington, D.C., PST Catalog No. 363; OTS 60-51133).
17. "Sedimentation Engineering," *Manual and Report on Engineering Practice No. 54*, V. A. Vanoni, ed., ASCE, 1976.
18. Shields, A., "Anvendung der Aenlichkeitsmechanik und der Turbulenz-forschung auf die Geschiebebewegung," *Mitteilungen der Preussischen Versuchsanstalt fur Wasserbau und Schiffbau*, Berlin, Germany, translated into English by W. P. Ott and J. C. van Uchelen, California Institute of Technology, Pasadena, Calif., 1936.
19. Van Bendegom, L., "Eenige beschouwingen over riviermorphologie en rivierverbetering," *De Ingenieur*, Vol. 59, No. 4, 1947, pp. 1–11.
20. White, C. M. "The Equilibrium of Grains on the Bed of a Stream," *Proceedings of the Royal Society*, London, England, Series A, No. 958, Vol. 174, Feb., 1940, pp. 322–338.
21. Yen, C. L., "Bed Configuration and Characteristics of Subcritical Flow in a Meandering Channel," thesis presented to The University of Iowa, at Iowa City, Iowa, in 1967, in partial fulfillment of the requirements for the degree of Doctor of Philosophy.
22. Zimmermann, C., and Kennedy, J. F., "Transverse Bed Slopes in Curved Alluvial Streams," *Journal of the Hydraulics Division*, ASCE, Vol. 104, No. HY1, Jan., 1978, pp. 33–48.

APPENDIX II.—NOTATION

The following symbols are used in this paper:

A = projected surface area of sediment particle;
a_1, a_2 = distances;
C = Chezy's coefficient;
c = constant;
c_1 = lift force coefficient;
c_2 = constant;
c_D = drag coefficient;
D = particle diameter;
D_{50} = mean sediment diameter;
d = flow depth;
d_c = flow depth at channel center line;
F = Froude number = $V/\sqrt{gd}$;
F_D = particle Froude number = $V/\{[(\rho_s-\rho)/\rho]gD\}^{1/2}$;
F_d = longitudinal drag component;
F_ℓ = lift force;
F_r = radial drag component;
f = friction factor;
f_f = flat-bed friction factor;
f_v = forced vortex distribution;
g = acceleration of gravity;
K = ratio of transverse slope to d/r;
M, N, N_f = functions of friction factors;
n, n_f = velocity-profile exponents;
p = pressure;
R_* = boundary Reynolds number = $V_* D/\nu$;
r = radius of curvature; radial coordinate;
r_c = mean channel radius;
S = longitudinal channel slope;
V = flow velocity;
V_* = shear velocity = $\sqrt{\tau_o/\rho}$;
$\bar{V}$ = depth-averaged flow velocity;
$\forall$ = particle volume;
W_s = particle submerged weight;
y = vertical distance;
α = projected area-volume ratio for particle normalized by that for sphere;
β = transverse inclination;
δ = deviation angle;
θ = Shields' parameter = $\tau_c/[(\rho_s-\rho)g\,D_c]$;
μ = dynamic friction coefficient;
ν = kinematic viscosity;
ρ = fluid density;
ρ_s = particle density;
τ = shear stress;

ϕ = angle of repose of submerged sediment; and
Φ = friction angle.

Subscripts

a = cross-sectional average;
c = critical; center line;
f = related to Darcy-Weisbach's flat-bed friction factor;
o = bottom;
r = radial direction; and
s = sediment.

SHEAR STRESS DISTRIBUTION AT CHANNEL CONSTRICTIONS

By Bishnu P. Das,[1] M. ASCE and Ronald D. Townsend[2]

INTRODUCTION

A channel constriction results in contracting and expanding flow through the gap. The flow is predominantly curvilinear, accelerating and decelerating while negotiating the constriction. An analysis of such a flow is incomplete without reference to the flow through a bend where the general pattern is strikingly similar.

Flow Through Bends.—For uniform rectilinear flow in a prismatic channel, the boundary shear stress distribution has been studied in the laboratory. Both the longstream isovels and the shear exhibit a symmetrical uniform pattern. If the flow negotiates a bend, generation of secondary currents before entry to the bend create asymmetry both for the velocity and shear distribution. Numerous researchers (7,15,16,18) have studied the flow through a single bend for channels having both rectangular and trapezoidal-shape cross sections. They have observed specific locations, such as close to the inner bank at entry and outer bank at exit to monitor maximum bed shear stress. The locus of the maximum shear filament shifts from the inner bank at entry to the outer bank at exit, more or less following the locus of the maximum velocity filament through the bend. It is postulated that the secondary flow generated by the stream curvature produces the distorted shear pattern.

Nouh and Townsend (15) have advanced the study by developing for a specific bend geometry, nondimensional contours of shear maxima treating the uniform shear stress in the straight reach, upstream of the bend, as the reference value.

Erosion of the outer bank is generally considered to be a consequence of the high shear stress occurring there. Yet, although the inner bank at entry experiences high shear, deposition occurs forming a point bar. This is explained by Yen (19) as follows: ". . . that deposition and scour are not directly related to the magnitude of the bed shear. Rather the secondary flow directed inward near the bottom which carries the sediment particles from the outer side of a bend to the inner side of the following bend determines the bed topography."

[1]Superintending Engr., (Civ.) Dept. of Irrigation, Orissa, India.
[2]Prof., Dept. of Civ. Engrg., Univ. of Ottawa, Ottawa, Ontario, Canada.

Note.—Discussion open until May 1, 1982. To extend the closing date one month, a written request must be filed with the Manager of Technical and Professional Publications, ASCE. Manuscript was submitted for review for possible publication on September 26, 1980. This paper is part of the Journal of the Hydraulics Division, Proceedings of the American Society of Civil Engineers, ©ASCE, Vol. 107, No. HY12, December, 1981. ISSN 0044-796X/81/0012-1695/$01.00.

Flow Through Constrictions.—Although laboratory studies on maximum depth of scour at long contractions (9,11), and abrupt contractions (10,12,13) in alluvial channels, have been conducted extensively, actual measurement of shear stress along the constriction boundary and downstream has not been reported. The analytical derivation of maximum scour depth, however, has been made by reference to the shear stress concept.

Closure of alluvial channels is often done by end dumping loose fill from one or both banks. Such closures, which result in an abrupt constriction, are

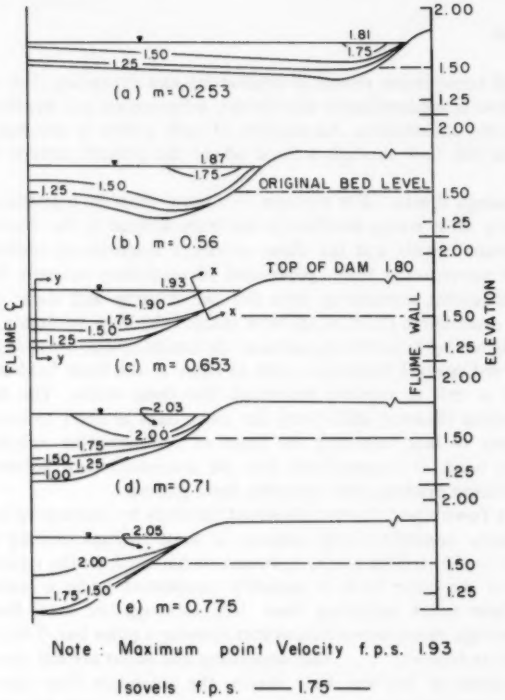

FIG. 1.—Velocity Distribution Variation with Contraction

of frequent necessity for siting a hydraulic structure. A bridge on an alluvial river is generally provided with a constricted waterway keeping the well-defined bankful stage within the bridge vents, and closing the overbank flow by the embankment approaches. Even in deep valleys, abutments frequently protrude into the main stream causing partial constriction of the deep channel. Often cofferdams built with loose fill are pushed into a stream from one bank to encircle a work area which can obstruct up to 20–30% of the waterway. Studies by Lane (11), Kindsvater and Carter (10), Valentine (18), Izbash and Lebdev

(8), Liu, Chang and Skinner (13), Komura (9), Laursen (12), and Neill (14) have been directed mostly towards derivation of the backwater rise and scour depth at contractions. Studies of scour at spur dikes, which are abrupt constrictions, have been made by Awazu (1), Garde et al. (5), and Gill (6). Although these studies did not report boundary shear measurements, Das (2,3,4) has experimentally studied and analyzed for end-dump constrictions the stability of closure material forming the body of the dam, and the associated depth of maximum scour downstream, by relating them to the maximum shear consequent to that imposed constriction.

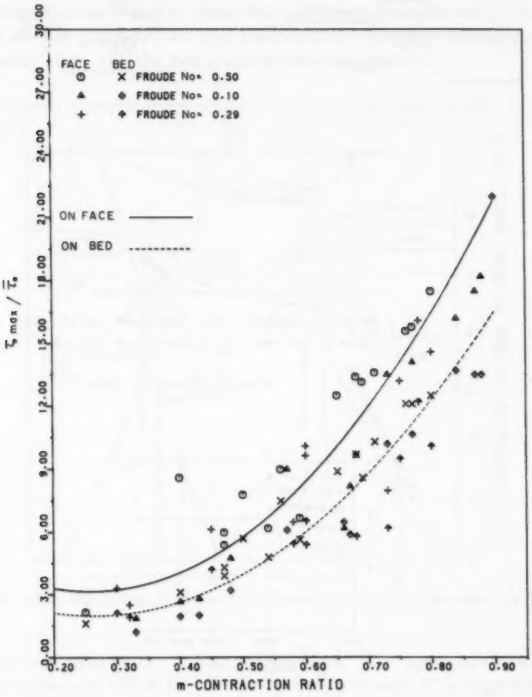

FIG. 2.—Shear Stress Computation from Velocity Profiles

This University of Alberta study (3) also examined flow characteristics and related boundary shear stress distributuions on both the advancing face of an end-dump constriction and on the channel bed in the vicinity of the constriction. Sample velocity and boundary shear stress distributions from the study are presented herein (Figs. 1, 2, and 4).

To examine further the applicability of such laboratory studies to field problems, a similar investigation was performed at the University of Ottawa's laboratory.

This particular study was concerned with the redistribution of boundary shear stress in a channel formed in sand, and having a cross section consisting of a deep central section flanked by relatively shallow berms. The redistribution of shear stress occurs as a result of flow on the berms suddenly being channelled towards the deep central section by abrupt lateral constrictions extending partway across the berms.

Fig. 5 shows the basic shape of the cross section and also presents scour patterns relating to two flow stages, and three different contraction ratios

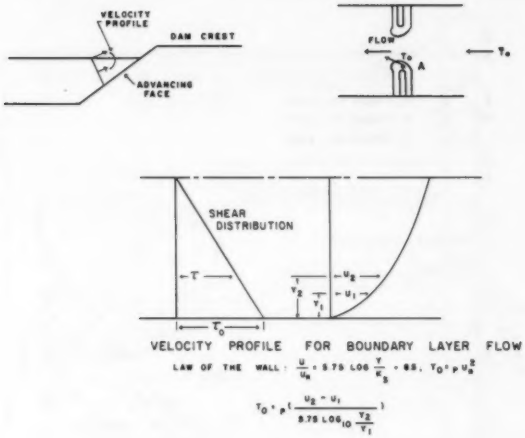

FIG. 3.—Variation of Nondimensional Shear Maxima with Contraction Ratio

examined in the study. A more detailed discussion of these tests is contained elsewhere in the paper.

Analytical Considerations

A uniform flow implies constant energy expenditure in the direction of the flow and, accordingly, the uniform shear stress on the bed $\bar{\tau}_o$ is given as

$$\bar{\tau}_o = \gamma h s \quad \ldots \ldots \ldots

in which γ = unit weight of water; h = uniform flow depth; and s = slope assumed as the same for bed and water surface.

Introduction of a constriction will result in the flow contracting sharply through the gap. The flow against the constriction face will be curvilinear and will accelerate up to the *vena contracta*. It would then decelerate, the live stream expanding beyond the *vena contracta* to diffuse gradually into the full downstream width of the channel (Fig. 6).

In Fig. 6, a channel of width B is constricted by end dumping to an average width b, and the flow further contracts to a width b_c at the vena contracta. The contraction ratio m is defined as $(B - b)/B$.

It is obvious that the boundary shear through the constriction would be modified depending on the geometry of the constriction, the flow characteristics, the fluid characteristics, and the bed material characteristics.

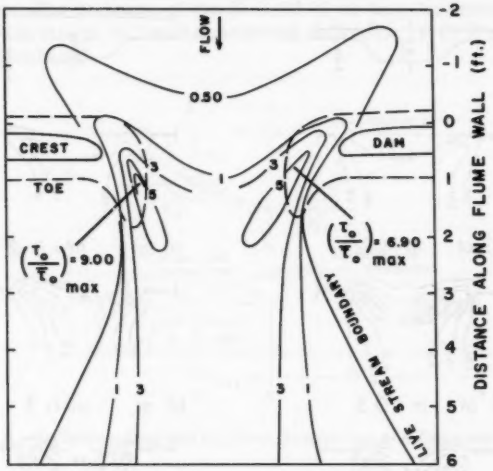

FIG. 4.—Nondimensional Shear Distribution ($\tau_o/\bar{\tau}_o$) in Constriction Region

The following parameters define the problem: B = approach channel mean width; b = mean gap width for end-dump constrictions; V = approach channel mean velocity; h = approach channel mean depth; ρ_w = specific gravity of water; g = acceleration due to gravity; ν = kinematic viscosity; d = median size of bed material; σ_{gd} = geometric standard deviation of the bed material; ρ_s = specific gravity of bed material; and $\tau_{max f}$, $\tau_{max b}$ = maximum local shear against the advancing face and downstream bed.

As the flow against the closure material will be fully turbulent, kinematic viscosity ν is considered unimportant. Similarly, ρ_s and ρ_w, being constants for noncohesive sediment and water, are ignored in the analysis.

Dimensional analysis indicates that the nondimensional increase in shear stress will be given by

$$\frac{\tau_{max}}{\bar{\tau}_o} = fn\left(\frac{B-b}{B}, \frac{V}{\sqrt{gh}}, \frac{d}{h}, \frac{B}{h}\right) \quad \ldots\ldots\ldots\ldots\ldots\ldots\ldots\ldots\ldots\ldots (2)$$

The principal nondimensional terms are considered to be m, the contraction ratio, and $V/\sqrt{gh}$, the Froude number of the approach flow. The terms d/h and B/h are not significant as determined from the experimental findings. Observations by Ippen and Drinker (7), and Replogle and Chow (17) also attest to this.

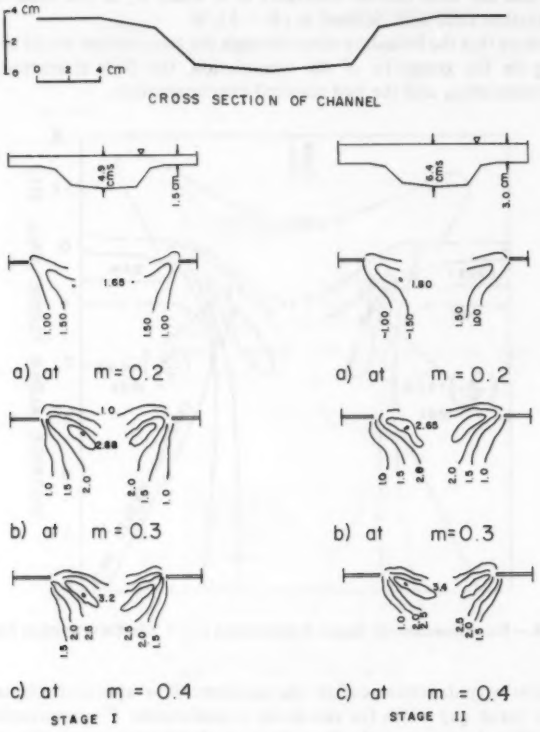

FIG. 5.—Nondimensional Shear Distribution for Overbank Channel Constrictions

Awazu (1) studied scour around spurdikes and concluded that with an increase in the contraction ratio, τ_{max} increases exponentially and the nondimensional shear maxima is related to m in the form

$$\frac{\tau_{max}}{\bar{\tau}_o} = 10^{j_1 m} + j_2 \quad \ldots\ldots\ldots\ldots\ldots\ldots\ldots\ldots\ldots\ldots\ldots\ldots (3)$$

in which j_1 and j_2 = coefficients primarily dependent on F.

In view of the aforementioned limitations of past laboratory investigations in this area, it was decided to proceed with a laboratory study in which actual boundary shear stress distributions in a model channel constriction were determined from velocity measurements. The study used Froude numbers and contraction ratios in the range 0.10–0.50 and 0.10–0.90, respectively.

Experimental Setup

Flume, Material in Bed and Closure Dam.—Experiments were carried out in a flume 60 ft (18.3 m) long, 7.5 ft (2.3 m) wide by 4 ft (1.2 m) deep with a horizontal bottom resting on the laboratory floor. Of the 4 ft (1.2 m) depth available in the flume, the bottom 1.5 ft (0.46 m) filled with the bed material over a 50 ft (15.25 m) length. A head tank, an upstream stilling pool, and a drop box downstream of the tailgate occupied the remaining 10 ft (3.05 m) length of flume. The beginning of the 50 ft (15.25 m) long "sediment" section was designated as station "0," with downstream stations (at 1 ft (0.31 m) spacing) numbered sequentially.

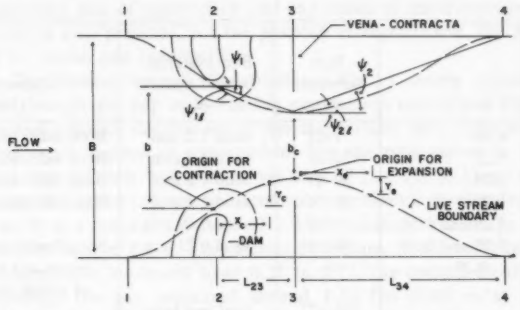

FIG. 6.—Definition Diagram for Flow Contraction and Expansion

A 30 ft (9.2 m) stretch from Station 13–43, where uniform water surface slope could be obtained, was selected as the test reach. End-dump dams with three sizes of pebbles of D_{75} equal to 6.60 mm, 18.00 mm, and 25 mm were built symmetrically into the flow at Station 24. Three sizes of sand of 1.20 mm, 0.60 mm, and 0.25 mm median diameter were used as representative bed material for alluvial channels.

Channel flows ranging up to 3 cfs (0.085 m^3/s) maximum were provided by two centrifugal pumps.

Measuring Devices.—The principal recording instruments comprised the following:

1. A point gage for measuring the water surface elevation and the static bed elevation.
2. An electronically-sensed propeller meter for velocity measurement. The propeller meter was mounted on a special swivel so that continuous velocity

traverses could be taken at any inclination (in particular, the normal to the curved advancing face). The propeller meter was connected to an autograph recorder which permitted measurements of velocity to the nearest 0.01 fps (03 mm/sec).

3. An electronic bed probe (working on the optical principle) was connected to an autograph recorder to measure bed elevations to the nearest 0.001 ft (0.3 mm) as scour progressed.

All the equipment was mounted on an instrument carriage that moved on rails located on the side of the flume.

Test Series and Flow Parameters.—Since the Froude number of flows in mild-sloping natural channels rarely exceeds 0.5, even during flood conditions, the experimental program was conducted using 0.1, 0.29, and 0.5 as the principal test Froude numbers. For each Froude number a basic series of runs were carried out. For each run, the boundary shear maxima and pattern were obtained

TABLE 1.—Outline of Experimental Program

Series identification (1)	F (2)	Run numbers (3)	Bed material, in millimeters (4)	Remarks (5)
A and *B*	0.50	1–21	sand 1.2 mm	Both side closure
C	0.29	24–38	sand 1.2 mm	Both side closure
D	0.29	39–49	sand 1.2 mm	Both side closure
E–H	0.29	50–74	sand 1.2 mm	One side closure
J–L	0.29 and 0.50	75–89	sand 0.60 mm	
M–R	0.50 and 0.50, 0.29	90–105	sand 0.25 mm	Specifically for bed scour and verification of actual closures
S–T	—	106–127	coal and large pebbles	

from velocity measurements. The outline of the experimental program is presented in Table 1.

Procedure.—Equilibrium and steady flow conditions were produced by fine adjustment of the tailgate control. Closure material dumping from both sides symmetrically, or one side, was arbitrarily stopped to correspond to a particular contraction ratio. The water surface profiles, the live stream boundary and velocity profiles, normal to the boundary, were then recorded starting at the section of maximum backwater upstream, and ending where the flow widened more or less uniformly to the parent channel width. The readings were taken fairly close in plan to the end-dump face and at 1 ft (0.3 m) intervals elsewhere. The bed profiles were recorded by the "optical" probe at suitable intervals so as to complete the bed configuration upon which the water surface configuration and velocity pattern could be superimposed. This correlated data provided a detailed description of the flow field.

PRESENTATION AND ANALYSIS OF DATA

Table 2, in which experimental data obtained for test series *B*, *C*, and *D* are utilized, presents the measured variables pertinent to flow description and boundary shear.

Flow Characteristics

Contraction and Expansion of Live Stream Boundary.—The large-scale flow pattern was visualized by dye injection and also by dusting confetti on the water surface. The local angle of expansion, $\psi_{2'}$, is smaller than the local angle of contraction, $\psi_{1'}$, at the vena contracta (Fig. 6). In a rectangular constriction the contracting stream maintains a more or less vertical edge. For the end-dump constriction, the contracting stream edge is more or less vertical immediately upstream and downstream of the dam, but hugs to the end-dump face in between. It is therefore obvious that the geometry of the constriction has a decisive influence on the coefficient of contraction, as well as the flow pattern. The coefficient of contraction C_c, which is the ratio of b_c to b, was found to vary in the range 0.9–0.6, for the contraction ratio in the range 0.1–0.8. A nondimensional plot of contraction and expansion of the livestream is shown in Fig. 7, which also presents, for the purpose of comparison, the relationship developed by Isbash and Lebdev (8).

Velocity Distribution through Constriction.—Fig. 1 shows typical velocity distribution through the gap at increasing contraction ratios, and Fig. 8 shows the longitudinal velocity distribution at one contraction ratio. This latter pattern was evident at all degrees of constriction. For the runs shown in Fig. 1, the unrestricted channel flow had a mean velocity of 1.15 fps (0.35 m/s), whereas the flow negotiating the constriction attained a maximum point velocity of 1.81 fps (0.55 m/s) at a contraction ratio of 0.25, increasing to 2.05 fps (0.63 m/s) at a contraction ratio of 0.775. The interesting feature, however, is that although the contraction ratio increased from 0.25 to 0.77, the overall mean horizontal velocity through the gap remained around 1.50 fps (0.46 m/s) because of considerable local bed scour (Fig. 1). This phenomenon of mean longstream velocity in the "gap" region remaining more or less constant is, to a large extent, supported by field measurements of flow through bends, where a stream changes from a predominantly trapezoidal shape to a triangular shape while negotiating the bend (16).

The maximum velocity filament hugged to the livestream boundary, although the velocity decreased with time along with the progression of bed scour. It is pertinent to mention that neither the mean velocity through the gap nor the maximum velocity (against the face or at vena contracta before the beginning of scour) had satisfactory correlation with either the stability of the closure material or the maximum scour depth that occurred downstream.

Boundary Shear Distribution

On Advancing Face.—The contracting flow accelerating between Sections 1 and 3 (Fig. 6) was a case of boundary layer flow under an exceedingly favorable pressure gradient. The shear stress on the boundary was, therefore, determined using the Karman-Prandtl velocity distribution relationship for fully turbulent flow over a rough bed, namely:

TABLE 2.—Basic Experimental Data

Run number (1)	b Mean gap width, in feet (2)	V_{max} Maximum velocity through gap, in feet per second (3)	b_c Flow width at vena contracta, in feet (4)	L_{23} Length of contraction, in feet (5)	L_{34} Length of expansion in feet (6)	$\tau_{o\,max}/\bar{\tau}_o$ on face (7)	on bed (8)	m Contraction ratio (computed) (9)
(*a*) Series *B*, Q = 1.56 cfs, B = 7.5 ft, h = 0.18 ft, V = 1.15 fps, F = 0.50								
7	4.0	1.90	3.80	0.90	3.50	6.00	4.30	0.47
8	3.80	1.95	2.50	1.50	5.00	7.80	5.70	0.50
9	3.40	2.00	2.60	1.70	4.20	6.20	4.80	0.54
10	2.40	2.06	1.90	2.00	6.00	13.40	9.70	0.68
11	5.65	1.80	5.50	0.80	3.00	2.15	1.60	0.25
12	4.00	1.85	3.70	1.00	3.50	5.40	3.90	0.47
13	3.30	1.95	3.20	0.50	3.60	9.00	7.50	0.50
14	2.60	1.97	2.10	1.00	4.10	12.50	8.90	0.65
15	2.20	2.07	1.60	1.40	4.80	13.60	10.30	0.71
16	1.70	2.30	1.30	1.80	5.30	15.80	12.10	0.77
17	4.50	1.90	4.20	0.80	2.80	8.60	3.10	0.40
18	3.10	1.90	2.50	0.90	3.90	6.70	5.65	0.59
19	2.30	1.95	1.55	1.10	4.60	13.15	8.60	0.69
20	1.80	2.23	1.20	1.80	4.70	15.60	12.10	0.76
21	1.50	2.43	1.00	1.80	5.70	17.50	12.50	0.80
(*b*) Series *C*, Q = 1.00 cfs, B = 7.5 ft, h = 0.38 ft, V = 0.35 fps, F = 0.10								
24	4.30	0.80	3.80	1.00	5.00	2.80	2.00	0.43
25	2.56	1.27	2.20	0.90	6.00	6.20	6.50	0.66
26	2.03	1.40	2.00	2.30	5.00	13.50	10.20	0.73
27	5.05	0.63	4.00	1.10	5.00	1.85	1.20	0.33
28	3.90	0.86	3.00	1.50	5.00	4.75	3.20	0.48
29	2.45	1.40	2.00	1.70	5.20	8.20	5.90	0.67
30	1.20	2.07	0.90	2.10	7.00	16.20	13.70	0.84
31	0.95	2.20	0.85	2.20	—	17.50	13.50	0.87
32	4.50	0.73	3.80	1.10	6.00	2.65	1.95	0.40
33	3.20	1.04	2.40	1.10	6.00	9.00	6.10	0.57
34	1.70	1.53	1.50	1.40	7.00	14.10	10.65	0.77
35	0.90	2.17	0.88	1.50	6.50	18.20	13.50	0.88
36	0.75	2.27	0.70	—	—	30.00	22.00	0.90
37	0.60	2.63	0.60	—	10.00	—	—	0.92
(*c*) Series D_1, Q = 1.70 cfs, B = 7.5 ft, h = 0.26 ft, V = 0.87 fps, F = 0.29								
39	5.25	1.40	4.60	1.00	5.50	3.30	2.10	0.30
40	4.15	1.47	3.60	1.00	6.00	6.15	4.20	0.45
41	3.00	1.87	2.30	1.00	8.00	10.10	6.55	0.60
42	2.35	1.80	1.50	1.30	7.50	9.70	5.80	0.68
(*d*) Series D_2, Q = 1.70 cfs, B = 7.5 ft, h = 0.26 ft, V = 0.87 fps, F = 0.29								
43	5.10	1.53	4.50	1.00	5.00	2.50	1.90	0.32

TABLE 2.—*Continued*

(1)	(2)	(3)	(4)	(5)	(6)	(7)	(8)	(9)
44	3.15	1.90	2.10	1.30	6.20	6.50	5.45	0.58
45	2.05	2.10	1.10	1.60	6.50	8.00	6.20	0.73
46	1.60	2.00	0.90	1.70	6.80	14.60	10.10	0.80
47	3.00	1.63	2.30	1.10	6.50	9.65	5.40	0.60
48	1.90	1.78	1.10	1.60	8.00	13.20	9.50	0.75
49	1.60	2.23	0.80	2.00	7.60	16.10	12.20	0.78

Note: 1 ft = 0.305 m.

$$\frac{u}{u_*} = 5.75 \log \frac{y}{K_s} + 8.5 \quad \ldots \ldots \ldots

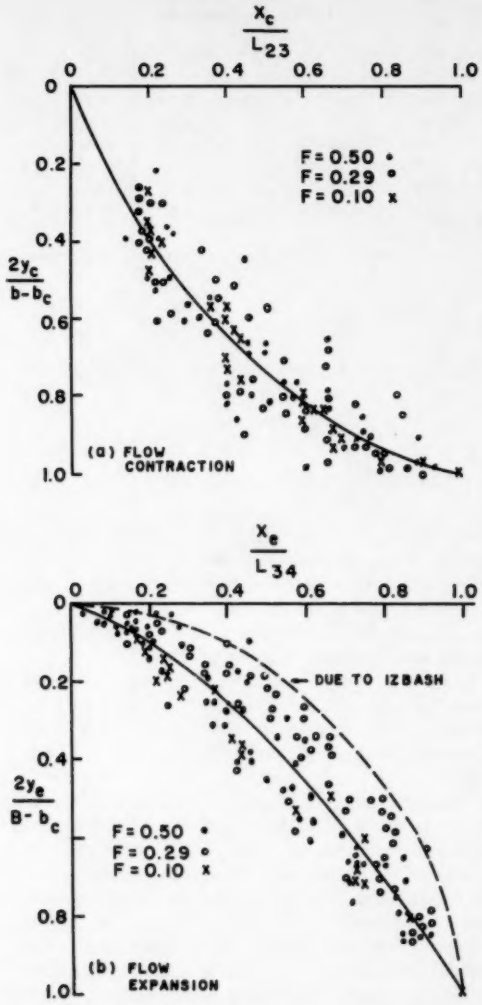

FIG. 7.—Nondimensional Profiles of Livestream Boundary

which an exponential relationship is seen. As will be noted from Table 2, although the maximum velocity against face was less than double the mean velocity, the shear increase exceeded 15 times the normal at contraction ratios exceeding 0.75.

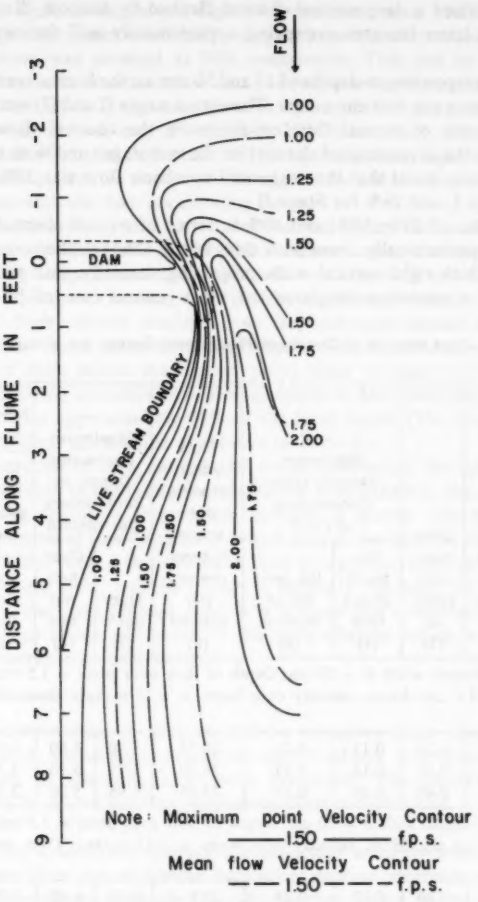

FIG. 8.—Typical Longitudinal Velocity Distribution

University of Ottawa Study

As mentioned earlier the preceding sections refer to a major study conducted at the University of Alberta (3). A second study, employing a 4 m long physical model of a typical river channel, recently was completed by the senior writer at the University of Ottawa.

The model channel in this recent study was moulded in a 10 cm thick sand bed (d_{50} = 0.7 mm) in a laboratory flume. As shown in Fig. 5, the river cross

section comprised a deep central channel flanked by shallow 'flood plains' or 'berms'—the latter features occupying approximately half the overall channel width.

Flows, corresponding to depths of 15 and 30 mm on the berms, were introduced without initiating any bed movement. These two stages (I and II) were considered as representative of normal flow conditions in the channel. Boundary shear distribution in the unconstricted channel for the two-stage conditions are presented in Fig. 5. It was noted that the segmental overbank flow was 18% of the total flow for Stage I, and 26% for Stage II.

Constrictions of 20%, 30%, and 40% in terms of overall channel width were introduced, symmetrically, from both sides of the channel (the constriction units were 4 mm thick rigid vertical walls projecting, laterally, into the flow field). This type of constriction simulates the most general case of bridge crossing

TABLE 3.—Test Results of Overbank Flow Constrictions on Natural Channels

Run number (1)	Gap width, in centimeters per second, b (2)	Contraction ratio, m (3)	Maximum Velocity Upon Constricting at $t = 0$		Flow width at vena contracta, in centimeters per second (6)	Maximum Backwater Depth, in centimeters per second		Nondimensional Shear Maxima	
			On berm above face (4)	On center of channel (5)		Over berm (7)	Over channel bed (8)	Over berm along face of constriction (9)	Over central channel (10)
(a) Series I. Normal width B = 30 cm; Depth of flow over berm = 1.5 cm, Over center of channel = 4.9 cm; Mean velocity over berm = 0.10 m/sec; Over central channel = 0.22 m/sec.									
1	24	0.20	0.13	0.25	20.75	1.70	5.00	1.13	1.65
2	21	0.30	0.18	0.29	16.20	1.75	5.10	1.75	2.88
3	18	0.40	0.25	0.33	13.45	1.95	5.20	2.80	3.20
(b) Series II. Normal with B = 30 cm; Depth of flow over berm = 3.0 cm; Over center of channel = 6.4 cm; Mean velocity over berm = 0.14 m/sec; Over central channel = 0.27 m/sec.									
4	24	0.20	0.17	0.28	20.1	3.10	6.40	1.25	1.80
5	21	0.30	0.20	0.32	17.5	3.45	6.55	1.81	2.65
6	18	0.40	0.31	0.38	12.80	3.75	6.85	3.10	3.40

on alluvial channels with adjoining flood plains, where the uninterrupted portion of the waterway is, generally, marginally in excess of the central channel width.

The velocity redistributions, immediately upon introduction of the constriction units, as well as under equilibrium scour conditions, were measured and from which the boundary shear pattern for the constricted flow was subsequently computed.

The measured redistribution of the boundary shear in the constricted region followed, in general, the pattern already observed for end-dump constrictions

in channels of uniform depth. At higher contraction ratios (0.30 and 0.40) pronounced high shear zones were observed against the constriction face, whereas the shear increase was nominal at 20% contraction. This can be explained. For the Stage II case, the overbank flow that was redirected towards the midstream zone was 18% and 22% of the total flow at 30% and 40% contraction ratios, respectively, while it was only 9% for the 20% contraction. The deflection of the overbank flow into the midstream was thus substantial at higher contraction ratios; consequently, the live stream profile against the constriction face became more curvilinear with the flow accelerating faster.

The significant feature is that the nondimensional shear maxima for the 40% contraction attained values of 2.88 and 3.40 for the two stages of flow, whereas the corresponding longstream velocity increase was only 1.40 and 1.50, respectively. Another pertinent feature was that the high shear zone conformed to the path of the high velocity filament from the backwater section to the *vena contracta* section. Scour holes developed adjacent to the downstream face of the constriction units where the highest point shear stresses were measured immediately following introduction of the constriction. Maximum depth of scour was observed to be approximately 28% of the local depth. (The observed data on velocity and shear distribution are shown in Table 3.)

These observations of flow pattern and shear distribution through overbank constrictions can only be considered as qualitative. Nevertheless, they do confirm that the resulting boundary shear stress increase is greater than the velocity increase for constricted flow situations, which also is the case for flow through bends. In situations where the overbank flow component exceeds about 30% of the main channel flow, and the former is suddenly confined, by abrupt side constrictions, to the main channel zone, it is obvious that a substantial increase in boundary shear stress will occur in the main channel which will result in a comparable increase in local scour.

Summary and Conclusions

The flow characteristics, in general, and the boundary shear distribution, in particular, through end-dump constrictions and overbank flow constrictions of natural channels in alluvium, have been presented. The following general conclusions can be drawn for flow through channel constrictions:

1. The velocity distribution through a constriction is highly nonuniform; the flow accelerates from the maximum backwater section upstream to the *vena contracta* and decelerates gradually thereafter to that section downstream where teh expanding flow field extends, finally, over the entire width of channel. The maximum longitudinal velocity filament, whose path is highly curvilinear, clings to the constriction face and remains close to the livestream boundary throughout.
2. The increase, both in mean flow velocity through the gap and local velocity against the upstream face of the constriction, over that in the unconstricted channel, is nominal and only a small fraction of the corresponding increase in local-boundary shear stress.
3. Because of the curvilinear and accelerating flow field at the channel constriction boundary, shear maxima, τ_{max}, on the upstream face of the constriction, and on the channel bed in the region of the vena contracta, may reach

values many times higher than the corresponding uniform bed shear stress, $\bar{\tau}_o$, in the unconstricted reach. Furthermore, experimental evidence suggests that the shear maxima increase exponentially with increase in the contraction ratio.

4. As is generally the case for flow in channel bends, the locus of boundary shear stress maxima through the constriction follows, closely, the path of the maximum velocity filament.

5. For a given contraction ratio, the stable size of closure material required to form an end-dump dam can be evaluated satisfactorily using a shear stress analysis approach. Furthermore, this approach can quantify the extent of related local scouring, and can assist also in establishing criteria for any bed protection scheme that might be considered. Nondimensional curves of shear maxima versus contraction ratio have been developed with this purpose in mind. The conventional design approach, which uses critical velocity as its criterion, is deficient in the case of curvilinear and accelerating flow fields.

Appendix I.—References

1. Awazu, S., "On Scour Around Spur Dike," *Proceedings*, 12th International Association of Hydraulic Research Congress at Fort Collins, Colo., Vol. 3, 1967, pp. 97–104.
2. Das, B. P., "Stability of Rockfill in End-Dump River Closures," *Journal of the Hydraulics Division*, ASCE, Vol. 98, No. HY11, Proc. Paper 9381, Nov., 1972, pp. 1947–1967.
3. Das, B. P., and Nuttall, J. B., "Backwater Effects at End-Dump Constrictions on Alluvial Channels," *Proceedings*, First Canadian Hydraulics Conference at Edmonton, Canada, 1973, pp. 30–43.
4. Das, B. P., "Bed Scour at End-Dump Channel Constrictions," *Journal of the Hydraulics Division*, ASCE, Vol. 99, No. HY12, Proc. Paper 10228, Dec., 1973, pp. 2273–2291.
5. Garde, R. J., Subramanya, K., and Nambudripad, K. D., "Study of Scour Around Spur-Dikes," *Journal of the Hydraulics Division*, ASCE, Vol. 87, No. HY6, Proc. Paper 2978, Nov., 1961, pp. 23–37.
6. Gill, M. A., "Erosion of Sand Beds around Spur-Dikes," *Journal of the Hydraulics Division*, ASCE, Vol. 98, No. HY9, Proc. Paper 9198, Sept., 1972, pp. 1587–1601.
7. Ippen, A. T., and Drinker, A., "Boundary Shear Stresses in Curved Trapezoidal Channels," *Journal of the Hydraulics Division*, ASCE, Vol. 88, No. HY5, Proc. Paper 3273, Sept., 1962, pp. 143–179.
8. Izbash, S. V., and Lebder, I. V., "Change of Natural Streams During Constrictions of Hydraulic Structures," *Proceedings*, 9th International Association of Hydraulic Research Congress at Dubrovnik, Sept., 1961, pp. 1114–1121.
9. Komura, S., "Equilibrium Depth of Scour in Long Constrictions," *Journal of the Hydraulics Division*, ASCE, Vol. 92, No. HY5, Proc. Paper 4898, Sept., 1966, pp. 17–37.
10. Kindsvater, C. E., and Cante, R. W., "Tranquil Flow Through Open Channel Constrictions," *Transactions*, ASCE, Vol. 120, 1953, pp. 955–980.
11. Lane, E. W., "Experiments on the Flow of Water through Contractions in an Open Channel," *Transactions*, ASCE, Vol. 83, 1919-20, pp. 1149–219.
12. Laursen, E. M., "Scour at Bridge Crossings," *Transactions*, ASCE, Vol. 127, Part I, 1962, p. 166.
13. Liu, K. H., Chang, F. M., and Skinner, M. M., "Effect of Bridge Constrictions on Scour and Backwater," *Civil Engineering Section Report CER60, HKL22*, Colorado State University, Fort Collins, Colo., Feb., 1961.
14. Neill, C. R., *Guide to Bridge Hydraulics*, Roads and Transport Association of Canada, University of Toronto Press, Toronto, Canada, 1973.
15. Nouh, M., and Townsend, R. D., "Shear Stress Distribution in Stable Channel Bends," *Journal of the Hydraulics Division*, ASCE, Vol. 105, No. HY10, Proc. Paper 14898, Oct., 1979, pp. 1235–1245.

16. Nwachukwu, B. A., "Laboratory Study of Scour at Channel Bends," *Proceedings*, First Canadian Hydraulics Conference at Edmonton, Canada, 1973.
17. Replogle, J. A., and Chow, V. T., "Tractive Force Distribution in Open Channels," *Journal of the Hydraulics Division*, ASCE, Vol. 92, No. HY2, Proc. Paper 4727, March, 1966, pp. 169–191.
18. Valentine, H. R., "Flow in Rectangular Channels with Lateral Constriction Plates," *Houille Blanche*, Vol. 13, No. 1, Jan./Feb. 1958, pp. 75–84.
19. Yen, C. L., "Bed Topography Effect on Flow in a Meander," *Journal of the Hydraulics Division*, ASCE, Vol. 96, No. HY1, Proc. Paper 7003, Jan., 1970, pp. 57–73.

Appendix II.—Notation

The following symbols are used in this paper:

B = mean width of approach channel;
b = width of opening at dump line;
b_c = width of livestream at vena contracta;
C_c = coefficient of contraction;
d = nominal size of bed material representing median size;
F = Froude number of approach flow;
g = acceleration due to gravity;
h = average depth of normal flow;
j_1, j_2 = exponents in $\tau_{o_{max}}/\bar{\tau}_o$-$m$ relationship;
K_s = effective boundary roughness;
L_{23} = length of contraction from dumpline to vena contracta;
L_{34} = length of expansion from vena contracta to full channel width;
m = contracton ratio = $(B - b)/B$;
s = bed and water surface slope for normal flow;
u_1, u_2 = velocity of flow at depths y_1 and y_2 above boundary;
u_* = shear velocity;
V = approach channel mean velocity;
x_c, x_e = coordinates along flow direction for contracting and expanding profile (Fig. 5);
y_1, y_2 = flow depths above bed at which velocity u_1, u_2 are measured;
y_c, y_e = coordinates transverse to flow direction for contracting and expanding profile (Fig. 5);
γ = unit weight of water;
ν = kinematic viscosity;
ρ_s, ρ_w = specific gravity of bed material and water;
σ_{gd} = geometric standard deviation of bed material;
$\tau_o, \bar{\tau}_o$ = local intensity of shear stress on constriction region, average intensity of shear stress in unconstricted channel;
$\tau_{max}, \tau_{max\,b}, \tau_{max\,f}$ = maximum intensity of shear stress on boundary, on channel bed, downstream of constriction, on face of constriction;
$\psi_1, \psi_{1'}$ = overall angle of contraction, local angle of contraction (Fig. 5); and
$\psi_2, \psi_{2'}$ = overall angle of expansion, local angle of expansion (Fig. 5).

CONFORMAL MAPPING FOR CHANNEL JUNCTION FLOW

By Pashupati N. Modi,[1] Pitamber D. Ariel,[2] and Mohan M. Dandekar[3]

INTRODUCTION

The analysis of flow behavior at channel junctions where two streams combine to form a third is a problem which, so far, has received little attention in the field of open channel hydraulics. Such flows occur in a wide variety of situations and their analysis is of considerable importance to engineers engaged in the design of irrigation systems, storm sewers, power installations, and allied projects. The complex flow pattern which results from the meeting of the two streams makes a complete analysis of the problem impossible. However, by adopting conformal mapping techniques, a two-dimensional approximation of the flow pattern at rectangular channel junctions may be carried out. This method of analysis, though it involves oversimplifying assumptions, is quite useful. Similar analytical solutions already have been obtained, with the help of conformal mapping, for other problems in the field of open channel hydraulics, such as flow past a hump or a step in the bed of a channel, dividing flow at channel junctions, etc.

The conformal mapping approach was first adopted for the problem of channel junctions with combining flow by Greated (2). By using the Schwarz-Christoffel transformation, Greated developed expressions for locating the stagnation point (where the dividing streamline meets the boundary) for the particular case of rectangular channel junction having a junction angle α equal to 90° and all the channels of identical bed-width. Further, by using the free-streamline concept, Greated also obtained a streamline pattern for a 90° rectangular channel junction with separation.

The method proposed by Greated is not applicable to junction angles other than 90°. It is also not applicable for channels of different bed-widths. Thus it lacks a generality of approach. A more generalized analysis of the problem

[1]Reader, Dept. of Civ. Engrg., Malaviya Regional Engrg. Coll., Jaipur, India.
[2]Lect., Dept. of Maths., Malaviya Regional Engrg. Coll., Jaipur, India.
[3]Prof., Dept. of Civ. Engrg., Malaviya Regional Engrg. Coll., Jaipur, India.

Note.—Discussion open until December 1, 1982. To extend the closing date one month, a written request must be filed with the Manager of Technical and Professional Publications, ASCE. Manuscript was submitted for review for possible publication on September 3, 1980. This paper is part of the Journal of the Hydraulics Division, Proceedings of the American Society of Civil Engineers, ©ASCE, Vol. 107, No. HY12, December, 1981. ISSN 0044-796X/81/0012-1713/$01.00.

is presented in this paper. It is applicable to rectangular channel junctions having any junction angle and different bed-widths.

Formulation of Problem

A two-dimensional junction of rectangular channels with horizontal bed is considered as shown in Fig. 1(*a*). The main assumptions in this method of analysis are:

1. The fluid is inviscid, i.e., viscous effects are absent.
2. The flow is irrotational.
3. The loss of energy is absent or, if present, it takes place downstream of the junction.

Although all these assumptions are not exactly valid in real flow situations, such an analysis does give a good insight into the flow pattern at channel junctions.

The two distinct cases which need to be considered are:

1. Nonseparated flow.
2. Flow with separation occurring at some point on the boundary.

Analyses based on the method of conformal mapping for both these cases are presented.

Case (A) Nonseparated Flow at Channel Junction

By using the theorem of Schwarz-Christoffel, the various boundaries of a channel junction, as represented in the z-plane [Fig. 1(*a*)], may be transformed to the real axis of a ζ-plane [Fig. 1(*b*)], and the points within the region of flow between the boundaries are transformed to the corresponding points in the upper half of the ζ-plane. Referring to Fig. 1(*b*), the expression for the transformation function has been found to be

$$\frac{dz}{d\zeta} = \frac{K\,\zeta^{(1-\alpha/\pi)}}{(\zeta+1)(\zeta-a)(\zeta-b)} \quad \ldots\ldots\ldots\ldots\ldots\ldots\ldots\ldots\ldots\ldots\ldots\ldots (1)$$

But, as may be verified by placing the following fractions over a common denominator

$$\frac{dz}{d\zeta} = K\,\zeta^{-(\alpha/\pi)}\left[-\frac{1}{(1+a)(1+b)}\,\frac{1}{(1+\zeta)} + \frac{a}{(1+a)(b-a)}\,\frac{1}{(a-\zeta)}\right.$$

$$\left. - \frac{b}{(1+b)(b-a)}\,\frac{1}{(b-\zeta)}\right] \quad \ldots\ldots\ldots\ldots\ldots\ldots\ldots\ldots\ldots\ldots\ldots\ldots (2)$$

in which K = a complex constant; and a and b = real unknowns which can be evaluated as follows.

With F as origin in the z-plane [Fig. 1(*a*)] and using the standard results

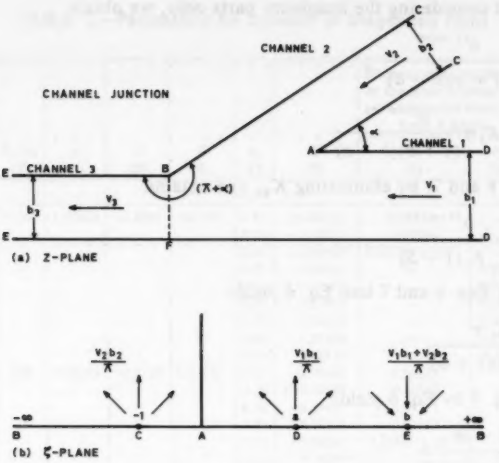

FIG. 1.—Transformation Layout for Locating Stagnation Point

of integration given by Copson (1), the integration of Eq. 2 between A and B gives

$$[b_2 \operatorname{cosec} \alpha + (b_1 - b_3) \cot \alpha + \iota (b_1 - b_3)] = K \pi \left[\frac{1}{(1+a)(1+b)} + \frac{a^{(1-\alpha/\pi)} \cos \alpha}{(1+a)(b-a)} - \frac{b^{(1-\alpha/\pi)} \cos \alpha}{(1+b)(b-a)} \right] \operatorname{cosec} \alpha \quad \ldots \ldots \ldots \ldots \ldots \ldots \ldots \ldots (3)$$

in which b_1, b_2, and b_3 = are bed-widths of the channels 1, 2, and 3, respectively.

Assuming $K = K_1 + iK_2$, and separating the real and imaginary quantities, yields

$$[b_2 + (b_1 - b_3) \cos \alpha] = K_1 \pi \left[\frac{1}{(1+a)(1+b)} + \frac{a^{(1-\alpha/\pi)} \cos \alpha}{(1+a)(b-a)} - \frac{b^{(1-\alpha/\pi)} \cos \alpha}{(1+b)(b-a)} \right] \quad \ldots \ldots \ldots \ldots \ldots \ldots \ldots \ldots \ldots \ldots \ldots \ldots \ldots \ldots \ldots \ldots (4)$$

and $$(b_1 - b_3) = K_2 \pi \left[\frac{1}{(1+a)(1+b)} + \frac{a^{(1-\alpha/\pi)} \cos \alpha}{(1+a)(b-a)} - \frac{b^{(1-\alpha/\pi)} \cos \alpha}{(1+b)(b-a)} \right] \operatorname{cosec} \alpha \quad \ldots \ldots \ldots \ldots \ldots \ldots \ldots \ldots \ldots \ldots \ldots \ldots \ldots \ldots \ldots \ldots (5)$$

Further, integrating Eq. 2 separately in the limits $a - \epsilon$ and $a + \epsilon$ for the point D, and $b - \epsilon$ and $b + \epsilon$ for the point E in ζ-plane (in which ϵ = infinitesimal distance on either side of points D and E on real axis of ζ-plane, such that

$\epsilon \to 0$), and considering the imaginary parts only, we obtain

$$b_1 = K_1 \pi \frac{a^{(1-\alpha/\pi)}}{(1+a)(b-a)} \quad \ldots\ldots (6)$$

and $$b_3 = K_1 \pi \frac{b^{(1-\alpha/\pi)}}{(1+b)(b-a)} \quad \ldots\ldots (7)$$

From Eqs. 6 and 7, by eliminating K_1, one obtains

$$\frac{a^{(1-\alpha/\pi)}}{b_1(1+a)} = \frac{b^{(1-\alpha/\pi)}}{b_3(1+b)} \quad \ldots\ldots (8)$$

Introducing Eqs. 6 and 7 into Eq. 4 yields

$$b_2 = \frac{K_1 \pi}{(1+a)(1+b)} \quad \ldots\ldots (9)$$

Dividing Eq. 9 by Eq. 6 yields

$$\frac{b_2}{b_1} = \frac{(b-a)}{(1+b)\, a^{(1-\alpha/\pi)}} \quad \ldots\ldots (10)$$

The preceding expressions, which correspond to the most general case, may be used for evaluating the unknown quantities, namely, a, b, K_1, and K_2 for the known values of b_1, b_2, b_3, and α. For a particular case of the channel junction with $b_1 = b_3$, Eqs. 8–10 were programmed for solution on an IBM 1130. The values of a, b, and K obtained for α equal to 30°, 60°, and 90°, and b_2/b_1 equal to 0.5 and 1.0, are given in Table 1 sections (*a*)–(*c*).

As shown in Fig. 1(*b*), if in the ζ-plane two sources, one each at points C and D of strength $V_2 b_2/\pi$ and $V_1 b_1/\pi$, respectively, and a sink at point E of strength $(V_1 b_1 + V_2 b_2)/\pi$ are considered, then the complex potential in the ζ-plane takes the form

$$w = \frac{V_1 b_1 + V_2 b_2}{\pi} \ln(\zeta - b) - \frac{V_1 b_1}{\pi} \ln(\zeta - a) - \frac{V_2 b_2}{\pi} \ln(\zeta + 1) \quad \ldots\ldots (11)$$

in which V_1 and V_2 = the mean velocities of flow in channels 1 and 2, respectively.

Differentiating both sides of Eq. 11 yields

$$\frac{dw}{d\zeta} = \frac{V_1 b_1 + V_2 b_2}{\pi} \frac{1}{(\zeta - b)} - \frac{V_1 b_1}{\pi} \frac{1}{(\zeta - a)} - \frac{V_2 b_2}{\pi} \frac{1}{(\zeta + 1)} \quad \ldots\ldots (12)$$

from which the expression for the velocity at any point is obtained as

$$-\frac{dw}{dz} = -\left(\frac{dw}{d\zeta}\frac{d\zeta}{dz}\right) = (-V_x + iV_y) = \left[\frac{V_1 b_1}{\pi} \frac{(\zeta+1)(\zeta-b)}{K\zeta^{(1-\alpha/\pi)}} + \frac{V_2 b_2}{\pi} \frac{(\zeta-a)(\zeta-b)}{K\zeta^{(1-\alpha/\pi)}} - \frac{V_1 b_1 + V_2 b_2}{\pi} \frac{(\zeta+1)(\zeta-a)}{K\zeta^{(1-\alpha/\pi)}}\right] \quad \ldots\ldots (13)$$

in which V_x and V_y = the velocity components in the x and y directions, respectively.

TABLE 1.—Parameters for Location of Stagnation Point

α (1)	b_1/b_3 (2)	b_2/b_3 (3)	a (4)	b (5)	K (6)	n_s (7)	ζ (8)	Distance per Unit Width of the Main Channel, of Stagnation Point from A Along: AC (9)	AD (10)	n_{dcr} (11)
						(*a*) 30°				
30°	1.00	0.50	1.87460	17.4430	26.510	0.10	−0.66562	0.09911	—	0.31047
						0.20	−0.34315	0.02266	—	
						0.30	−0.03198	0.25758×10^{-3}	—	
						0.40	0.26850	—	0.01201	
						0.50	0.55883	—	0.04541	
						0.60	0.83950	—	0.09823	
						0.70	1.11090	—	0.17557	
						0.80	1.37370	—	0.29319	
						0.90	1.62810	—	0.50532	
30°	1.00	1.00	0.96319	62.8120	125.270	0.10	−0.79808	0.36275	—	0.50156
						0.20	−0.59745	0.16843	—	
						0.30	−0.39807	0.07117	—	
						0.40	−0.19995	0.01903	—	
						0.50	−0.00307	0.08849×10^{-4}	—	
						0.60	0.19259	—	0.01799	
						0.70	0.38703	—	0.06931	
						0.80	0.58028	—	0.16584	
						0.90	0.77232	—	0.35948	
						(*b*) 60°				
60°	1.00	0.50	1.13250	3.6691	4.9785	0.10	−0.63789	0.12601	—	0.32417
						0.20	−0.32791	0.03621	—	
						0.30	−0.05956	0.00207	—	
						0.40	0.17503	—	0.01289	
						0.50	0.38185	—	0.05079	
						0.60	0.56555	—	0.10827	
						0.70	0.72981	—	0.18996	
						0.80	0.87755	—	0.31155	
						0.90	1.01110	—	0.52832	
60°	1.00	1.00	0.68894	6.6786	12.9680	0.10	−0.78942	0.43855	—	0.53101
						0.20	−0.59008	0.22737	—	
						0.30	−0.40110	0.11227	—	
						0.40	−0.22171	0.04151	—	
						0.50	−0.05118	0.00373	—	
						0.60	0.11112	—	0.01453	
						0.70	0.26578	—	0.06934	
						0.80	0.41332	—	0.17110	
						0.90	0.55423	—	0.37132	
						(*c*) 90°				
90°	1.00	0.50	0.60962	1.6404	2.1250	0.10	−0.64338	0.19828	—	0.39038
						0.20	−0.37162	0.08585	—	
						0.30	−0.15767	0.02551	—	
						0.40	0.02616	—	0.00194	
						0.50	0.15768	—	0.03251	
						0.60	0.27721	—	0.08851	
						0.70	0.37892	—	0.16990	
						0.80	0.46649	—	0.29158	
						0.90	0.54270	—	0.50854	
90°	1.00	1.00	0.38196	2.6180	4.9999	0.10	−0.78940	0.60442	—	0.61803
						0.20	−0.60198	0.36977	—	
						0.30	−0.43410	0.22808	—	
						0.40	−0.28286	0.12652	—	
						0.50	−0.14590	0.05109	—	
						0.60	−0.02129	0.00320	—	

TABLE 1.—*Continued*

(1)	(2)	(3)	(4)	(5)	(6)	(7)	(8)	(9)	(10)	(11)
						0.70	0.09257	—	0.03390	
						0.80	0.19701	—	0.12991	
						0.90	0.29315	—	0.32688	

It is evident that somewhere along the boundary CAD there must be a point of stagnation where the dividing streamline, $\Psi = V_1 b_1$, meets the boundary. At the stagnation point $-dw/dz = 0$.

Thus from Eq. 13, we obtain

$$\frac{V_1 b_1}{\pi} \frac{(\zeta + 1)(\zeta - b)}{K \zeta^{(1-\alpha/\pi)}} + \frac{V_2 b_2}{\pi} \frac{(\zeta - a)(\zeta - b)}{K \zeta^{(1-\alpha/\pi)}}$$

$$- \frac{V_1 b_1 + V_2 b_2}{\pi} \frac{(\zeta + 1)(\zeta - a)}{K \zeta^{(1-\alpha/\pi)}} = 0$$

$$\text{or} \quad \zeta = \frac{V_2 b_2 a(1 + b) - V_1 b_1 (b - a)}{V_1 b_1 (b - a) + V_2 b_2 (1 + b)} \quad \ldots\ldots\ldots\ldots\ldots\ldots\ldots\ldots \quad (14)$$

Let the discharge ratio n_q be defined as the ratio of the discharge in channel 2 to the discharge in channel 3, which, since the flow is two-dimensional, is

$$n_q = \frac{V_2 b_2}{V_1 b_1 + V_2 b_2} \quad \ldots\ldots\ldots\ldots\ldots\ldots\ldots\ldots\ldots\ldots\ldots\ldots \quad (15)$$

Introducing Eq. 15 into Eq. 14, we obtain

$$\zeta = \frac{n_q b (1 + a) - (b - a)}{n_q (1 + a) + (b - a)} \quad \ldots\ldots\ldots\ldots\ldots\ldots\ldots\ldots\ldots\ldots\ldots \quad (16)$$

From Eq. 16, the position of the stagnation point may be located in the ζ-plane. It may be seen from Eq. 16 that for any value of α, the value of ζ corresponding to the stagnation point depends on the value of the discharge ratio, n_q. In other words, as the value of n_q varies, the stagnation point moves along the boundary CAD from C to D and, correspondingly, the value of ζ varies from -1 to a. Thus, when the stagnation point lies along the boundary CA, ζ varies from -1 to 0, and when it lies along the boundary AD, ζ varies from 0 to a. The stagnation point will coincide with corner A when $\zeta = 0$, corresponding to which the value of n_q may be considered as critical, namely, $n_{q_{cr}}$, which is obtained from Eq. 16 as

$$n_{q_{cr}} = \frac{(b - a)}{b (1 + a)} \quad \ldots\ldots\ldots\ldots\ldots\ldots\ldots\ldots\ldots\ldots\ldots\ldots \quad (17)$$

In order to locate the stagnation point in the z-plane, Eq. 2 may be integrated along AC and AD, which for $b_1 = b_3$ gives

$$\int_{(b_2 \operatorname{cosec}\alpha + ib_1)}^{z} dz = K \int_0^{\zeta} \frac{\zeta^{(1-\alpha/\pi)}\, d\zeta}{(\zeta + 1)(\zeta - a)(\zeta - b)} \quad \ldots\ldots\ldots\ldots\ldots\ldots \quad (18)$$

in which $-1 < \zeta < a$.

In order to obtain the distance of the stagnation point from the corner A along the boundary AC or AD, the integral on R.H.S. of Eq. 18 has been evaluated numerically by using Simpson's rule on an IBM 1130. The values of the distance of the stagnation point so obtained for the different values of n_q, α, and b_2/b_1 are given in nondimensional form in Table 1. The corresponding values of ζ as given by Eq. 16, and the values of $n_{q_{cr}}$ as given by Eq. 17, are also given in Table 1.

Case (B) Flow Separating at Boundary: Free-Streamline Theory

According to the idealized theory described in the previous case, with no separation at any point on the boundary, the velocity at the downstream corner B is infinite, which is not possible in reality. Any fluid flowing past a sharp corner has to separate from the boundary at the corner, thereby developing a finite velocity at the corner. In order to account for this actual physical condition of flow, the free-streamline approach of Helmholtz can be used. The streamline, which separates the fluid in motion from the fluid at rest, is called

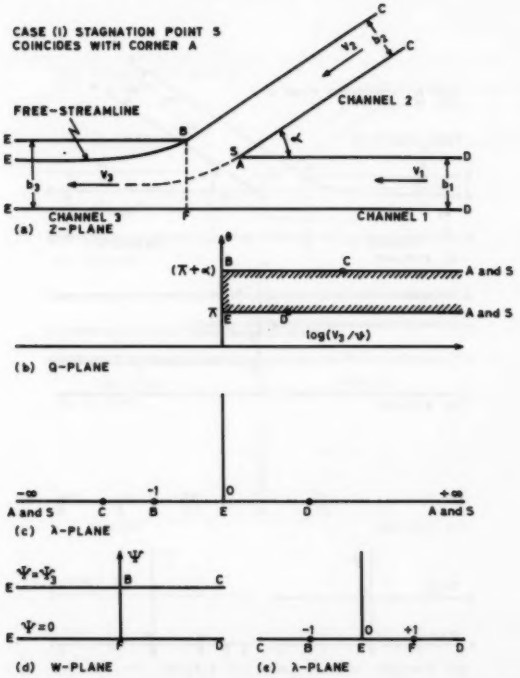

FIG. 2.—Transformation Layout for Locating Free-Streamline when Stagnation Point S Coincides with Corner A

a free-streamline. The velocity as well as the pressure remains constant along a free-streamline. Accordingly, as shown in Fig. 2(*a*), the streamline BE, starting from the downstream corner *B* of the junction, may be considered to be a free-streamline. The fluid between the streamline BE and the channel boundary BE is assumed to be stagnant. Consequently, the flow on the downstream of the junction is confined between the free-streamline BE and the channel boundary DE. In the study of the flow pattern at the junction, it is, therefore, essential to locate the free-streamline starting from the downstream corner *B* of the junction. In the following paragraphs the method for the location of the free-streamline is examined.

The analytic function, $Q = \{[\ln (V_3/v)] + i\,\theta\} = \ln [V_3\,(dz/dw)]$ (in which v = the modulus of $V_x - iV_y$), transforms the boundaries of the z-plane to the Q-plane, in which the hodographs or the velocity planes assume one of the three shapes shown in Figs. 2(*b*), 3(*b*), and 4(*b*) according to: (1) The stagnation point S being coincident with corner A; (2) the stagnation point S lying in channel 1 along the boundary AD; and (3) the stagnation point S lying in channel 2 along the boundary AC. The free-streamline for each of these cases may be located as follows.

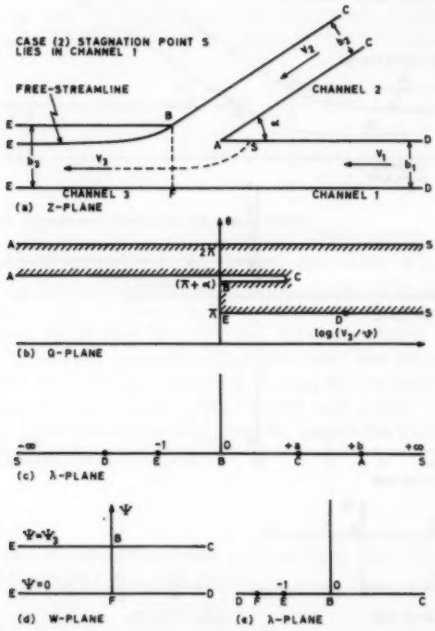

FIG. 3.—Transformation Layout for Locating Free-Streamline when Stagnation Point S Lies in Channel 1 on Boundary AD

I. Stagnation Point S Coinciding with Corner *A*:—Using the Schwarz-Christoffel theorem, the region included in the semi-infinite strip of the Q-plane of Fig. 2(*b*) can be transformed onto the upper half of the λ-plane, as shown in Fig. 2(*c*). The corresponding expression for the transformation is

$$\frac{dQ}{d\lambda} = \frac{K}{\lambda^{1/2}(\lambda + 1)^{1/2}} \quad \ldots \ldots \ldots \ldots \ldots \ldots \ldots \ldots \ldots \ldots \ldots \ldots \quad (19)$$

Integration of Eq. 19 yields

$$Q = 2K \ln (\sqrt{1 + \lambda} - \sqrt{\lambda}) + C \quad \ldots \ldots \ldots \ldots \ldots \ldots \ldots \ldots \ldots \quad (20)$$

in which C = constant of integration, which, along with K, may be evaluated by using the boundary conditions as follows.

For point E: $\lambda = 0$, $Q = i\pi$; and for point B: $\lambda = -1$, $Q = i(\pi + \alpha)$; thus $C = i\pi$, and $K = \alpha/\pi$. Eq. 20 then becomes

$$Q = \frac{2\alpha}{\pi} \ln (\sqrt{1 + \lambda} - \sqrt{\lambda}) + i\pi \quad \ldots \ldots \ldots \ldots \ldots \ldots \ldots \ldots \quad (21)$$

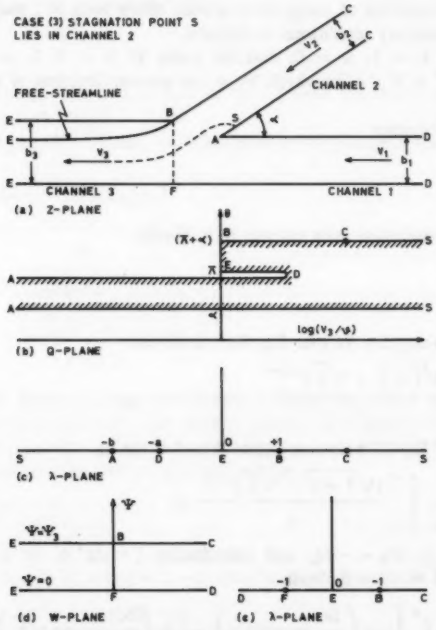

FIG. 4.—Transformation Layout for Locating Free-Streamline when Stagnation Point S Lies in Channel 2 on Boundary AC

As $Q = \left[\ln\left(\frac{V_3}{v}\right) + i\theta\right] = \ln\left[V_3\left(\frac{dz}{dw}\right)\right]$;

$$\ln\left[V_3\left(\frac{dz}{dw}\right)\right] = \frac{2\alpha}{\pi}\ln\left[(\sqrt{1+\lambda} - \sqrt{\lambda})\right] + i\pi \quad \text{or} \quad V_3\left(\frac{dz}{dw}\right)$$

$$= -(\sqrt{1+\lambda} - \sqrt{\lambda})^{2\alpha/\pi} \quad \ldots\ldots\ldots\ldots\ldots\ldots\ldots\ldots\ldots\ldots \quad (22)$$

Since the flow near the free-streamline is of prime interest, a relation between w and λ must be found which maps the interior of the infinite strip in w-plane onto the upper half of the λ-plane, with correspondence between the points B, E, F, D and C shown in Figs. 2(*d*) and 2(*e*). The corresponding transformation is

$$\frac{dw}{d\lambda} = \frac{K'}{\lambda} \quad \ldots\ldots\ldots\ldots\ldots\ldots\ldots\ldots\ldots\ldots\ldots\ldots\ldots\ldots \quad (23)$$

in which K' = a complex constant.

Integration of Eq. 23 yields

$$w = K' \ln(\lambda) + C' \quad \ldots\ldots\ldots\ldots\ldots\ldots\ldots\ldots\ldots\ldots\ldots\ldots\ldots\ldots \quad (24)$$

in which C' = constant of integration which, along with K', may be evaluated by using the boundary conditions as follows.

For point F: $\lambda = 1$, $w = 0$; and for point B: $\lambda = -1$, $w = i\,\Psi_3$; thus $C' = 0$, and $K' = \Psi_3/\pi$, in which Ψ_3 = the stream function of free-streamline BE.

Eq. 24 then becomes

$$w = \frac{\Psi_3}{\pi}\ln\lambda \quad \ldots\ldots\ldots\ldots\ldots\ldots\ldots\ldots\ldots\ldots\ldots\ldots\ldots\ldots \quad (25)$$

which, on differentiation with respect to z, yields

$$\frac{dw}{dz} = \frac{\Psi_3}{\pi\lambda}\frac{d\lambda}{dz} \quad \ldots\ldots\ldots\ldots\ldots\ldots\ldots\ldots\ldots\ldots\ldots\ldots\ldots\ldots \quad (26)$$

Further, introducing Eq. 26 into Eq. 22, we obtain

$$\frac{dz}{d\lambda} = -\frac{\Psi_3}{\pi V_3}\frac{(\sqrt{1+\lambda} - \sqrt{\lambda})^{2\alpha/\pi}}{\lambda} \quad \ldots\ldots\ldots\ldots\ldots\ldots\ldots\ldots\ldots\ldots \quad (27)$$

Integration of Eq. 27 between points B and E yields

$$z - ib_3 = -\frac{\Psi_3}{\pi V_3}\int_{-1}^{-\lambda}\frac{(\sqrt{1+\lambda} - \sqrt{\lambda})^{2\alpha/\pi}}{\lambda}\,d\lambda \quad \ldots\ldots\ldots\ldots\ldots\ldots\ldots \quad (28)$$

in which $\lambda = -\xi$; $d\lambda = -d\xi$; and introducing $\xi = \sin^2\phi$, or $\phi = \arcsin\sqrt{\xi}$; and taking $\sqrt{-1} = -i$, we obtain

$$z - ib_3 = -\frac{\Psi_3}{\pi V_3}\int_1^{\xi}\frac{\left[\cos\left(\frac{2\alpha}{\pi}\arcsin\sqrt{\xi}\right) + i\sin\left(\frac{2\alpha}{\pi}\arcsin\sqrt{\xi}\right)\right]}{\xi}\,d\xi \quad (29)$$

Separating the real and imaginary quantities gives the equations for the free-streamline in the parametric form:

$$x = -\frac{\Psi_3}{\pi V_3}\int_1^{\xi}\frac{\cos\left(\frac{2\alpha}{\pi}\arcsin\sqrt{\xi}\right)}{\xi}\,d\xi\,;$$

$$y = b_3 - \frac{\Psi_3}{\pi V_3}\int_1^{\xi}\frac{\sin\left(\frac{2\alpha}{\pi}\arcsin\sqrt{\xi}\right)}{\xi}\,d\xi \quad \ldots\ldots\ldots\ldots\ldots\ldots \quad (30)$$

Further, introduction of an auxiliary variable $\xi = \eta^2$, $d\xi = 2\eta\, d\eta$, permits the preceding equations to be expressed as

$$x = -\frac{2\Psi_3}{\pi V_3}\int_1^{\eta}\frac{\sin\left(\frac{2\alpha}{\pi}\arcsin\eta\right)}{\eta}\,d\eta\,;$$

$$y = b_3 - \frac{2\Psi_3}{\pi V_3}\int_1^{\eta}\frac{\sin\left(\frac{2\alpha}{\pi}\arcsin\eta\right)}{\eta}\,d\eta \quad \ldots\ldots\ldots\ldots\ldots\ldots \quad (31)$$

Eq. 31 represents the coordinates of the points on the free-streamline in the z-plane with F as origin.

Since $\Psi_3 = V_3 b_3$, Eq. 31 may be expressed in nondimensional form as

$$\frac{x}{b_3} = -\frac{2}{\pi}\int_1^{\eta}\frac{\cos\left(\frac{2\alpha}{\pi}\arcsin\eta\right)}{\eta}\,d\eta\,;$$

$$\frac{y}{b_3} = 1 - \frac{2}{\pi}\int_1^{\eta}\frac{\sin\left(\frac{2\alpha}{\pi}\arcsin\eta\right)}{\eta}\,d\eta \quad \ldots\ldots\ldots\ldots\ldots\ldots \quad (32)$$

II. Stagnation Point S Lying in Channel 1 Along Boundary AD.—Using the Schwarz-Christoffel theorem, the shaded region of Q-plane of Fig. 3(*b*) can be transformed onto the upper half of the λ-plane, as shown in Fig. 3(*c*). The corresponding expression for the transformation is

$$\frac{dQ}{d\lambda} = \frac{K(\lambda - a)}{(\lambda - b)\sqrt{\lambda(\lambda + 1)}} \quad \ldots\ldots\ldots\ldots\ldots\ldots\ldots\ldots \quad (33)$$

Integration of Eq. 33 between 0 to $-\lambda$, that is, from B towards E, yields

$$Q - i(\pi + \alpha) = \int_0^{-\lambda}\frac{K(\lambda - a)}{(\lambda - b)\sqrt{\lambda(\lambda + 1)}}\,d\lambda \quad \ldots\ldots\ldots\ldots\ldots \quad (34)$$

in which $\lambda = -\sin^2\phi$; $d\lambda = -2\sin\phi\cos\phi\, d\phi$; and taking $\sqrt{-2} = -i$,

converts the preceding expression to

$$Q - i(\pi + \alpha) = -2iK\left[\phi - \frac{(b-a)}{\sqrt{b(1+b)}} \arctan\left(\sqrt{\frac{1+b}{b}}\tan\phi\right)\right]_0^{\phi} \quad (35)$$

For point E: $\lambda = -1$, thus $\phi = \pi/2$; and $Q = i\pi$. Introducing these values into Eq. 35, we obtain

$$\alpha = K\pi\left[1 - \frac{(b-a)}{\sqrt{b(1+b)}}\right] \quad \ldots\ldots\ldots\ldots\ldots\ldots\ldots\ldots \quad (36)$$

Again, integration of Eq. 33 in the limits, $b - \epsilon$, and $b + \epsilon$, for the point A (such that $\epsilon \to 0$), yields

$$(\pi - \alpha) = \frac{K(b-a)\pi}{\sqrt{b(1+b)}} \quad \ldots\ldots\ldots\ldots\ldots\ldots\ldots\ldots \quad (37)$$

From Eqs. 36 and 37, $K = 1$; thus

$$\frac{(b-a)}{\sqrt{b(1+b)}} = \left(1 - \frac{\alpha}{\pi}\right) \quad \ldots\ldots\ldots\ldots\ldots\ldots\ldots\ldots \quad (38)$$

Further, integrating Eq. 33 between points B and C we obtain

$$\ln\left(\frac{V_3}{V_2}\right) = \int_a^a \frac{(\lambda - a)}{(\lambda - b)\sqrt{\lambda(\lambda+1)}}\, d\lambda \quad \ldots\ldots\ldots\ldots\ldots\ldots \quad (39)$$

in which $\lambda = \sinh^2\theta$; $d\lambda = 2\sinh\theta\cosh\theta\, d\theta$; and integrating the preceding expression, we obtain

$$\frac{V_3}{V_2} = (\sqrt{a} + \sqrt{1+a})^2\left[\frac{\sqrt{b(1+a)} - \sqrt{a(1+b)}}{\sqrt{b(1+a)} + \sqrt{a(1+b)}}\right]^m \quad \ldots\ldots\ldots \quad (40)$$

in which $m = (b-a)/\sqrt{b(1+b)} = 1 - \alpha/\pi$ from Eq. 38.

The factor, V_3/V_2, is representative of the discharge ratio n_q, since $b_3 V_3/b_2 V_2 = 1/n_q$. Thus, Eq. 40 may be expressed as

$$\frac{b_3 V_3}{b_2 V_2} = \frac{1}{n_q} = \frac{b_3}{b_2}(\sqrt{a} + \sqrt{1+a})^2\left[\frac{\sqrt{b(1+a)} - \sqrt{a(1+b)}}{\sqrt{b(1+a)} + \sqrt{a(1+b)}}\right]^m \quad \ldots \quad (41)$$

From Eq. 38 and 41, for given values of α, n_q, and b_2/b_3, the values of the parameters a and b can be obtained for this case.

Since the flow near the free-streamline is of prime interest, a relation between w and λ has to be found which maps the interior of the infinite strip in the w-plane onto the upper half of the λ-plane, with correspondence between the points B, E, F, D and C as shown in Fig. 3(d) and 3(e). The corresponding transformation may be written

$$\frac{dw}{d\lambda} = \frac{K'}{(\lambda+1)} \quad \ldots\ldots\ldots\ldots\ldots\ldots\ldots\ldots\ldots\ldots \quad (42)$$

Integration of the preceding expression in the limits, $-1 + \epsilon$, and $-1 - \epsilon$, for the point E (such that $\epsilon \to 0$), yields

$$K' = -\left(\frac{\Psi_3}{\pi}\right) \quad \ldots\ldots\ldots\

TABLE 3.—Dimensionless Coordinates of Points on Free-Streamline with F as Origin when Stagnation Point Lies Along AD in Channel 1

$n_q = 0.06$ (1)	$n_q = 0.7$ (2)	$n_q = 0.8$ (3)	$n_q = 0.9$ (4)
(a) $\alpha = 30°$; $(b_1/b_3) = 1.0$; $(b_2/b_3) = 1.0$ (Limiting value of (y/b_3) at $n_g = 0.6$–0.9, is 0.7660, 0.7583, 0.7424, and 0.7117, respectively).			
(x/b_3) −0.0086	−0.0086	−0.0086	−0.0086
−0.0357	−0.0356	−0.0355	−0.0352
−0.0839	−0.0838	−0.0834	−0.0826
−0.1580	−0.1576	−0.1568	−0.1552
−0.2657	−0.2651	−0.2639	−0.2611
−0.4222	−0.4214	−0.4196	−0.4157
−0.6613	−0.6603	−0.6580	−0.6531
(y/b_3) 0.9954	0.9954	0.9954	0.9953
0.9829	0.9827	0.9825	0.9819
0.9636	0.9632	0.9623	0.9605
0.9388	0.9378	0.9358	0.9318
0.9095	0.9077	0.9039	0.8965
0.8767	0.8737	0.8676	0.8556
0.8413	0.8369	0.8278	0.8102
(b) $\alpha = 60°$; $(b_1/b_3) = 1.0$; $(b_2/b_3) = 1.0$ (Limiting value of (y/b_3) at $n_g = 0.6$–0.9, is 0.5161, 0.4934, 0.4628, and 0.4207, respectively).			
(x/b_3) −0.0054	−0.0054	−0.0053	−0.0052
−0.0242	−0.0239	−0.0233	−0.0224
−0.0610	−0.0598	−0.0581	−0.0554
−0.1218	−0.1194	−0.1159	−0.1104
−0.2162	−0.2122	−0.2064	−0.1975
−0.3606	−0.3550	−0.3468	−0.3342
−0.5901	−0.5830	−0.5727	−0.5570
(y/b_3) 0.9919	0.9919	0.9918	0.9917
0.987	0.9684	0.9680	0.9674
0.9320	0.9309	0.9294	0.9272
0.8831	0.8805	0.8769	0.8718
0.8235	0.8186	0.8117	0.8020
0.7550	0.7467	0.7353	0.7193
0.6794	0.6669	0.6498	0.6261
(c) $\alpha = 90°$; $(b_1/b_3) = 1.0$; $(b_1/b_2) = 1.0$ (Limiting value of (y/b_3) at $n_g = 0.7$–0.9, is 0.2662, 0.2373, and 0.2028, respectively).			
	(x/b_3) −0.0008	−0.0007	−0.0005
	−0.0067	−0.0057	−0.0043
	−0.0239	−0.0210	−0.0168
	−0.0608	−0.0548	−0.0465
	−0.1297	−0.1199	−0.1066
	−0.2499	−0.2363	−0.2180
	−0.4597	−0.4427	−0.5799
	(y/b_3) 0.9903	0.9903	0.9903
	0.9610	0.9609	0.9607
	0.9121	0.9112	0.9103
	0.8433	0.8409	0.8381

TABLE 3.—*Continued*

(1)	(2)	(3)	(4)
	0.7556	0.7504	0.7442
	0.6506	0.6411	0.6298
	0.5311	0.5161	0.4981

$$\exp Q = V_3 \left(\frac{dz}{dw}\right) = V_3 \left(\frac{dz}{d\lambda}\frac{d\lambda}{dw}\right) \quad \ldots\ldots\ldots\ldots\ldots\ldots\ldots\ldots\ldots\ldots \quad (45)$$

Substituting for $d\lambda/dw$ from Eq. 44 yields

$$\exp Q = -\frac{V_3 \pi (\lambda + 1)}{\Psi_3}\frac{dz}{d\lambda} \quad \ldots\ldots\ldots\ldots\ldots\ldots\ldots\ldots\ldots\ldots \quad (46)$$

Integration of the preceding expression from B towards E yields

$$\int_{ib_3}^{z} dz = -\frac{\Psi_3}{V_3 \pi}\int_o^{\lambda}\frac{\exp Q}{(\lambda + 1)}d\lambda \quad \ldots\ldots\ldots\ldots\ldots\ldots\ldots\ldots\ldots\ldots \quad (47)$$

in which $\lambda = -\sin^2 \phi$; and $d\lambda = -2 \sin \phi \cos \phi \, d\phi$. On integration, the preceding expression yields:

$$z - ib_3 = \frac{2\Psi_3}{V_3 \pi}\int_o^{\phi} \exp Q \tan \phi \, d\phi \quad \ldots\ldots\ldots\ldots\ldots\ldots\ldots\ldots\ldots\ldots \quad (48)$$

Using Eq. 35, $\exp Q$ may be expressed as

$$\exp Q = \exp [i(\pi + f)] = -\exp (if) \quad \ldots\ldots\ldots\ldots\ldots\ldots\ldots\ldots\ldots\ldots \quad (49)$$

$$\text{in which} \quad f = \left\{\alpha - 2\left[\phi - \frac{(b-a)}{\sqrt{b(1+b)}} \arctan\left(\sqrt{\frac{1+b}{b}} \tan \phi\right)\right]\right\} \quad (50)$$

$$\text{Thus,} \quad (z - ib_3) = -\frac{2\Psi_3}{V_3 \pi}\int_o^{\phi} (\cos f + \imath \sin f) \tan \phi \, d\phi \quad \ldots\ldots\ldots\ldots \quad (51)$$

Separating the real and imaginary quantities gives the equations for the free-streamline in parametric form:

$$x = -\frac{2\Psi_3}{V_3 \pi}\int_o^{\phi} \cos f \tan \phi \, d\phi \quad \ldots\ldots\ldots\ldots\ldots\ldots\ldots\ldots\ldots\ldots \quad (52)$$

$$y = b_3 - \frac{2\Psi_3}{V_3 \pi}\int_o^{\phi} \sin f \tan \phi \, d\phi \quad \ldots\ldots\ldots\ldots\ldots\ldots\ldots\ldots\ldots\ldots \quad (53)$$

Eqs. 52 and 53 represent the coordinates of the points on the free-streamline in the z-plane with F as origin.

Further, since $\Psi_3 = b_3 V_3$, Eqs. 52 and 53 may be expressed in nondimensional form as

$$\frac{x}{b_3} = -\frac{2}{\pi}\int_o^{\phi} \cos f \tan \phi \, d\phi \quad \ldots\ldots\ldots\ldots\ldots\ldots\ldots\ldots\ldots\ldots \quad (54)$$

TABLE 4.—Dimensionless Coordinates of Points on Free-Streamline with F as Origin when Stagnation Point Lies along AC in Channel 2

$n_q = 0.1$ (1)	$n_q = 0.2$ (2)	$n_q = 0.3$ (3)	$n_q = 0.4$ (4)	$n_q = 0.5$ (5)	$n_q = 0.6$ (6)
(a) $\alpha = 30°$; $(b_1/b_3) = 1.0$; $(b_2/b_3) = 1.0$ (Limiting value of (y/b_3) at $n_g = 0.1$–0.5, is 0.8333, 0.8005, 0.7841, 0.7763, and 0.7729, respectively).					
(x/b_3) −0.0087	−0.0087	−0.0086	−0.0086	−0.0086	
−0.0361	−0.0359	−0.0358	−0.0358	−0.0357	
−0.0853	−0.0847	−0.0843	−0.0842	−0.0841	
−0.1608	−0.1595	−0.1588	−0.1585	−0.1583	
−0.2702	−0.2682	−0.2671	−0.2665	−0.2663	
−0.4285	−0.4257	−0.4241	−0.4233	−0.4230	
−0.6691	−0.6656	−0.6637	−0.6627	−0.6622	
−1.1000	−1.0961	−1.0939	−1.0927	−1.0922	
(y/b_3) 0.9956	0.9955	0.9955	0.9955	0.9955	
0.9839	0.9834	0.9831	0.9830	0.9830	
0.9671	0.9654	0.9646	0.9641	0.9639	
0.9470	0.9430	0.9410	0.9401	0.9396	
0.9249	0.9175	0.9137	0.9119	0.9111	
0.9021	0.8898	0.8836	0.8806	0.8793	
0.8790	0.8607	0.8515	0.8471	0.8451	
0.8561	0.8308	0.8181	0.8120	0.8094	
(b) $\alpha = 60°$; $(b_1/b_3) = 1.0$; $(b_2/b_3) = 1.0$ (Limiting value of (y/b_3) at $n_g = 0.1$–0.5, is 0.7144, 0.6586, 0.6216, 0.5960, and 0.5785, respectively).					
(x/b_3) −0.0058	−0.0057	−0.0056	−0.0056	−0.0056	
−0.0267	−0.0261	−0.0257	−0.0254	−0.0252	
−0.0684	−0.0667	−0.0654	−0.0645	−0.0638	
−0.1371	−0.1336	−0.1310	−0.1290	−0.1276	
−0.2413	−0.2357	−0.2314	−0.2282	−0.2258	
−0.3962	−0.3883	−0.3822	−0.3776	−0.3742	
−0.6348	−0.6250	−0.6173	−0.6115	−0.6072	
−1.0647	−1.0536	−1.0449	−1.0382	−1.0333	
(y/b_3) 0.9922	0.9921	0.9921	0.9920	0.9920	
0.9709	0.9704	0.9700	0.9697	0.9695	
0.9399	0.9379	0.9365	0.9355	0.9348	
0.9029	0.8978	0.8942	0.8916	0.8898	
0.8631	0.8527	0.8455	0.8404	0.8368	
0.8233	0.8050	0.7924	0.7836	0.7774	
0.7852	0.7562	0.7367	0.7230	0.7135	
0.7491	0.7073	0.6795	0.6601	0.6467	
(c) i$\alpha = 90°$; $(b_1/b_3) = 1.0$; $(b_2/b_3) = 1.0$ (Limiting value of (y/b_3) at $n_g = 0.1$–0.6, is 0.5443, 0.5290, 0.4824, 0.4470, 0.4196, and 0.3986, respectively).					
(x/b_3) −0.0015	−0.0015	−0.0014	−0.0013	−0.0013	−0.0012
−0.0123	−0.0116	−0.0111	−0.0102	−0.0102	−0.0098
−0.0414	−0.0392	−0.0374	−0.0346	−0.0346	−0.0334
−0.0979	−0.0933	−0.0894	−0.0832	−0.0832	−0.0809
−0.1925	−0.1845	−0.1779	−0.1673	−0.1673	−0.1632
−0.3408	−0.3292	−0.3194	−0.3038	−0.3038	−0.2979
−0.5795	−0.5608	−0.5482	−0.5281	−0.5281	−0.5204

TABLE 4.—*Continued*

(1)	(2)	(3)	(4)	(5)	(6)
−1.0043	−0.9869	−0.9722	−0.9488	−0.9488	−0.9400
(y/b_3) 0.9904	0.9904	0.9904	0.9904	0.9903	0.9903
0.9626	0.9624	0.9622	0.9620	0.9619	0.9618
0.9197	0.9184	0.9175	0.9167	0.9161	0.9156
0.8660	0.8623	0.8594	0.8571	0.8552	0.8537
0.8070	0.7982	0.7915	0.7861	0.7818	0.7784
0.7477	0.7303	0.7173	0.7071	0.6989	0.6926
0.6920	0.6620	0.6399	0.6228	0.6093	0.5988
0.5911	0.5949	0.5613	0.5356	0.5155	0.5000

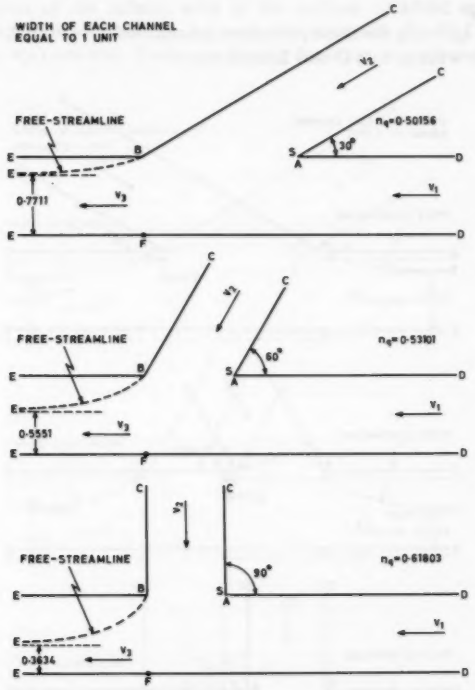

FIG. 5.—Free-Streamlines for 30°, 60°, and 90° Junctions when Stagnation Point S Coincides with Corner *A*

$$\frac{y}{b_3} = 1 - \frac{2}{\pi}\int_o^{\phi} \sin f \tan\phi \, d\phi \quad \ldots\ldots\ldots\ldots\ldots\ldots\ldots\ldots\ldots\ldots \quad (55)$$

III. Stagnation Point S Lying in Channel 2 Along Boundary AC.—Using the

Schwarz-Christoffel theorem, the shaded region of Q-plane of Fig. 4(*b*) can be transformed onto the upper half of the λ-plane as shown in Fig. 4(*c*). The corresponding expression for the transformation is

$$\frac{dQ}{d\lambda} = \frac{K(\lambda + a)}{(\lambda + b)\sqrt{\lambda(\lambda - 1)}} \quad \ldots\ldots\ldots\ldots\ldots\ldots\ldots\ldots\ldots\ldots \quad (56)$$

in which $\lambda = \cos^2 \phi$; $d\lambda = -2 \cos \phi \sin \phi \, d\phi$; and taking $\sqrt{-2} = -i$, the integration of Eq. 56 from B towards E yields

$$Q - i(\pi + \alpha) = -2iK\left[\phi - \frac{(b-a)}{\sqrt{b(1+b)}} \text{ arc tan}\left(\sqrt{\frac{b}{(1+b)}} \tan \phi\right)\right]_0^{\phi} \quad (57)$$

Further, it may be shown that for this case also the parameters K, a, and b satisfy Eqs. 36–38.

Again, by adopting the same procedure as indicated in section 2, the integration of Eq. 56 between points D and E leads to

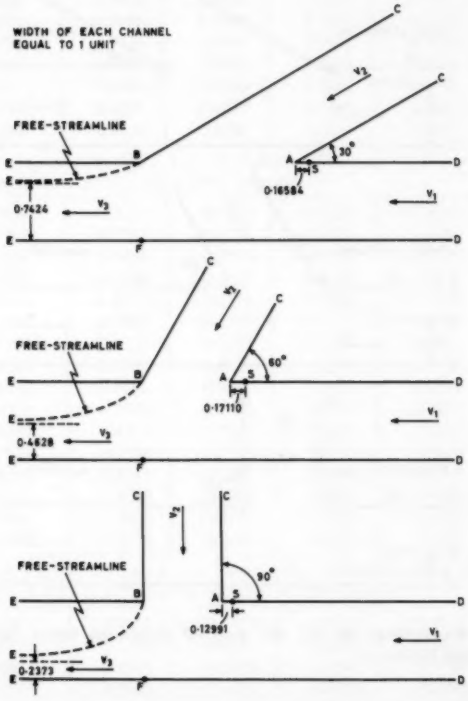

FIG. 6.—Free-Streamlines for 30°, 60°, and 90° Junctions when Stagnation Point S Lies in Channel 1 on Boundary AD, Discharge Ratio $n_q = 0.8$

$$\frac{V_3}{V_1} = (\sqrt{a} + \sqrt{1+a})^2 \left[\frac{\sqrt{b(1+a)} - \sqrt{a(1+b)}}{\sqrt{b(1+a)} + \sqrt{a(1+b)}}\right]^m \quad \ldots\ldots\ldots (58)$$

in which $m = (b-a)/\sqrt{b(1+b)} = (1 - \alpha/\pi)$ from Eq. 38.

The factor V_3/V_1 is representative of discharge ratio n_q, since $b_3 V_3/b_1 V_1 = 1/1 - n_q$. Thus, Eq. 58 may be expressed as

$$\frac{b_3 V_3}{b_1 V_1} = \frac{1}{(1-n_q)} = \frac{b_3}{b_1}(\sqrt{a} + \sqrt{1+a})^2 \left[\frac{\sqrt{b(1+a)} - \sqrt{a(1+b)}}{\sqrt{b(1+a)} + \sqrt{a(1+b)}}\right]^m \quad (59)$$

From Eqs. 38 and 59, for given values of α, n_q, and b_1/b_3, the values of the parameters a and b can be obtained for this case.

Next, for this case also, a relationship between w and λ may be found which maps the interior of the infinite strip in the w-plane onto the upper half of the λ-plane, with correspondence between the points B, E, F, D, and C as shown in Figs. 4(*d*) and 4(*e*). Further, adopting the same procedure as in section

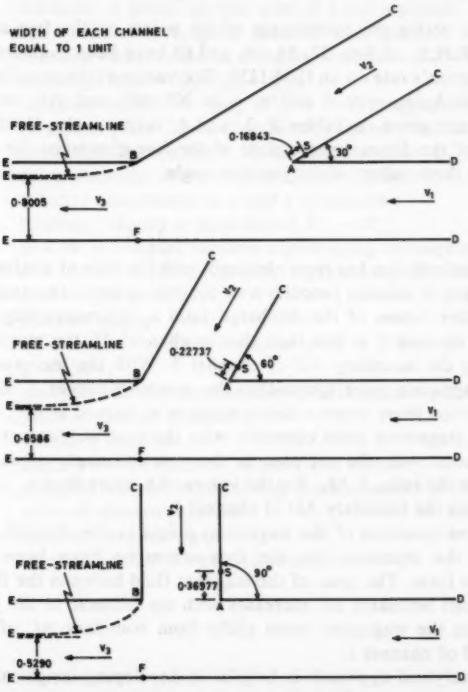

FIG. 7.—Free-Streamlines for 30°, 60°, and 90° Junctions when Stagnation Point S Lies in Channel 2 on Boundary AC, Discharge Ratio $n_q = 0.2$

2, gives the equations for the free-streamline for this case in parametric form:

$$x = -\frac{2\Psi_3}{V_3\pi}\int_o^{\phi} \cos f \tan\phi \, d\phi \quad \ldots\ldots\ldots\ldots\ldots\ldots\ldots\ldots \quad (60)$$

$$y = b_3 - \frac{2\Psi_3}{V_3\pi}\int_o^{\phi} \sin f \tan\phi \, d\phi \quad \ldots\ldots\ldots\ldots\ldots\ldots\ldots\ldots \quad (61)$$

$$\text{in which} \quad f = \left\{\alpha - 2\left[\phi - \frac{(b-a)}{\sqrt{b\,(1+b)}} \arctan\left(\sqrt{\frac{b}{(1+b)}}\tan\phi\right)\right]\right\} \quad (62)$$

Further, since $\Psi_3 = V_3 b_3$, Eqs. 60 and 61 may be expressed in nondimensional form as

$$\frac{x}{b_3} = -\frac{2}{\pi}\int_o^{\phi} \cos f \tan\phi \, d\phi; \quad \frac{y}{b_3} = 1 - \frac{2}{\pi}\int_o^{\phi} \sin f \tan\phi \, d\phi \quad \ldots\ldots\ldots \quad (63)$$

In order to obtain the coordinates of the points on the free-streamline, the integrals on R.H.S. of Eqs. 32, 54, 55, and 63 have been evaluated numerically by using Simpson's rule on an IBM 1130. The values of the coordinates obtained for b_1/b_3 and b_2/b_3 = to 1 and α = to 30°, 60°, and 90°, for each of the three cases, are given in Tables 2, 3, and 4, respectively. Further, Figs. 5–7 show some of the dimensionless plots of the free-streamline for each of these cases for the three values of the junction angle.

Conclusions

An analytical solution has been obtained, with the help of conformal mapping, for the problem of channel junction with combining flow. The analysis indicates that for smaller values of the discharge ratio n_q (corresponding to which the discharge in channel 2 is less than that in channel 1), the stagnation point is located along the boundary AC of channel 2. With the increase in the value of n_q, the stagnation point approaches the upstream corner A of the junction. For each junction there exists a unique value of n_q termed as $n_{q_{cr}}$, corresponding to which the stagnation point coincides with the upstream corner A. The value of $n_{q_{cr}}$ increases with the increase in the junction angle α, as well as with the increase in the ratio, b_2/b_3. For the values of n_q more than $n_{q_{cr}}$, the stagnation point lies along the boundary AD of channel 1.

For different locations of the stagnation points in the channel junctions, the solutions of the equations for the free-streamline have been presented in dimensionless form. The zone of the stagnant fluid between the free-streamline and the channel boundary BE increases with the increase in the junction angle α, and also as the stagnation point shifts from boundary AC of channel 2 to boundary AD of channel 1.

Such an analytical approach is helpful in developing insight about the flow behavior at the junction. It also presents quantitative conclusions which could be compared with model studies in order to understand the effect of the assumptions made in the analytical development.

Acknowledgment

The work presented in this paper forms part of the doctoral thesis of the senior writer. The encouragement given by the Principal, Malaviya Regional Engineering College, Jaipur, is gratefully acknowledged.

Appendix I.—References

1. Copson, E. T., "Theory of Function of a Complex Variable," *Oxford University Press*, Oxford, England, 1961, p. 141.
2. Greated, C. A., "A Theoretical Study of Flow Behaviour at Open-Channel Junctions," *Research Report No. 6*, University of Southampton, Department of Civil Engineering, England, Feb., 1964.

Appendix II.—Notation

The following symbols are used in this paper:

a, b = distances of points on real axes of ζ and λ planes;
b_1, b_2, b_3 = bed-widths of rectangular channels 1, 2, and 3;
K = constant which could be complex number = $K_1 + iK_2$;
n_q = discharge ratio = $Q_2/(Q_1 + Q_2)$;
Q = complex variable = $[\log (V_3/v) + i\theta]$ representing a transformation plane for boundaries of channel junction;
Q_1, Q_2, Q_3 = discharges in channels 1, 2, and 3 ($Q_1 + Q_2 = Q_3$);
V_1, V_2, V_3 = mean velocities of flow in channels 1, 2, and 3;
V_x, V_y = velocity components in x and y directions;
v = filament velocity = modulus of $V_x - iV_y$;
w = $\phi + i\Psi$ = complex variable representing rectangular flow field;
z = $x + iy$ = complex variable representing physical plane for channel junction;
α = junction angle;
ϵ = infinitesimal distance on either side of points on real axis of ζ, λ plane;
ζ = complex variable representing transformation plane for boundaries of channel junction;
η, ϕ = auxiliary variables;
θ = angle between filament velocity and channel 1;
λ = complex variable representing transformation plane for boundaries of channel junction;
ξ = auxiliary variable; and
Ψ_3 = stream function for free-streamline.

DISCUSSION

Note.—This paper is part of the Journal of the Hydraulics Division, Proceedings of the American Society of Civil Engineers, ©ASCE, Vol. 107, No. HY12, December, 1981. ISSN 0044-796X/81/0012-1737/$01.00.

Discussions

Discussions may be submitted on any Proceedings paper or technical note published in any *Journal* or on any paper presented at any Specialty Conference or other meeting, the *Proceedings* of which have been published by ASCE. Discussion of a paper/technical note is open to anyone who has significant comments or questions regarding the content of the paper/technical note. Discussions are accepted for a period of 4 months following the date of publication of a paper/technical note and they should be sent to the Manager of Technical and Professional Publications, ASCE, 345 East 47th Street, New York, N.Y. 10017. The discussion period may be extended by a written request from a discusser.

The original and three copies of the Discussion should be submitted on 8-1/2-in. (220-mm) by 11-in. (280-mm) white bond paper, typed double-spaced with wide margins. The length of a Discussion is restricted to two *Journal* pages (about four typewritten double-spaced pages of manuscript including figures and tables); the editors will delete matter extraneous to the subject under discussion. If a Discussion is over two pages long it will be returned for shortening. All Discussions will be reviewed by the editors and the Division's or Council's Publications Committees. In some cases, Discussions will be returned to discussers for rewriting, or they may be encouraged to submit a paper or technical note rather than a Discussion.

Standards for Discussions are the same as those for Proceedings Papers. A Discussion is subject to rejection if it contains matter readily found elsewhere, advocates special interests, is carelessly prepared, controverts established fact, is purely speculative, introduces personalities, or is foreign to the purposes of the Society. All Discussions should be written in the third person, and the discusser should use the term "the writer" when referring to himself. The author of the original paper/technical note is referred to as "the author."

Discussions have a specific format. The title of the original paper/technical note appears at the top of the first page with a superscript that corresponds to a footnote indicating the month, year, author(s), and number of the original paper/technical note. The discusser's full name should be indicated below the title (see Discussions herein as an example) together with his ASCE membership grade (if applicable).

The discusser's title, company affiliation, and business address should appear on the first page of the manuscript, along with the *Proceedings* paper number of the original paper/technical note, the date and name of the *Journal* in which it appeared, and the original author's name.

Note that the discusser's identification footnote should follow consecutively from the original paper/technical note. If the paper/technical note under discussion contained footnote numbers 1 and 2, the first Discussion would begin with footnote 3, and subsequent Discussions would continue in sequence.

Figures supplied by the discusser should be designated by letters, starting with A. This also applies separately to tables and references. In referring to a figure, table, or reference that appeared in the original paper/technical note use the same number used in the original.

It is suggested that potential discussers request a copy of the *ASCE Authors' Guide to the Publications of ASCE* for more detailed information on preparation and submission of manuscripts.

Heat Loss from Sidearms of Cooling Lakes[a]

Closure by Terry W. Sturm,[5] A. M. ASCE
and John F. Kennedy,[6] M. ASCE

The writers are gratified by Jain's (11) use of their numerical results and the verification he obtained of their proposed correlations for surface heat loss from cooling-lake sidearms. The contention by Jain and Yildirim that the boundary condition, $(T)_{\eta=0} = T_o$, is incorrect requires some clarification and comment. One of the principal advantages of the Kármán-Pohlhausen approach to numerical analysis of equations of the boundary-layer type, which was used by the writers, is that it is unnecessary to know precisely the vertical distributions of the variables of interest (temperature and velocity in the present instance), but only to reproduce their essential features. The experiments conducted by the writers were used as a guide in selecting an acceptable profile shape, shown in Fig. 2, for the vertical temperature distribution, which then was used in the Kármán-Pohlhausen analysis of the equations. Although the experimental results exhibited some small longitudinal variation in the temperature at $\eta = 0$, the experiments verified that the condition $(T)_{\eta=0} = T_o$ is approximately correct, and no more than this was claimed by the writers. An ordering analysis of the continuity equation and the equations of motion clearly shows that a representative vertical velocity V is of order δU, where $\delta = D/L$ and U is a representative horizontal velocity (10). The authors imposed the restriction $L >> D$ or $\delta << 1$ in their analysis, in which case the vertical velocity is much smaller than the horizontal velocity. Now in the main reach of the sidearm, where the flow is nearly parallel and for the case of $\lambda_T \geq \lambda$, it is apparent from Fig. 3 that the temperature of the fluid convected from the inflow current downward to the outflow current is nearly equal to T_o at the point $\eta = \lambda$, in which the vertical velocity attains its maximum but is still much smaller than the characteristic velocity U. Furthermore, vertical turbulent diffusion downward into the outflow current from the inflow current is inhibited by the strong vertical stratification in the main reach of the sidearm. The vertical heat transfer is dominated by the heat loss at the water surface, and the experimental temperature profiles shown in Fig. 4 reflect this overriding influence.

The equations developed by Jain and Yildirim can also be used to develop a line of reasoning that differs from theirs, as follows. Eq. 63 shows that $(\theta'')_{\eta=0} = 0$, and the condition $(\theta)_{\eta=0} = 0$ in Eq. 64 would require that $(\theta''')_{\eta=0} = 0$ as well. However, Eq. 62 shows that the denominator of Eq. 65 then is also zero, so $(f'')_{\eta=0}$, and therefore $(\partial u/\partial y)_{y=0}$, may have finite, determinate values. Viewed more simply, Eq. 62 shows that $(\theta)_{\eta=0} = 0$ is compatible if k_m approaches the constant fluid viscosity near the wall and f is no more than a third-degree

[a]May, 1980, by Terry W. Sturm and John F. Kennedy (Proc. Paper 15398).
[5]Asst. Prof., School of Civ. Engrg., Georgia Inst. of Tech., Atlanta, Ga.
[6]Dir. and Prof., Iowa Inst. of Hydr. Research, The Univ. of Iowa, Iowa City, Iowa.

polynomial, or $(f^{iv})_{\eta=0}$ is otherwise zero. In other words, the discussers' relations are not incompatible with $(\theta)_{\eta=0} = 0$.

Finally, it should be emphasized that the writers' results were not generated just for use with sidearms having lengths greater than or equal to equilibrium length, but were intended also for sidearms with $L < L_e$, in which case the equilibrium length results merely provide convenient length and heat-loss scales for sidearms of length $L < L_e$, as shown by Fig. 8. In this case, the vertical velocities become large in the closed end reach as a result of the fixed boundary. The inflow current is abruptly deflected and returns along the bottom as the outflow. It is in the relatively short closed-end reach that these large downflow currents establish the value of T_o which is then advected along the sidearm bottom by the outflow current. This was confirmed by the writers' experimental results which showed that $(\theta)_{\eta=0} = 0$ is a good approximation for $L < L_e$.

Errata.—The following correction should be made to the discussion by Jain and Yildirim (April, 1981):

Page 523, Ref. 11: Should read "*Journal of the Energy Division,*" instead of "*Journal of the Hydraulics Division,*"

Transverse Mixing Tests in Natural Streams[a]

Closure by Spyridon Beltaos[3]

The writer thanks Fischer for his interest in the paper. The discussion focuses on two items: (1) Concern about the accuracy of the transverse mixing coefficients reported in the paper; and (2) a theoretical explanation offered by the discusser of why H rather than R gives somewhat more consistent results when nondimensionalizing E_z.

Under item (1), the discusser voiced several objections to the approach used in the paper but has not explicitly stated whether he considers these objections sufficiently serious to render the reported coefficients unacceptable from the engineering point of view. The writer is inclined to discount this possibility: If the contrary were true, the discusser would not have attempted to theoretically explain the writer's results (refer to item 2) since such an attempt would, in that case, have been meaningless.

Before dealing with items (1) and (2) in detail, the writer would like to establish a few basic points. Firstly, it must be recognized that ϵ_{zd}, ϵ_z, and E_z are *not*

[a]October, 1980, by Spyridon Beltaos (Proc. Paper 15731).

[3]Research Scientist, Environmental Hydr. Section, Hydr. Div., National Water Research Inst., Canada Centre for Inland Waters, Burlington, Ontario; formerly Research Officer, Alberta Research Council, Edmonton, Canada.

directly measurable quantities in the sense that flow depth, e.g., is measurable at a point. These coefficients can only be estimated as those values which optimize agreement between measured concentrations and those predicted via an analytical or numerical solution of a differential equation, such as Eqs. 1 and 2. (Note that these equations already involve several assumptions and approximations; with these assumptions, they can be derived from a more general 3-dimensional equation by a depth-averaging operation—see also Ref. 10.) The selected value of a coefficient will thus depend on the computational algorithm used if a numerical solution is pursued or on the simplifying assumptions made in deriving an analytical solution. All coefficients so determined are "accurate" if applied in conjunction with the corresponding method and "inaccurate" if used in conjunction with a method other than the one employed in their evaluation. It thus seems to the writer that the question at hand is not so much one of "accuracy" but, rather, of "acceptability." For example, if a numerical algorithm or an analytical solution involve assumptions that contradict established knowledge or experience and if such contradictions have a significant effect on the solution, they should be discarded even if they occasionally succeed in producing "good" predictions by manipulating the coefficients. Those methods that are free of such shortcomings are acceptable while the final choice will depend on proven performance under varied conditions and on ease of application. In the subject of transverse mixing, a final choice of this type has yet to be made. (One of the aims of the paper was to contribute *toward* making a final choice and not to advocate what *the* final choice should be.)

Several algorithms have been developed to numerically solve Eq. 2 (or its meandering channel version—see Ref. 18, e.g.), including the one mentioned by the discusser. On the analytical side, two basic methods have been developed: (1) The constant velocity-depth-E_z-method (see also Ref. 27) that leads to Eq. 21; and (2) the streamtube method that has been used in the paper. The former method clearly contradicts experience and is not popular at present. The streamtube method also contradicts experience ($h^2 u_d \epsilon_{zd}$ varies across a stream) but this contradiction does not seriously affect the solution, as shown in Ref. 17 and as additional evidence will show later in this closure. (As one illustration of the latter method's superiority over the former, one may compare the scatter of the paper's σ_η^2 versus $\int_0^x f dx$ graphs versus that of σ_z^2 versus x graphs given in previous literature, such as Ref. 16, e.g.; other illustrations may be found in Ref. 17.) Clearly, numerical solutions have the advantage of not requiring any obvious compromises in logic, other than those involved in deriving the differential equation that is being solved; however, they are far from being "exact" solutions because of the following major shortcomings:

1. The region of computation must be discretized, i.e., an equation that is derived for an infinitesimally small stream volume is applied to elements of finite and sometimes large volume. This inevitably introduces errors and leads to a dependency of the evaluated mixing coefficient on the particular algorithm used.
2. If a significant advantage is to be gained from a numerical scheme's ability to deal with variable h and u_d, then these quantities should be known throughout the region of computation. In practice, however, transverse variations of h and u_d are only known at a few cross sections that are considered "representative."

(This is caused by practical limitations: e.g., to obtain adequate depth and velocity information at, say, 15 points across a stream, a crew of three experienced persons using a boat for access require two to three hours; this is not counting "unproductive" work time, i.e., travel, boat loading, and launching etc.) Between "metered" cross sections, h and u_d are generated by some kind of interpolation technique; however, the detailed river geometry does not obey neat mathematical laws and thus one can only hope that the errors introduced by such interpolations do not appreciably affect the results. As an illustration, consider the following quotation, taken from the discusser's suggested example (16) for a 33,000 ft long reach of the Missouri River.

> On the basis of *the two measured sections*, the following velocity distributions were assumed: For the reach from the injection point to measuring station 5 (at the end of the bend to the left), the velocity distribution measured upstream from the injection point was assumed to apply to all sections. At mile 645 the measured velocity distribution was used, except that the 70-ft width of shallow water near the left bank was omitted as being, from visual observations, not representative of the reach. At a point halfway from section 8 to section 9, the velocity distribution was assumed to be the inverse of the distribution at mile 645; that is, the same velocities and depths were used as at mile 645, except that distances measured from the right bank were assumed to be measured from the left bank. At station 10 (in the middle of a bend to the right), the velocity distribution was assumed to be the mirror image of the velocity distribution upstream from the injection point, except that at this point the width of the stream is only 510 ft, so that all transverse distances were reduced by the factor 510/600 and all depths were increased by the inverse of the same factor. For cross sections between the above sections, depths, widths, and velocities were interpolated linearly from the nearest assumed distributions.

(Italics placed by the writer.) Where so many unverified and subjective assumptions are introduced, one may reasonably ask what happens then to the "accuracy" of E_z? It is also reasonable to remark that, where such gross approximations are considered acceptable, it is only a very small additional compromise that one has to make in order to use the streamtube method (which on many occasions has been found to perform adequately). This compromise is done in exchange of the many advantages of analytical solutions, i.e., incomparably easier application; plus an ability to provide the designer with a complete appreciation of the effects of various pertinent factors without having to perform a separate numerical computation for each possible combination of such factors. (It is noted here that, usually, more than two cross sections are metered for any particular test, the number varying up to about 10. This, however, only moderates the basic deficiency identified in the foregoing: The region of unknown stream geometry and flow properties is still orders of magnitude greater than that of known geometry and flow properties.)

With this background, the discusser's comments are now considered in detail:

1. The discusser states "In earlier work (16) the author has also used the

stream tube method to ascertain the value of E_z, but did not require the assumption that $h^2 u_d \epsilon_{zd}$ is constant." (By the term "the author" the discusser must be referring to himself and not to the writer because Ref. 16 is authored by Yotsukura, Fischer, and Sayre.) The writer would like to clarify that his use of the term "streamtube method" implies the mathematical transformation that results when z is substituted by q *and* the subsequent analytical solution that is afforded when the assumption $h^2 u_d \epsilon_{zd} = \text{const}$ is made (see also text following Eq. 9).

2. The discusser states, as a matter of *fact*, that "$\epsilon \approx u_* h \approx h^{3/2}$." (Note that the "proportional to" sign, $\propto$, is more appropriate here than the "approximately equal" sign, $\approx$.) The only *fact* in this case is that putting $\epsilon_{zd} \propto u_* h \propto h^{3/2}$ is only one of a multitude of possible hypotheses concerning the variation of ϵ_{zd} across a stream; the basic cause of this state of affairs is the previously mentioned fact that ϵ_{zd} cannot be directly measured at a point. For two-dimensional flow ($h = \text{const} = H$; $u_d = \text{const} = V$; and $u_* = \text{const} = V_*$), it has been established that $\epsilon_{zd} \propto u_* h = V_* H$. This finding does not *necessarily* lead to the discusser's extrapolation to channels in which h, u_d, and u_* vary with z. The *only logical* conclusion that results from the two-dimensional flow findings may be articulated as:

> The depth-averaged transverse mixing coefficient ϵ_{zd} is an unknown function of z (or of q); in the case of two-dimensional flow, this function becomes a constant and this constant is proportional to $V_* H$.

The discusser's assumed functional relationship is "possible" because it satisfies the aforementioned requirement, but it is by no means the *only* possible assumption. In strict logical terms, there exists an infinite number of such "possible" relationships (e.g., put $\epsilon_{zd} \propto V_* H f(h/H)$ with $f(h/H)$ being *any* "well behaved" function of h/H). Of this multitude, a few "plausible" functions have been suggested and studied in the past decade. For example, Ref. 10 gives the following possibilities:

$\epsilon_{zd} \propto V_* H$	(ϵ_{zd} does not vary across the stream)
$\epsilon_{zd} \propto u_d h$	(ϵ_{zd} varies across the stream)
$\epsilon_{zd} \propto u_* h$	(discusser's extrapolation)

The following quotation from Ref. 10 is particularly pertinent at this point:

> It is recognized that there are dangers in using equations like Eq. 18 and 19 (writer's note: means equations like the foregoing) because their derivation makes a local application of relationships which were obtained for cross-sectional average values. In presenting these equations, it is not felt that they necessarily represent the exact variation of K_z (writer's note: K_z is equivalent to ϵ_{zd}). Rather, they are represented as possible assumptions.

Though ϵ_{zd} cannot be measured directly, considerable indirect evidence concerning the variation of ϵ_{zd} is available in the literature, as described next.

(i) Holly and Simons (23) studied the comparative merits of various possible

functional dependencies of ϵ_{zd} in a triangular laboratory channel; this rather extreme cross-sectional geometry was deliberately chosen so as to produce strong lateral variations of h, u_d, and u_*.

Three possibilities for ϵ_{zd} were considered, i.e.: (1) $\epsilon_{zd} \propto H^{3/2} = \text{const}$; (2) $\epsilon_{zd} \propto u_d h = \text{variable}$; and $\epsilon_{zd} \propto h^{3/2} = \text{variable}$: discusser's postulate. The governing differential equation was solved numerically for each of these cases and the predictions were compared against the test results. The outcome was conclusively in favor of the constant ϵ_{zd} assumption as may be seen in the abstract of that paper:

Turbulent dispersion experiments in a triangular laboratory channel suggest that the transverse diffusivity does not vary with transverse position as previously suggested. The invariance of the diffusivity may reflect an interaction between mixing due to bed shear and due to transverse shear, the relative contributions of which cannot be determined.

(ii) A similar study with trapezoidal prismatic channels by Lau and Krishnappan (25) concludes:

The results of numerical simulations using different assumptions for the variation of e_z (writer's note: e_z is equivalent to ϵ_{zd}) across a channel showed that none of the assumptions appeared to be definitely superior. For the sake of convenience and because of the availability of published data, it is suggested that e_z should be considered constant across the channel at this time.

(Writer's note: this finding does not necessarily moderate the strong evidence presented by Holly and Simons (23) in favor of the constant $-\epsilon_{zd}$ assumption; it is likely that the superiority of this assumption was not as evident in the case of Ref. 25 because the channel geometry was close to that of a two-dimensional channel.)

The previously mentioned investigations deal with straight prismatic channels where ϵ_{zd} should be mostly diffusive (though dispersive effects may well be present due to secondary currents that occur even in straight channels). Dispersive effects introduced by stream curvature and the associated helical flows have not been considered so far. The following pertinent findings with meandering channels.

(iii) The effects of meanders on transverse mixing were studied in a rectangular meandering flume by Chang (22). Of particular interest is Chang's Fig. 43 where the *dispersive* part of E_{zd} (defined by ϵ_{zD} in Eq. 11 of the paper) was plotted versus z in a nondimensional form. The data points showed considerable scatter but no consistent variation. The coefficient ϵ_{zD} was calculated from measurements according to the well-known and widely-used hypothesis: $\epsilon_{zD} = -(w'C')_d/(\partial C_d/\partial Z)$ in which $w' = w - w_d$; w = local lateral velocity component; $C' = C - C_d$; C = local concentration. (For steady-state conditions, C and w may be considered time-averaged values; for unsteady conditions, they are defined as ensemble averages.)

(iv) Krishnappan and Lau (24) noted that meandering flumes with rectangular

cross sections do not adequately represent natural stream conditions. To better reproduce typical river geometries, they used a meandering flume with "equilibrium" bed (i.e., the bed was initially mobile and its final configuration was formed by the flow itself). Again, several possible variations of E_{zd} were examined, including the assumption E_{zd} = const. It was found that the latter yielded the most consistent results and thus it was concluded that, for all practical purposes, the transverse mixing coefficient can be assumed to be constant across the stream.

(v) Recently, Lau and Krishnappan (26) performed a comprehensive comparison of various assumptions for E_z, using the results of a field test as the basis of evaluation. The governing differential equation for meandering flow was first transformed to x and q coordinates and then solved by a numerical scheme. The diffusion factor D_z (see Eq. 10 of the paper) was assumed to take five different forms; of these, two are particularly pertinent at present, viz:

$$D_z = (h^2 u_d m_x) E_z; \quad E_z = \text{const} \quad \ldots \quad (27)$$

$$D_z = (h^2 u_d m_x) (\alpha V_* h); \quad \alpha = \text{const} \quad \ldots \quad (28)$$

In Eq. 28, E_{zd} is assumed to vary in proportion to h rather than $u_* h$ as hypothesized by the discusser but this variation is much closer to the discusser's hypothesis than to the constant $-E_{zd}$ assumption. If the discusser's hypothesis were true, Eq. 28 would give better results than Eq. 27. However, Ref. 26 shows that there is no difference in the respective prediction abilities of Eqs. 27 and 28.

The above evidence is indirect and thus does not conclusively "prove" that the transverse mixing coefficient is indeed constant across a stream. However, this evidence strongly suggests that even if E_{zd} varies across a stream, its variation must be mild and nowhere near the $h^{3/2}$ proportionality that the discusser has stated as a fact. It thus makes good engineering sense to use a constant E_{zd} since this assumption not only "works" in practice but also happens to be the simplest.

3. The preceding discussion renders practically irrelevant the discusser's objections concerning the definition of ψ and the validity of Eqs. 6, 7, and 12. Academically speaking, even if ϵ_{zd} is assumed to vary with z (or with q), the resulting correlation term can be absorbed in the definition of e_z which will then differ from ϵ_{zd}. Eq. 8 is indeed incorrect, as may be seen by a check of the dimensions of the two sides. The correct form is given in the "Errata," at the end of this closure.

4. The quantity $h^2 u_d \epsilon_{zd}$ does vary with z (or q) as pointed out by the discusser though not as h^4 but more likely as $h^{2.5}$. The discusser is referred to the text following Eq. 4 where it is stated that, even though $h^2 u_d \epsilon_{zd}$ *does vary* with q, this variation does *not greatly influence* the solution of Eq. 4. Such fortunate coincidences are not uncommon in engineering and it is a good practice to exploit them. Since Yotsukura and Cobb's (17) first evidence in favor of this assumption, additional evidence has been published (14,26). Briefly, this information shows again that the transverse variation of $h^2 u_d \epsilon_{zd}$ does not significantly affect the solution of the governing differential equation; more serious is the *longitudinal* variation of $h^2 u_d \epsilon_{zd}$ which we have no way of even guessing at

present. Even the latter effect, however, is small compared to the range of uncertainty that must be allowed for in pertinent designs. The methods used in the paper provide estimates of reach-averaged values of E_z; investigation of the longitudinal variation of E_z was not attempted. (An illustration of the latter is however given implicitly in Figs. 6, 8, 10, and 11: e.g., join individual data points by a continuous curve and consider how much the slope of this

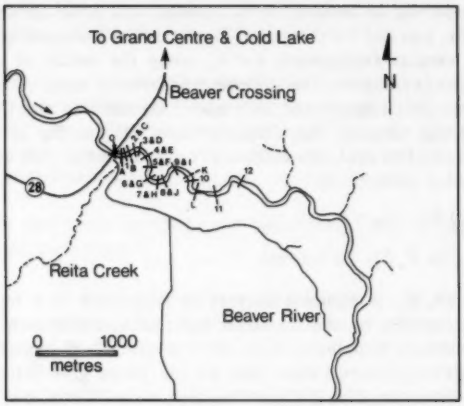

FIG. 14.—Reach of Tests 3 and 4 (Test 3; Sites 1–12; Test 4: Sites A–L)

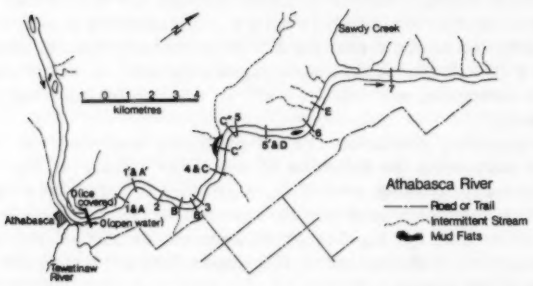

FIG. 15.—Reach of Tests 5 and 6 (Test 5: Sampling at Sites 1–7; Test 6: Sampling at Sites A–E; Primes Denote Additional Metered Sites)

curve at any one value of the abscissa deviates from the slope of the straight line that has been drawn.)

5. There is one instance where the streamtube method may not produce satisfactory results, i.e., where a plume is mostly within a region very near a river bank where (usually) maximum lateral gradients of h occur. Such conditions generally prevail for short distances downstream of side sources. If accurate predictions are required in such regions, it might be advisable to use a numerical

solution where E_{zd} may be taken equal to the reach-average value but h and u_d are allowed to vary as measured.

6. Maps of the test reaches for tests 3–4 and 5–6 are given in Figs. 14 and 15. At the same time, it is pointed out that Ref. 2 may be obtained simply by addressing an ordinary reprint request to: Transportation and Surface Water Engineering Department, Alberta Research Council, 4th Floor, Terrace Plaza Office Tower, 4445 Calgary Trail South, Edmonton, Alta., Canada, T6H 5R7.

7. The discusser's explanation concerning the use of H in place of R would have been satisfactory had the experiments been performed in straight prismatic channels. In such instances, one may reasonably expect that E_z reflects mostly (though not entirely) diffusion caused by the random motions of turbulence, whereby the discusser's arguments about length and velocity scales follow logically. However, the writer's experiments were performed in *natural streams* where, as is well known and as pointed out in the paper, a large part of E_z reflects dispersive effects caused by helical motions. The discusser himself was one of the first investigators to identify and study this effect (8). Because transverse dispersion of this kind has little to do with turbulence, the writer does not consider the discusser's explanation satisfactory.

8. Finally, the writer objects to the discusser's statement "The author's use of R implies that the effect of the ice cover is to halve the length scale of the turbulence." The suggested implication is purely the result of the discusser's own interpretation. The writer listed $E_z/RV_* (= K_z)$ in Table 1 simply because this enables a direct comparison with the finding of Ref. 6 where $K2_z$ was about the same for both open-water and ice-covered conditions. The writer has nowhere endorsed this idea and the discusser is reminded of the following sentences, quoted from p. 1622:

> However, inspection of Table 1 shows that values of K_z are larger under an ice cover than with open water flow by as much as two and one-half times. It is probably premature to attempt an explanation of this finding, however, it is believed that much may be learned by studying the helical bend flow under an ice cover (see also Ref. 8).

APPENDIX.—REFERENCES

22. Chang, Y., "Lateral Mixing in Meandering Channels," thesis presented to the University of Iowa, at Iowa City, Iowa, in 1971, in partial fulfillment of the requirements for the degree of Doctor of Philosophy.
23. Holly, F. M., Jr., and Simons, D. B., "Transverse Mixing of Neutrally-Buoyant Tracers in Nonrectangular Channels," *Proceedings of the XVIth Congress of the International Association for Hydraulic Research*, 1975, Vol. 3, pp. 467–474.
24. Krishnappan, B. G., and Lau, Y. L., "Transverse Mixing in Meandering Channels with Varying Bottom Topography," *Journal of Hydraulic Research*, International Association for Hydraulic Research, Delft, the Netherlands, Vol. 15, 1977, No. 4, pp. 351–371.
25. Lau, Y. L., and Krishnappan, B. G., "Transverse Dispersion in Trapezoidal Channels," *Proceedings of Transport Processes and River Modeling Workshop*, held at the National Water Research Institute, Burlington, Ontario, Canada, in 1978.
26. Lau, Y. L., and Kishnappan, B. G., "Modeling Transverse Mixing in Natural Streams," *Journal of the Hydraulics Division*, ASCE, Vol. 107, No. HY2, Proc. Paper 16048, Feb., 1981, pp. 209–226.
27. Sayre, W. W., and Chang, F. M., "A Laboratory Investigation of Open-Channel

Dispersion Processes for Dissolved, Suspended, and Floating Dispersants," *United States Geological Survey Professional Paper 433-E*, United States Geological Survey, Washington, D.C., 1968, 71 p.

Errata.—The following corrections should be made to the original paper:

Page 1609, first line after Eq. 5: Should read ". . . q denotes an . . ." instead of ". . . q = an . . ."

Page 1609, Eq. 8 should read " . . . $\frac{1}{Q}\int_o^Q \left(\frac{h}{H}\right)^2 \left(\frac{u_d}{V}\right) dq$" instead of "... $= \frac{1}{Q}\int_o^Q h^2 u_d\, dq$"

Page 1613, 5th line after Fig. 2: should read "adjusted" instead of "adjuusted"

Page 1614, Table 1, Column 8: Should read "1.44 -11- 2.1[a] -11- 3.1[a] -11-" instead of "1.44 11 2.1[a] 11 3.1[a] 11"

Page 1614, 5th line from bottom: Should read "reasonably" instead of "reasonable"

Page 1617, Table 2, Column 6: Should read "$\int_o^x$" instead of "$\int_\sigma^x$"

Page 1617, 7th line from bottom: Should read "hydraulic" instead of "hydralic"

Page 1620, 9th line from top: Should read ". . . in a single . . ." instead of ". . . in single. . . .".

Sedimentation in Iron Gates Reservoir on The Danube[a]

Discussion by S. Bruk,[3] M. ASCE, Vera Miloradov,[4] and V. Milišić[5]

Sedimentation in Iron Gates Reservoir has been the preoccupation of writers for many years. The first forecast of sedimentation was made in 1962, at an early stage of the design, and since then investigations have continued to the present. Several papers have been published on this, but only a few of them in easily accessible international periodicals. The writers wish, therefore, to commend the author for bringing up this topic in the ASCE Journal.

The investigations can be divided into two phases: (1) The first, before the construction of the dam, which led to the formulation of the mathematical model and a preliminary forecast of reservoir sedimentation (5); and (2) the

[a]October, 1980, by Vlad Focsa (Proc. Paper 15782).

[3]Deputy Dir., Jaroslav Černi Inst., Belgrade, Yugoslavia.
[4]Former Head of Dept., Jaroslav Černi Inst., Belgrade, Yugoslavia.
[5]Asst., Prof., Faculty of Civ. Engrg., Subotica, Yugoslavia.

second phase, after completion of the dam, which consists of field measurements and research work for the improvement of predictions of reservoir sedimentation. The writers particularly wish to discuss this second phase of the research work, which is partly reflected in the references at the end of this discussion.

Suspended Load Measurements.—Suspended load is the main factor of morphology of the river reach in question, as can be seen from the considerable overlapping of grain sizes found in the bed material and also carried in suspension. Great attention has, therefore, been given to developing reliable methods for suspended load measurement.

In the first years of the program, standard sampling methods were used with the usual one liter sampler, as described also by the author. However, the results were rather unsatisfactory; the vertical distribution of sediment concentrations was random and irregular, and the amount of sediment in the sample was too small for grain size analysis, which is crucial in sedimentation calculations. Thus, use of the one liter samplers was abandoned on the Yugoslav side more

TABLE 13.—Data Summary

Year (1)	Input (2)	Output (3)	Deposited (4)	Mean discharge Q, in meters per second (5)
	in millions of tons of sediment			
1972	27.4	2.3	25.1	4,991
1973	31.3	1.9	29.4	4,490
1974	30.7	4.3	26.4	6,384
1975	20.0	3.6	16.6	6,056
1976	21.7	3.1	18.6	5,206
1977	16.4	4.4	12.0	6,031
1978	23.2	3.7	19.5	5,951
1979	19.9	5.0	14.9	6,363
Total	190.6	28.1	162.5	
%	100	14.74	85.26	

than 15 years ago. A new type of sampler was developed in the Jaroslav Černi Institute, which has been in use ever since (14–15). It consists of a vacuum tank and a suction pipe, with a nozzle mounted on the weight of the current meter. The volume of samples varies between 10 and 14 L, depending on the concentration of sediments (of the order of 20–300 ppm). The sampling is done simultaneously with velocity measurements using the current meter, so that information is obtained on sediment and water discharge, at the same time. This is necessary for good correlation. It is worthwhile noting that the vertical distribution of concentrations obtained by this sampler is regular and rather close to the expected theoretical curve. The amount of sediment collected at each point is sufficient to analyze the grain size distribution, so that the transport of suspended sediments can be broken up into grain size classes. By using this method, good information about the quantity and grain size of suspended sediment input in the reservoir could be obtained. A comparative study of five different types of suspended sediment samplers, including the one described, was carried out in 1979 on the Danube, in cooperation with the Delft Hydraulics

Laboratory (13). The results confirmed the excellent performance of the vacuum sampler.

Sediment Balance 1972–1979.—The input of sediment is monitored by regular measurements on the Danube and tributaries, and the output is measured daily immediately downstream of the dam. Table 13 summarizes the data obtained: The foregoing figures are in disagreement with findings of the author, the actual percentage of sediments trapped being considerably higher than that given in the paper. Table 10 of the paper gives the yearly average discharges of suspended load at Orsova, downstream from the dam, for the period 1972–1975. Based on this data, the total amount of sediment transported for the four years in question can be calculated. It amounts to 56.6 million tons. From the writers' Table 13 it can be seen that for the same period an output of only 12.1 million tons was obtained by concentration measurements immediately downstream from the dam. The difference can probably be attributed to different methods of suspended load determination, and only underlines the great importance of applying reliable methods of measurement.

Density of Sediment Deposits.—Since the sediment balance is calculated in weight, and the morphological changes are given in volume, the density of deposited sediment is a very significant parameter. In order to obtain reliable information on the density of reservoir deposits, several hundred samples were taken along the backwater reach by a new instrument specially constructed for this purpose (12). A cylinder is pushed into the muddy deposit and the sample frozen in the cylinder. It is then brought to the surface in a solid state. The sample is then cut into slices so that the density and grain size distribution of each layer can be determined. The densities obtained vary between 0.5 and 1.5, depending mainly on the grain size distribution. The average value of 1 ton/m^3 which was used by the author, in the writers opinion, can only serve as a preliminary estimate. Consolidation with time is of secondary importance, as compared with the other factors upon which the density of deposits depends.

Improvement of Mathematical Model.—The exact prediction of how sedimentation in the reservoir will progress in time is of significant practical importance. Along a length of about 200 k, the flood plain is protected by levees, and an increase of water levels, due to the deposited sediment in the river bed, may reduce the factor of safety of the levees. Remedial measures consist of removing the deposited sediment by dredging, or increasing the height of the levees. Either of these measures is very expensive thus, the prediction of sedimentation is of great interest. Apart from the regular program consisting of monitoring the sediment input and output, research has been conducted to improve the mathematical model which is being used for predictions.

Some of the most important research topics in this respect are the following:

1. Calibration of the sediment transport formula used in the model by field measurements and observations.
2. Investigation of the mobility of sediment deposits in the reservoir.
3. Determination of the settling properties of the suspended sediment by direct measurements in the field, with particluar attention given to modification of the grain size distribution of suspended sediments during settling.
4. Analysis of computational problems by applying appropriate techniques to the channel geometry, selection of time intervals, and reach lengths, etc.

Parallel to these efforts, basic research work is being conducted to obtain a theoretically more justified approach to sedimentation calculations, by making use of the modern concepts of turbulence modeling (11).

Appendix.—References

5. Bruk, S., "An Engineering Approach to Fluvial Processes in Nontidal Rivers with Sandy Bed," *International Symposium on River Sedimentation*, Beijing, China, 1980.
6. Bruk, S., "Reservoir Sedimentation," *IAHR/UNESCO Seminar on Hydraulic Research and River Basin Development*, Nairobi, Kenya, 1980.
7. Bruk, S., and Miloradov, V., "Calculation of sedimentation in backwater affected rivers with particular reference to the Djerdap High Dam," *Symposium on Current Problems in River Training and Sediment Movement*, Budapest, Hungary, 1968.
8. Bruk, S., and Miloradov, V., "Transport Capacity of Turbulent Two-Phase Flow," *Proceedings XIII Congress IAHR*, Tokyo, Japan, 1969.
9. Bruk, S., and Miloradov, V., "Bed Deformation due to Settling of Non-uniform Sediments in Backwater Affected Rivers," XIV Congress IAHR, Paris, France, 1971.
10. Gruat, J., and Milišić, V., "Role de la Turbulence dans le Mécanisme de Maintien des Particules Solides en Suspension," *XVII Congress IAHR*, Baden-Baden, Germany, 1977.
11. Hanjalić, K., Ivanović, M., Vujović, V., and Milišić, V., "Buoyancy Effects and Mutual Interaction of Suspended Particles and Velocity Field in Turbulent Shear Flow, *Symposium on the Structure of Turbulence and Heat and Mass Transfer*, Dubrovnik, Yugoslavia 1980.
12. Milišić, V., "Nouvel Appareil pour Prélever des Sediments au Fond des Rivieres," *XIX Congress IAHR*, New Delhi, India, 1981.
13. Milišić, V., "Comparative measurements of sediment transport, *IAHR Workshop on Particle Motion and Sediment Transport*, Rapperswil, Switzerland, 1981.
14. Miloradov, V., "Investigation of Suspended Sediment in the Danube and Confluents, Symposium on Current Problems in River Training and Sediment Movement," Budapest, Hungary, 1968.
15. Miloradov, V., and Bruk, S., "Mathematical Model of Sedimentation in Reservoirs and Rivers," *XVII Congress IAHR*, Baden-Baden, Yugoslavia, 1977.
16. Miloradov, V., and Djordjević, B., "Suspended Load Research," *Transactions*, Jaroslav Černi Institute, No. 41–42, Belgrade, Yugoslavia, 1967.
17. Miloradov, V., et al., Ionescu, E., et al., "Study of the Movement of Sediment Upstream from the Djerdap (Iron Gates) Dam," *Transactions*, Jaroslav Černi Institute, No. 50–52, Belgrade, Yugoslavia, 1972.
18. Petković, S., Milišić, V., and Božinović, M., "River Hydraulics and River Regulation," *Transactions*, Jaroslav Černi Institute, Belgrade, Yugoslavia, No. 60–63, 1977.

Total Load Transport in Alluvial Channels[a]

Discussion by William R. Brownlie,[4] A. M. ASCE

The authors have presented an interesting dimensional analysis of the sediment transport process in alluvial channels. Unfortunately, in working with the same data bank used by the authors, the writer has discovered a significant number of errors. Therefore, some of the statistical analyses presented may be inaccurate.

The data bank in question is the compilation of Peterson and Howells (9). This first attempt at developing a computerized data base is to be commended. However, before it can be used with total satisfaction, all of the errors must be eliminated.

A careful, item-by-item check suggests that four types of errors were made in the preparation of the data compendium (9).

1. Incorrect individual entries—these entries usually have incorrectly ordered digits or misplaced decimal points.
2. Conversion errors—errors made in converting the data to a standard format, typically involving conversion of transport rates to sediment format, typically involving conversion of transport rates to sediment concentrations.
3. Misinterpretation of data—this error usually involved whole columns of data, and probably occurred as a result of confusing notation in the data source.
4. Source errors—errors originating from incorrect publication of data, determined by checks on internal consistency. Also encountered were omissions of entries such as bed form and the gradation parameter (geometric standard deviation of bed particles), which could be determined, but were not given explicitly in original data sources.

The authors Table 1 indicates that all four types of errors are present in the subset of the data used here. The following is a description of some of the apparent errors that might be important to the present analyses. In the data of Sato and Kikkawa, authors set number 6, the grain size given in centimeters was read as millimeters. Therefore, the median sediment size should be 1.0 m, and not 0.1 m. The Straub data, set number 15, contains 3 concentration values which are a factor of 10 too high. For two sets of data by Vanoni and Hwang, numbers 17 and 19, the values given for discharge are really flow velocity, and the slope and depth entries are interchanged. An incorrect interpretation of the transport rate of the Williams data (set 38) as being given in dry unit weight per time instead of submerged weight resulted in an error of about 60% in the sediment concentration readings. The transport rate for

[a]February, 1981, by Kittur G. Ranga Raju, Ramachandra J. Garde, and Ramesh C. Bhardwaj (Proc. Paper 16020).

[4]Graduate Research Asst., W. M. Keck Lab. of Hydr., California Inst. of Tech., Pasadena, Calif. 91125.

the Indian Canal data, set number 49, given in metric tons was read as English short tons, causing a 12% error in sediment concentration.

A review of Table 1 suggests that perhaps about 10% of the data used contains serious errors. To reiterate, these apparent errors were not made by the authors, but rather in the preparation of the data compendium of Peterson and Howells (9). The exact effect on the statistical analyses is not known.

A new data compilation, with a computer format similar to (9) has been prepared at Caltech. Documentation for general release is now underway. The new compilation contains most, but not all, of the data sets in (9), as well as many additional data sets.

This discussion is based upon work supported by the National Science Foundation, under Grant CME79-20311.

Technical Papers

Original papers should be submitted in triplicate to the Manager of Technical and Professional Publications, ASCE, 345 East 47th Street, New York, N.Y. 10017. Authors must indicate the Technical Division or Council, Technical Committee, Subcommittee, and Task Committee (if any) to which the paper should be referred. Those who are planning to submit material will expedite the review and publication procedures by complying with the following basic requirements:

1. Titles must have a length not exceeding 50 characters and spaces.

2. The manuscript (an original ribbon copy and two duplicate copies) should be double-spaced on one side of 8-1/2-in. (220-mm) by 11-in. (280-mm) paper. Three copies of all figures and tables must be included.

3. Generally, the maximum length of a paper is 10,000 word-equivalents. As an *approximation*, each full manuscript page of text, tables or figures is the equivalent of 300 words. If a particular subject cannot be adequately presented within the 10,000-word limit, the paper should be accompanied by a rationale for the overlength. This will permit rapid review and approval by the Division or Council Publications and Executive Committees and the Society's Committee on Publications. Valuable contributions to the Society's publications are not intended to be discouraged by this procedure.

4. The author's full name, Society membership grade, and a footnote stating present employment must appear on the first page of the paper. Authors need not be Society members.

5. All mathematics must be typewritten and special symbols must be identified properly. The letter symbols used should be defined where they first appear, in figures, tables, or text, and arranged alphabetically in an appendix at the end of the paper titled Appendix.—Notation.

6. Standard definitions and symbols should be used. Reference should be made to the lists published by the American National Standards Institute and to the *Authors' Guide to the Publications of ASCE*.

7. Figures should be drawn in black ink, at a size that, with a 50% reduction, would have a published width in the *Journals* of from 3 in. (76 mm) to 4-1/2 in. (110 mm). The lettering must be legible at the reduced size. Photographs should be submitted as glossy prints. Explanations and descriptions must be placed in text rather than within the figure.

8. Tables should be typed (an original ribbon copy and two duplicates) on one side of 8-1/2-in. (220-mm) by 11-in. (280-mm) paper. An explanation of each table must appear in the text.

9. References cited in text should be arranged in alphabetical order in an appendix at the end of the paper, or preceding the Appendix.—Notation, as an Appendix.—References.

10. A list of key words and an information retrieval abstract of 175 words should be provided with each paper.

11. A summary of approximately 40 words must accompany the paper.

12. A set of conclusions must end the paper.

13. Dual units, i.e., U.S. Customary followed by SI (International System) units in parentheses, should be used throughout the paper.

14. A practical applications section should be included also, if appropriate.